Numerical Study of Pathways for Homogeneous Nucleation

Numerical Study of Pathways for Homogeneous Nucleation

Academisch Proefschrift

ter verkrijging van de graad van doctor aan de Universiteit van Amsterdam, op gezag van de Rector Magnificus prof. dr. J.J.M. Franse ten overstaan van een door het college voor promoties ingestelde commissie in het openbaar te verdedigen in de Aula der Universiteit op vrijdag 23 oktober 1998 te 9.00 uur

door

Pieter Reinder ten Wolde

geboren te Groningen

Promotiecommissie

Promotor: Prof. dr. D. Frenkel

Overige leden:
Dr. J. G. E. M. Fraaije
Dr. V. I. Kalikmanov
Prof. dr. H. N. W. Lekkerkerker
Prof. dr. D. W. Oxtoby
Prof. dr. B. Smit
Dr. W. L. Vos
Prof. dr. J. T. M. Walraven

Faculteit der Scheikunde

Cover: Froukje Bultsma

The work described in this thesis was performed at the FOM-Institute for Atomic- and Molecular Physics, Kruislaan 407, 1098 SJ, Amsterdam, The Netherlands. The work was supported in part by the Stichting Scheikundig Onderzoek Nederland (SON) with financial aid from the Nederlandse Organisatie voor Wetenschappelijk Onderzoek (NWO). The work of the FOM-institute is part of the research program of the Stichting Fundamenteel Onderzoek der Materie (FOM) and is supported by NWO. The work was sponsored by the National Computing Facilities Foundation (NCF).

ISBN 90-9012058-0

Subject headings: nucleation/ crystallization/ condensation/ computer simulation

This thesis is based on the following papers:

Chapter 3:
Numerical Evidence for bcc Ordering at the Surface of a Critical fcc Nucleus,
P. R. ten Wolde, M. J. Ruiz-Montero, and D. Frenkel,
Phys. Rev. Lett. **75**, 2714 (1995).

Numerical calculation of the rate of crystal nucleation in a Lennard-Jones system at moderate undercooling,
P. R. ten Wolde, M. J. Ruiz-Montero, and D. Frenkel,
J. Chem. Phys. **104**, 9932 (1996).

Chapter 4:
Simulation of homogeneous crystal nucleation close to coexistence,
P. R. ten Wolde, M. J. Ruiz-Montero, and D. Frenkel,
Faraday Discuss. **104**, 93 (1996).

Chapter 5:
Computer-simulation study of gas-liquid nucleation in a Lennard-Jones system,
P. R. ten Wolde and D. Frenkel,
accepted for publication in J. Chem. Phys.

Chapter 6:
Numerical calculation of the rate of homogeneous gas-liquid nucleation in a Lennard-Jones system,
P. R. ten Wolde, M. J. Ruiz-Montero, and D. Frenkel,
submitted to J. Chem. Phys.

Chapter 7:
Numerical study of gas-liquid nucleation in partially miscible binary mixtures,
P. R. ten Wolde and D. Frenkel,
accepted for publication in J. Chem. Phys.

Chapter 8:
Coil-Globule Transition in Gas-Liquid Nucleation of Polar Fluids,
P. R. ten Wolde, D. W. Oxtoby, and D. Frenkel,
accepted for publication in Phys. Rev. Lett.

Chain formation in homogeneous gas-liquid nucleation of polar fluids,
P. R. ten Wolde, D. W. Oxtoby, and D. Frenkel,
to be submitted to J. Chem. Phys.

Chapter 9:
Enhancement of Protein Crystal Nucleation by Critical Density Fluctuations,
P. R. ten Wolde and D. Frenkel,
Science **277**, 1975 (1997).

Enhanced protein crystallization by metastable critical point,
P. R. ten Wolde and D. Frenkel,
accepted for publication in Theoretical Chemistry Accounts.

Contents

1 Introduction

1.1 Undercooling

It is widely believed that if air containing water vapor is cooled to its dew point, droplets of water are formed. Similarly, it is commonly thought that if water is cooled to 0°C, it freezes. Although common experience seems to support both views, they are not correct. It is only when vapor and liquid are cooled *well* below the condensation and freezing point, respectively, that the transition from one phase to the other occurs.

Already in the beginning of the 18th century observations of this phenomenon of undercooling were reported. Fahrenheit [1] found that boiled water could be kept overnight at the undercooled temperature of −9°C (16°F) without freezing. Only when small ice particles were introduced was the crystallization process initiated, and the temperature of the ice-water mixture rose to 0°C, the "freezing" point of water. At the end of the last century Ostwald [2] noted that highly supercooled melts, which he called "labil", crystallize spontaneously, whereas weakly undercooled liquids, which he called "metastabil", only crystallize after, for instance, "ein leises Überstreichen eines Menschenhaares".

Why can we supersaturate a vapor or undercool a liquid? This is not obvious because, beyond the saturation point, the liquid is more stable than the vapor and below the freezing point the solid is more stable than the liquid. It would seem natural that when a phase is cooled to its coexistence point, small amounts of the new phase will appear. In fact, in many textbooks it is asserted that when a phase is progressively cooled below its coexistence point, steadily increasing amounts of the new phase will indeed be formed.

In this context it is instructive to consider the generic phase diagram in Fig. 1.1. Depending on the temperature and density, the system can occur in three phases–a vapor, a liquid, and a crystalline phase. Now suppose that we prepare our system in state A, i.e. in the vapor phase, and slowly compress the system towards state B, the saturation point. If we then increase the density even further, macroscopic thermodynamics would tell us that we enter the vapor-liquid coexistence region, and, according to the lever rule, increasing amounts of the liquid phase should be formed. However, in practice, when we slightly compress the system beyond the saturation point B, we will not observe the formation of liquid at all. The system remains in the vapor state and behaves as if the saturation point simply does not exist.

The problem is illustrated in Fig. 1.2, which shows the chemical potential μ as a function of pressure P at a given temperature. At the liquid-vapor coexistence point B, the chemical potential of the vapor is equal to that of the liquid. For higher pressures, the liquid is more stable than the vapor. However, when the system is compressed

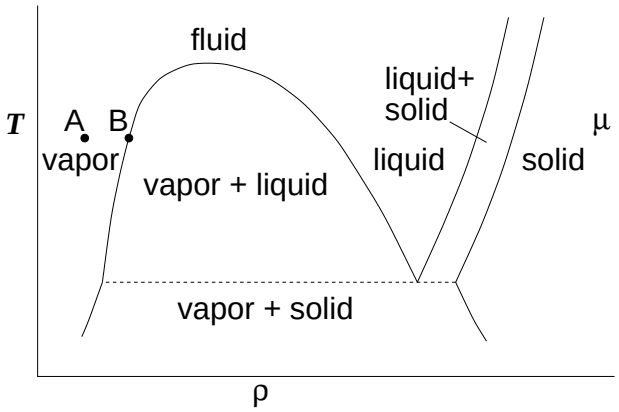

FIGURE 1.1 Generic temperature-density phase diagram.

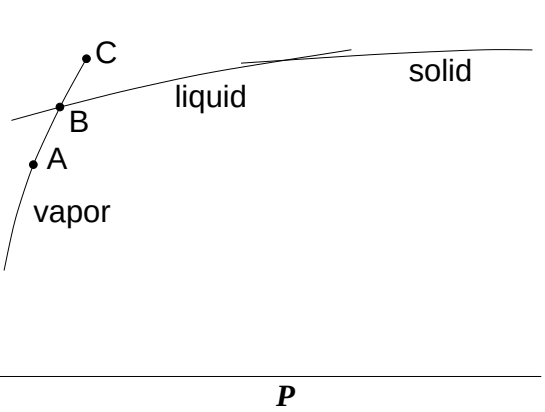

FIGURE 1.2 Chemical potential μ as a function of the pressure P.

beyond the coexistence point, it will follow the vapor isotherm, and not "jump" to the liquid isotherm.

So far I have only indicated why it should not be possible to supersaturate a system. What is then the reason for this phenomenon? The answer is that the only route to the more stable state is via the formation of small *nuclei* [1]. The free energy of such nuclei is determined not only by the difference in chemical potential between vapor and liquid, which drives the nucleation process, but also by the surface free energy. The surface free energy term is always positive, because of the work that must be done to create an interface. Moreover, initially this term dominates and hence the free energy of a nucleus increases with size. Only when the droplet has reached a certain "critical" size, the volume term takes over, and the free energy decreases. It is only from here on that the nucleus grows spontaneously into a bulk liquid.

Gibbs [3] was the first to realize that the stability of a phase is related to the work that has to be done to create a critical nucleus of the new phase. However, the relevance of his work to nucleation remained largely unrecognized until the 1920's and 1930's when Volmer and Weber [4], and Becker and Döring [5] laid the foundations for what is now called classical nucleation theory. In classical nucleation theory it is assumed that the nuclei are compact, spherical objects, that behave like small droplets of bulk phase. As will be discussed in more detail in chapter 2, the free energy of a spherical liquid droplet of radius R in a vapor is then given by

$$\Delta G = 4\pi R^2 \gamma + \frac{4}{3}\pi R^3 \rho \Delta\mu, \tag{1.1}$$

where γ is the surface free energy, ρ is the density of the bulk liquid, and $\Delta\mu$ is the difference in chemical potential between bulk liquid and bulk vapor. Clearly, the first term on the right hand side of Eq. (1.1) is the surface term, which is positive, and the second term is the volume term, which is negative. Fig. 1.3 shows the free energy of a nucleus as a function of R. It is seen that the free energy goes through a maximum. The height of the nucleation barrier can easily be obtained from the above expression,

[1] We will not discuss the mechanism of spinodal decomposition; thus we consider states between points B and C, but not too close to point C, in Fig. 1.2.

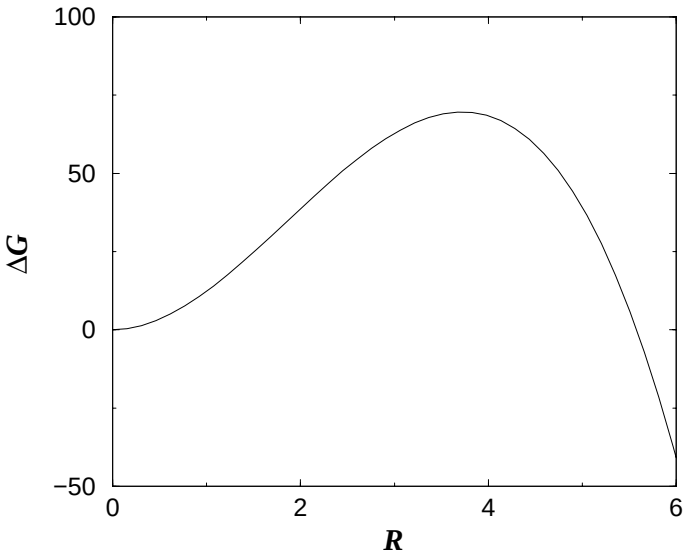

FIGURE 1.3 The free-energy ΔG of a spherical nucleus as a function of its radius R.

yielding

$$\Delta G^* = \frac{16\pi\gamma^3}{3\rho^2\Delta\mu^2}. \tag{1.2}$$

This equation shows that the barrier height depends not only on the surface free energy γ (and the density ρ), but also on the difference in chemical potential $\Delta\mu$. The difference in chemical potential is related to the supersaturation, as can be seen from Fig. 1.2. Hence, the height of the free-energy barrier that separates the stable from the metastable phase depends on the degree of supersaturation. At coexistence, the difference in chemical potential is zero, and the height of the barrier is infinite. Although the system is equally likely in the liquid and vapor phase, once the system is one state or the other, the system will remain in this state; it simply cannot transform into the other state.

The phenomenon of undercooling is not only interesting from an academic point of view, but also has many practical consequences. In materials science, it is well known that the structural and mechanical properties of metals that are formed from an undercooled melt are determined by the rate of crystallization [6, 7]. In particular, in rapid solidification techniques metastable phases are selected over the thermodynamically most stable phase by exploiting the higher nucleation rate of the metastable phases [8]. Bosio *et al.* [9, 10] demonstrated that when a gallium melt is cooled around -75°C, the stable α phase is nucleated, but that when the melt is undercooled further, more than four different metastable phases can be formed. In atmospheric science, the nucleation of both water droplets and ice crystals in the atmosphere has a major effect both in the short term on the weather and in the long term on the climate. Furthermore, certain biological processes that lead to diseases such as sickle-cell anemia, cataracts, Alzheimer's, and prion diseases like Creutzfeld-Jacob, are thought to involve the nucleation of a protein condensate.

Because of its importance in many fields of science and technology, nucleation has been the subject of extensive experimental and theoretical study. Many attempts have been made to refine classical nucleation theory [11]. In addition, extensions of classical nucleation theory have been proposed [12, 13] and novel theoretical methods have been

developed that make it possible to go beyond the essentially macroscopic description of classical nucleation theory [14]. In parallel, over the past years the experimental techniques have greatly been improved and nucleation rates can be measured with unprecedented accuracy [6, 15, 16]. However, our understanding of the nucleation process at a microscopic level is still limited. The reason is that nucleation is an activated process.

In experiments the height of the barrier is typically on the order of $75k_BT$, where k_BT is the thermal energy. This means that the probability to find a nucleus at the top of the nucleation barrier is extremely small, on the order of 10^{-12} per cm^3. Moreover, once the system is at the top of the barrier, it quickly proceeds to the liquid state, or returns to the vapor state–the time it spends at the top of the barrier is on the order of pico-seconds to nano-seconds for atomic or simple molecular systems. Hence, nucleation is both infrequent and fast. It is precisely for this reason that it is very difficult to study the critical nuclei directly in an experiment. Yet, it is the structure and dynamics of these critical nuclei that play a crucial role in the nucleation process. Computer simulations are a natural tool to study the nucleation process.

The most straightforward application of molecular dynamics simulations to nucleation is to supercool the system and then simply *wait* for nuclei to appear [17–25]. However, this approach cannot be used to study nucleation under typical experimental conditions. In computer simulations, we are limited to studying relatively small systems (say, of the order of a million particles or less). This means that the volume of the simulation box is less than 10^{-16} cm^3. Experimentally observable nucleation rates of the order of one nucleus per cm^3 per second, would correspond to the formation of one nucleus per 10^{16} seconds in our simulation box. If we take a typical value of 10^{-14} seconds for the length of the molecular-dynamics time-step, then to observe on average one nucleation event, 10^{30} time-steps would be needed in a simulation of 10^6 particles. As the nucleation barrier decreases as $1/\Delta T^2$, where ΔT is the degree of supercooling, very large supercoolings (in the order of 40%) have to be imposed to observe spontaneous nucleation in a conventional simulation.

However, we are interested in nucleation at moderate, i.e. more realistic undercooling. We therefore separate the problem into two parts: 1) the computation of the free-energy barrier for nucleation and 2) the computation of the rate at which this barrier is crossed. For the computation of the free-energy barrier that separates the stable phase from the metastable phase, we use the umbrella sampling scheme [26, 27]. The rate at which this barrier is crossed is computed using the Bennett-Chandler scheme [28–31]. Over the past years, much progress has been made in deriving statistical mechanical expressions for the rate of activated process that are convenient to use in numerical simulations. However, much of this work is concerned with relatively simple barrier crossings, involving a reaction coordinate that is *local*, rather than *global*. In contrast, in the present work the reaction coordinate that connects the metastable phase with the stable phase is a global order parameter, that depends on the positions of *all* particles in the system. In this thesis, we compute the rate of barrier crossings associated with such complex (many-body) reaction coordinates.

Finally, let me come back to the opening paragraph, in which I stated that daily experience suggests that water freezes around 0°C and that water vapor condenses around 100°C. What is misleading us? The answer is that in practice phase transitions are

usually assisted by impurities, dust particles, container walls, or, in general, any foreign body that is present in the system. The nuclei that initiate the phase transformation are then formed at the surfaces of these foreign bodies. The nucleation barrier for this process, called heterogeneous nucleation, is usually much lower than for homogeneous nucleation occurring in the bulk of a pure phase. Consequently, in practice vapor and liquids usually condense and freeze at a much smaller degree of supersaturation than can be reached for pure substances.

This thesis is devoted to homogeneous nucleation. One reason is that homogeneous nucleation is still not well understood, let alone heterogeneous nucleation. The second reason is that almost all nucleation theories are concerned with homogeneous nucleation. For the same reason, most experiments are devoted to studying homogeneous nucleation. They are therefore designed such as to exclude the heterogeneous nucleation process. Obviously, one can reduce the effect of impurities by purifying the sample, although in practice this can be quite difficult, especially for liquids. Another approach, in case of crystal nucleation from the melt, is to study nucleation in small liquid droplets, rather than in a bulk liquid. To this end, several techniques have been developed. One is the droplet emulsion technique [6], in which the liquid is dispersed into a large number of small droplets in an appropriate medium; another technique for metals is to levitate droplets in an electro-magnetic field [6]. The basic idea behind these techniques is that if the droplets are sufficiently fine, a significant number of them will contain no impurities and thus no such heterogeneous sites. However, another source of heterogeneous nucleation is much more difficult to eliminate: the surface of the container, or, in case of the droplet technique, the surface of the droplet. The effect of surface nucleation can be reduced by providing a less active coating of the container wall or by choosing the right medium for the droplet suspension, but it can never be eliminated entirely. Even liquid droplets in vacuum have a free surface that can affect the nucleation process. It is thus clear that in an experiment it is very hard to eliminate heterogeneous sites. However, in a computer simulation this is trivial. Computer simulations are therefore an excellent instrument to study homogeneous nucleation.

1.2 Overview

Macroscopic thermodynamics dictates that the phase which is formed in a supersaturated system is the one that has the lowest free energy. However, nucleation is an essentially dynamic process, and therefore one cannot expect *a priori* that, on supersaturating the system, the thermodynamically most stable phase will be formed. In 1897, Ostwald [2] formulated his "step" rule, stating that the crystal phase that is nucleated from the melt need not be the one that is thermodynamically most stable, but the one that is closest in free energy to the fluid phase. In this thesis we will demonstrate several manifestations of the Ostwald step rule. However, the picture that will emerge is more complex.

In chapter 3 we study crystal nucleation in a Lennard-Jones system at moderate supercooling. The stable structure of the Lennard-Jones solid is known to be face-centered cubic (fcc). However, according to the Ostwald step rule the formation of metastable phases cannot be excluded. More recently, Alexander and McTague [32] have argued on the basis of Landau theory, that at least for small undercooling, nucleation

of the body-centered cubic (bcc) phase should uniquely be favored. However, in nearly all simulation studies the formation of fcc nuclei was observed. Of interest is a study by Swope and Andersen [25] on a system of one million Lennard-Jones particles. They showed that although both bcc and fcc crystallites are formed in the early stages of the nucleation process, only the fcc nuclei grow into larger crystallites. It should be noted however, that in all these simulation studies very large degrees of undercooling had to be imposed to see any crystal formation on the time scale of the simulation. For such large undercoolings, the free-energy barrier for nucleation into essentially all possible crystal phases is very small. It is therefore not obvious that crystal nucleation at large undercooling will proceed in the same way as close to coexistence. Using the umbrella-sampling technique [26, 27], we are able to study nucleation at experimental degrees of undercooling. We find that the precritical nuclei are predominantly bcc ordered. But as the nucleus grows to its critical size, the core becomes fcc ordered. However, the interface of the critical nucleus retains a high degree of bcc-like ordering. The crystal nucleation process in the Lennard-Jones system can be interpreted as a manifestation of the Ostwald step rule. First a metastable bcc phase is nucleated, which is then transformed into the stable fcc phase.

The Ostwald-step rule is usually applied to fluid-solid transitions. However, in chapter 8 we demonstrate that also in gas-liquid nucleation the Ostwald-step rule is sometimes "obeyed". In this chapter we study homogeneous gas-liquid nucleation in a strongly polar Stockmayer fluid. While the nucleation rates of non-polar substances are in fair agreement with the predictions of classical nucleation, the nucleation rates of strongly polar substances, such as as acetonitrile, nitrobenzene and benzonitrile [33, 34], are seriously overestimated by classical nucleation theory. It has therefore been suggested that the anisotropic nature of the dipole-dipole interaction plays a crucial role in determining the structure and free energy of the nuclei. Indeed, for bulk hard-sphere and soft-sphere dipolar fluids at low temperature, it has been observed that particles associate into chains [35, 36]. On the other hand, the bulk liquid phase of the Stockmayer fluid, in which also dispersive attractions are present, is isotropic and does not exhibit significant chain formation. We find that the condensation process is initiated by chain-like clusters, rather than by small liquid droplets. As the cluster size is increased, the chains become longer. However, beyond a certain size, the clusters collapse to form compact, spherical clusters. Surprisingly though, in the interface a high degree of chain formation is preserved.

Another manifestation of the Ostwald-step rule is found in the case of protein crystal nucleation, which is discussed in chapter 9. Proteins are notoriously difficult to crystallize and the experiments indicate that the success of protein crystallization depends very sensitively on the physical conditions of the initial solution. In particular, it has been found that a variety of globular proteins only crystallize in a rather narrow region in the phase-diagram [37, 38]. However, the origin of this crystallization "window" remained unclear. Our simulations show that the presence of a metastable critical point in this window strongly reduces the free-energy barrier for crystal nucleation and hence increases the nucleation rate by many orders of magnitude. The reason for this is that the metastable critical point drastically changes the pathway for the formation of the critical nucleus. Near the critical point, the nucleus that is formed initially, is not simply

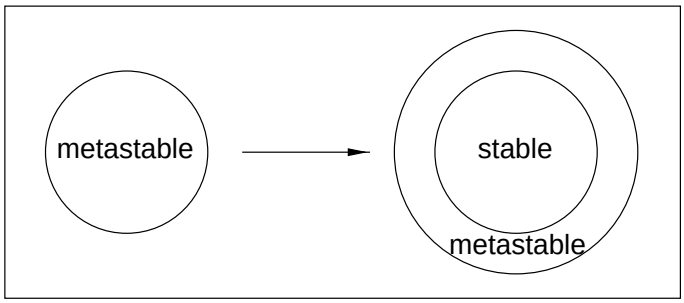

FIGURE 1.4 Sketch of the pathway for the formation of a critical nucleus. In the case of crystal nucleation from the melt in a Lennard-Jones system the metastable phase is the body-centered cubic phase and the stable phase is the face-centered cubic phase. In gas-liquid nucleation of a polar fluid the metastable phase corresponds to chains and the stable phase to an isotropic liquid. In the case of protein crystal nucleation the intermediate phase is a high-density liquid and the stable phase is the crystalline phase.

a small crystallite, but rather a high-density liquidlike droplet; only when the droplet has reached a certain size, does it start to crystallize inside the core.

In Fig. 1.4 we have sketched the path for the formation of a critical nucleus in the systems discussed above. In all these cases the nucleation process can be interpreted as a manifestation of the Ostwald-step rule. First a metastable phase is nucleated (bcc/chains/liquid), which then slowly transforms into the stable phase (fcc/liquid/fcc-crystal). Interestingly, in the interface of the larger nuclei traces of the structure of the smaller nuclei are retained.

Nucleation does not always proceed via intermediate steps, as predicted by the Ostwald step rule. In chapters 5 and 6 we study homogeneous gas-liquid nucleation in a Lennard-Jones system. In this case the nucleation process only involves "one step", namely the formation of a liquid droplet. In these chapters we compare the barrier height, the critical nucleus size, and the kinetic prefactor with the predictions of classical nucleation theory. In agreement with the relations recently proposed by McGraw and Laaksonen [12, 13], we find that the size of the critical nucleus is correctly predicted by classical nucleation theory, and that the offset between the predicted barrier height and the height of the nucleation barrier as found from the simulations is constant, and independent of supersaturation. The kinetic prefactor is about one order of magnitude larger than predicted by classical nucleation theory.

Furthermore, in chapter 5 we discuss the difference between the mechanical and the thermodynamic definition of the surface tension and surface of tension. We find that both definitions are not equivalent, which implies that we cannot use a simple "mechanical" expression to compute the height of the nucleation barrier.

In chapter 7 we study homogeneous gas-liquid nucleation in a binary Lennard-Jones system. Recently, Talanquer and Oxtoby [39] suggested a new pathway for the formation of partially miscible binary mixtures. This path would involve nuclei of cylindrical shape inside which the species are phase separated. We find that the nucleation of mixtures that show a macroscopic miscibility gap, is initiated by clusters in which both species are mixed. However, when the cluster size is increased the path bifurcates and two channels

develop, corresponding to nuclei enriched in one of the two components. In all cases, the critical nuclei are spherical. The cylindrical, micro-phase separated nuclei predicted by Talanquer and Oxtoby only appear at the top of the free-energy ridge separating the two types of critical nuclei. These clusters correspond to local free-energy *maxima* and they probably play no role in the nucleation process.

In chapter 4 we discuss a more technical aspect of the simulations, namely the choice of the reaction coordinate. But first, in chapter 2, we review some aspects of the thermodynamics of small droplets for readers who are not familiar with this subject.

2 Thermodynamics of small droplets

In this chapter we briefly review the thermodynamics of small droplets. Subsequently, we discuss the theory that is most widely used to describe the nucleation process: classical nucleation theory. Next, we consider the discrepancy between experiments and classical nucleation theory and discuss the extensions of classical nucleation theory that McGraw and Laaksonen proposed to resolve this discrepancy. We present a simple derivation of the nucleation theorem. This theorem plays a crucial role in the analysis of experimental nucleation data because it allows us to determine the size and composition of the critical nucleus from the measured nucleation rates.

2.1 Introduction

When a vapor is supersaturated, the liquid is more stable than the vapor. However, the vapor will not condense immediately. First, nuclei of the liquid phase have to be formed. This is an activated process. The droplets have to cross a free-energy barrier in order to grow into a bulk liquid. Nuclei at the top of the free-energy barrier are called critical nuclei. Nuclei that are smaller than the critical nucleus size, the so-called precritical nuclei, have a tendency to shrink, because in that way they can lower their free energy. For the same reason, nuclei that are larger than the critical size, the so-called postcritical nuclei, tend to grow.

The nuclei at the top of the barrier play a crucial in the nucleation process. It is the structure and the free energy of the critical nuclei that determine the height of the nucleation barrier and hence the nucleation rate. For this reason all nucleation theories are concerned with the description of the nuclei at the top of the nucleation barrier.

In this chapter we first discuss some aspects of the thermodynamics of droplets that are useful to understand nucleation. In this discussion we borrow heavily from the excellent reviews by Ono and Kondo [40] and Rowlinson and Widom [41], as well as from the earlier papers by Gibbs [3] and Tolman [42]. We then describe classical nucleation theory and the extensions recently proposed by McGraw and Laaksonen [12, 13]. We conclude with a derivation of the nucleation theorem. Using the nucleation theorem it is possible to derive the size and composition of critical nuclei from the variation of the nucleation rate with supersaturation.

2.2 Thermodynamics of droplets

2.2.1 Fundamental thermodynamic relations

Consider a spherical drop of phase α surrounded by a phase β. The two phases meet in a thin transition layer of physical inhomogeneity. However, it is convenient to treat the two phases as being uniform up to an imaginary geometrical surface that divides the two phases. This surface was called by Gibbs [3] the *dividing surface*.

In the following, we focus our attention on a small part of the system contained in a conical vessel, as indicated in Fig. 2.1. Here ω is the solid angle and R denotes the location of the dividing surface. After we have specified the position of the dividing surface, we can define the volumes V_α and V_β. From the geometry of the cone we find

$$\begin{aligned} V_\alpha &= \frac{1}{3}\omega\left\{R^3 - R_\alpha^3\right\}, \\ V_\beta &= \frac{1}{3}\omega\left\{R_\beta^3 - R^3\right\}. \end{aligned} \tag{2.1}$$

The area of the dividing surface A is given by

$$A = \omega R^2. \tag{2.2}$$

Let us now derive the total internal energy of the system. We postulate that the internal energy U is a homogeneous first-order function of the extensive parameters S, ω and N:

$$U = U(S, \omega, N). \tag{2.3}$$

We identify S with the total entropy of the system and N is the total number of particles. The first differential of the fundamental equation is given by

$$dU = TdS + \eta d\omega + \mu dN, \tag{2.4}$$

where T is the temperature, μ is the chemical potential and η is the intensive variable conjugate to the extensive variable ω. The term $\eta d\omega$ is related to the work dW associated

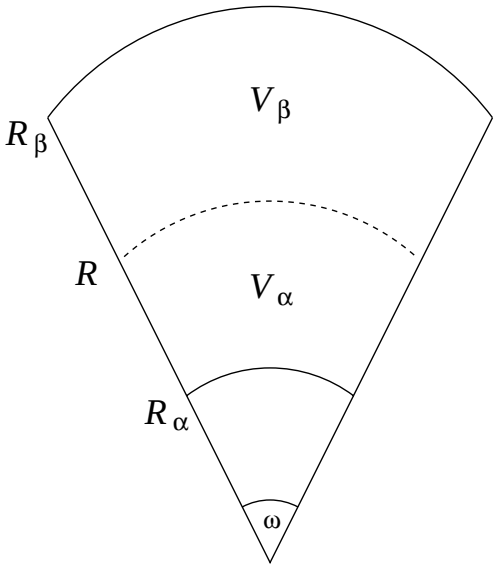

FIGURE 2.1 Conical section of the spherical drop of phase α surrounded by a phase β. ω is the opening angle of the cone and R denotes the location of the dividing surface.

with an increase $d\omega$ of the opening angle. It is given quantitatively by

$$dW = -\eta d\omega = p_\alpha dV_\alpha + p_\beta dV_\beta - \gamma dA. \tag{2.5}$$

Here p_α and p_β are the pressures in phase α and β, respectively. The last term γdA takes into account the contribution of the interface. The coefficient γ is the surface tension. It is an (intensive) parameter yielding the change in free energy upon an increase in the area of the interface *at constant curvature*.

The total internal energy now follows from the definition of the homogeneous first-order property [43] of the fundamental relation in Eq. (2.3). We find

$$U = TS + \eta\omega + \mu N = TS - p_\alpha V_\alpha - p_\beta V_\beta + \gamma A + \mu N. \tag{2.6}$$

The Helmholtz free energy F is obtained by a Legendre transformation of the internal energy:

$$F = \eta\omega + \mu N = \gamma A - p_\alpha V_\alpha - p_\beta V_\beta + \mu N. \tag{2.7}$$

2.2.2 Laplace equation

When a droplet is in equilibrium with the vapor, the pressure of the fluid inside is larger than that of the vapor outside. However, the larger pressure inside the drop is counterbalanced by the surface tension. The magnitude of the pressure difference depends not only on the surface tension, but also on the size of the droplet.

The Laplace equation provides a relation between the pressure difference over the droplet, the surface tension and the droplet size. It can be derived from Eq. (2.5). We note that the changes in V_α and V_β are caused by a variation in ω. It then follows from the geometry of the cone that

$$\gamma = \frac{1}{3}R(p_\alpha - p_\beta) + \frac{1}{R^2}\left(\eta + \frac{1}{3}R_\beta^3 p_\beta - \frac{1}{3}R_\alpha^3 p_\alpha\right). \tag{2.8}$$

The Laplace equation is now obtained by differentiating Eq. (2.8) with respect to R:

$$p_\alpha - p_\beta \equiv \Delta p = \frac{2\gamma}{R} + \left[\frac{\partial\gamma}{\partial R}\right]. \tag{2.9}$$

The second term is enclosed in square brackets to indicate that it denotes the change in the surface tension associated with a *mathematical* displacement of the location of the dividing surface; it does not correspond to any *physical* change. In the following we will call such a derivative a notational derivative.

The concept of a dividing surface has only been introduced for mathematical convenience. This implies that the free energy of the system should not depend on its location. To see that this is indeed so, let us first consider the work done by the system by not only a variation in ω, but also by a change in R_α and R_β. It is given by

$$dW = -\eta d\omega + p_\beta \omega R_\beta^2 dR_\beta - p_\alpha \omega R_\alpha^2 dR_\alpha. \tag{2.10}$$

The change in free energy F associated with these changes is given by

$$dF = -dW - SdT + \mu dN. \tag{2.11}$$

Using Eq. (2.9), and Eqs. (2.1) and (2.2), we then find

$$\begin{aligned} dF &= -SdT - p_\alpha dV_\alpha - p_\beta dV_\beta + \gamma dA + \left[\frac{d\gamma}{dR}\right] AdR + \mu dN \\ &= -SdT - p_\alpha dV_\alpha - p_\beta dV_\beta + \gamma dA + \left\{(p_\alpha - p_\beta) - \frac{2\gamma}{R}\right\} AdR + \mu dN. \end{aligned} \tag{2.12}$$

From this equation it is easily found that that $dF = 0$ for an infinitesimal variation of the location of the dividing surface, for which the following relations hold:

$$dV_\alpha = -dV_\beta = AdR, dA = 2A\frac{dR}{R}. \tag{2.13}$$

It is clear that the free energy of the total system does not depend on the location of the dividing surface. However, the surface tension does depend on our choice for the location of the dividing surface. Below, we discuss this in more detail.

2.2.3 The surface of tension

The pressure difference over the surface of a drop is a well-defined quantity, which is insensitive to the choice of the location of the dividing surface. It then follows from the generalized Laplace equation, i.e. Eq. (2.9), that, in general, γ must formally be a function of R. Following Gibbs [3] we now define the surface for which

$$\left[\frac{\partial\gamma}{\partial R}\right]_{R_s} = 0 \tag{2.14}$$

to be the *surface of tension*. It is only for this dividing surface that the generalized Laplace equation reduces to

$$p_\alpha - p_\beta = \frac{2\gamma_s}{R_s}, \tag{2.15}$$

where the subscript s denotes that we consider the surface of tension.

The complete dependence of γ on R can easily be obtained. Using the above equation and Eq. (2.8) for $R = R_s$ (with $\gamma(R_s) \equiv \gamma_s$), we can write η in terms of R_s and γ_s:

$$\eta = \frac{1}{3}\gamma_s R_s^2 - \frac{1}{3}R_\beta^3 p_\beta + \frac{1}{3}R_\alpha^3 p_\alpha \tag{2.16}$$

Substituting the expression for η in Eq. (2.8) and writing $p_\alpha - p_\beta$ in terms of γ_s and R_s gives

$$\begin{aligned} \gamma &= \frac{R_s^2\gamma_s}{3R^2} + \frac{2\gamma_s R}{3R_s}. \\ &= \gamma_s\left\{1 + \frac{(R-R_s)^2}{R_s^2} + \mathcal{O}\left(\frac{R-R_s}{R_s}\right)^3\right\}. \end{aligned} \tag{2.17}$$

In Fig. 2.2 we have plotted, for a given droplet, γ as a function of the position of the dividing surface denoted by R. It is seen that the surface tension γ exhibits a minimum at the surface of tension. Note also that from the last line in the above equation it follows that, as long as the thickness of the interface is small compared to the size of the droplet, γ is close to the minimum value γ_s.

2.2.4 Equimolar dividing surface

Before we discuss the equimolar dividing surface, let us first consider the free energies of the phases α and β. We define the free energies to be

$$\begin{aligned} F_\alpha &= -p_\alpha V_\alpha + \mu N_\alpha, \\ F_\beta &= -p_\beta V_\beta + \mu N_\beta, \end{aligned} \tag{2.18}$$

where N_α and N_β are the number of particles in phase α and β, respectively. We can then obtain the surface free energy F_s by subtracting the free energies of the "homogeneous" phases α and β from the total free energy F, as given in Eq. (2.7):

$$F_s = \gamma A + \mu N_s, \tag{2.19}$$

where we have used that $N = N_\alpha + N_\beta + N_s$, with N_s the number of particles at the dividing surface. Note also that we have exploited the fact that at the top of the barrier the droplet is in equilibrium with the vapor, so that the chemical potential is uniform throughout the system. Now the surface for which N_s is zero is called the *equimolar dividing surface*. The equimolar dividing surface is not only convenient because N_s is zero, it is also useful because for this (and only this) dividing surface the change in the surface tension due to an actual change of the radius of the droplet (which, in general, is associated with some change in p_α and p_β), is equal to the change in surface tension due to a mathematical displacement of the location of the dividing surface (in which the physical conditions are unaltered). That is,

$$\left[\frac{\partial \gamma}{\partial R}\right]_{R=R_e} = \left(\frac{\partial \gamma_e}{\partial R_e}\right)_T. \tag{2.20}$$

The above relation can easily be derived from the Gibbs-Duhem relation for the interface. This is shown in appendix A.

2.2.5 Curvature dependence of surface tension

2.2.5.1 *Tolman length* The Tolman length is an important quantity as it describes the first-order curvature correction to the surface tension. The Tolman length is defined

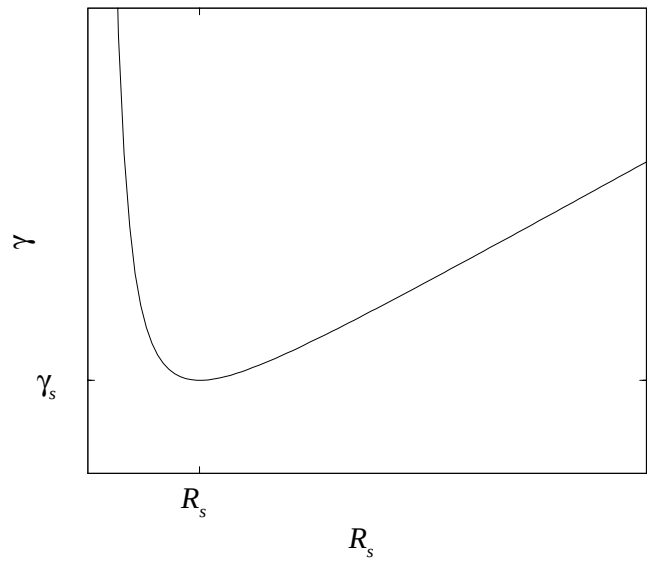

FIGURE 2.2 The surface tension γ as a function of R, as given by Eq. (2.17). The surface for which γ possesses a minimum is called the surface of tension.

as the difference δ between the radius of the surface of tension and the radius of the equimolar dividing surface:

$$\delta = R_e - R_s. \tag{2.21}$$

The Tolman-length can be related to the superficial density , $_s = N_s/A_s$ at the surface of tension. It follows from the Gibbs-Duhem relations for the interface and the two phases α and β that this superficial density determines the variation of the surface tension with droplet size.

At constant temperature and at the surface of tension, the Gibbs-Duhem relation (see appendix A) reduces to

$$d\gamma_s = -, \, _s d\mu. \tag{2.22}$$

The Gibbs-Duhem relations for the homogeneous phases α and β, are, for isothermal variations,

$$d\mu = \frac{dp_\alpha}{\rho_\alpha} = \frac{dp_\beta}{\rho_\beta} \tag{2.23}$$

where ρ_α and ρ_β are the densities of the liquid and gas phase. Combing Eqs. (2.22) and (2.23) gives

$$d\gamma_s = -\frac{, \, _s}{\rho_\alpha} dp_\alpha = -\frac{, \, _s}{\rho_\beta} dp_\beta = -\frac{, \, _s}{\rho_\alpha - \rho_\beta} d(p_\alpha - p_\beta). \tag{2.24}$$

The pressure difference $p_\alpha - p_\beta$ can be related to the surface tension via the Laplace equation. This yields

$$\frac{1}{\gamma_s}\frac{d\gamma_s}{dR_s} = \frac{[2/R_s^2][, \, _s/(\rho_\alpha - \rho_\beta)]}{1 + [2/R_s][, \, _s/(\rho_\alpha - \rho_\beta)]}. \tag{2.25}$$

As shown in appendix B, the superficial density is related to the Tolman-length via

$$, \, _s = (\rho_\alpha - \rho_\beta)\delta[1 + (\delta/R_s) + \frac{1}{3}(\delta^2/R_s^2)]. \tag{2.26}$$

We can substitute this expression into Eq. (2.25) and integrate it with respect to R_s, which can be taken as an independent state variable. Neglecting the terms δ/R_s and $\delta^2/3R_s^2$, that are usually small in comparison with unity, and taking δ to be constant, we can easily carry out the integration and arrive at the well-known Tolman formula

$$\frac{\gamma_s(R_s)}{\gamma_\infty} = \frac{R_s}{R_s + 2\delta}. \tag{2.27}$$

The above equation allows us to write the Laplace equation in terms of the radius of the equimolar dividing surface and the surface tension of the planar interface. This is useful, because the computation of the position of the surface of tension is more cumbersome than that of the equimolar dividing surface, as the position of the equimolar dividing surface, in contrast to that of the surface of tension, can be obtained from the density profile of the droplet. Moreover, the surface tension of a planar interface is more easily determined than the surface tension of a droplet in a supersaturated vapor. From Eqs. (2.15), (2.21) and (2.27) it follows that

$$\Delta p = \frac{2\gamma_s}{R_s} = \frac{2\gamma_\infty}{R_s + 2\delta} = \frac{2\gamma_\infty}{R_e(1 + \delta/R_e)}. \tag{2.28}$$

In order to arrive at Eq. (2.27), we have neglected terms of δ/R_s and higher. It is therefore natural to expand $1/(1+\delta/R_e)$ up to first order to arrive at

$$\Delta p = \frac{2\gamma_\infty}{R_e}\left(1 - \frac{\delta}{R_e}\right). \tag{2.29}$$

The above equation gives the pressure difference in terms of the equimolar dividing surface and in terms of the surface tension of the planar interface, modified by a first-order correction "due to" the Tolman-length.

2.2.5.2 *Helfrich equation* In general, the surface free energy of a curved interface depends on the two principal radii of curvature R_1 and R_2. Helfrich [44] introduced the following expansion of the surface free energy in the inverse radii of curvature:

$$\gamma(R_1, R_2) = \gamma_\infty - \frac{k}{2}C_0^2 + \frac{k}{2}\left(\frac{1}{R_1} + \frac{1}{R_2} + C_0\right)^2 + \overline{k}\frac{1}{R_1 R_2}, \tag{2.30}$$

where γ_∞ is the surface tension of the planar interface, C_0 is the spontaneous curvature, k is the bending rigidity constant, and $\overline{k}$ is the rigidity constant associated with Gaussian curvature. From Eq. (2.30) it follows that for spherical interface with $R_1 = R_2 = R$ the surface free energy is given by

$$\gamma(R) = \gamma_\infty + 2kC_o\frac{1}{R} + (2k + \overline{k})\left(\frac{1}{R}\right)^2, \tag{2.31}$$

and its derivative with respect to R by

$$\frac{\partial\gamma}{\partial R} = -2kC_o\left(\frac{1}{R}\right)^2 - 2(2k + \overline{k})\left(\frac{1}{R}\right)^3. \tag{2.32}$$

In the previous sections we have seen that the definition of the radius of the droplet is ambiguous. We will identify R with the radius of the equimolar dividing surface, i.e. $R = R_e$ and $\gamma = \gamma_e$. In section 2.2.4 we derived that for this dividing surface the notational derivate of the surface tension with respect to R equals the actual derivative. Hence, the Laplace equation becomes

$$\Delta p = \frac{2\gamma_e}{R_e} + \left[\frac{\partial\gamma}{\partial R}\right]_{R_e} = \frac{2\gamma_e}{R_e} + \frac{\partial\gamma_e}{\partial R_e} = \frac{2\gamma_\infty}{R_e} + 2kC_o\left(\frac{1}{R_e}\right)^2. \tag{2.33}$$

By comparing this equation with Eq. (2.29), we find that the Tolman-length is given by

$$\delta = -\frac{kC_0}{\gamma_\infty}. \tag{2.34}$$

This formula shows that the Tolman-length is determined by the bending rigidity, the surface tension and the spontaneous curvature. The Tolman-length has been calculated both theoretically and numerically for the vapor-liquid interface in the Lennard-Jones system [45–47]. The studies indicate that the Tolman-length is close to zero. In chapter 5 we present a new numerical method by which the Tolman-length can be computed. We also find that the Tolman-length is zero within the numerical accuracy. Provided that the bending rigidity is non-zero, it is clear that this implies that the spontaneous curvature for the Lennard-Jones vapor-liquid interface is zero.

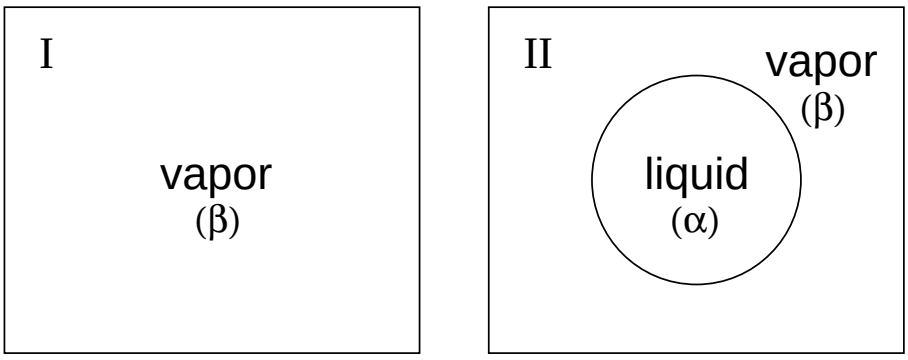

FIGURE 2.3 The formation of a nucleus from the parent phase. Initially, in state I, the system only contains a homogeneous parent phase. In state II the system contains a cluster in equilibrium with the parent phase. The free-energy barrier is given by the difference in Gibbs free energy between the two states. As an illustration, the parent phase β is the vapor phase and the new phase α is the liquid phase.

2.2.6 General expressions for the height of the nucleation barrier

We have now reached the point that we have obtained all the required relations to derive some useful expressions for the height of the nucleation barrier. In most nucleation experiments the volume and temperature are fixed and nucleation of clusters from the parent phase leads to a decrease of the pressure. However, the concentration of nuclei is usually so small that the drop in pressure is negligible. This means that not only the temperature, but also the pressure and chemical potential effectively remain constant during the nucleation process. In order to determine the height of the nucleation barrier, we therefore have to calculate the change in (Gibbs) free energy when a critical cluster of the new phase is formed at constant pressure and temperature.

Consider the two states of the system depicted in Fig. 2.3. Initially, in state I, the system only contains the parent phase β (say vapor). In state II the system contains a critical nucleus of the new phase α (say liquid) in (unstable) equilibrium with the parent phase β. Now the height of the nucleation barrier is given by the difference in Gibbs free energy between these two states. Let us first determine the difference in internal energy

$$\Delta U = U^{\mathrm{II}} - U^{\mathrm{I}}. \tag{2.35}$$

The internal energy of system I is given by

$$U^{\mathrm{I}} = T^{\mathrm{I}} S^{\mathrm{I}} - p^{\mathrm{I}} V^{\mathrm{I}} + \mu^{\mathrm{I}} N, \tag{2.36}$$

whereas the internal energy of system II is given by Eq. (2.6),

$$\begin{aligned} U^{\mathrm{II}} &= T^{\mathrm{II}} S^{\mathrm{II}} - p_\alpha^{\mathrm{II}} V_\alpha^{\mathrm{II}} - p_\beta^{\mathrm{II}} V_\beta^{\mathrm{II}} + \gamma A + \mu^{\mathrm{II}} N. \\ &= T^{\mathrm{II}} S^{\mathrm{II}} + (p_\beta^{\mathrm{II}} - p_\alpha^{\mathrm{II}}) V_\alpha^{\mathrm{II}} - p_\beta^{\mathrm{II}} V^{\mathrm{II}} + \gamma A + \mu^{\mathrm{II}} N. \end{aligned} \tag{2.37}$$

As the nucleus is formed at constant pressure and temperature, we have $p^{\mathrm{I}} = p_\beta^{\mathrm{II}} = p$, $T^{\mathrm{I}} = T^{\mathrm{II}} = T$ and $\mu^{\mathrm{I}} = \mu^{\mathrm{II}} = \mu$. Then the difference in internal energy is given by

$$\Delta U = T\Delta S + (p - p_\alpha^{\mathrm{II}}) V_\alpha^{\mathrm{II}} + \gamma A - p\Delta V, \tag{2.38}$$

where $\Delta S = S^{\rm II} - S^{\rm I}$ and $\Delta V = V^{\rm II} - V^{\rm I}$. We now immediately find for the Gibbs free energy difference and hence for the nucleation barrier

$$\Delta G = \Delta U + p\Delta V - T\Delta S = (p - p_\alpha^{\rm II})V_\alpha^{\rm II} + \gamma A. \tag{2.39}$$

Note that this equation holds for every dividing surface and that no approximations are made concerning the compressibility of the liquid or the surface tension. If we now take for the dividing surface the surface of tension, then, by making use of the Laplace equation, the height of the barrier is given by

$$\Delta G = \frac{4}{3}\pi R_s^2 \gamma_s = \frac{2}{3}\Delta p R_s^3. \tag{2.40}$$

In chapter 5 we show how using these the relations the surface tension and the radius of the surface of tension can be obtained from the measured barrier height.

2.3 Classical nucleation theory

In the previous section we derived an expression for the height of the nucleation barrier, written in terms of the surface tension and surface of tension. However, in general, it is difficult to determine these quantities. In particular, the only condition under which the surface tension can be measured experimentally, is at coexistence. One therefore has to make assumptions.

In this section we discuss classical nucleation theory, which is based on macroscopic thermodynamics. Classical nucleation theory (CNT) was originally developed more than half a century ago by Volmer and Weber [4], Becker and Döring [5], Zeldovich [48] and Frenkel [49]. We first derive the predictions of classical nucleation theory for the nucleation barrier and critical-nucleus size. We then indicate how the equilibrium distribution of cluster sizes is obtained. Finally, we derive the expressions for the rate of nucleation.

2.3.1 Nucleation barrier

We start by considering the change in Gibbs free energy when a nucleus of phase α (liquid) is formed from the parent phase β (vapor), at constant temperature and pressure (see Fig. 2.3).

The internal energy of the system in state I is given by Eq. (2.36). Concerning the system in state II, we will assume that the temperature is uniform, i.e. $T_\alpha^{\rm II} = T_s^{\rm II} = T_\beta^{\rm II}$. However, as we will not only consider critical droplets, we do not assume beforehand that the chemical potentials are uniform in system II. So we have for the internal energy of the system in state II

$$\begin{aligned} U^{\rm II} =& T^{\rm II}S^{\rm II} - p_\beta^{\rm II}V^{\rm II} + (p_\beta^{\rm II} - p_\alpha^{\rm II})V_\alpha^{\rm II} + \gamma A + \\ & (\mu_\alpha^{\rm II} - \mu_\beta^{\rm II})N_\alpha^{\rm II} + (\mu_s^{\rm II} - \mu_\beta^{\rm II})N_s^{\rm II} + \mu_\beta^{\rm II} N. \end{aligned} \tag{2.41}$$

As we consider a transformation at constant temperature and pressure, i.e. $T^{\rm I} = T^{\rm II}$ and $p^{\rm I} = p_\beta^{\rm II} = p$, we have $\mu_\beta^{\rm II} = \mu^{\rm I}$. We then obtain for the change in free energy

$$\Delta G = (p - p_\alpha^{\rm II})V_\alpha^{\rm II} + \gamma A + (\mu_\alpha^{\rm II} - \mu_\beta^{\rm II})N_\alpha^{\rm II} + (\mu_s^{\rm II} - \mu_\beta^{\rm II})N_s^{\rm II}. \tag{2.42}$$

Note that ΔG does not have to correspond to the top of the barrier. From now on, we denote the top of the nucleation barrier by an asterix. In order to obtain a useful

expression for ΔG, we have to make assumptions. In classical nucleation theory it is assumed that

1. the nucleus is spherical;
2. the phase in the nucleus is characterized by bulk properties;
3. the phase in the nucleus is incompressible;
4. the surface tension is independent of R, the radius of the droplet. This implies that the Gibbs adsorption at the surface of tension is zero and that the Tolman length is zero (see Eq. (2.26) and Eq. (2.27)). Thus we have that the surface of tension is equal to the equimolar dividing surface, i.e. $R_s = R_e$.

The mathematical dividing surface will now be put at the equimolar dividing surface (or equivalently, at the surface of tension), i.e. $R = R_e = R_s$. This implies that $N_s^{\mathrm{II}} = 0$. The excess free energy is then

$$\Delta G = (p - p_\alpha^{\mathrm{II}})\frac{4}{3}\pi R^3 + \gamma_\infty 4\pi R^2 + [\mu_\alpha^{\mathrm{II}}(p_\alpha^{\mathrm{II}}) - \mu_\beta^{\mathrm{II}}(p_\beta^{\mathrm{II}})]N_\alpha^{\mathrm{II}}. \tag{2.43}$$

As the droplet is assumed to be incompressible we have

$$\mu_\alpha^{\mathrm{II}}(p_\alpha^{\mathrm{II}}) = \mu_\alpha^{\mathrm{II}}(p_\beta^{\mathrm{II}}) + \frac{1}{\rho_\alpha}(p_\alpha^{\mathrm{II}} - p_\beta^{\mathrm{II}}). \tag{2.44}$$

We then obtain for the excess free energy

$$\Delta G = 4\pi R^2\gamma_\infty + \frac{4}{3}\pi R^3\rho_\alpha\Delta\mu, \tag{2.45}$$

with $\Delta\mu$

$$\Delta\mu = \mu_\alpha^{\mathrm{II}}(p_\beta^{\mathrm{II}}) - \mu_\beta^{\mathrm{II}}(p_\beta^{\mathrm{II}}). \tag{2.46}$$

Note that the chemical potential of the phase α in the nucleus has to be evaluated at the pressure of the vapor phase.

We can now take the derivative of Eq.2.45 with respect to R to obtain for the maximum of the free-energy barrier

$$R^* = \frac{2\gamma_\infty}{\rho_\alpha\Delta\mu}, \tag{2.47}$$

$$\Delta G^* = \frac{16\pi\gamma_\infty^3}{3\rho_\alpha^2\Delta\mu^2}. \tag{2.48}$$

By combining Eq. (2.47) with Eq. (2.44) we find the Laplace equation within classical nucleation theory:

$$\Delta p = \frac{2\gamma_\infty}{R^*}. \tag{2.49}$$

2.3.2 Equilibrium distribution of cluster sizes

In the previous section we discussed the difference in Gibbs free energy between a system consisting of only vapor molecules (phase β) and a system containing one liquid cluster (of phase α) surrounded by vapor molecules. Now imagine that the number of particles in the liquid cluster, which we from now on denote by n, is equal to the total number of particles N in the respective systems, i.e. $n = N$. Then, obviously, in state II, the system only contains one liquid cluster and no vapor molecules. But the important point

to note is that we can now identify the Gibbs free energy of the system in state II with the chemical potential of the liquid cluster, i.e. $G^{\rm II} = \mu_n(p,T)$. Hence, we have

$$\Delta G_{CNT} = G^{\rm II} - G^{\rm I} = \mu_n(p,T) - n\mu_1(p,T), \tag{2.50}$$

where $\mu_1(p,T)$ is the chemical potential of monomers at pressure p and temperature T and $G^{\rm II}$ is

$$G^{\rm II} = \gamma A + N_\alpha^{\rm II}\mu_\alpha^{\rm II}(p_\beta) = \gamma A + n\mu_\alpha(p,T). \tag{2.51}$$

We are now able to compute the equilibrium distribution of cluster sizes in a metastable supersaturated vapor. We will assume that the concentration of clusters is so low that the interactions between them can be ignored. This means that we can consider an ideal gas mixture of clusters and monomers. We treat the clusters of different sizes as separate species, so that the system is a mixture consisting of N_1 monomers, N_2 dimers,..., N_n n-mers, and so on. The mixture is at temperature T and at pressure p. After mixing, every n-mer exerts a partial pressure p_n, such that $\sum_{n=1}^{\infty} p_n = p$. As the mixture is considered to be ideal, the chemical potential of the different clusters is given by

$$\mu_n = \mu_n(p,T) + k_B T \ln[p_n/p] = \mu_n(p,T) + k_B T \ln[N_n/N_t], \tag{2.52}$$

where k_B is Boltzmann's constant and $N_t = \sum_{n=1}^{\infty} N_n$ is the total number of clusters. The total Gibbs free energy of the mixture is given by

$$G_{CNT} = \sum_{n=1}^{\infty} N_n \left\{\mu_n(p,T) + k_B T \ln[N_n/N_t]\right\} = \sum_{n=1}^{\infty} N_n \mu_n(p,T) - TS_{mix}, \tag{2.53}$$

where $S_{mix} = -k_B \sum_{n=1}^{\infty} N_n \ln[N_n/N_t]$ is the entropy of mixing the clusters. We can now obtain the cluster distribution from the equilibrium condition

$$\mu_n = n\mu_1. \tag{2.54}$$

Combining Eqs. (2.50), (2.52) and (2.54), and exploiting the fact that, to a good approximation, the total number of clusters is given by the number of monomers, we find

$$\exp[-\beta\Delta G_{CNT}(n)] = \frac{N_n/N_t}{(N_1/N_t)^n} = \frac{N_n}{N_1}, \tag{2.55}$$

which is simply a Boltzmann distribution. The monomers are often in large excess, which gives $N_1 = N$. We can then define an intensive probability

$$P(n) \equiv \frac{N_n}{N} = \exp[-\beta\Delta G_{CNT}(n)] \tag{2.56}$$

In chapters 4–9 we show how we can calculate the cluster size distribution $P(n)$ by computer simulation. In the simulations, we define the free energy of a nucleus by its probability $P(n)$:

$$\beta\Delta G_{sim}(n) \equiv -\ln[P(n)]. \tag{2.57}$$

Hence, using computer simulations its not only possible to study pathways for homogeneous nucleation, but also to compute free energy barriers which can be compared with theory.

2.3.3 Nucleation rate

Thus far we have not discussed the kinetics of nucleation. In order to calculate the nucleation rate, we again have to make several assumptions. First of all, we assume that clusters grow or shrink via the attachment of single molecules. This should be a reasonable assumption for gas-liquid nucleation as the concentration of monomers greatly exceeds that of even the dimers, and the collisions between clusters is expected to be rare. For crystal nucleation from the melt it is less obvious that the growth of a clusters proceeds via the attachment of single molecules. Making this assumption, the net rate at which nuclei containing n monomers become nuclei containing $n+1$ monomers is then

$$k_n(t) = f_n N_n(t) - b_n N_{n+1}(t), \tag{2.58}$$

where $N_n(t)$ denotes the time dependent number of clusters of size n, f_n denotes the forward rate at which a cluster gains particles, and b_n denotes the backward rate at which a cluster looses particles.

When a vapor is supersaturated, first a new cluster distribution has to be established. We can expect however, that after a transient time τ, the system reaches a steady-state in which the cluster distribution no longer changes with time and the nucleation rate is constant. The solution of Eq. (2.58), obtained by recurrence from Eq. (2.58) [7], is then

$$k = N_1 \left[\sum_{i=1}^{\infty} \frac{1}{f_n \xi_n} \right]^{-1}, \tag{2.59}$$

with ξ_n

$$\xi_n = \prod_{j=1}^{n-1} \frac{f_n}{b_{n+1}}, \qquad n > 1. \tag{2.60}$$

The rate *constants* are independent of whether the system is in equilibrium or not. We can then associate the ratio of products of rate constants in Eq. (2.60) with the equilibrium constant K for the following reaction

$$n N_1^{eq} \longleftrightarrow N_n^{eq}. \tag{2.61}$$

We already know the equilibrium constant for this reaction, as it is precisely given by Eq. (2.55). Hence, Eq. (2.59) becomes

$$k = N_1 \left[\sum_{n=1}^{\infty} \frac{1}{f_n \exp[-\beta \Delta G_{CNT}(n)]} \right]^{-1}. \tag{2.62}$$

We now have to make some *mathematical* approximations to obtain the final solution. The terms corresponding to nuclei near the top of the barrier dominate the sum in Eq. (2.62). We therefore expand the free energy in a Taylor series about its maximum at $n = n^*$. Truncating the series after the second-order term and replacing the sum by an integral, we find [7]

$$k = \sqrt{\frac{|\Delta G_{CNT}(n^*)|''}{2\pi k_B T}} f_{n^*} N_1 \exp[-\beta \Delta G_{CNT}(n^*)], \tag{2.63}$$

where $|\Delta G_{CNT}(n^*)''|$ is the second derivate of the Gibbs free energy $\Delta G_{CNT}(n)$ with respect to cluster size n, evaluated at the top of the barrier. The factor $\sqrt{|\Delta G_{CNT}(n^*)|''/2\pi k_B T}$ is called the Zeldovich factor [48]. It relates the steady-state cluster distribution to the equilibrium cluster distribution. In classical nucleation theory it can be obtained from Eq. (2.45), yielding

$$k = \sqrt{\frac{|\Delta\mu|}{6\pi k_B T}} f_{n^*} N_1 \exp[-\beta \Delta G_{CNT}(n^*)]. \tag{2.64}$$

This is the general expression of classical nucleation theory for the nucleation rate. One can interpret it is as follows: the rate of nucleation is given by the number of nuclei at the top of the barrier ($N_1 \exp[-\beta \Delta G_{CNT}(n^*)]$) times the rate at which they cross the barrier (f_{n^*}), times a correction factor (the Zeldovich factor) that takes care of the fact that some nuclei that cross the barrier do not end up in the final state, but recross the barrier to the initial state. In chapters 3 and 6 we numerically determine the kinetic prefactors for crystal nucleation from the melt and for gas-liquid nucleation in a Lennard-Jones system. We find that the kinetic prefactor in the case of crystal nucleation is about two orders of magnitude larger and in the case of gas-liquid nucleation about one order of magnitude larger than predicted by classical nucleation theory.

2.4 Extensions of classical nucleation theory

Nucleation experiments indicate that classical nucleation theory does not correctly predict the nucleation rate. However, in recent experiments on gas-liquid nucleation it has been observed that this theory does accurately predict the critical-nucleus size [15, 50, 51]. Moreover, in these experiments it has been found that the ratio of the experimentally determined nucleation rates and the rates as predicted by classical nucleation theory, while depending on temperature, are only weakly dependent on supersaturation [51].

Recently, McGraw and Laaksonen [12, 13] derived relations for the nucleation barrier that could provide an explanation for these observations. Below we discuss their derivation which is based on the droplet model as introduced in section 2.2.1. We will refer to this model as the diffuse droplet model. This is contrast to the capillary droplet model in CNT, which assumes a sharp interface.

The starting point for the derivation is the generalized Laplace equation, i.e. Eq. (2.9). The pressure difference over the drop is a well-defined quantity that is not only insensitive to the location of the dividing surface, but also independent of which model is used to represent the drop. We therefore have

$$\Delta p = \frac{2\gamma_s}{R_s} = \frac{2\gamma_e}{R_e} + \frac{\partial \gamma_e}{\partial R_e} = \frac{2\gamma_\infty}{R^*_{CNT}}. \tag{2.65}$$

The first equality is given by Eq. (2.15), the second is obtained by combining Eqs. (2.9) and (2.20), and the third equality is the classical Laplace equation, as shown in Eq. (2.49).

The key assumption of the analysis by McGraw and Laaksonen [13] is that CNT correctly predicts the location of the equimolar dividing surface. They therefore make the Ansatz

$$R_e = R^*_{CNT}. \tag{2.66}$$

Then from Eq. (2.65) it follows that

$$\gamma_\infty = \gamma_e + \frac{R_e}{2}\frac{\partial \gamma_e}{\partial R_e}, \tag{2.67}$$

$$\frac{\gamma_\infty}{R_e} = \frac{\gamma_s}{R_s}. \tag{2.68}$$

We can now integrate Eq. (2.67) at constant temperature to arrive at

$$R_e^2 \gamma_e = R_e^2 \gamma_\infty + k_s(T). \tag{2.69}$$

We can now rewrite the above expression to obtain the curvature dependence of the surface tension γ_e

$$\gamma_e = \gamma_\infty + \frac{k_s}{R_e^2}. \tag{2.70}$$

It is seen that the surface tension at the equimolar dividing surface is given by the surface tension of the planar interface plus a curvature correction that is proportional to k_s. We therefore identify k_s with the bending rigidity coefficient. Note also that the pair of conditions $\gamma_e = \gamma_\infty$ and $\partial \gamma_e / \partial R_e = 0$ assumed in CNT arise as a special case for which $k_s = 0$.

We can now evaluate Eq. (2.17), which gives the dependence of $\gamma(R)$ on the location of the dividing surface, at $R = R_e$, and use Eq. (2.68) to eliminate γ_s, to obtain

$$\gamma_\infty = \frac{3\gamma_e R_e^3}{R_s^3 + 2R_e^3}. \tag{2.71}$$

The nucleation barrier in the diffuse droplet model is given by Eq. (2.40), which, using Eq. (2.68) and Eq. (2.71), can be rewritten as

$$\Delta G^* = \frac{4\pi R_s^2 \gamma_s}{3} = 4\pi R_e^2 \gamma_e \left(\frac{R_s^3}{R_s^3 + 2R_e^3} \right). \tag{2.72}$$

In the capillary droplet model of CNT we obtain

$$\Delta G^*_{CNT} = \frac{4\pi R_e^2 \gamma_\infty}{3} = 4\pi R_e^2 \gamma_e \left(\frac{R_e^3}{R_s^3 + 2R_e^3} \right). \tag{2.73}$$

The first equality is obtained by combining Eqs. (2.47) and (2.48), after applying the Ansatz $R_e = R^*_{CNT}$. The second equality uses Eq. (2.71).

We can now subtract the two above equations to arrive at

$$\Delta G^*_{CNT} - \Delta G^* = 4\pi R_e^2 (\gamma_\infty - \gamma_e) = -4\pi k_s(T). \tag{2.74}$$

Hence, by assuming that CNT correctly predicts the location of the equimolar dividing surface, we find that the difference between the actual barrier height and the height of the barrier as predicted by CNT, is independent of supersaturation and only dependent on temperature. As the variation in the nucleation rate is dominated by the variation in the barrier height, it implies that the ratio of the actual nucleation rate over the nucleation rate as predicted by classical nucleation theory, is constant.

Let us now discuss the main assumption leading to Eq. (2.74). The starting point for the above derivation is the Ansatz $R_{CNT} = R_e$. From Eq. (2.65) it is seen that this means that

$$\Delta p = \frac{2\gamma_\infty}{R_e}. \tag{2.75}$$

However, in section 2.2.5.1 we have shown that the Laplace pressure, written in terms of R_e and γ_∞, is to first order

$$\Delta p = \frac{2\gamma_\infty}{R_e}\left(1 - \frac{\delta}{R_e}\right). \tag{2.76}$$

A comparison of the two above equations shows that McGraw and Laaksonen have implicitly assumed that the Tolman-length, and hence the spontaneous curvature, is zero. In chapter 5 we show that this, in fact, is a reasonable assumption for the vapor-liquid interface in the Lennard-Jones system. Note also that, by comparing Eq. (2.70) with Eq. (2.31), the bending-rigidity constant k_s can be identified with $k_s = 2k + \overline{k}$

Finally, let us discuss some of the main problems of classical nucleation theory that have been under debate since the 1960's. It is clear that the use of macroscopic quantities has both it advantages and disadvantages. However, even if we accept the approximations of classical nucleation theory, there are still inconsistencies within the theory, which we now briefly address. Already in 1961 Courtney argued that the CNT-prediction for the cluster distribution (see Eq. (2.55)) does not satisfy the law of mass action [52], and suggested that this problem could be resolved by introducing the factor $1/S$, where S is the supersaturation, into Eq. (2.55). Although the factor $1/S$ does bring CNT into line with the law of mass action, its introduction seems rather ad hoc [53]. Moreover, Lothe and Pound realized that a more fundamental omission in the original theory still persists [54]. They argued that classical nucleation theory does not properly take into account the mechanical and rotational degrees of freedom of a cluster. This problem is now often referred to as the problem of the "replacement free energy". Both problems have been the subject of controversy.

The root of the problems lies in the fact that the connection between a statistical mechanical description of droplets and a macroscopic thermodynamic theory, such as classical nucleation theory, is ambiguous. From statistical mechanics it follows that the free energy of an ideal mixture of clusters is given by

$$F = -k_B T \sum_{n=1}^{\infty} N_n[\ln(Q_n) - \ln N_n + 1], \tag{2.77}$$

where Q_n is the partition function of an n-mer. The chemical potential of an n-mer can be obtained via

$$\mu_n = \left(\frac{\partial F_n}{\partial N_n}\right)_{V,T,N_{n'\neq n}} = -k_B T \ln[Q_n/N_n]. \tag{2.78}$$

From the law of mass action 2.54 it then follows that

$$N_n = \exp[-\beta(-k_B T \ln[Q_n] - n\mu_1)] \equiv \exp[-\beta(F_n - n\mu_1)]. \tag{2.79}$$

Now the basic problem is how to express the configuration integral in terms of macroscopic thermodynamic quantities. Recently, Reiss *et al.* [11] argued that the configurational integral should be given by

$$\begin{aligned} Q_n &= (V/v_o)\exp[-\beta(G^{\mathrm{II}} - pv_n/k_BT)] \\ &= (V/v_o)\exp[-\beta(n\mu_\alpha + \gamma A - pv_n/k_BT)], \end{aligned} \tag{2.80}$$

where v_n is the volume of the droplet and v_o is the volume scale for the droplet. In the analysis of Ref. [11] v_o is given by $v_o = \sigma_{v_n}$, where σ_{v_n} is the variance of the volume fluctuations of the droplet. The introduction of v_o implies that the free-energy of such a droplet is given by the CNT-prediction plus a contribution associated with the translational degrees of freedom of the cluster minus a correction term which corrects for double counting configurations. Thus v_o plays a role in resolving states in coordinate space similar to that of Planck's constant in phase space. The effect on the expression for the cluster distribution in Eq. (2.55) is that N_n/N_1 is now given by $\exp[-\beta\Delta G_{CNT}]/\sigma_{v_n}\rho_\beta$, which implies a correction of the order 10^4. At the moment it seems that these issues are still not settled and we will not address them in more detail here.

2.5 Nucleation theorem

The formation of critical nuclei is infrequent. But when clusters are formed, they are also short-lived. It is for these reasons that it is difficult to study the structure of critical nuclei in any direct way in an experiment and for many years most experimental nucleation studies only provided information about the nucleation rates and critical supersaturations, but not about the structure of the critical nuclei. But in recent years it has been noticed by Kashchiev and others [15, 55–57] that the *variation* of the nucleation rate with supersaturations does contain information about the size and composition of the critical nucleus. The connection is made via the so-called nucleation theorem. The nucleation theorem states that the excess number of molecules of a given component in the critical nucleus is given by the variation of the barrier height with the chemical potential, $\mu_{v,i}$ of that component in the vapor phase:

$$\frac{\partial \Delta G^*}{\partial \mu_{v,i}} = -\Delta n_i^*. \tag{2.81}$$

Here Δn_i^* is the excess number of particles of component i in the critical droplet. The excess number of particles is given by

$$\Delta n_i = 4\pi \int_0^\infty [\rho(r) - \rho_v] r^2 dr, \tag{2.82}$$

where $\rho(r)$ is the density in a spherical shell at distance r from the center of the droplet and ρ_v is the density in the vapor. While the size of the nucleus is ambiguous because of the diffusive nature of the interface, the excess number of particles is well-defined.

In the literature both thermodynamic [55, 56] and statistical mechanical [15] derivations have been reported. In appendix C we present a derivation that is based on a thermodynamical derivation given by Oxtoby and Kashchiev [56]. However, it is conceivable that a thermodynamic approach fails for small droplets. Here we therefore present a compact derivation which is based on statistical mechanics.

Consider a system in the grand-canonical ensemble. The probability to find n particles in the system is given by

$$P(n) = \exp(\beta\mu n)Q(n,V,T)/\Xi(\mu,V,T) \; , \tag{2.83}$$

where Ξ is the grand-canonical partition function. The total grand potential Ω ($=-PV$) is given by

$$\Omega = -k_B T \ln \Xi \; . \tag{2.84}$$

We can associate a Landau free energy (strictly speaking, a Landau "grand potential") $\omega(n)$ with the probability distribution $P(n)$

$$\omega(n) = -k_B T \ln\left[\exp(\beta\mu n)Q(n,V,T)\right] = -\mu n + F(n,V,T) \tag{2.85}$$

where $F(n,V,T)$ is the Helmholtz free energy of a system of n particles in volume V at temperature T. The free energy difference between two states with different number of particles, say n_1 and n_2, is

$$\begin{aligned} \Delta\omega \equiv \omega(n_2) - \omega(n_1) = &-\mu(n_2 - n_1) + \\ &F(n_2,V,T) - F(n_1,V,T) \; . \end{aligned} \tag{2.86}$$

Let us now consider how $\Delta\omega$ varies with μ. Note that the Helmholtz free energy does not depend on μ. Hence

$$\frac{\partial\Delta\omega}{\partial\mu} = -(n_2 - n_1) \equiv -\Delta n \; . \tag{2.87}$$

This result is general. Hence it also holds for the case where n_1 corresponds to the (local) maximum of $P(n)$, i.e. the homogeneous metastable phase, while n_2 corresponds to the top of the (nucleation) barrier. In that case, it is immediately clear that Δn corresponds to the excess number of particles in the critical nucleus. The extension to mixtures is straightforward.

In a sense, this result is trivial. It is easy to extend it to other ensembles. Consider first the N,P,T ensemble. In that case, the fluctuating quantity is the volume, the Landau free energy has the form of a Gibbs free energy and we obtain

$$\frac{\partial\Delta g}{\partial P} = (V_2 - V_1) \equiv -\Delta V \; . \tag{2.88}$$

Hence the variation of the barrier height with pressure is given by the (usually negative) excess volume of the critical nucleus. However, although that quantity is well defined, it is intuitively not very appealing. Of course, if we use the Gibbs-Duhem relation to write $dP = \rho d\mu$, then Eq. (2.88) reduces to Eq. (2.87).

Finally, consider a variation in temperature, rather than pressure or chemical potential. Then, for both the grand-canonical and the isothermal-isobaric ensemble we obtain the same results:

$$\frac{\partial\Delta g}{\partial T} = -(S_2 - S_1) \equiv -\Delta S \; . \tag{2.89}$$

and

$$\frac{\partial\beta\Delta g}{\partial\beta} = (E_2 - E_1) \equiv \Delta E \; . \tag{2.90}$$

It is worth pointing out that, in practice, the observable quantity is $\beta\Delta G$, and hence the second relation is more useful.

Note that although Δn in Eq. (2.87) is a useful order parameter for small systems, it becomes less meaningful for larger systems. To be more specific, it becomes meaningless if the volume V is so large that the spontaneous fluctuations in the number of particles become comparable to Δn. In general,

$$\langle N^2\rangle - \langle N\rangle^2 = Nk_BT\kappa$$

where κ denotes the isothermal compressibility. For an ideal gas,

$$\langle N^2\rangle - \langle N\rangle^2 = N$$

Hence, a problem arises when $n^*_{nucleus}$ is of order $\sqrt{N}$. When this happens, the change in free energy associated with a small, homogeneous fluctuation in the density is smaller than the change in free energy due to the formation of a liquidlike droplet and Δn is no longer a useful order parameter. Note that this situation can always arise when the volume is large enough and that it becomes even more serious close to the critical point or close to the spinodal. However, in practice, the problem is less serious because nucleation experiments do not probe the probability of arbitrary density fluctuations but only those that result in the formation of a critical nucleus.

Appendix A Gibbs-Duhem relations for the interface

The variations in the free-energy of the homogeneous phases α and β are given by

$$\begin{aligned} dF_\alpha &= -p_\alpha dV_\alpha - S_\alpha dT + \mu dN_\alpha, \\ dF_\beta &= -p_\beta dV_\beta - S_\beta dT + \mu dN_\beta. \end{aligned} \tag{2.91}$$

Subtracting these equations from Eq. (2.12) yields for the variation of the surface free energy

$$dF_s = -S_s dT + \gamma dA + \mu dN_s + \left[\frac{d\gamma}{dR}\right] AdR. \tag{2.92}$$

The Gibbs-Duhem relation for the interface is obtained by differentiating the expression for the surface free energy F_s (i.e. Eq. (2.19)) and combining the result with Eq. (2.92). We find

$$Ad\gamma + S_s dT + N_s d\mu = \left[\frac{d\gamma}{dR}\right] AdR, \tag{2.93}$$

or,

$$d\gamma + s_s dT + , \, d\mu = \left[\frac{d\gamma}{dR}\right] dR, \tag{2.94}$$

where s_s and , are the superficial entropy density and number density, respectively.

At the equimolar dividing surface, , is zero, from which immediately follows that

$$\left[\frac{\partial\gamma}{\partial R}\right]_{R=R_e} = \left(\frac{\partial\gamma_e}{\partial R_e}\right)_T. \tag{2.95}$$

Appendix B Tolman-length and superficial density

In this appendix we show how the Tolman-length, which is defined as the difference $\delta = R_e - R_s$, is related to the superficial density , $_s$ at the surface of tension.

The number of surface molecules at the surface of tension is

$$N_s(R_s) = 4\pi \int_0^{R_s} (\rho(R) - \rho_\alpha) R^2 dR + 4\pi \int_{R_s}^{R_{max}} (\rho(R) - \rho_\beta) R^2 dR. \tag{2.96}$$

The number of surface of molecules at the equimolar dividing surface is

$$\begin{aligned} N_e(R_e) = 0 =& 4\pi \int_0^{R_e} (\rho(R) - \rho_\alpha) R^2 dR + 4\pi \int_{R_e}^{R_{max}} (\rho(R) - \rho_\beta) R^2 dR \\ =& 4\pi \int_0^{R_s} (\rho(R) - \rho_\alpha) R^2 dR + 4\pi \int_{R_s}^{R_e} (\rho(R) - \rho_\alpha) R^2 dR + \\ & 4\pi \int_{R_s}^{R_{max}} (\rho(R) - \rho_\beta) R^2 dR + -4\pi \int_{R_s}^{R_e} (\rho(R) - \rho_\beta) R^2 dR. \end{aligned} \tag{2.97}$$

Combining both the above equations we obtain

$$\begin{aligned} N_s(R_s) &= 4\pi \int_{R_s}^{R_e} (\rho_\alpha - \rho_\beta) R^2 dR \\ &= 4\pi (\rho_\alpha - \rho_\beta)(R_e^3 - R_s^3), \end{aligned} \tag{2.98}$$

and for the superficial density at the surface of tension

$$\begin{aligned} , _s &= \frac{N_s}{4\pi R_s^2} = (\rho_\alpha - \rho_\beta) \frac{R_e^3 - R_s^3}{R_s^2} \\ &= (\rho_\alpha - \rho_\beta)\delta[1 + (\delta/R_s) + \frac{1}{3}(\delta^2/R_s^2)]. \end{aligned} \tag{2.99}$$

The above equation becomes more transparent when we consider the planar limit. For a planar interface, for which R_s goes to infinity, we have

$$, _s/(\rho_\alpha - \rho_\beta) = \delta. \tag{2.100}$$

Appendix C The nucleation theorem

In this appendix we give a thermodynamic derivation of the nucleation theorem. It is based on the derivation presented by Oxtoby and Kashchiev [56].

The height of the nucleation barrier is given by the difference in Gibbs free energy between the two systems in Fig. 2.3:

$$\Delta G = (p - p_\alpha^{\mathrm{II}}) V_\alpha^{\mathrm{II}} + \gamma A. \tag{2.101}$$

In order to derive the nucleation theorem we have to evaluate $\frac{\partial \Delta G}{\partial \mu}$. $V_\alpha^{\mathrm{II}}, A, p_\alpha^{\mathrm{II}}$, and p^{II} are a function of μ. The surface free energy is a function of both R and μ. In principle, they are independent, i.e. at constant μ, we could make a mathematical displacement of R, leading to a change in γ. However, when the chemical potential is changed, it is natural to follow one and the same surface, for instance the surface of tension, or the equimolar dividing surface. Then R is a function of μ, and we have $\gamma(R(\mu), \mu)$.

For the variation in ΔG with respect to a variation of μ we now get

$$\begin{aligned}
\frac{\partial \Delta G}{\partial \mu} =& \frac{\partial V_\alpha^{\rm II}}{\partial \mu}(p - p_\alpha^{\rm II}) + V_\alpha^{\rm II}\frac{\partial (p - p_\alpha^{\rm II})}{\partial \mu} + \gamma \frac{\partial A}{\partial \mu} + A\frac{\partial \gamma}{\partial \mu}\bigg|_R + A\frac{\partial \gamma}{\partial R}\bigg|_\mu \frac{\partial R}{\partial \mu} \\
=& -A\frac{\partial R}{\partial \mu}\left\{\frac{2\gamma}{R} + \left[\frac{\partial \gamma}{\partial R}\right]\bigg|_\mu\right\} + V_\alpha^{\rm II}\frac{\partial (p - p_\alpha^{\rm II})}{\partial \mu} + \\
& \frac{2A}{R}\gamma\frac{\partial R}{\partial \mu} + A\frac{\partial \gamma}{\partial \mu}\bigg|_R + A\frac{\partial \gamma}{\partial R}\bigg|_\mu \frac{\partial R}{\partial \mu} \\
=& V_\alpha^{\rm II}\frac{\partial (p - p_\alpha^{\rm II})}{\partial \mu} + A\frac{\partial \gamma}{\partial \mu}\bigg|_R \\
=& V_\alpha^{\rm II}\frac{\partial p}{\partial \mu} - V_\alpha^{\rm II}\frac{\partial p_\alpha^{\rm II}}{\partial \mu} + A\frac{\partial \gamma}{\partial \mu}\bigg|_R .
\end{aligned}$$

We now make use of the Gibbs-Duhem relations. For the center of the droplet and for the parent phase β we have

$$\begin{aligned}
V_\alpha^{\rm II} dp_\alpha^{\rm II} &= N_\alpha^{\rm II} d\mu \\
V_\beta^{\rm II} dp_\beta^{\rm II} &= V_\beta^{\rm II} dp = N_\beta^{\rm II} d\mu,
\end{aligned} \tag{2.102}$$

from which we obtain

$$\begin{aligned}
\frac{\partial p_\alpha^{\rm II}}{\partial \mu} &= \frac{N_\alpha^{\rm II}}{V_\alpha^{\rm II}} = \rho_\alpha \\
\frac{\partial p_\beta^{\rm II}}{\partial \mu} &= \frac{N_\beta^{\rm II}}{V_\beta^{\rm II}} = \rho_\beta .
\end{aligned} \tag{2.103}$$

For the surface we have from Eq. (2.93)

$$-A d\gamma + \left[\frac{\partial \gamma}{\partial R}\right]\bigg|_\mu A dR = N_s^{\rm II} d\mu, \tag{2.104}$$

from which we obtain

$$d\gamma = -\frac{N_s^{\rm II}}{A} d\mu + \left[\frac{\partial \gamma}{\partial R}\right]\bigg|_\mu dR. \tag{2.105}$$

From this it follows that the variation of γ with respect to μ at constant R is given by the surface density of molecules $\frac{N_s^{\rm II}}{A}$, i.e.

$$\frac{\partial \gamma}{\partial \mu}\bigg|_R = -\frac{N_s^{\rm II}}{A}. \tag{2.106}$$

We now have for the variation of the height of the barrier ΔG with respect to μ

$$\begin{aligned}
\frac{\partial \Delta G}{\partial \mu} &= V_\alpha^{\rm II}\rho_\beta - V_\alpha^{\rm II}\rho_\alpha - N_s^{\rm II} \\
&= -\left\{V_\alpha^{\rm II}(\rho_\alpha - \rho_\beta) + N_s^{\rm II}\right\} \\
&\equiv -\Delta n^* ,
\end{aligned} \tag{2.107}$$

where Δn^* is the excess number of particles in the critical cluster.

3 Rate of crystal nucleation in a Lennard-Jones system at moderate undercooling

We report a computer-simulation study of the rate of homogeneous crystal nucleation and the structure of crystal nuclei in a Lennard-Jones system at moderate undercooling. The height of the nucleation barrier has been determined using umbrella sampling, whereas the barrier crossing rate is calculated using molecular dynamics simulation. The simulations clearly show that the barrier crossing is a diffusive process. Nevertheless, the kinetic prefactor in the nucleation rate is found to be some two orders of magnitude larger than predicted by classical nucleation theory. The height of the barrier is in good agreement with the theoretical prediction. Although the Lennard-Jones system has a stable face-centered cubic (fcc) phase below the melting line, the precritical nuclei are found to be mainly body-centered cubic (bcc) ordered. As they grow to their critical size, they become more fcc ordered in the core. However, the critical and postcritical nuclei retain a high degree of bcc ordering in the interface. Furthermore it is found that in the interface the density falls of faster than the structural order parameter, which is in agreement with the predictions of density functional calculations (P. Harrowell and D. W. Oxtoby, J. Chem. Phys. **80***, 1639 (1984)).*

3.1 Introduction

At the end of last century Ostwald [2] formulated his so-called 'step rule', which states that the phase that is formed from the melt need not be the most stable phase, but rather the phase that is closest in free energy to the liquid phase. Stranski and Totomanow [58] reexamined this rule and argued that the nucleated phase is the phase that has the lowest free-energy barrier of formation, rather than the phase that is globally stable under the conditions prevailing. More recently Alexander and McTague [32] extended the Landau free energy expansion to freezing transitions that are weakly first order and concluded from general symmetry considerations that, in three dimensions, formation of the body-centered cubic phase (bcc) phase is uniquely favored for simple fluids. A theoretical study by Klein and Leyvraz [59] also suggests that a metastable bcc phase can easily be formed from the undercooled liquid. In experiments on rapidly cooled metal melts, which have a stable face-centered cubic (fcc) phase below the melting line, nucleation of a metastable bcc phase has been observed [60–62].

However, when the formation of metastable bcc nuclei was investigated on a microscopic scale using computer simulation, the picture that emerged was not fully in agreement with the Alexander-McTague scenario. Although in some studies nucleation of the metastable bcc phase was observed [17–19, 27], most studies found evidence for

the formation of the stable fcc phase [20–25]. Of particular interest is a simulation study by Swope and Andersen [25] of a one million particle Lennard-Jones system, which has a stable fcc phase below the melting line. This study showed that although both bcc and fcc crystallites are formed in the early stages of the nucleation process, only the fcc nuclei grow and become postcritical. What should be stressed, however, is that they performed their simulation at a very large degree of undercooling (of more than 40% with respect to the melting temperature). At such a large degree of undercooling one should expect the free-energy barrier to be quite small for essentially all possible crystalline phases. It is therefore not obvious that crystal nucleation at large undercooling will proceed in the same way as close to coexistence.

In the present work we study homogeneous nucleation in the Lennard-Jones system for two different pressures closer to the freezing point, i.e. at 20% supercooling. Rather than using a "brute-force" approach where we wait for nuclei to form spontaneously, we separate the problem into two parts: 1) the computation of the free-energy barrier for crystal nucleation and 2) the computation of the rate at which this barrier is crossed. For the computation of the free-energy barrier that separates the solid phase from the undercooled liquid, we use the scheme developed by Van Duijneveldt and Frenkel [27]. The rate at which this barrier is crossed is computed using the Bennett-Chandler scheme [28–31]. The advantage of this approach is that it can be used even at small undercooling (i.e. realistic) undercooling where the straightforward molecular dynamics approach will not work, because the nucleation barrier diverges at coexistence. Moreover, the umbrella-sampling technique [26] allows us to stabilize the critical nucleus and study its structure in detail. For readers who are less interested in the technical details of the simulations, the next section summarizes the main results.

3.2 Summary of results

Our simulations suggest that the small precritical nuclei have a bcc-like structure rather than the stable fcc structure. However, as the crystallites grow to the critical size, their cores become increasingly fcc ordered. Nevertheless, a high degree of bcc ordering in the interface is retained. This may explain why in earlier simulations on small systems nucleation of a metastable bcc phase was observed [17–19, 27], while in similar simulations on larger systems the formation of the fcc nuclei was observed [20–25]. In the smaller systems the critical nuclei will be so small that their structure is almost completely surface dominated, leading to a high degree of bcc ordering.

Our simulations show that, although the density in the core of the critical nuclei is slightly lower than the density in the bulk solid, the structural order parameter reaches a bulk solid value in the core. The interface between the crystal nuclei and the surrounding liquid is diffuse – both the density and the structural order parameter decay smoothly to a liquidlike value. Moreover, our simulations support the prediction from density-functional theory [63] that the density falls off faster than the structural order parameter.

We compare our numerical results with the predictions of classical nucleation theory for the height of the barrier and the rate of barrier crossing. On the whole, the computed barrier height is in quite good agreement with classical nucleation theory. The present study clearly shows that the barrier-crossing is a diffusive process. This is in agreement with the low Zeldovich factor given by classical nucleation theory. The simulations yield

a kinetic prefactor that is two orders of magnitude larger than the one predicted by classical nucleation theory. To our knowledge, the present simulations provide the first "atomistic" calculation of a crystal-nucleation rate at moderate undercooling.

The rest of this chapter is organized as follows. In section 3.3 we describe the numerical techniques to calculate the free-energy barriers and the nucleation rates. The method of identifying solidlike particles and determining the crystal structure of the nuclei is presented in section 3.4. In section 3.5 we give the computational details of the simulation and in section 3.6 we discuss the results.

3.3 Numerical technique

3.3.1 Free-energy barriers

In order to compute the free-energy barrier that separates the liquid from the crystalline phase, we should first define a "reaction coordinate" that connects the two phases. It is most convenient to choose as the reaction coordinate an, as yet unspecified, order parameter Φ, that is sensitive to the degree of crystallinity in the system. The Gibbs free energy of the system, G, is a function of this order parameter [64]:

$$\beta\Delta G(\Phi) = \text{constant} - \ln[P(\Phi)], \tag{3.1}$$

where $P(\Phi)$ is the probability per unit interval to find the order parameter around a given value of Φ. Below the freezing point $P(\Phi)$ is strongly peaked around a finite, solidlike value of Φ, whereas above the freezing point $P(\Phi)$ will be peaked around a low, liquidlike value. At coexistence $P(\Phi)$ is double-peaked and the area under the two peaks should be the same. This expresses the fact that, at coexistence, the system is equally likely to be in the solid or liquid phase.

In the isobaric-isothermal ensemble (NPT-ensemble) the probability $P(\Phi)d\Phi$ that the system has a value between Φ and $\Phi + d\Phi$ is given by

$$P(\Phi) = \frac{\int dV \int d\mathbf{r}^N \exp[-\beta(U(\mathbf{r}^N) + PV)]\, \delta(\Phi - \Phi(\mathbf{r}^N))}{Q_{NPT}}, \tag{3.2}$$

where $\beta \equiv 1/k_BT$ is the reciprocal temperature, T is the temperature , k_B is the Boltzmann constant, N is the number of particles, $U(\mathbf{r}^N)$ is the potential energy of the configuration with coordinates $\mathbf{r}^N$, V is the volume, P is the applied pressure and Q_{NPT} is the configurational part of the partition function. Q_{NPT} is given by

$$Q_{NPT} = \int dV \int d\mathbf{r}^N \exp[-\beta(U(\mathbf{r}^N) + PV)]. \tag{3.3}$$

As $P(\Phi)$ is an equilibrium property of the system it can be obtained both by Monte Carlo (MC) and molecular dynamics (MD) simulations. In order for Eq. (3.1) to be useful, one should compute $P(\Phi)$ for all values of Φ between the solid and liquid. In particular, one should obtain an accurate measure of $P(\Phi)$ near the top of the nucleation barrier. But this is precisely the point where $P(\Phi)$ will be very small. As a consequence, Eq. (3.1) cannot be used to calculate $G(\Phi)$ in a conventional simulation. To circumvent this problem and to obtain good statistics on $P(\Phi)$ for intermediate values of Φ, the umbrella sampling technique of Torrie and Valleau [26] is used. The basic idea of this

scheme is to bias the sampling of configuration space in such a way that configurations with a large free energy will be sampled frequently.

We can bias the sampling of configuration space by adding a fictitious potential to the true potential-energy function of our model system. Clearly, the optimum choice for the biasing potential would be $-G(\Phi)$, because in that case all values of Φ are sampled with the same probability. But, of course, we do not know $G(\Phi)$ as it is precisely the quantity that we wish to compute. The approach of Van Duijneveldt and Frenkel [27] and Lynden-Bell *et al.* [65] was to construct the biasing potential step-by-step. An initial, local, estimate of $G(\Phi)$ is obtained from an unbiased simulation of the liquid phase (say). This estimate is then extrapolated to higher values of Φ and used to construct the biasing potential for the next run (at higher values of the order parameter), and so on. The disadvantage of this approach is that if simulations are performed on a large system with a steep free-energy barrier, it becomes difficult to obtain a good estimate for the free-energy barrier. We therefore use a slightly different approach in that we chose our biasing potential $W(\Phi)$ to be a harmonic function of Φ:

$$W(\Phi(\mathbf{r}^N)) = \frac{1}{2} k_\Phi (\Phi(\mathbf{r}^N) - \Phi_o)^2 \tag{3.4}$$

The result of introducing such a potential is that in each run a certain window of values of the order parameter will be sampled. Note that the width and "location" of this window depend on k_Φ and Φ_o. The window will be wider if the harmonic constant k_Φ is smaller. By changing the center value of the harmonic potential, Φ_o, we can change the crystallinity in our system.

3.3.2 Nucleation rates

With umbrella sampling it is in principle possible to compute the free-energy barrier that separates the liquid from the solid phase, but it does not provide us with any dynamical information. In order to calculate the nucleation rate, we exploit the fact that nucleation is an activated process and that the rate of nucleation can therefore be considered as the product of two terms, namely, (1) the probability to find the system at the top of the free-energy barrier to nucleation and (2) the rate at which this activated state (a "transition state" in the Eyring picture of chemical reactions [66]) transforms into a stable crystalline phase. Denoting the transition state separating the liquid from the solid state by Φ^*, we consider configurations for which $\Phi < \Phi^*$ as liquid and configurations for which $\Phi > \Phi^*$ as solid. We now apply standard linear-response theory [67] to calculate chemical rate constants, to compute the actual transition rate from the liquid to the solid state [29, 30]. This transition rate $k(t)$ is given by [29]

$$k(t) = \frac{\langle \dot{\Phi} \delta(\Phi - \Phi^*) \theta[\Phi(t) - \Phi^*] \rangle}{\langle \theta(\Phi^* - \Phi) \rangle}, \tag{3.5}$$

where θ is the Heaviside function. Eq. (3.5) is obtained under the assumption that the actual time-scale on which crystallization takes place is very long compared to the time that it takes a critical nucleus to move away from the top of the barrier. It should also be noted that it is somewhat suspect to apply the (equilibrium) linear-response formalism to a system that has been prepared far from equilibrium (namely, in the metastable liquid phase). However, we consider an ensemble of systems, most of which will be in

the crystalline state, while a small fraction will be in the metastable liquid. The linear-response theory then tells us how the system relaxes after an initial, weak perturbation has changed the number of systems in the metastable liquid phase. It is in the spirit of the Onsager regression hypothesis [67] to assume that this relaxation rate is precisely the crystallization rate that we are interested in.

In what follows, we make the assumption that the rate-limiting step in the crystallization rate is the barrier crossing, rather than for instance, the subsequent crystal growth. Therefore, we can identify the crystallization rate with the nucleation rate.

It is convenient to rewrite Eq. (3.5) as:

$$k(t) = \frac{\langle \delta(\Phi - \Phi^*) \rangle}{\langle \theta(\Phi^* - \Phi) \rangle} \frac{\langle \dot{\Phi} \delta(\Phi - \Phi^*) \theta[\Phi(t) - \Phi^*] \rangle}{\langle \delta(\Phi - \Phi^*) \rangle} = P_o(\Phi^*) R(t). \tag{3.6}$$

It is seen that $k(t)$ is the product of two contributions. The first contribution is $P_o(\Phi^*)$, which is given by

$$P_o(\Phi^*) = \frac{P(\Phi^*)}{\int_0^{\Phi^*} d\Phi P(\Phi)} = \frac{\exp(-\beta G(\Phi))}{\int_0^{\Phi^*} d\Phi \exp(-\beta G(\Phi))}. \tag{3.7}$$

Noting that if $\Phi < \Phi^*$ the system is in the liquid state, it is clear that $P_o(\Phi^*)$ is the probability of finding the system at the top of the barrier divided by the probability of finding it in the liquid state. It is an equilibrium quantity and can be measured both by Monte Carlo and by Molecular Dynamics as indicated above.

The second contribution to $k(t)$ is $R(t)$, which gives the average flux over the top of the barrier, provided that the system was prepared at the top of the barrier. $R(t)$ is a dynamical quantity and can only be measured by Molecular Dynamics. The basic idea to separate the simulation into a calculation of the barrier height and a dynamic simulation of trajectories starting at the top of the barrier, was formulated by Bennett [28] and Chandler [29]. As explained in Ref. [67], the initial rate $k(t \to 0^+)$ corresponds to the transition-state theory approximation for the rate constant:

$$k_{TST} = \lim_{t \to 0^+} k(t) = \frac{\langle \dot{\Phi} \delta(\Phi - \Phi^*) \theta[\dot{\Phi}] \rangle}{\langle \theta(\Phi^* - \Phi) \rangle}. \tag{3.8}$$

Transition-state theory assumes that all trajectories initially heading from the top of the barrier towards the solid state will indeed end up in the solid state and all trajectories heading towards the liquid, will end up in the liquid. This assumption is only correct if no trajectories recross the top of the barrier. In the present case, recrossing turns out to be quite significant and, as a consequence, we will find that $k(t)$ decays to a value that is much smaller than k_{TST}. It is conventional to express the reduction of $k(t)$ due to recrossings in terms of the transmission coefficient κ, defined as:

$$\kappa = \frac{k(t)}{k_{TST}} = \frac{R(t)}{R(0^+)}. \tag{3.9}$$

As explained in the previous section, we use umbrella sampling to calculate the free-energy barrier and hence, $P(\Phi^*)$. To compute the crossing rate $R(t)$, we make use of the so-called "blue-moon ensemble" technique of Refs. [30] and [31]. In this technique, constrained MD simulations are used to generate a sequence of uncorrelated configurations of the system under the constraint $\Phi = \Phi^*$ (i.e. at the top of the barrier). We use conventional constraint-MD [68] to keep the system at the top of the barrier. However,

it should be noted that the quantity that we constrain is a global order parameter that depends on the positions of *all* the particles in the system. The configurations at the top of the barrier that are generated in the constrained-MD simulations are then used as initial states to compute the time correlation function in $R(t)$. However, as explained in Refs. [30, 31], the use of a constrained MD introduces a bias in the sampling of states at the top of the barrier. It is possible to correct for this bias by giving the trajectories starting from the top of the barrier an appropriate weight in the averaging:

$$R(t) = \frac{\langle \dot{\Phi}\theta[\Phi(t) - \Phi^*]|H|^{-1/2}\rangle_c}{\langle |H|^{-1/2}\rangle_c}. \tag{3.10}$$

The subscript c denotes that we are using a constrained initial state. In the general case of a system with many constraints, $|H|$ is the determinant of a matrix H. However, in the present case, there is only one constraint and H reduces to a scalar:

$$H = \sum_{i=1}^{N} m_i^{-1} \left(\frac{\partial \Phi}{\partial \vec{r}_i}\right)^2. \tag{3.11}$$

The weighting factors in the ratio in (3.10) would cancel if the reaction coordinate Φ were a linear function of the cartesian coordinates. However, in the present case, Φ is a non-linear function of all coordinates and its influence cannot be ignored. More computational details are discussed in Ref. [69].

3.3.3 Order parameters

Both for the calculation of the nucleation barrier and for the computation of the crossing rate, we need to define a "reaction" coordinate that measures the degree of crystallinity of the system as it moves from the liquid to the solid phase. We have to choose as our reaction coordinate an order parameter that is only sensitive to the overall degree of crystallinity of the system, but fairly insensitive to the differences between the various possible crystal structures. This requirement is important because otherwise we would force the system to go towards a specific crystal structure. A second requirement is that the order parameter should be insensitive to the orientation of the crystal in space. Van Duijneveldt and Frenkel [27] have shown that a particular set of bond-order parameters introduced by Steinhardt *et al.* [70] are particularly suited to act as the reaction coordinate. These order parameters are sensitive to the degree of spatial orientational correlation of the vectors that join neighboring particles. In a liquid where there is only local orientational order, these correlations decay rapidly and, as a consequence, all bond-order parameters are small (zero in the thermodynamic limit). In a crystal, the orientation of vectors joining neighboring atoms are correlated throughout the solid and hence the bond-order parameter is large (of $\mathcal{O}(1)$).

In Appendix 3.6.4 we briefly summarize the definition of the bond-order parameters used in our simulations. In Table 3.1 values for several of these order parameters are given for simple cluster geometries. As can be seen from Table 3.1, Q_6 has the desirable feature that it vanishes in the bulk liquid phase, while it is large ($\mathcal{O}(1)$) for the simple crystal lattices of interest. We therefore use Q_6 as *the* crystalline order parameter. The reaction coordinate from isotropic fluid to crystal then corresponds to a path of increasing Q_6. By increasing Q_6 from the liquid we do not favor a specific crystalline structure. Rather, the system is allowed to select its 'own' specific reaction path from the fluid

	Q_4	Q_6	$\widehat{W}_4$	$\widehat{W}_6$
fcc	0.191	0.575	-0.159	-0.013
hcp	0.097	0.485	0.134	-0.012
bcc	0.036	0.511	0.159	0.013
sc	0.764	0.354	0.159	0.013
Icosahedral	0	0.663	0	-0.170
(liquid)	0	0	0	0

TABLE 3.1 Bond orientational order parameters for a number of simple cluster geometries. fcc: face-centered-cubic structure, hcp: hexagonal close-packed structure, bcc: body-centered-cubic structure and sc: simple cubic structure.

to one of the crystal structures listed in Table 3.1. The other order parameters listed in Table 3.1 were used to analyze the configurations and distinguish between different crystal structures.

3.4 Structure analysis

Although the concept of a crystal nucleus is intuitively clear, it is not easy to give an unambiguous numerical criterion that will identify atoms as either solid- or liquidlike. In fact, a great variety of criteria to identify solidlike clusters in the liquid have been proposed. Here, we briefly review those criteria that are based on the structure (rather than the dynamics) of crystalline nuclei. In the earliest simulation studies of nucleation in a Lennard-Jones system, Mandell *et al.* [17] used the "local" structure function in order to identify crystalline nuclei. The main disadvantage of the method is that it does not have high spatial resolution and, more seriously, can be rather sensitive to the orientation of the crystal nuclei. The structure analysis used by Honeycutt and Andersen [71] is based on the observation [72] that there are many nearly collinear triplets of neighboring particles in the Lennard-Jones solid, whereas there are comparatively few such triplets in the liquid. The criterion used by Honeycutt and Andersen for deciding whether a given atom was solidlike, was that the atom must have at least five distinct pairs of its nearest neighbors with which it forms a triplet whose angle is greater than a specified cutoff angle near 180°. However, they observed that the size of the critical nucleus strongly depends on the cutoff angle used. Yang *et al.* [73] adopted a criterion that is based on the observation that crystalline solids, unlike liquids, can be constructed by periodically repeating a unit cell. In Ref. [73] solidlike regions are identified by searching for such periodically repeating units.

A more widely used technique for studying both crystalline and amorphous structures is the Voronoi-analysis of the topology of the environment of a given particle [18, 19, 21, 23, 25, 27]. The Voronoi polyhedron associated with a given particle is defined as the set of all points of space that are closer to that particle than to any of the others. In a perfect crystal, the Voronoi polyhedron reduces to the Wigner-Seitz cell. It is customary to define the signature of a Voronoi polyhedron as a set of integers $(n_3, n_4, n_5, ...)$, where n_l is the number of l-sided faces of the polyhedron. For example,

the Voronoi polyhedron of a perfect fcc structure, the rhombic dodecahedron (that has twelve lozenge-shaped faces), is denoted by (0 12 0 0 ...), while the Voronoi polyhedron of a particle in a body-centered cubic (bcc) structure, is denoted by (0 6 0 8 0 ...) (six squares, eight hexagons).

In practice, the Voronoi signatures of the particles in a crystal will be modified by the thermal vibrations. For instance, the characteristic Voronoi polyhedron of the fcc lattice, the rhombic dodecahedron, will be removed by the *tiniest* thermal motion. Of the 14 vertices of the rhombic dodecahedron there are six where *four* faces meet. Any thermal motion will make these fourfold vertices break up into sets of threefold vertices connected by short edges. The result is that a variety of polyhedra such as (0364), (0365), (0446), (0447) occur in a thermally equilibrated fcc crystal. Such tiny displacements of particles do not affect the signature of the bcc Voronoi polyhedron, because it has only threefold vertices. This is why it is often said that the bcc Voronoi polyhedron is stable against thermal distortions. However, although this may be true for cold bcc crystals, we find that a bcc crystal close to melting has many other Voronoi signatures in addition to the characteristic (06080). Hence, Voronoi signatures can only be used in a statistical sense to identify solidlike particles.

3.4.1 Identification of crystalline clusters

In the previous section, we described how we compute the degree of crystallinity of the system using global bond-order parameters [27]. We have extended this technique to identify individual solidlike particles and hence solid clusters. The advantage of the scheme is that it is rather insensitive to the crystal structure of the cluster.

To identify solidlike particles, we make use of the local orientational order parameter $\overline{q}_{lm}(i)$ as defined below in Eq. (3.27). From the $\overline{q}_{lm}(i)$ we can construct local invariants:

$$q_l(i) \equiv \left(\frac{4\pi}{2l+1} \sum_{m=-l}^{l} |\overline{q}_{lm}(i)|^2 \right)^{1/2} \tag{3.12}$$

and

$$\widehat{w}_l(i) \equiv w_l(i) \Bigg/ \left(\sum_{m=-l}^{l} |\overline{q}_{lm}(i)|^2 \right)^{3/2}, \tag{3.13}$$

with $w_l(i)$ given by

$$w_l(i) \equiv \sum_{\substack{m_1,m_2,m_3 \\ m_1+m_2+m_3=0}} \begin{pmatrix} l & l & l \\ m_1 & m_2 & m_3 \end{pmatrix} \overline{q}_{lm_1}(i)\, \overline{q}_{lm_2}(i)\, \overline{q}_{lm_3}(i). \tag{3.14}$$

These local order parameters are measures for the local order around particle i. However, the local order is large not only in the solid, but also in the liquid. Hence, both in the liquid and in the solid the *local* order parameters $q_l(i)$ are non-zero, see Fig. 3.2. The reason that nevertheless a *global* order parameter, such as Q_6, vanishes in the liquid, is that all $\overline{q}_{6m}(i)$ add up incoherently. In the solid, the $\overline{q}_{6m}(i)$ add up coherently and, as a consequence, the global order parameters are non-zero. It is this coherence of local bond-order parameters that we use to identify solidlike particles.

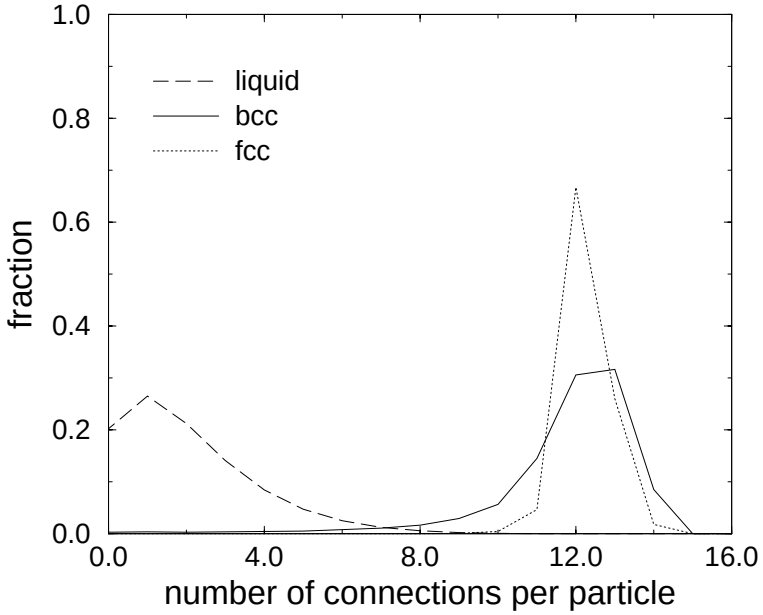

FIGURE 3.1 Distributions of the number of connections per particle in a Lennard-Jones system for a thermally equilibrated liquid, bcc and fcc structure at coexistence ($P = 5.68$, $T = 1.15$). The distributions are based on averages over 50 independent atomic configurations.

To every particle i we attribute a normalized $(2 \times 6 + 1)$-dimensional complex vector $\vec{q}_6(i)$, with components

$$\tilde{q}_{6m}(i) \equiv \frac{\overline{q}_{6m}(i)}{\left(\sum_{m=-6}^{6} |\overline{q}_{6m}(i)|^2\right)^{1/2}}. \tag{3.15}$$

We can now define a dot product of the vectors $\vec{q}_6$ of neighboring particles i and j:

$$\vec{q}_6(i).\vec{q}_6(j) \equiv \sum_{m=-6}^{6} \tilde{q}_{6m}(i)\tilde{q}_{6m}(j)^*. \tag{3.16}$$

By construction, $\vec{q}_6(i).\vec{q}_6(i) = 1$.

We now consider particles i and j to be "connected" if the dot-product $\vec{q}_6(i).\vec{q}_6(j)$ exceeds a certain threshold, in our case 0.5. It is clear that in the solid almost all $\vec{q}_6(i)$ are in phase with one another and add up coherently to produce a non-zero $\overline{Q}_{6m}$. Using this criterion all particles in the solid will turn out to be connected with one another. However, to identify a particle as "solidlike", it is not enough that its bond-order is in phase with only one of its neighbors. After all, even in the liquid it will frequently happen that the bond-order of neighboring particles is in phase and hence the two particles are considered "connected". We therefore only identify a particle as solidlike if the number of connections with its neighboring particles exceeds a threshold value. To illustrate this technique, Fig. 3.1 shows the histograms of the number of connections per particle for the liquid, the bcc structure and the fcc structure of the Lennard-Jones system, all equilibrated at the fcc-liquid coexistence point. As is to be expected, the average number of connections per particle in the liquid is less than in either solid. More importantly, the histogram for the liquid phase exhibits very little overlap with the histograms of the two solid phases. We find that, with a threshold value of seven connections per particle, more than 99% of the particles in an fcc structure are identified as being solidlike. Even for the bcc structure, which is rather open and disordered, this method identifies more than 97% of the particles as solidlike. In contrast, for the liquid less than 1% of the particles

were identified as being solidlike. Thus this analysis method gives an unambiguous, local criterion to identify solidlike particles. Once we have identified the individual solidlike particles, we can perform standard cluster analysis to recognize crystallites. We apply the criterion that any two solidlike particles that are neighbors belong to the same solid cluster.

3.4.2 Crystal-structure determination

As discussed above, the typical Voronoi polyhedra of the different crystal structures will be distorted by thermal vibrations of the particles around their lattice positions. As a consequence, a given structure will be characterized by a *distribution* of signatures, rather than a single one. In fact, each crystal structure has its own unique distribution of Voronoi signatures. Similarly, every structure has its own unique distribution of local bond-order parameters. We can use *either* distribution as a "fingerprint" that enables us to identify the crystal structure of crystalline nuclei.

To see how this method of analysis works, consider, for instance, the Voronoi histogram of a solid cluster. We represent this histogram as a n-dimensional unit vector $\hat{\mathbf{v}}$, where the number of components (n) corresponds to the number of "bins" of the histogram. We then decompose the vector $\hat{\mathbf{v}}$ corresponding to the cluster in a linear combination of the corresponding vectors for the equilibrated liquid, bcc and fcc structures. That is, we minimize

$$\Delta^2 = (\hat{\mathbf{v}}_{cl} - (f_{liq}\,\hat{\mathbf{v}}_{liq} + f_{bcc}\,\hat{\mathbf{v}}_{bcc} + f_{fcc}\,\hat{\mathbf{v}}_{fcc}))^2, \tag{3.17}$$

where $\hat{\mathbf{v}}_{cl}$, $\hat{\mathbf{v}}_{liq}$, $\hat{\mathbf{v}}_{bcc}$ and $\hat{\mathbf{v}}_{fcc}$ are the vectors associated with the histograms of the cluster, the liquid, the bcc structure and the fcc structure, respectively. Clearly, the coefficients f_{liq}, f_{bcc} and f_{fcc} are indicative of the type of crystal structure of the cluster. The value of Δ^2 is an indication of the quality of the fit. For instance, if we were to apply our analysis to an equilibrated fcc crystal, we would find $f_{fcc} = 1$, $f_{bcc} = 0$, $f_{liq} = 0$ and $\Delta = 0$.

Analogously, we can interpret the histogram of the probability distribution function of the local bond-order parameters as a multi-dimensional vector. Fig. 3.2 shows the probability distribution functions of the most interesting orientational order parameters for the liquid, bcc and fcc structures. The important thing to note is that, although the distributions of the local order parameters are quite broad, in particular in the liquid phase, there is still a considerable difference between the distributions that correspond to different phases. For instance, the distribution of $\widehat{w}_6(i)$ is strongly peaked in either solid phase, but not in the liquid. The distribution of $q_4(i)$ has a characteristic double-peaked structure in the fcc phase, but not in the bcc or liquid phases. We found that the probability distribution of $\widehat{w}_4(i)$ of the bcc phase is almost identical to that of the liquid. It could still be used to distinguish fcc structures from liquid or bcc. However, we found that the information contained in the $\widehat{w}_4$-distribution function did not add to the information obtained by using the q_4, q_6 and $\widehat{w}_6$ distributions. It is only the latter distributions that we have used in our structure analysis. To be more precise, we first concatenate the distribution functions of $q_6(i)$, $q_4(i)$ and $\widehat{w}_6(i)$ for each structure to form a single, unique distribution function. With the histogram of this distribution function we then associate a (normalized) vector. As with the Voronoi histograms, we

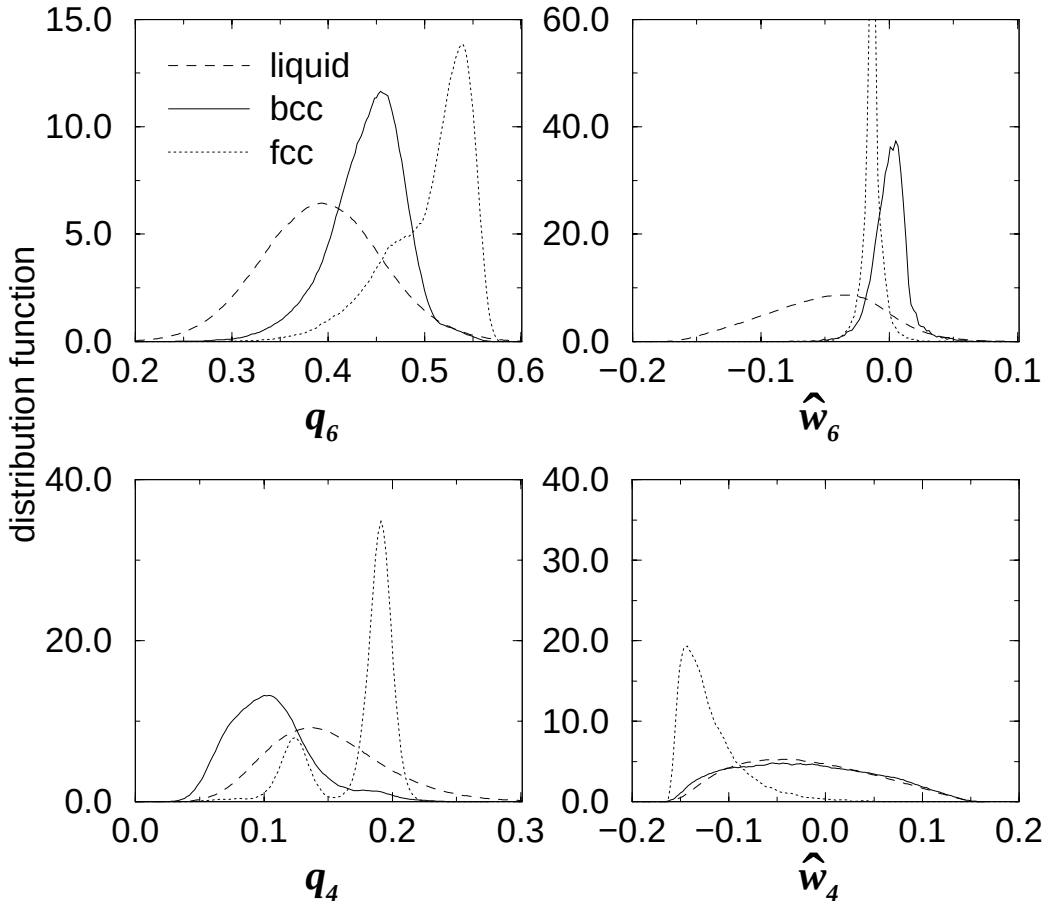

FIGURE 3.2 Probability distribution functions of the local order parameters, as defined in Eq. (3.12) and (3.13), in a Lennard-Jones system for a thermally equilibrated liquid, bcc and fcc structure at 20% undercooling ($P = 5.68$, $T = 0.92$). The distribution functions are based on averages over 50 independent atomic configurations.

can then decompose the order-parameter histogram of our solid cluster in the components corresponding to pure fcc, bcc and liquid.

When comparing the structure analysis based on Voronoi histograms with the local bond-order parameter method, we found that the Voronoi method was not very robust: a slight disordering of a bcc crystal led to a strong change in the Voronoi histogram (for instance, the characteristic (0608) signature is almost completely destroyed) and the Voronoi signatures of the disordered bcc and fcc structures end up looking quite similar. For this reason we have only used the more sensitive bond-order histogram method in our structure analysis.

3.5 Simulations

All simulations were performed in the isobaric-isothermal (constant-NPT) ensemble. Both Monte Carlo simulations and molecular dynamics simulations were performed. The

advantage of MD is that it facilitates equilibration through collective particle motions. Moreover, MD is essential to study the *kinetics* of crystal nucleation. The advantage of Monte Carlo simulations is that it is particularly suited for umbrella sampling. In what follows, we use reduced units, such that the Lennard-Jones well depth ϵ is the unit of energy, while the Lennard-Jones diameter σ is the unit of length.

In the Monte Carlo simulations each trial move consisted either of an attempted displacement of a particle or a trial volume change. The choice between trial volume moves and trial particle moves was made at random, with 92% probability for the latter. The acceptance ratio of the particle moves was maintained at 25%, while that of the volume moves was kept at 50%. For more details of the Monte Carlo scheme, see Refs. [27, 74]. In order to keep the pressure and temperature constant in our molecular dynamics simulations, we applied the extended system method proposed by Nosé and Andersen [75]. The equations of motion were integrated by a predictor-corrector version of the velocity Verlet algorithm [68] and the time step used in the molecular dynamics simulations was in the range 0.005-0.01τ, where τ is the unit of time. This was adequate for energy conserving dynamics.

The cutoff radius for intermolecular interactions was chosen such that $r_c = 2.5$. For the calculation of bond-order parameters, the cutoff distance for nearest-neighbor "bonds" was chosen at $r_q = 1.5$, which corresponds approximately to the first minimum of $g(r)$ in an fcc crystal at coexistence (in the Monte Carlo simulations the cutoff radii scale with the linear dimensions of the simulation box, but this is a small effect). To minimize the anisotropy in the system due to the periodic boundary conditions, we used a truncated octahedral simulation box [76]. To speed up the simulation, we used a Verlet neighbor list to calculate energies and forces and a linked list [68] to update the neighbor list. In Appendix 3.6.4 we describe how we combined the linked list method with truncated octahedral boundary conditions.

All simulations were started from a liquid configuration, obtained by melting a crystal. The first run in a series of umbrella samplings was performed without any weighting function. By changing the biasing potential, the next simulation was performed in an adjacent Q_6 interval. In this way we could slowly increase the crystallinity in the system and cross the free-energy barrier that separates the liquid phase from the solid phase. Once we had crossed the top of the barrier, we checked whether the path was reversible by lowering Q_6. We observed no significant hysteresis at the top of the barrier, although very long simulations were required to equilibrate the system.

As the equilibration time and the order-parameter fluctuations are much larger at the top of the barrier than on either side of it, we tuned the biasing potential in such a way that, at the top of the barrier, only narrow windows in Q_6 were sampled. A typical simulation in a given window consisted of an equilibration period of 10000-50000 cycles (MC)/time steps (MD), followed by a production run of 25000-75000 cycles/time steps.

The individual probability distribution functions $P(Q_6)$ obtained in different runs were fitted simultaneously to a polynomial [27]. We used a polynomial fit rather than the self-consistent procedure of Ferrenberg and Swendsen [77], because a good polynomial fit can be obtained even when the adjacent histograms do not overlap or overlap only slightly. The reason is that even a very narrow histogram yields an estimate of the local *derivative* of the free energy. From this local information, the global free-energy barrier can then be reconstructed using a polynomial fit.

Having determined the free energy barrier, we used constrained MD to generate a sequence of configurations at Q_6^*, the position of the top of the barrier. The duration of this MD simulation was of 100τ (25000 time steps) and from this run we kept 50 independent configurations separated by 2τ (500 time steps) to be used as initial states for the computation of the barrier crossing flux $R(t)$, as given by Eq. (3.10). At the beginning of the unconstrained MD runs to compute $R(t)$, all particles were given a velocity drawn from a Maxwell-Boltzmann distribution. The duration of these runs was 5τ, which appeared long enough for the system to reach a stationary state. In order to improve the statistics, we assigned different initial velocities to the same configurations, and we also made use of the time reversal property:

$$R(t) = -\frac{\langle \dot{Q}_6 \theta[Q_6(-t) - Q_6^*] |H|^{-1/2} \rangle}{\langle |H|^{-1/2} \rangle} = -R(-t)\,. \tag{3.18}$$

This means that the flux was computed by averaging over the trajectories obtained propagating forwards and backwards our set of initial configurations obtained from a constrained run at the top of the barrier. The results that we present here for the rate were averaged over 200 trajectories.

3.6 Results and discussion

We studied the formation of a critical nucleus and the rate of nucleation for a Lennard-Jones system at 20% undercooling with respect to the melting temperature. Although this degree of supercooling is appreciably less than what is used in "brute force" simulations of crystal nucleation, it is still large compared to the degree of supercooling that can be reached experimentally for simple liquids such as argon. In our choice of this particular degree of supercooling we tried to strike a compromise between making the supercooling as small as possible and, at the same time, keeping the critical nucleus much smaller than the system size. As we studied a system of $\mathcal{O}(10^4)$ particles, we tried to ensure that the supercooling was strong enough to make the critical nucleus at least one order of magnitude smaller. A rough estimate, based on classical nucleation theory, suggests that the size of the critical nucleus is about 100 particles for 20% undercooling. However, several studies indicate that, although the core of the nucleus might be quite small, the interface between the liquid and the solid is rather diffuse [17, 63, 71, 78], so in practice the number of solidlike particles may be appreciably larger. After testing the method on a small system, we performed all production runs on a system of 10648 particles.

We performed the simulations at two different reduced pressures: $P = 0.67$ and $P = 5.68$. We used the data of Hansen and Verlet [79] to estimate the location of the melting points (see Table 3.2).

P	T	ρ_{liquid}	$\rho_{crystal}$
0.67	0.75	0.875	0.973
5.68	1.15	0.936	1.024

TABLE 3.2 Transition data for the Lennard-Jones system at the reduced pressures $P = 0.67$ and $P = 5.68$. From Hansen and Verlet [79].

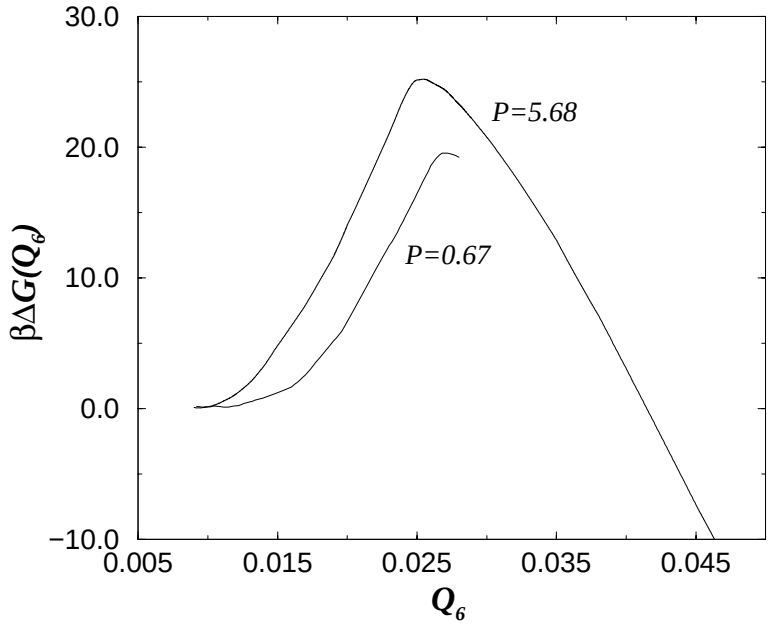

FIGURE 3.3 The Gibbs free energy of a Lennard-Jones system as a function of crystallinity (Q_6) at 20% undercooling for two different pressures, i.e. $P = 5.68$ ($T = 0.92$) and $P = 0.67$ ($T = 0.6$). The Gibbs free-energy barriers are approximately $25.1k_BT$ at $P = 5.68$ and $19.4k_BT$ at $P = 0.67$.

Figure 3.3 shows the free-energy barriers computed for these two pressures. Let us first describe qualitatively what happens as the system crosses the barrier. Initially, the system is in the metastable liquid phase. Due to spontaneous fluctuations, some small solidlike clusters are present in the liquid. We find that the solidlike clusters rarely comprise more than 16 particles. When Q_6 is increased from the liquid, both the number and size of these solidlike clusters in the liquid increase. The reason why there are, initially, several small solidlike clusters is that is is entropically favorable for the system to distribute a given amount of crystallinity over several clusters. For a given overall degree of crystallinity, there is a competition between translational entropy, favoring the formation of many small clusters, and surface free energy, which favors the formation of a single large crystallite. When the top of the barrier is approached, the surface free energy dominates and the small solidlike clusters merge. Indeed, at the top of the barrier only one cluster, the critical nucleus, is observed, apart from a number of small solidlike fluctuations that are always present in the liquid. This implies that the Gibbs free energy of the system at the top of the barrier corresponds to the Gibbs free energy of the critical nucleus, the nucleation barrier.

In the following we first discuss the structure of the nuclei as a function of our "reaction coordinate". Next, we consider the structure of the critical nucleus in more detail by examining the radial profiles for the density and our structural order parameters. We will only present the results of the structure analysis for the system at $P = 5.68$, as the ones for $P = 0.67$ are qualitatively similar. Finally, we discuss the transition rate and make a comparison with classical nucleation theory.

3.6.1 Crystallite structure

As mentioned in the previous section, only small crystallites are observed on the liquid side of the barrier. The size of the largest crystallites ranges from 16 particles in the metastable liquid to 26 particles as the top of the barrier is approached. Previous theoretical [80], experimental [81] and computer simulation studies [81–83] indicate that

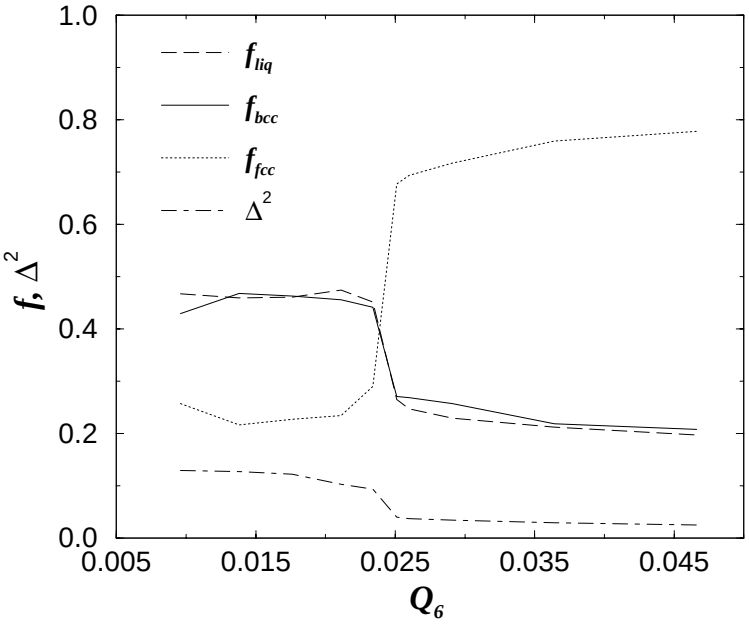

FIGURE 3.4 Structural composition of the largest cluster in a Lennard-Jones system, indicated by f_{liq}, f_{bcc}, f_{fcc} and Δ^2, as a function of Q_6 (the reaction coordinate) at 20% undercooling ($P = 5.68$, $T = 0.92$). This figure is based on averages over 50 independent atomic configurations.

for small clusters of Lennard-Jones atoms *in vacuo* the icosahedral structure is more stable than any of the crystalline structures. Besides, it has been suggested [70] that long-ranged icosahedral order would be favored in strongly supercooled liquids. When we applied a conventional Voronoi analysis to our system in the liquid state, we could identify on average 1 % of the atoms as being icosahedrally surrounded. However, the larger crystallites that were present in the liquid never contained any atom with the characteristic (0 0 12 0) signature of an icosahedron. Also an examination of the local bond order parameter $\widehat{w}_6$, which is most sensitive to icosahedral order (see Table 3.1), supported the conclusion that the largest crystallites do not contain icosahedrally ordered atoms. In fact, the bond-order analysis indicates that the larger solidlike clusters in the metastable liquid have appreciable bcc character, whereas at the top of the barrier and beyond, they are predominantly fcc-like. To make this analysis more quantitative, we determined f_{liq}, f_{bcc} and f_{fcc} as defined in Eq. (3.17) for the largest cluster in the system.

Fig. 3.4 shows the structural "composition" of the largest cluster in the system, as a function of the "reaction coordinate", Q_6. The figure shows that the precritical nuclei are predominantly bcc- and liquidlike. However, near the top of the barrier, at $Q_6 = 0.025$, there is a clear change in the nature of the solid nuclei from bcc- and liquidlike to mainly fcc-like. The fact that the precritical nuclei are rather liquidlike is not surprising as they are quite small and almost all interface. The important point to note is that these nuclei have clearly more bcc than fcc character. This suggests that, at least for small crystallites, we find the behavior predicted by Landau theory [32]. Yet, as the critical and postcritical clusters are predominantly fcc-like, the present results are also compatible with the findings of Swope and Andersen [25], who observed that nucleation proceeded through fcc crystallites. In fact, the nucleation process as observed in the present simulations might be interpreted as a manifestation of the Ostwald step rule [2]: first a metastable, bcc, phase is nucleated, which is then transformed into a

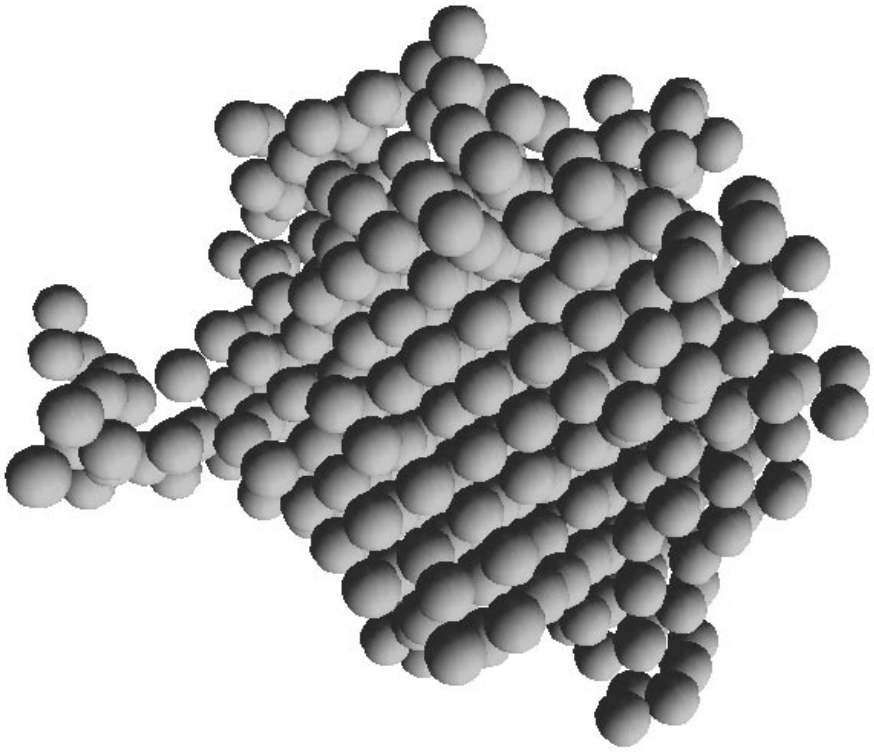

FIGURE 3.5 Snapshot of the critical nucleus at 20% undercooling ($P = 5.68$, $T = 0.92$) in a Lennard-Jones system.

more stable, fcc, phase. What is remarkable is that we find that the transformation from bcc to fcc takes place before the critical nucleus is reached.

3.6.2 Critical nucleus

Visual inspection of the critical and postcritical nuclei showed that the nuclei at this moderate degree of undercooling are fairly compact, more or less spherical objects (see Fig. 3.5). This finding appears to be in contrast to what is found in simulations of crystal nuclei at large supercooling [71, 73] where ramified structures were observed. Although we find the critical nucleus to be fairly spherical, rudimentary facets can be distinguished. Facetting of crystal nuclei was also observed by Báez and Clancy [84], who studied the growth and dissolution of critical fcc nuclei implanted in a liquid at 26% undercooling. Báez and Clancy found that during the earliest stages of growth the nuclei are distinctly octahedral, with facets corresponding to the (111) planes of the fcc crystal.

In order to quantify the degree of non-sphericity of the critical nucleus, we expand the mass distribution of the crystallite in rank four spherical harmonics (Y_{4m}) and constructed quadratic invariants, denoted by $S_4(cl)$. For a spherical cluster $S_4(cl)$ is, of course, zero. But for an octahedral cluster it has a value of 0.11. We find that, both

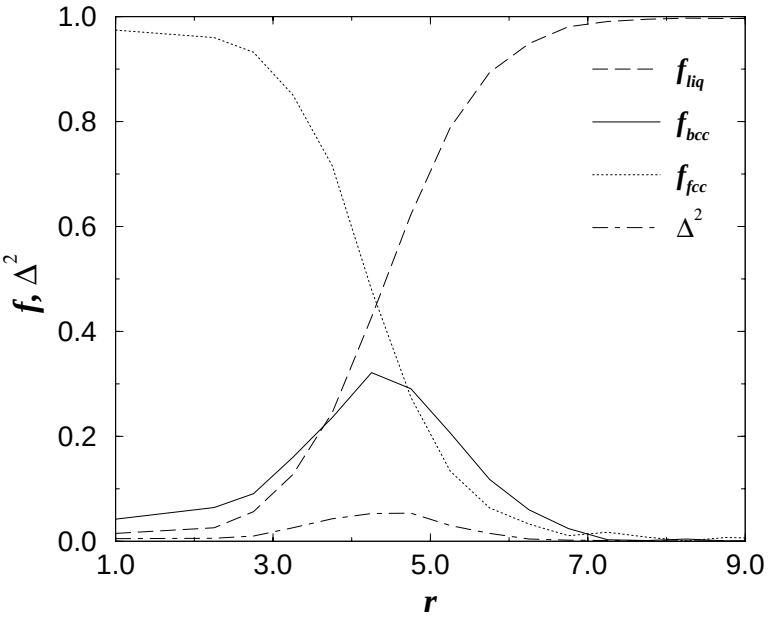

FIGURE 3.6 Structure of the critical nucleus, indicated by f_{liq}, f_{bcc}, f_{fcc} and Δ^2, as a function of r, the distance to its center-of-mass, at 20% undercooling ($P = 5.68$, $T = 0.92$) in a Lennard-Jones system. This figure is based on averages over 50 independent atomic configurations.

for the critical and postcritical nuclei, $S_4(cl)$ is much smaller than is compatible with an octahedral shape. Hence the critical and postcritical nuclei in our simulations are indeed quite spherical, which supports the assumption of classical nucleation theory. However, this finding seems hard to reconcile with the strong faceting of crystal nuclei that was observed by Báez and Clancy [84]. It should be recalled that Broughton and Gilmer, who have computed the interfacial free energy of a Lennard-Jones system for three different orientations of the fcc crystal-liquid interface [85], found the surface free energies for the (111), (100) and (110) faces to be equal to within the statistical error. If the interfacial free energy is indeed completely isotropic, one should expect to see a spherical crystal nucleus. Slight anisotropies in the interfacial free energy might lead to fairly spherical crystal shapes, such as the truncated octahedron. It should be stressed, however, that interfacial free energies only determine the equilibrium crystal shape and not the non-equilibrium shape that develops during growth. It is conceivable that the strongly octahedral crystal shape found in Ref. [84] is determined by kinetics.

In the previous section we found that the critical nucleus has mainly fcc character. Yet it still has considerably liquidlike and bcc-like character. In fact, it is not surprising that the critical nucleus has some liquidlike character. After all, it consists only of some 642 particles and has therefore a large surface-to-volume ratio. However, the bcc-like character is more intriguing. We have therefore studied the local order of the critical nucleus in more detail.

Given the spherical shape of the critical nucleus it is meaningful to calculate f_{liq}, f_{bcc} and f_{fcc} in a spherical shell of radius r around the center-of-mass of the cluster. Fig. 3.6 shows the radial profile of the local order of the critical nucleus. As expected, we find that the core of the nucleus is almost fully fcc-ordered and that far away from the center of the nucleus, f_{fcc} decays to zero and f_{liq} approaches unity. More surprisingly however, is that f_{bcc} increases in the interface and becomes even larger than f_{fcc} , before it decays to zero in the liquid. Hence, the present simulations suggest that the fcc-like core of the equilibrated nucleus is "wetted" by a shell which has more bcc character. This finding

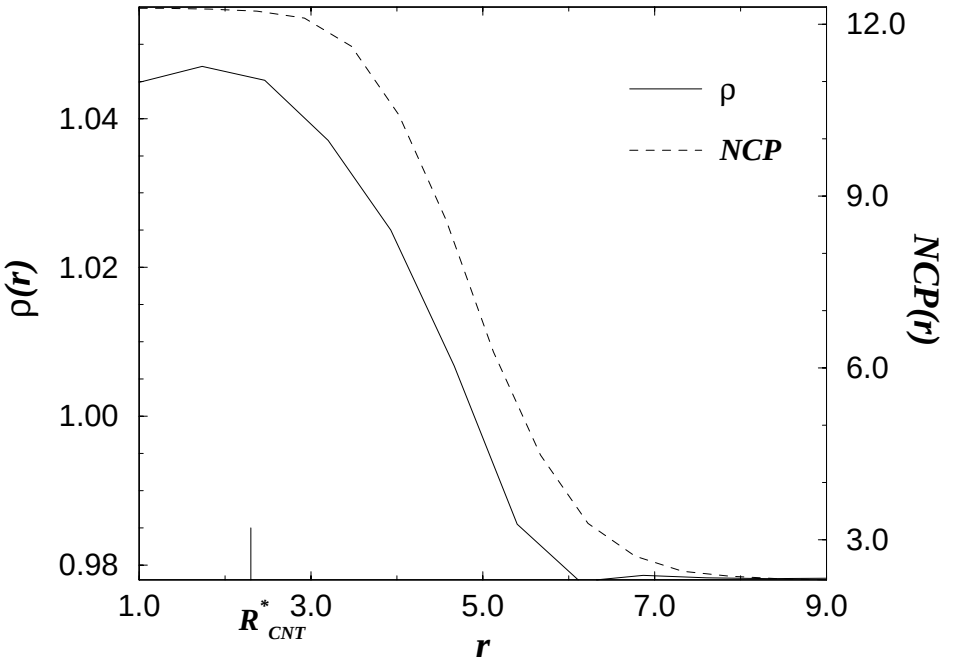

FIGURE 3.7 The density ρ and the number of connections per particle (NCP) as a function of r, the distance to the center-of-mass, for the critical nucleus in a Lennard-Jones system at 20% undercooling ($P = 5.68$, $T = 0.92$). The coordinate-axes are such that they range from a liquid to a bulk solid value, both for the density and the structural order parameter. R_{CNT} is the radius of the critical nucleus as given by classical nucleation theory. Based on averages over 50 independent atomic configurations.

explains why Fig. 3.4 shows that even fairly large nuclei do not have a pure fcc signature: there is always a residual bcc signature due to the interface. It also explains the strong bcc character of the small clusters, such as appear on the liquid side of the barrier: they are so small that their structure is strongly surface-dominated.

As can be seen from Fig. 3.6 the interface between the nucleus and the surrounding liquid is quite diffuse (some 4 atomic layers). Such a diffuse interface is predicted by recent theories of homogeneous nucleation [63, 78]. In contrast, classical nucleation theory assumes a sharp interface. A more specific prediction about the solid-liquid interface of crystal nuclei is made in the density functional theory of Harrowell and Oxtoby [63]. This theory predicts that the density profile of the clusters reaches liquidlike values *well before* the order-parameter profile does. In other words, this theory predicts that there exists a "shell" with liquidlike density but solidlike order around the nucleus. To test this prediction we plotted both the density and the "degree of crystallinity" as measured by the number of bond-order connections per particle (NCP) (see section 3.4.1). The number of such connections per particle is a measure for the local bond orientational order and can be used as a structural order parameter. Fig. 3.7 shows the density and the number of connections per particle as a function of r. We see that the density in the core of the nucleus is somewhat lower than the density of the bulk fcc solid under

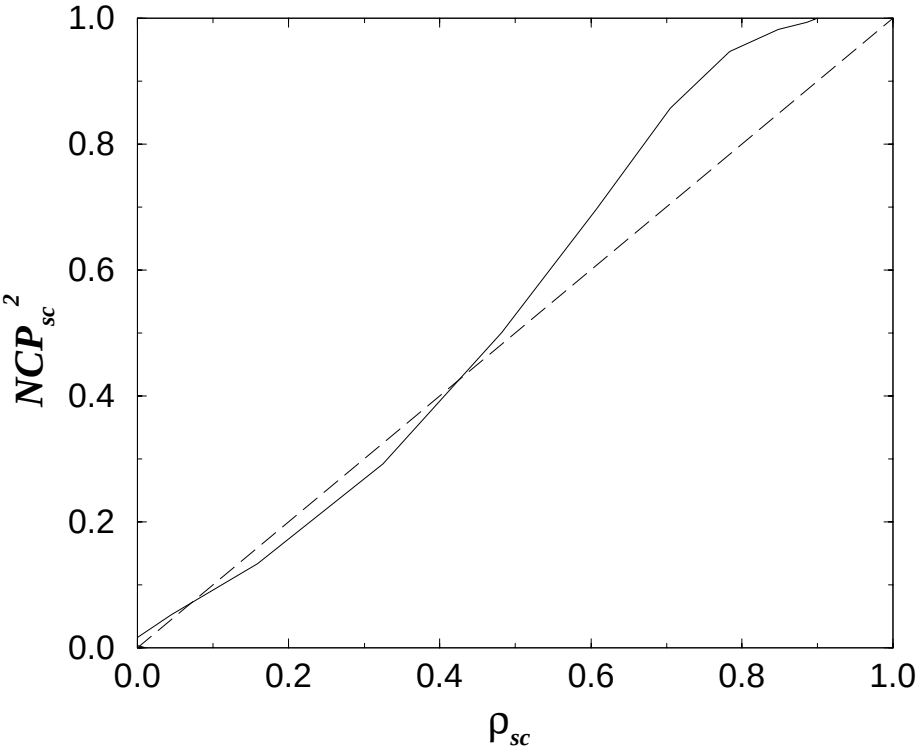

FIGURE 3.8 Square of the scaled structural order parameter as a function of the scaled density ρ_{sc} for the critical nucleus in a Lennard-Jones system at 20% undercooling (P=5.68, T=0.92). The scaled structural order parameter is given by $NCP_{sc} \equiv \frac{NCP-NCP_{liq}}{NCP_{sol}-NCP_{liq}}$, and the scaled density is given by $\rho_{sc} \equiv \frac{\rho-\rho_{liq}}{\rho_{sol}-\rho_{liq}}$, where NCP is the number of connections per particle, and *liq* and *sol* denote that the quantities are computed in the bulk liquid and bulk solid, respectively. The solid line is the result from the simulations, and the dashed straight line is the prediction of the density functional theory of Oxtoby [86]. Based on averages over 50 independent atomic configurations.

similar conditions. In contrast, the structural order parameter reaches the same value in the core of the nucleus as in the bulk solid. This finding is in agreement with the density functional calculations of Ref. [63].

The figure also shows that both the density and the structural order parameter decay smoothly to a liquidlike value outside the nucleus. Moreover, as predicted theoretically [63], the density falls off faster than the structural order parameter. The latter profile appears to be displaced by some 0.7σ with respect to the density profile. Hence the cluster is indeed surrounded by a thin layer that is liquidlike in density, but solidlike in structure. In fact, in the density-functional theory of Oxtoby [86] the density change varies algebraically with the structural order parameter. Figure 3.8 shows the relation between the square of the structural order parameter variation and the change in density, as obtained in the simulation. We should point out that our definition of the solid order parameter is not equivalent to the one used by Oxtoby [86]. Still, the figure

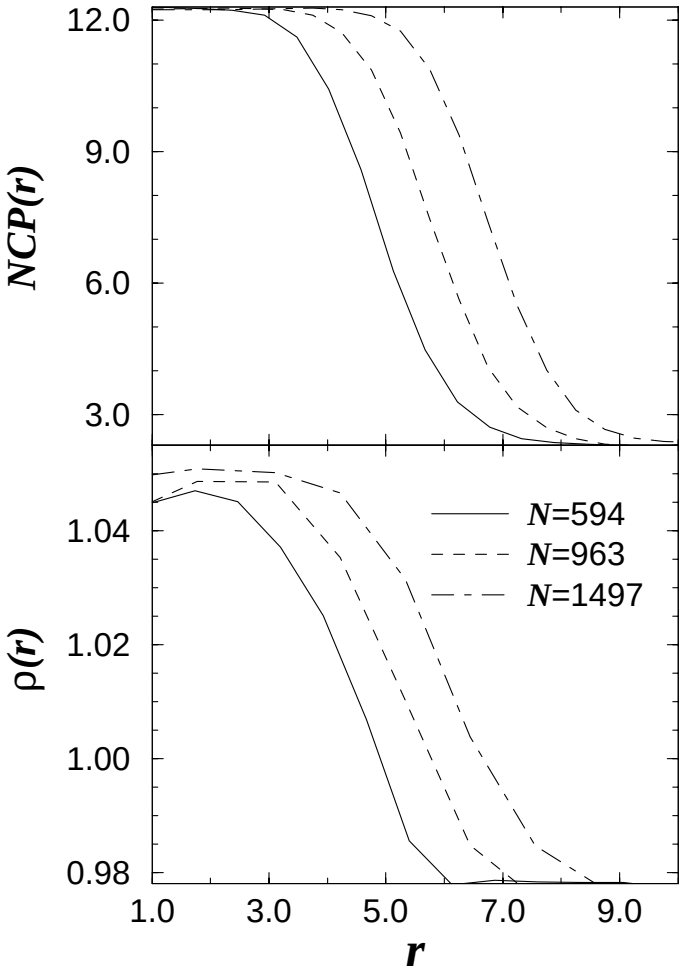

FIGURE 3.9 The density (ρ) and the number of connections per particle (NCP) as a function of r, the distance to the center-of-mass, for the critical nucleus and several postcritical nuclei in a Lennard-Jones system, at 20% undercooling ($P = 5.68$, $T = 0.92$). The coordinate-axes are such that they range from a liquid to a bulk solid value, both for the density and the structural order parameter. Based on averages over 50 independent atomic configurations.

suggests that, at least far from the core (i.e. where the crystallinity and density is low) the quadratic relation between order parameter and density seems to be satisfied.

Both the diffuseness of the solid-liquid interface and the difference in the density and order-parameter profiles, make the definition of the *size* of the critical nucleus ambiguous. For instance, if we choose to locate the surface of the critical nucleus at the point where the order parameter is half-way between its bulk-solid and liquid values, then the radius of the nucleus would be 4.9σ and the number of particles in the critical nucleus would be 630. But if we use the half-way point of the density to define the crystallite surface, then we find a radius of 4.2σ, corresponding to 412 particles in the critical nucleus. A direct comparison of the size of the critical nucleus with the prediction of classical nucleation theory is therefore not very meaningful.

As the nucleus grows beyond its critical size, it retains its spherical shape and the core retains the same (fcc) crystal structure. More interestingly, the structure of the interface does not change either. The postcritical nuclei retain a high degree of bcc ordering at the interface and the density decays faster than the structural order parameter. In fact, as can be seen in Fig. 3.9, the width of the interface remains essentially constant. We have also studied the solid-liquid interface in the limit of an "infinitely large" crystal-nucleus, i.e. a planar interface. To this end, we brought the (100)-face of a slab of a

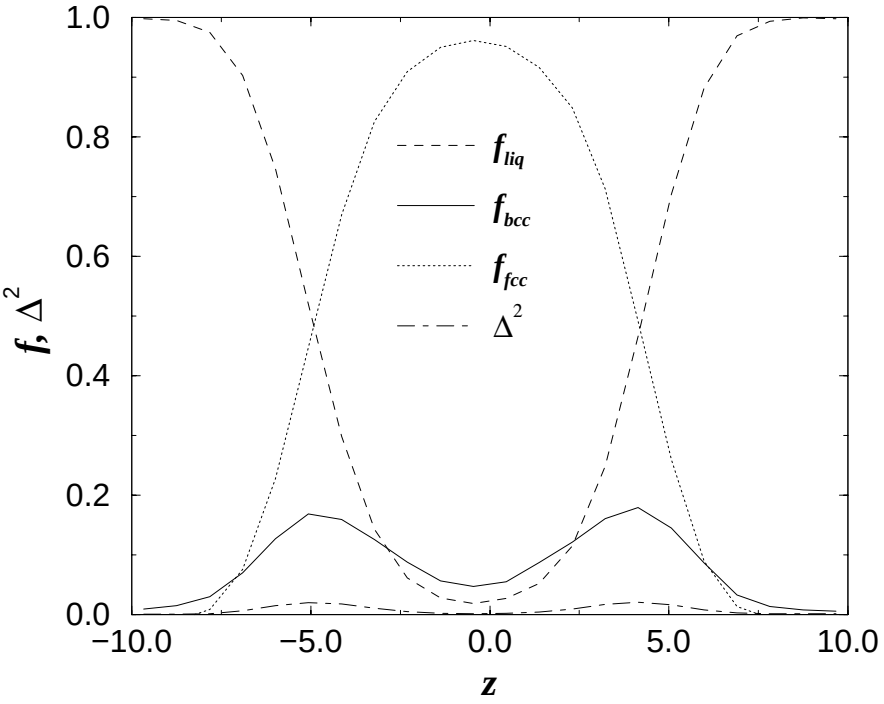

FIGURE 3.10 The structural composition, indicated by f_{liq}, f_{bcc}, f_{fcc} and Δ^2, of the Lennard-Jones system with the planar fcc-liquid interface, equilibrated at coexistence ($\rho = 0.978$, $T = 1.15$). The z-coordinate, in units of σ, is the coordinate perpendicular to the planar interface.

thermally equilibrated fcc crystal in contact with a liquid and equilibrated the interface in a constant-NVT molecular dynamics simulation ($\rho = 0.978$, $T = 1.15$, $N = 10532$). Fig. 3.10 shows that, just as with the small nuclei, f_{fcc} decreases monotonically in the interface while f_{bcc} peaks there. The bcc-like structure of the fcc-liquid interface appears to be quite general and should be observable experimentally.

3.6.3 Nucleation rate

Up to this point, we have only discussed the static aspects of crystal nucleation. Let us now consider the actual barrier crossing process. Most of the previous computer-simulation studies of nucleation rates were performed by rapidly quenching a liquid to temperatures well below its freezing point, and then measuring the time-lag until the first signs of crystallization appear [17, 21–23, 73, 83, 84]. This method, although straightforward, has some disadvantages. First and foremost, as the nucleation rate depends exponentially on the degree of undercooling, the brute-force method only works under conditions of extreme supercooling. Moreover, the method lumps two times together. The first is the *induction time*, i.e. the time it takes the cluster-size distribution to respond to the temperature quench. In the stable liquid, only small clusters appear, whereas in the supercooled liquid there is an enhanced (although still very small) probability to observe larger clusters. The second is the actual time it takes to cross the nucleation barrier, given a (quasi) Boltzmann distribution of precritical nuclei. Finally, even in a strongly supercooled system, nucleation remains a rare event, and hence the statistics on the nucleation rate is usually poor.

We therefore did not use the "brute-force" approach to compute the nucleation rate. Rather, we employed the fact that nucleation is an activated process and that the rate is given by Eq. (3.6). The advantage of this approach is that we do not have to wait for the

critical nucleus (or the activated state) to form spontaneously: we prepare the system at the top of the free energy barrier and simply measure the time correlation between the initial order-parameter velocity and the probability of finding the system in the solid side of the barrier at a later time t. This correlation function is expected to reach a plateau value relatively quickly (at least, compared to the actual times involved in the nucleation process) and hence the nucleation rate can be determined from comparatively short runs. By performing many runs, we can improve the statistical accuracy of the measurement of the nucleation rate. Even so, the simulations become quite time-consuming.

The first step in the computation of the flux is to identify the "transition state" from our knowledge of the shape of the free energy barrier. We denote this point by Q_6^*. We then performed a MD simulation of the system under the constraint $Q_6 = Q_6^*$, to generate a set of independent configurations at the top of the barrier. Note that constraining Q_6 does not necessarily imply that the size of the critical nucleus is constrained. However, a structure analysis of the configurations at the top of the barrier showed that the average size of the largest cluster did not change significantly during the constrained run. The set of configurations obtained in this way was used as initial state for the computation of $R(t)$ from Eq. (3.10).

Figure 3.11 shows the transmission coefficient κ, as defined in Eq. (3.9) for $P = 0.67$. The figure shows that initially the transmission coefficient decreases rapidly from the value $\kappa = 1$ at $t = 0$. This is due to recrossing at short times. However, after a short transient relaxation period of approximately 0.5τ, $\kappa(t)$ appears to reach a plateau value (shown as a dashed line in the graph). As it is clear from the figure, the statistical accuracy of $\kappa(t)$ is rather poor, even though averages over 200 trajectories were taken. A direct analysis of the trajectories of the system in Q_6-space showed that its behavior is distinctly diffusive. The system does not clearly fall into either minima (solid or liquid one) in the duration of the run, but remains close to the top of the barrier in most cases. The largest cluster present in the system, the critical cluster, did not grow or shrink monotonically, but its size fluctuated, although in most cases a clear tendency to the liquid or to the solid minimum could be observed. Hence, to speak in the language of chemical kinetics, crystal nucleation is closer to the Kramers limit of diffusive escape over a barrier [87] than to the "ballistic" crossing of Eyring's transition-state theory [66].

Indeed, due to the diffusive nature of the barrier crossing, the plateau value of the transmission coefficient is quite small, $\kappa \sim 0.05$ for $P = 5.68$ and $\kappa \sim 0.2$ for $P = 0.67$. The prediction of transition-state theory (TST) for the rate can be obtained by combining the initial value of the forward flux, $R(0^+)$, with the earlier results for the barrier height. It was found from the simulations that for $P = 5.68$, $R(0^+) = 5.85 \cdot 10^{-3}\tau^{-1}$, and hence $k_{TST} = 7.35 \cdot 10^{-14}\tau^{-1}$. From k_{TST} and the plateau value of the transmission coefficient we can then get the full nucleation rate, which is found to be $k = 4.04 \cdot 10^{-15}\tau^{-1}$. In the low pressure case the values were $k_{TST} = 2.40 \cdot 10^{-11}\tau^{-1}$ and $k = 4.79 \cdot 10^{-12}\tau^{-1}$.

The rates obtained in our simulation are measured in units of Q_6 per unit time, as the quantity computed was the flux of Q_6. Nucleation rates are usually measured in number of solid particles produced in the unit volume per unit time. To get such a quantity for the results of the simulation we would have to multiply k by $\rho_{liq} dN_{sol}/dQ_6$, where ρ_{liq} is the density of the liquid and N_{sol} is the number of solid particles. We assume that there is a linear relationship between Q_6 and the number of solid particles (this is certainly

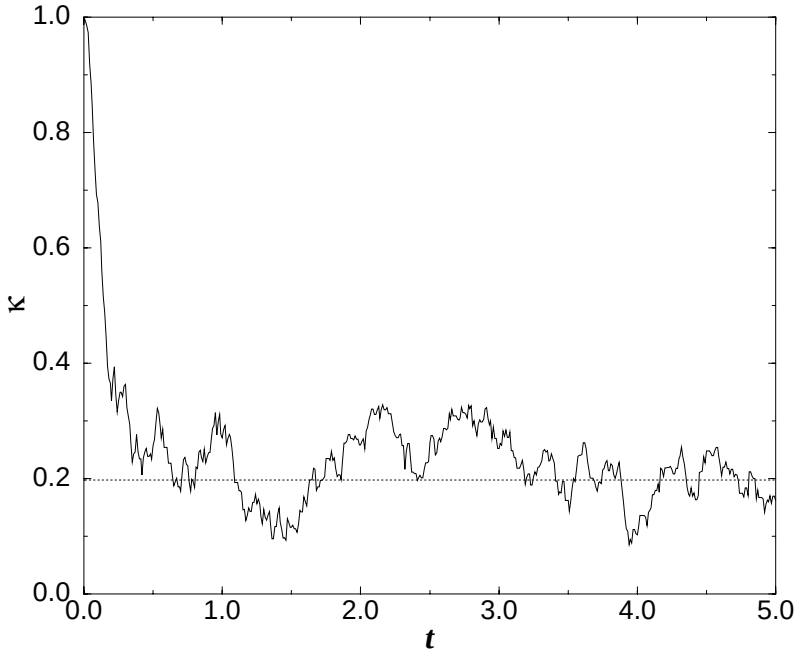

FIGURE 3.11 Transmission coefficient as a function of time at 20% undercooling (P =0.67, T=0.6). The dotted line shows the plateau value that is established after 0.5τ. This figure is based on averaging over 200 trajectories.

true for large crystallites). We then can write

$$\frac{dN_{sol}}{dQ_6} = \frac{N^*_{sol} - N^{liq}_{sol}}{Q^*_6 - Q^{liq}_6},$$

where the superscript liq denotes that the corresponding quantity is evaluated in the liquid minimum. Taking into account the results of the previous sections we finally obtain $k_{TST} = 2.23 \cdot 10^{-9}\sigma^{-3}\tau^{-1}$, $k = 1.23 \cdot 10^{-10}\sigma^{-3}\tau^{-1}$ for $P = 5.68$ and for $P = 0.67$ we get $k_{TST} = 4.09 \cdot 10^{-7}\sigma^{-3}\tau^{-1}$, $k = 8.19 \cdot 10^{-8}\sigma^{-3}\tau^{-1}$.

The value of the rate k implies that in order to observe nucleation in a system of 10648 particles at 20% undercooling at $P = 5.68$, a simulation time of the order of $10^6\tau$ would be required (this estimate is obtained by taking the inverse of k and dividing the result by the volume of the system). Taking into account that a time step in a MD simulation is typically of the order of $10^{-2}\tau$, runs of a duration of at least 10^8 time steps would have to be performed. This is not in disagreement with previous studies that were not able to see crystallization in liquids with a degree of undercooling smaller than about 26% during runs of a duration of $\sim 1000\tau$ [84].

3.6.4 Comparison with classical nucleation theory

Turnbull and Fisher [88] applied the Becker-Döring formalism to nucleation in condensed systems and derived the following expression for the nucleation rate [6, 88]:

$$k = A(T)e^{-\beta\Delta G^*}, \tag{3.19}$$

where ΔG^* is the nucleation barrier and $A(T)$ is a kinetic prefactor. We are now in a position to test the predictions of classical nucleation theory (CNT), both concerning the height of the free-energy barrier to nucleation and the value of the kinetic prefactor. As argued in the previous section, predictions concerning the size of the critical nucleus

P	γ	Δh $(T = T_m)$	$\Delta\mu$ $(T = 0.8T_m)$	v_{fcc} $(T = 0.8T_m)$
0.67	0.35	-1.31	-0.262	0.998
5.68	0.35	-1.46	-0.292	0.948

TABLE 3.3 Data used to calculate the nucleation rate as given by classical nucleation theory; the average of the surface free energies, γ, calculated by Broughton and Gilmer [85], the enthalpy change per particle on freezing, Δh, at coexistence [79], the estimated difference in chemical potential $\Delta\mu$ between the bulk fcc solid and bulk liquid at 20% undercooling, and the volume per particle in the bulk fcc solid at 20% undercooling, v_{fcc}, both for $P = 0.67$ and $P = 5.68$.

are harder to test, as the size of the critical nucleus, as computed in the simulations, is ill defined.

In classical nucleation theory the height of the free-energy barrier is given by [6]

$$\Delta G^* = \frac{16\pi\gamma^3 v^2}{3(\Delta\mu)^2}, \tag{3.20}$$

where γ is the surface free energy per unit area of the liquid-crystal interface, v is the volume per particle in the solid and $\Delta\mu$ is the difference in chemical potential between the bulk solid and bulk liquid.

Two problems arise when applying Eq. (3.20). The first is that we do not know the solid-liquid interfacial free energy for Lennard-Jones crystals in contact with a supercooled liquid. However, as already mentioned above, Broughton and Gilmer [85] have calculated the surface free energy for three different orientations of the fcc crystal-liquid interface. They performed their calculations at coexistence, near the triple point (i.e. low pressure), and found the surface free energies to be equal within their error bars. In our comparison we will use the average of their estimates for the surface free energies of the different faces.

The second problem is that we do not know the difference in chemical potential between the bulk solid and bulk liquid at 20% undercooling. However, close to coexistence the difference in chemical potential can be approximated by [6]

$$\Delta\mu \approx \Delta h(T_m - T)/T_m, \tag{3.21}$$

where Δh is the enthalpy change per particle on freezing at coexistence and T_m is the melting temperature. We have taken the enthalpy change per particle in the liquid-solid transition at coexistence from the data of Hansen and Verlet [79]. In Table 3.3 we have collected for both pressures the average value of the surface free energies estimated by Broughton and Gilmer [85], the enthalpy change per particle on freezing at coexistence [79], the estimated difference in chemical potential between the bulk fcc solid and bulk liquid at 20% undercooling and the volume per particle in the bulk fcc solid at 20% undercooling.

Using the data shown in Table 3.3, classical nucleation theory yields the following predictions for the nucleation barriers: $\beta\Delta G^* = 17.4$ at $P = 0.67$ and $\beta\Delta G^* = 8.2$ at $P = 5.68$. We find from our simulations that $\beta\Delta G^* \approx 19.4$ for the lower pressure and $\beta\Delta G^* \approx 25.1$ for the higher pressure (see Fig. 3.3). As Broughton and Gilmer have calculated the surface free energy at a temperature and pressure which are closer to

the temperature and pressure of the simulation at $P = 0.67$, we expect the agreement between the theoretical prediction and the results of the simulation to be better for this lower pressure than for the higher pressure, $P = 5.68$. In fact, for the lower pressure the agreement between the predicted height of the barrier and the height of the barrier as computed in our simulation is surprisingly good if one takes into account the crude approximations made in classical nucleation theory. The discrepancy for the higher pressure between the CNT-prediction and the results of the simulation is most likely mainly due to the fact that the surface free energy at this higher pressure and temperature is somewhat larger than the Broughton and Gilmer estimate. As the surface free energy comes in with the third power in the theoretical expression for the height of the barrier, a difference of only 40% in the surface free energy could account for the discrepancy between theory and simulation. If we make the assumption that the surface free energy is proportional to the latent heat [6] (which increases with pressure), then we arrive at an estimate for the barrier height at the higher pressure that is within 20% of the simulation results.

In classical nucleation theory the radius of the critical nucleus is given by [6]

$$R^* = \frac{2\gamma v}{|\Delta\mu|}. \tag{3.22}$$

Using the data form Table 3.3, CNT gives the following predictions for the radius of a critical fcc nucleus: 2.7σ for $P = 0.67$ and 2.3σ for $P = 5.68$. We have indicated this radius for the critical nucleus at the higher pressure in Fig. 3.7. Although the exact boundary between the core and the interface of the nucleus is not clear, it seems that CNT significantly underestimates the size of the critical nucleus.

Let us next consider the kinetic prefactor. The following expression for $A(T)$ has been proposed [6]:

$$A(T) = Z\rho_{liq}\frac{24Dn^{*2/3}}{\lambda^2}. \tag{3.23}$$

D is the diffusion coefficient, ρ_{liq} is the density of the liquid, n^* is the size of the critical nucleus and λ is the atomic jump distance in the liquid. Z is the Zeldovich factor, which relates the number of solid clusters in the steady state with the equilibrium value,

$$Z = \left(\frac{|\Delta G''(n^*)|}{2\pi k_B T}\right)^{1/2}, \tag{3.24}$$

where $\Delta G''(n^*)$ is the second derivative of the Gibbs free energy with respect to the cluster size at n^*. Using the CNT-expression for ΔG we get:

$$Z = \left(\frac{|\Delta\mu|}{6\pi k_B T n^*}\right)^{1/2}. \tag{3.25}$$

When making the comparison between the CNT-prediction for $A(T)$ and the value obtained from the simulations, we use the value of n^* obtained in the simulation. For $P = 5.68$ we obtained in the simulation $n^* \sim 642$, so Eq. (3.25) leads to a value of the Zeldovich factor of $Z = 5.12 \cdot 10^{-3}$, while for $P = 0.67$, $n^* \sim 500$ and $Z = 6.81 \cdot 10^{-3}$. Similar values are obtained if we use Eq. (3.24) directly, although in this case the statistical accuracy is poor. The appearance of the Zeldovich factor in the expression for the rate-constant is a consequence of the fact that the barrier crossing is

considered as a *diffusive* rather than a *ballistic* process [6]. It is precisely this diffusive behavior near the top of the barrier that leads to recrossings and hence to a reduction of $\kappa(t)$. The small value of the Zeldovich factor, as given by Eq. (3.24), is in qualitative agreement with the strong reduction of κ due to recrossings, as found in the simulations.

The diffusion coefficient in the supercooled liquid was computed in a separate simulation and was found to be $D \approx 1 \cdot 10^{-2}\sigma^2\tau^{-1}$, for both pressures. The atomic jump distance was approximated by $\rho_{liq}^{-1/3}$, which gives $\lambda \approx 1.0\sigma$ for $P = 5.68$ and $\lambda \approx 0.97\sigma$ for $P = 0.67$. This leads to a prediction of the kinetic prefactor of $A = 8.76 \cdot 10^{-2}\sigma^{-3}\tau^{-1}$ for $P = 5.68$ and $A = 0.113\sigma^{-3}\tau^{-1}$ in the low pressure case. The value of the kinetic prefactor in the simulation can easily be obtained by dividing the value of the rate k by $\exp(-\Delta G^*/k_BT)$. The resulting value is $A = 9.78\sigma^{-3}\tau^{-1}$ for $P = 5.68$ and $A = 21.83\sigma^{-3}\tau^{-1}$ for $P = 0.67$. This means that the kinetic prefactor obtained in the simulation is about two orders of magnitude larger than the one predicted by classical nucleation theory, leading to a larger value of the nucleation rate.

Broughton *et al.* [89, 90] performed a simulation study of crystal growth of a Lennard-Jones fcc crystal in contact with the melt. They observed that the (100) face crystallized two to three times faster than the (111) face. In fact, they found that for the (100) face the energy barrier for crystallization vanishes and that the rate is not limited by the mobility of atoms in the liquid, but is determined by the ideal gas thermal velocity, $(3k_BT/m)^{1/2}$. If we assume that the growth mechanism of the critical nucleus is that of the (100) face, and take $A(T)$ to be

$$A(T) = Z\rho_{liq}\frac{4n^{*2/3}(3k_BT/m)^{1/2}}{0.4a}, \tag{3.26}$$

where a is the interatomic spacing [89, 90], then we get a predicted prefactor of $6.45\sigma^{-3}\tau^{-1}$ for the higher pressure and $6.31\sigma^{-3}\tau^{-1}$ for the lower pressure. Note that the agreement with the simulation results is much better, although the measured prefactors are still higher than the predicted ones. Most experiments also indicate that the kinetic prefactor is significantly larger than predicted by classical nucleation theory [6]. However, it is interesting to note that in recent experiments by Brugmans *et al.* [91] the opposite was found: a kinetic prefactor that is many orders of magnitude smaller than the estimate of classical nucleation theory.

Finally, we should point out that the nucleation rate at 20 % supercooling, although very small on the time scale of a computer simulation, is still very large from an experimental point of view. If we use the values of argon for σ and τ, and express the nucleation rate at $P = 5.68$ in the usual units, we find $k = 1.44 \cdot 10^{24}\mathrm{cm}^{-3}\mathrm{s}^{-1}$. This means that liquid argon at 20% undercooling would crystallize essentially instantly. Indeed, argon cannot be supercooled by 20% (in fact, it is notoriously difficult to supercool liquid argon).

Appendix A Order parameter definition

First we define the set of neighbors of a particle i as all particles j that are within a given radius r_q from i. The vectors $\mathbf{r}_{ij}$ joining neighbors are called bonds. The unit vector $\hat{\mathbf{r}}_{\mathbf{ij}}$ specifies the orientation of the bond $\mathbf{r}_{ij}$. In a given coordinate frame, the orientation of the unit vector $\hat{\mathbf{r}}_{\mathbf{ij}}$ uniquely determines the polar and azimuthal angles θ_{ij} and ϕ_{ij}. In

order to construct invariants, we first consider the spherical harmonics $Y_{lm}(\theta_{ij}, \phi_{ij}) \equiv Y_{lm}(\hat{\mathbf{r}}_{\mathbf{ij}})$. We can now characterize the local structure around particle i by

$$\overline{q}_{lm}(i) \equiv \frac{1}{N_b(i)} \sum_{j=1}^{N_b(i)} Y_{lm}(\hat{\mathbf{r}}_{ij}), \tag{3.27}$$

where the sum runs over all $N_b(i)$ bonds that particle i has with its neighbors. The $\overline{q}_{lm}(i)$ are still *local* order parameters. By calculating the average of $\overline{q}_{lm}(i)$ over all N particles, we obtain *global* orientational order parameters $\overline{Q}_{lm}$:

$$\overline{Q}_{lm} \equiv \frac{\sum_{i=1}^{N} N_b(i) \overline{q}_{lm}(i)}{\sum_{i=1}^{N} N_b(i)}. \tag{3.28}$$

The $\overline{Q}_{lm}$ still depend on the choice of reference frame. However, from the $\overline{Q}_{lm}$, rotationally invariant combinations can be constructed:

$$Q_l \equiv \left(\frac{4\pi}{2l+1} \sum_{m=-l}^{l} |\overline{Q}_{lm}|^2 \right)^{1/2} \tag{3.29}$$

and

$$\widehat{W}_l \equiv W_l \Bigg/ \left(\sum_{m=-l}^{l} |\overline{Q}_{lm}|^2 \right)^{3/2}, \tag{3.30}$$

with W_l given by

$$W_l \equiv \sum_{\substack{m_1,m_2,m_3 \\ m_1+m_2+m_3=0}} \begin{pmatrix} l & l & l \\ m_1 & m_2 & m_3 \end{pmatrix} \overline{Q}_{lm_1} \overline{Q}_{lm_2} \overline{Q}_{lm_3}. \tag{3.31}$$

Q_l and W_l are the second-order and third-order invariants, respectively. The term in brackets in Eq. (3.31) is a Wigner-3j symbol.

The order parameter Q_6 as defined above and used in Ref. [27] is not suited for constraint MD simulations, because the presence of a cut-off radius r_q means that Q_6 is not a continuously differentiable function of all particle coordinates. This problem can be remedied by attributing a weight $\alpha(r_{ij})$ to the contribution of a given pair ij to the Q_{lm}, where $\alpha(r)$ is a function that goes to zero smoothly at $r = r_q$. In the present simulations, we have chosen $\alpha(r)$ to be a quadratic function that has its minimum at r_q and equals one at $r_{ij} = \sigma$:

$$\alpha(r_{ij}) \equiv \left(\frac{r_{ij} - r_q}{\sigma - r_q} \right)^2 \tag{3.32}$$

The corresponding definitions of $\overline{q}_{lm}(i)$ is

$$\overline{q}_{lm}(i) \equiv \frac{\sum_{j=1}^{N_b(i)} Q_{lm}(\mathbf{r}_{ij}) \alpha(r_{ij})}{\sum_{j=1}^{N_b(i)} \alpha(r_{ij})}, \tag{3.33}$$

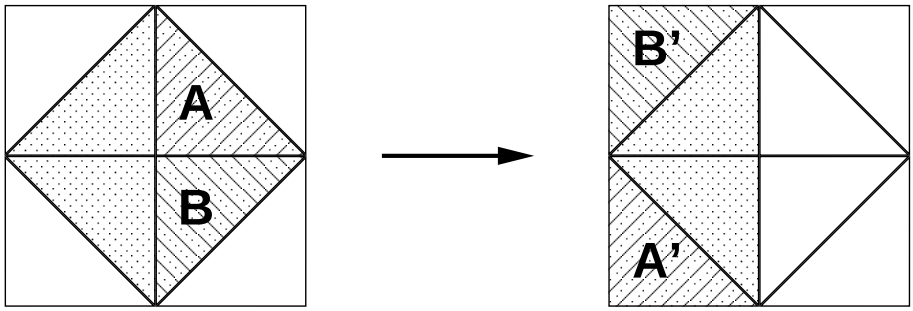

FIGURE 3.12 The two-dimensional analog of the translation of all particles in the right half of the truncated octahedron, our simulation box, to the space between the left half of the truncated octahedron and the containing cube (containing the truncated octahedron), in order to set up the cell list. The rotated square in the middle corresponds to the truncated octahedron and the containing square corresponds to the containing cube. In this analog the translation of the particles corresponds to a translation of all particles in area A to the area A' and all particles in area B to the area B'.

and $\overline{Q}_{lm}$ becomes

$$\overline{Q}_{lm} \equiv \frac{\sum_{i=1}^{N} \sum_{j=1}^{N_b(i)} Q_{lm}(\mathbf{r}_{ij}) \alpha(r_{ij})}{\sum_{i=1}^{N} \sum_{j=1}^{N_b(i)} \alpha(r_{ij})}. \tag{3.34}$$

We find that the present definition of Q_6 leads to values that differ little from those obtained with the definition of Q_6 used in Ref. [27].

Appendix B Linked lists for octahedral boundary conditions

We use a truncated octahedral periodic unit cell in our simulations. At first sight, it would seem that a truncated octahedron is not a convenient shape to use when setting up a mesh of cubic cells for the linked list that we use to speed up the computation. However, it should be noted that the truncated octahedron is a Wigner-Seitz cell of a bcc lattice. The unit cell of this cubic lattice has twice the volume of the truncated octahedron. Clearly, it is easy to partition this cubic unit cell into small cubic mesh cells. However, we should take care to avoid double counting, i.e. there should be a one-to-one correspondence between every point in the truncated octahedral box and one of the cubic mesh cells. To this end, we map all particles in the right half ($x > 0$) of the truncated octahedron to their periodic image that is in the left half ($x < 0$) of the cubic unit cell. This mapping is unique. And, as the volume of the truncated octahedron is equal to half the volume of the cube, we have thus mapped the position of every particle in our simulation box to the left half of the cube. Once we have mapped all particles to the left half of the cube, we can divide that volume into $0.5M \times M \times M$ cells and use the conventional techniques to construct the linked list [68]. Fig. 3.12 shows a two-dimensional analog of this procedure. In the two-dimensional analog, all particles in area A are mapped to area A' and all particles in area B to area B'.

4 Choice of reaction coordinate

In this chapter we discuss the choice for the reaction coordinate. We point out that there is a fundamental difference between the use of a global and local order parameter to measure the amount of the new phase. Using a global order parameter, precritical nuclei may break up spontaneously for entropic reasons. At some point, however, the nuclei combine to form a relatively large luster. The transition from small clusters to one large cluster is discussed in detail. Finally, we present a method that allows us to avoid this entropic cluster break up.

4.1 One or many clusters

When a liquid phase solidifies, it will tend to form the solid structure with the lowest free energy. It is usually assumed that the lowest free-energy state in the two-phase region is one in which a single large crystallite has formed. The reason why this is the lowest free energy state is, of course, that a single crystal has a lower surface area than a larger number of crystallites with the same total volume. And, indeed, it seems obvious that, once crystallization is complete, the single crystal must correspond to the (overwhelmingly) most likely situation.

However, in a simulation, we can constrain a system to be at a given point in the two phase region. That is, the crystalline phase takes up a fixed volume fraction ϕ_{cr} of the total available volume. The question is: *is the single crystal still, necessarily, the most stable configuration*?

In the early work of Salsburg and Wood [92], the free-energy barrier that is responsible for hysteresis in constant NVT simulations is estimated assuming that a system in the two-phase region will always try to minimize its surface free energy. However, one should also consider the fact that, by breaking up a single crystal into a large number of smaller crystallites, the system may gain entropy. The question is if and when this entropic gain outweighs the surface free-energy cost.

To arrive at an estimate, we consider the following simple model. The total Helmholtz free energy of a system consisting of M particles (of which N particles are in the solid phase) in volume V at temperature T, is denoted by F. The fraction of all particles that are in the crystalline state is

$$X_{cr} = N/M \tag{4.1}$$

Let us now compute the excess free energy per solidlike particle in a two-phase system, using the Helmholtz free energy of the neat liquid as our reference state. The Helmholtz free energy of the two-phase system contains three contributions.

1. A negative "bulk" contribution
$$\frac{\beta F_b}{N} = -\Delta\beta\mu \ , \tag{4.2}$$
where $\Delta\mu$ is the chemical potential difference between solid and liquid and $\beta = 1/k_BT$. This term does not change as we redistribute particles over different numbers of crystallites. We need not consider this term in the rest of our analysis.
2. A surface free energy term,
$$\frac{\beta F_s}{N} = \frac{n_{cr}}{N} 4\pi r_c^2 \beta\gamma_{sl} \ , \tag{4.3}$$
where n_{cr} is the number of crystallites, r_c is the crystallite radius and γ_{sl} is the free energy per unit area of the solid-liquid interface. We can easily relate r_c to the volume fraction occupied by the solid:
$$n_{cr}\rho_{cr}(4\pi/3)r_c^3 = N \tag{4.4}$$
where ρ_{cr} is the number density of the crystal. Hence,
$$r_c = \left(N(3/4\pi\rho_{cr}n_{cr})\right)^{1/3} \ . \tag{4.5}$$
If we insert this in the expression for F_s, we obtain
$$\frac{\beta F_s}{N} = \frac{n_{cr}}{N} 4\pi\beta\gamma_{sl} \left(N(3/4\pi\rho_{cr}n_{cr})\right)^{2/3} = \left(\frac{n_{cr}}{N}\right)^{1/3} 4\pi\beta\gamma_{sl} \left((3/4\pi\rho_{cr})\right)^{2/3} \tag{4.6}$$
$$\equiv \left(\frac{n_{cr}}{N}\right)^{1/3} \beta f_0 \ . \tag{4.7}$$
The last line defines the parameter
$$f_0 \equiv 4\pi\gamma_{sl} \left((3/4\pi\rho_{cr})\right)^{2/3} \tag{4.8}$$
For the Lennard-Jones system near the triple point, βf_0 is a number of order 1.
3. The final term is a translational entropy term. To estimate this term, we simply assume that the crystallites behave like a gas of identical spherical particles. The free energy of such a gas could, for instance, be estimated using the Carnahan-Starling equation of state. However, we shall assume that the volume fraction of solid is low, and we therefore ignore all non-ideal terms in this free energy.
$$\frac{\beta F_{tr}}{N} \approx \frac{n_{cr}}{N} \left(\ln(n_{cr}/V) - 1\right) \tag{4.9}$$

It is convenient to rewrite the above expressions in terms of n_0, the number of particles per crystallite ($n_0 = N/n_{cr}$). If we combine the surface and translational free energies, we get:
$$\frac{\beta F(n_{cr})}{N} = \frac{1}{n_0^{1/3}} \beta f_0 + \frac{1}{n_0} \left(\ln\left(\frac{N/V}{n_0}\right) - 1 \right) \ . \tag{4.10}$$
Rather than carry out the minimization of the free energy with respect to n_0, we consider two limiting cases, namely $n_0 = N$ ($n_{cr} = 1$), i.e. a single crystallite and $n_{cr} = N_{max}$, a total breakup of the solid in small "nano" crystallites. The smallest cluster should still

be large enough to be recognized as a crystal. Hence, we should expect that there will be of the order of 12 particles in the minimal solid cluster. We call this number n_{min}. Hence $N_{max} = N/n_{min}$.

Before we proceed we should reconsider the "neat" liquid at coexistence. Even in the liquid there will be a finite concentration of small clusters or, what amounts to the same thing, the average number of crystalline particles ($\langle N \rangle_l$) is non-zero in the liquid. As we move into the two-phase region, the number of crystalline particles increases and we should look at the initial change in free energy.

To estimate $\langle n_{cr} \rangle_l$, the number of nano-crystallites in the neat fluid, we consider the expression for the free energy as a function of n_{cr}:

$$\beta F_l = n_{cr} \left(n_{min}^{2/3} \beta f_0 + \ln[n_{cr}/V] - 1 \right) \tag{4.11}$$

To find the state of lowest free energy, we minimize with respect to n_{cr}, to find

$$\beta f_0 n_{min}^{2/3} + \ln \left(\frac{n_{cr}}{V} \right) = 0 \tag{4.12}$$

Hence, the equilibrium concentration of nano-crystallites in the neat fluid is

$$\langle n_{cr}/V \rangle_l = \exp(-\beta f_0 n_{min}^{2/3}) \tag{4.13}$$

The second derivative of the free energy with respect to n_{cr} is

$$\frac{\partial^2 \beta F}{\partial n_{cr}^2} = \frac{1}{n_{cr}} \tag{4.14}$$

Therefore, close to coexistence, the dependence of the free energy on the number of crystalline particles is given by

$$\beta \Delta F = \frac{\exp(\beta f_0 n_{min}^{2/3})}{2V n_{min}^2} (\Delta N)^2 \tag{4.15}$$

or, in terms of the fraction of crystalline material $X_{cr} = (\Delta N)/M$,

$$\beta \Delta F = \frac{V \exp(\beta f_0 n_{min}^{2/3}) \rho^2}{2 n_{min}^2} X_{cr}^2 \tag{4.16}$$

Now consider the alternative scenario where all additional crystalline material is used to form a single cluster. The radius of this large cluster is related to the radius of the nano-clusters by

$$r_{large}^3 = r_{nano}^3 (\rho V X_{cr})/n_{min} \tag{4.17}$$

and then

$$\beta \Delta F = f_0 \left(\frac{\rho V X_{cr}}{n_{min}} \right)^{2/3} \tag{4.18}$$

Note that the free energy of a single cluster varies as $X_{cr}^{2/3}$. Hence, initially it is always more favorable to form many small crystallites, rather than a single large one. Let us now estimate the point where the single cluster becomes more stable. This happens when

$$f_0 \left(\frac{\rho V X_{cr}}{n_{min}} \right)^{2/3} = \frac{V \exp(\beta f_0 n_{min}^{2/3}) \rho^2}{2 n_{min}^2} X_{cr}^2 \tag{4.19}$$

This implies that

$$X_{cr}^{4/3} = f_0 \left(\frac{\rho}{n_{min}}\right)^{2/3} \frac{2n_{min}^2}{\exp(\beta f_0 n_{min}^{2/3})\rho^2} V^{-1/3} \tag{4.20}$$

or

$$X_{cr} \sim V^{-1/4} \tag{4.21}$$

This means that the break-even point depends on system size. For computer simulations of finite systems, this effect is certainly non-negligible, as illustrated by our simulation results. A more general problem with the use of such a "global" measure for the degree of crystallinity is that the size of the smallest cluster that is stable with respect to entropic breakup grows with system size:

$$N_{large} = \rho \left(\frac{\rho}{n_{min}}\right)^{1/2} \left(\frac{2f_0 n_{min}^2}{\exp(\beta f_0 n_{min}^{2/3})\rho^2}\right)^{3/4} V^{3/4} \tag{4.22}$$

Therefore, even if a cluster is "postcritical" in the sense of classical nucleation theory, it may still be "precritical" for entropic reasons.

We emphasize that the above derivation is oversimplified. However, it shows that problems may arise when using a *global* (i.e. total degree of crystallinity) rather than *local* (i.e. size of the largest cluster) order parameter in the construction of the free-energy barrier between liquid and solid.

Below, we present a new method that is based on the use of a local order parameter. It allows for the sampling of all cluster sizes with equal accuracy. But before we present the details of the method, let us discuss the statistical mechanics of the cluster distribution.

4.2 Cluster-size distribution

Consider a system in a volume V, at temperature T and at constant chemical potential μ (i.e. a system in the grand-canonical ensemble). The partition function is given by

$$\Xi(\mu, V, T) \equiv \sum_{N=0}^{\infty} \exp(\beta\mu N) Q(N, V, T), \tag{4.23}$$

where N is the number of particles, $\beta \equiv 1/k_B T$ is the reciprocal temperature, k_B is Boltzmann's constant, and $Q(N, V, T)$ is the canonical partition function:

$$Q(N, V, T) = \frac{1}{\Lambda^{3N} N!} \int d\mathbf{r}^N \exp[-\beta U(\mathbf{r}^N)] \; . \tag{4.24}$$

Here $U(\mathbf{r}^N)$ is the potential energy of the configuration with the coordinates $\mathbf{r}^N$, and $\Lambda \equiv h/\sqrt{2\pi m k_B T}$ is the thermal De Broglie wavelength.

We will assume that we have a criterion that enables us to define which particles make up a cluster. The total number of particles in the clusters will be denoted by N_c and the remaining particles in the parent phase will be denoted by N_o, hence $N = N_c + N_o$. Clearly, the potential energy U depends on $\mathbf{r}^{N_o}$ and $\mathbf{r}^{N_c}$, i.e. $U = U(\mathbf{r}^{N_c}; \mathbf{r}^{N_o})$, and we

rewrite the grand-canonical partition function as

$$\Xi(\mu,V,T) = \sum_{N_c=0}^{\infty} \exp(\beta\mu N_c) \sum_{N_o=0}^{\infty} \exp(\beta\mu N_o) \times \\ \frac{1}{\Lambda^{3N_o} N_o!} \frac{1}{\Lambda^{3N_c} N_c!} \int d\mathbf{r}^{N_o} \int d\mathbf{r}^{N_c} \mathcal{W}(\mathbf{r}^{N_c};\mathbf{r}^{N_o}) \exp[-\beta U(\mathbf{r}^{N_c};\mathbf{r}^{N_o})]. \tag{4.25}$$

where we have used the fact that there are $N!/(N_c!\ N_o!)$ ways to select N_c and N_o particles from a total number of $N_c + N_o$ particles. In the above equation, we have introduced a weight function $\mathcal{W}$ which is defined such that it is one when the number of particles that satisfy the cluster criterion equals N_c and zero otherwise. It should be stressed that we do not assume that there is only a single cluster in the system. Hence, later we have to consider the number of ways in which we can distribute N_c particles over the total number of clusters. In fact, $\mathcal{W}$ contains products of single-cluster weight functions. If we label the clusters by their size n and by $j_n = 1, .., N_n$, where N_n is the number of clusters of size n, it can be written as:

$$\mathcal{W}_{N_c} = \sum \prod_n \prod_{j_n=1}^{N_n} w_{j_n}(\mathbf{r}^n)$$

where $\sum$ indicates that we consider all cluster distributions and w_{j_n} is one if its arguments satisfy the criterion for a single j_n-particle cluster, and zero otherwise. With these definitions we can rewrite Eq. 4.25 as

$$\Xi(\mu,V,T) = \sum_{N_1=0}^{\infty} \sum_{N_2=0}^{\infty} \cdots \sum_{N_{n_{max}}=0}^{\infty} \frac{1}{N_1! N_2! \cdots N_{n_{max}}!} \prod_{n=1}^{n_{max}} (\exp(\beta\mu n) n^3/[\Lambda^{3n} n!])^{N_n} \\ \times \sum_{N_o=0}^{\infty} \exp(\beta\mu N_o) \frac{1}{\Lambda^{3N_o} N_o!} \int d\mathbf{r}^{N_o} \prod_n \left[\int d\mathbf{r}'^{n-1} \right]^{N_n} \\ \times \int \prod_{n=1}^{n_{max}} \prod_{j_n=1}^{N_n} d\mathbf{R}_{j_n} w_{j_n}(\mathbf{R}_{j_n}, \mathbf{r}'^{n-1}; \mathbf{r}^{N_o}) \exp[-\beta U(\mathbf{R};\mathbf{r}^{N_o})]. \tag{4.26}$$

Here $\mathbf{R}_{j_n}$ denotes the center-of-masses of the clusters and the primes indicate that the coordinates are taken with respect to the center-of-mass of the cluster. Note that we have not split the potential energy function yet. The product $\prod_n \prod_{j_n=1}^{N_n} w_{j_n}$ contains $\prod_n N_n$ distinct cluster functions w_n. In this equation we have somewhat arbitrarily introduced a maximum cluster size n_{max}.

For any given configuration of clusters we can define a potential of mean force $W(\mathbf{r}^{N_c};\mu)$ as

$$\exp[-\beta W(\mathbf{r}^{N_c};\mu)] \equiv \sum_{N_o=0}^{\infty} \exp(\beta\mu N_o)\frac{1}{\Lambda^{3N_o}N_o!} \times \int d\mathbf{r}^{N_o} \prod_{n=1}^{n_{max}} \prod_{j_n=1}^{N_n} w_{j_n}(\mathbf{R}_{j_n}, \mathbf{r}'^{n-1}; \mathbf{r}^{N_o}) \exp[-\beta U(\mathbf{r}^{N_c};\mathbf{r}^{N_o})]. \tag{4.27}$$

All possible configurations of the particles in the parent phase will contribute to $W(\mathbf{r}^{N_c};\mu)$. It is the average potential the particles in the clusters feel due to all interactions with the "solvent" particles. With the above definition for the potential of mean force, the grand-canonical partition function can be rewritten as

$$\Xi(\mu,V,T) = \sum_{N_1=0}^{\infty}\sum_{N_2=0}^{\infty}\cdots\sum_{N_{n_{max}}=0}^{\infty} \frac{1}{N_1!N_2!\cdots N_{n_{max}}!} \prod_{n=1}^{n_{max}} (\exp(\beta\mu n)n^3/[\Lambda^{3n}n!])^{N_n} \times \prod_{n=1}^{n_{max}} \left[\int d\mathbf{r}'^{n-1}\right]^{N_n} \int \prod_{n=1}^{n_{max}} \prod_{j_n=1}^{N_n} d\mathbf{R}_{j_n} \exp[-\beta W(\mathbf{r}^{N_c};\mu)]. \tag{4.28}$$

The potential of mean force depends on the interactions between particles of the same cluster and on the interactions between particles of different clusters. In nucleation the density of clusters is usually so low, that the interactions between them can be neglected. However, at this stage we will not yet ignore these, but assume that the inter-cluster interaction energy is pair-wise additive and only depends on the positions of the center-of-mass of the clusters. The interaction energy $W(\mathbf{r}^{N_c};\mu)$ can then be written as

$$W(\mathbf{r}^{N_c};\mu) = W_0 + \sum_{n}\sum_{j_n=1}^{N_n} W_n(\mathbf{r}^{n,j_n};\mu) + \frac{1}{2}\sum_{n,n'}\sum_{j_n,j_{n'}} W_{n,n'}(\mathbf{R}_{n,j_n}, \mathbf{R}_{n',j_{n'}};\mu). \tag{4.29}$$

The constant W_0 is a measure for the grand-potential in the absence of clusters. W_n denotes the intra-cluster interaction energy of cluster j_n of size n, and $W_{n,n'}$ is a measure for the effective interaction between clusters j_n and $j_{n'}$. With this assumption for the potential of mean force, the grand partition function becomes

$$\begin{aligned}\Xi(\mu,V,T) = \exp(-\beta W_0) &\sum_{N_1=0}^{\infty}\sum_{N_2=0}^{\infty}\cdots\sum_{N_{n_{max}}=0}^{\infty} \frac{1}{N_1!N_2!\cdots N_{n_{max}}!} \\ &\times \prod_{n=1}^{n_{max}} (\exp(\beta\mu n)n^3/[\Lambda^{3n}n!])^{N_n} \int d\mathbf{r}^{N_c} \prod_{n=1}^{n_{max}} \left[\int d\mathbf{r}'^{n-1} \exp[-\beta W_n(\mathbf{r}'^{n-1};\mu)]\right]^{N_n} \\ &\times \int \prod_{n=1}^{n_{max}} \prod_{j_n=1}^{N_n} d\mathbf{R}_{j_n} \exp[-\beta W_{n,n'}(\mathbf{R}_{n,j_n}, \mathbf{R}_{n',j_{n'}};\mu)]\end{aligned} \tag{4.30}$$

As a final simplification, we ignore the interactions between the clusters. The partition function then becomes

$$\Xi(\mu,V,T) = \exp(-\beta W_0) \sum_{N_1,N_2,..,=0}^{\infty} \prod_n [\exp(\beta\mu n N_n)] \times \prod_n \frac{1}{N_n!}\left[\frac{Vn^3}{\Lambda^{3n} n!}\int d\mathbf{r}'^{n-1} \exp[-\beta W_n(\mathbf{r}'^{n-1};\mu)]\right]^{N_n}. \tag{4.31}$$

We now define the partition function Z_n of an n-mer as

$$Z_n \equiv \frac{Vn^3}{\Lambda^{3n} n!}\int d\mathbf{r}'^{n-1} \exp[-\beta W_n(\mathbf{r}'^{n-1};\mu)]. \tag{4.32}$$

With the above definition of the partition function Z_n of an n-mer, the grand partition function can be rewritten as

$$\Xi(\mu,V,T) = \exp(-\beta W_0) \sum_{N_1,N_2,..,=0}^{\infty} \prod_n \frac{[\exp(\beta\mu n) Z_n]^{N_n}}{N_n!}. \tag{4.33}$$

We can interchange the order of the product and the summation to obtain for the partition function

$$\begin{aligned}\Xi(\mu,V,T) &= \exp(-\beta W_0) \prod_n \exp(\exp[\beta\mu n] Z_n) \\ &= \exp(-\beta W_0) \exp(\sum_n \exp[\beta\mu n] Z_n)\ .\end{aligned} \tag{4.34}$$

The average number of clusters of size n is then simply given by

$$\langle N_n \rangle = Z_n \exp[\beta\mu n]. \tag{4.35}$$

If we define the free energy of an n-mer as

$$F_n \equiv -k_B T \ln Z_n, \tag{4.36}$$

Eq. 4.35 can be rewritten as

$$\langle N_n \rangle = Z_n \exp[-\beta(F_n - n\mu)] = \exp[-\beta\Delta F]. \tag{4.37}$$

The number of clusters of size n is an extensive quantity that is proportional to the size of the system. Hence, it is useful to express the cluster size distribution in terms of a probability distribution function that is intensive. To this end, we define the probability $P(n)$:

$$P(n) \equiv \frac{N_n}{N}, \tag{4.38}$$

where N is the total number of particles in the system. We can now define an intensive Gibbs-free energy of the cluster

$$\Delta G(n) \equiv -k_B T \ln[P(n)]. \tag{4.39}$$

4.3 New method

In the previous chapter we have seen that by using a global order parameter as our reaction coordinate, it is not possible to study the structure and free energy of a cluster for all sizes. When a cluster is smaller than a certain size, it breaks up into smaller clusters for entropic reasons. We therefore devised a new scheme which enables us to grow a single cluster all the way from the liquid to the solid.

In this scheme we measure the probability distribution function of cluster sizes, as defined in Eq. 4.38. In an unbiased, free Monte-Carlo or Molecular-Dynamics run, we can only measure clusters that have a free-energy in the order of one k_BT. This means that we can only sample relatively small clusters. In order to sample clusters even near the top of the barrier, we have employed the umbrella-sampling technique. In the umbrella-sampling technique [26], we bias the sampling of configuration space by adding a biasing potential to the potential of our model system. In the previous chapter, the biasing potential was taken to be a function of a global order parameter. Rather than using a global order parameter, which is sensitive to the overall degree of crystallinity in the system, we now took as the order parameter the size of the largest cluster present in the system. The advantage of this scheme is that we can directly control the size of this cluster.

By measuring the size distribution of the largest cluster, we can compute the probability distribution function as defined in Eq. 4.38. This is maybe not entirely obvious. However, one should note that the probability $P(n)$ that a cluster of a certain size n is present in the system, is given by

$$P(n) = P_1(n) + 2P_2(n) + 3P_3(n) + ... \tag{4.40}$$

Here $P_1(n)$ is the probability that one cluster of size n is present, $P_2(n)$ is the probability that two clusters of size n are present, and so on. As we can safely assume that the fluctuations, by which nuclei are formed, are uncorrelated, we have

$$P_i(n) = P(n)^i. \tag{4.41}$$

Hence, Eq. 4.40 becomes

$$P(n) = P_1(n) + 2P_1^2 + 3P_1^3.. \tag{4.42}$$

Clusters that cannot be sampled in an unbiased run, are clusters for which $P_1(n)$ is small. We can therefore ignore the higher order terms in the above equation, yielding

$$P(n) \approx P_1(n). \tag{4.43}$$

This implies that for large clusters that cannot be sampled in an free run, we can obtain the probability distribution function as defined in Eq. 4.38, by measuring the size distribution of one cluster, the size of which is controlled by the form of the biasing potential.

In order to test the new method we performed NPT Monte Carlo simulations on a system consisting of soft repulsive spheres, interacting via $v(r) = \epsilon(\sigma/r)^n$, with $n = 12.5$. The degree of supercooling was 25% with respect to the coexistence point given by Agrawal and Kofke [93]. The number of particles was $N = 3456$, which was large enough to avoid serious finite size effects.

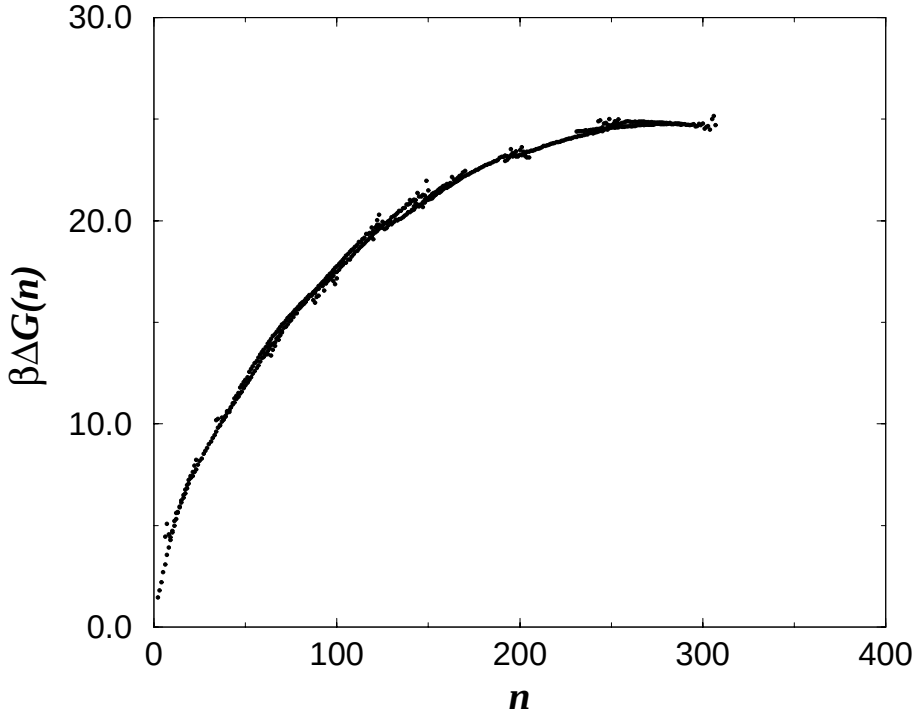

FIGURE 4.1 The Gibbs free energy of the $r^{-12.5}$ system as a function of the size of the largest cluster present in the system at 25% supercooling ($P = 22.54$, $T = 0.75$).

The biasing potential function W was taken to be a harmonic function of the order parameter, i.e. the size n of the largest cluster,

$$W[n(\mathbf{r}^N)] = \frac{1}{2}k_n[n(\mathbf{r}^N) - n_0]^2, \tag{4.44}$$

where $\mathbf{r}^N$ denotes the atomic coordinates. The constants k_n and n_0 determine the width and the "location" of the window. In order to determine the size of the cluster, we have used the techniques to identify solid clusters as explained in chapter 3. As our method of identifying solidlike particles is rather insensitive to the type of ordering, we do not favor one crystalline structure over the other.

In principle one could recalculate the size of the cluster after every trial displacement of a particle. However, this is computationally expensive. We therefore adopted a different procedure. We first perform a sequence of unbiased Monte Carlo cycles, that is, according to the potential of the original system, $U(\mathbf{r^N})$. We then recalculate the size of the cluster and accept the trajectory according to $\exp[-\beta\Delta W(\Phi(\mathbf{r}^N))]$, where $\Delta W(\Phi(\mathbf{r}^N))$ is the difference in biasing potential before and after the sequence of unbiased Monte Carlo cycles. This ensures that we generate configurations according to $\exp[\beta(U(\mathbf{r}^N) + W(\Phi(\mathbf{r^N})))]$.

Fig. 4.1 shows the Gibbs free energy of a crystalline nucleus as a function of its size n. With the new scheme we can sample all cluster sizes with equal accuracy. In order to illustrate this we have shown in Fig. 4.2 a snapshot of all solidlike particles in the system

FIGURE 4.2 Snapshot of all solid particles in the $r^{-12.5}$ system at the precritical side of the nucleation barrier, at 25% supercooling ($P = 22.54$, $T = 0.75$). The size of the large solid cluster in the middle is 150 particles.

when it is at the liquid side of the barrier. The large solid cluster in the middle of the box, comprising 150 particles, is clearly seen. To illustrate the difference with the old method, we have taken this configuration as the starting configuration for a run using the old, global order parameter Q_6. In Fig. 4.3 the size of the largest cluster present in the system is given as a function of "time". Initially, the size of the cluster drops because the system has to adjust itself to the new biasing potential. After that the size of the cluster fluctuates for 5000 cycles. Then, however, the size suddenly decreases to reach a new, much smaller plateau value. It is clear that using the global order parameter Q_6 the large precritical nucleus breaks up into many small crystallites. In fact, the process is "reversible", that is, if we use as the starting configuration for a run with the new order parameter, a configuration with only many small clusters and not a single relatively large cluster, we finally end up with a configuration containing one relatively large cluster, and some very small clusters that are always present in the supercooled liquid.

In summary, using a combination of umbrella sampling [26] and "blue-moon" ensemble simulations [30, 31], it is possible to compute nucleation rates at moderate supersaturation. However, it is useful to choose a local rather than a global order parameter

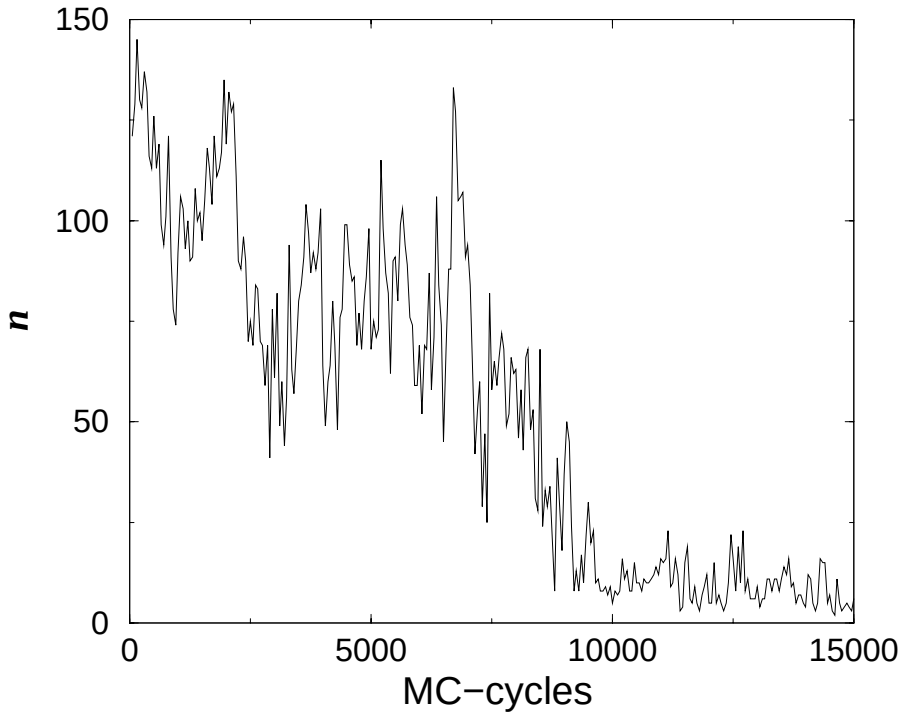

FIGURE 4.3 The size of the largest cluster present in the system as a function of the number of Monte Carlo cycles using the old global order parameter Q_6. As the starting configuration we have taken the precritical configuration that is obtained with the new scheme, see Fig. 4.2.

as a reaction coordinate, because in the case of a global order parameter, nuclei may spontaneously break up for entropic reasons.

5 Gas-Liquid nucleation in a Lennard-Jones system

We report a computer-simulation study of homogeneous gas-liquid nucleation in a Lennard-Jones system. Using umbrella sampling we compute the free energy of a cluster as a function of its size. A thermodynamic integration scheme is employed to determine the height of the nucleation barrier as a function of supersaturation. Our simulations illustrate that the mechanical and the thermodynamical surfaces of tension and surface tension differ significantly. In particular, we show that the mechanical definition of the surface tension cannot be used to compute the barrier height. We find that the relations recently proposed by McGraw and Laaksonen (J. Chem. Phys. **106***, 5284 (1997)) for the height of the barrier and for the size of the critical nucleus are obeyed.*

5.1 Introduction

The spontaneous formation of liquid droplets in a supersaturated vapor is probably the best known example of homogeneous nucleation. In view of its great practical importance, a large number of experimental studies of gas-liquid nucleation have been reported and the earliest theoretical description dates back to the 1920's [4, 5].

In recent years, research on gas-liquid nucleation has received a new impetus. This is partly due to the emergence of sophisticated experimental techniques that make it possible to measure nucleation rates with unprecedented accuracy [15, 16]. The so-called nucleation theorem [15, 55–57] makes it possible to deduce, from the experimental data on the nucleation rate, detailed information about the size and composition of the critical nucleus [15, 50, 94, 95]. In parallel, modifications and extensions of the classical nucleation theory have been proposed [54, 96–99] and novel theoretical tools [14] have made it possible to go beyond the essentially macroscopic description that lies at the basis of classical nucleation theory. In particular, expressions for the height of the barrier and for the size of the critical nucleus have been proposed that could provide a possible explanation for the systematic discrepancies between classical nucleation theory (CNT) and experiment [12, 13]. Furthermore, much theoretical progress has been made in calculating the Tolman length [45], which is an important quantity in nucleation as it describes how the surface free energy changes with droplet size.

However, despite the fact that nucleation rate measurements have become increasingly accurate, many of the theoretical predictions are difficult to test directly in an experiment as they are concerned with the microscopic structure of the critical nucleus. Computer simulation is a natural tool to study the details of the nucleation process, because it yields essentially exact microscopic information about the model studied.

Liquid clusters in vapor have been studied in detail by computer simulation [46, 100–106]. Most of these simulations were done in the canonical ensemble, that is, at constant number of particles N, constant temperature T and constant volume V. A simple analysis [102, 105] of the change in Helmholtz free energy when a liquid droplet is formed from the vapor shows that a liquid cluster can be in equilibrium with the vapor in a constant volume simulation. However, in most nucleation experiments the pressure or, equivalently, the chemical potential of the vapor, is held constant. Classical nucleation theory also usually considers the nucleation of a liquid drop from the vapor at constant chemical potential, i.e. at constant pressure of the vapor. Therefore, one would like to perform a simulation at constant pressure rather than a constant volume. At constant pressure a liquid cluster can be in equilibrium with the vapor at the top of the nucleation barrier. However, this equilibrium is unstable. If a cluster, due to spontaneous fluctuations, becomes larger than the critical size, it will grow, because in that way it can minimize its excess free energy. On the other hand, if a cluster by chance becomes smaller than this critical size, it will shrink, again because in that way it can lower its excess free energy.

Hence, in a standard NPT simulation it is virtually impossible to study a critical cluster. However, using the umbrella-sampling scheme [26] it is possible to stabilize the critical cluster at constant pressure. But, what is more important, it also makes it possible to stabilize the precritical (and postcritical) nuclei, thus allowing us to compute the excess free energy of a cluster as a function of its size at constant pressure. Hence, with the umbrella-sampling technique we obtain not only structural information about the precritical and critical nuclei, but also about the height of the nucleation barrier. Moreover, the umbrella sampling technique can be combined with a thermodynamic integration scheme, which enables the efficient computation of the height of the barrier as a function of supercooling.

This integration scheme is not only efficient, but also very accurate and allows us to test several theoretical predictions. First, we examine to what extent the nuclei behave like small droplets of bulk liquid, which is one of the main assumptions of classical nucleation theory. We then compare the size of the critical nuclei and the height of the nucleation barrier with the corresponding predictions of classical nucleation theory. Furthermore, we have investigated whether the deviations from classical nucleation theory can be accounted for by a curvature correction to the surface tension, as proposed by McGraw and Laaksonen [12, 13].

We have also computed the Tolman length [42], which describes the lowest order correction to the surface tension. As discussed in chapter 2, the Tolman length is defined as the difference in position between the equimolar dividing surface and the thermodynamically defined surface of tension. It is possible to give both a mechanical definition and a thermodynamic definition of the surface tension and surface of tension of a liquid droplet (see [40, 41]). However, we find that both definitions are not equivalent, which means that we cannot obtain the Tolman length from the mechanical description of the droplet. More importantly, this also implies that we cannot use a simple "mechanical" expression to compute the height of the nucleation barrier. Our simulations illustrate the fact that the thermodynamic and mechanical definitions cannot be used interchangeably and that any attempt to do so leads to an incorrect estimate of the height of the nucleation barrier.

We have performed our simulations for a Lennard-Jones system. The choice for this system was motivated by several factors. First of all, the phase behavior of this system is known [79]. Secondly, gas-liquid nucleation in this system has also been studied extensively with density functional theory [107–109]. And finally, the Tolman length has been computed both numerically and theoretically for the Lennard-Jones system [45–47].

The rest of the chapter is organized as follows. In the next section, we give relations for the cluster size distributions in terms of the free energy of the clusters. We then describe the numerical techniques to calculate the cluster size distributions and the nucleation barriers. In section 5.4 we discuss how we can obtain the mechanically and thermodynamically defined surface tension and surface of tension. We then give the computational details of the simulations in section 5.5 and in section 5.6 we discuss the results.

5.2 Cluster-size distribution

In order to perform a numerical study of the formation of a liquidlike droplet from the vapor phase, we need an unambiguous definition of an incipient liquidlike cluster. In what follows, we use an approach that is quite similar, but not quite identical, to the one introduced more than thirty years ago by Stillinger [110]. Consider a vapor in a constant volume V, at constant temperature T and at constant chemical potential μ. In gas-liquid nucleation the density of liquidlike clusters is usually so low that the interactions between them can be neglected. Furthermore, let us assume that we have a criterion that enables us to define which particles make up a liquid cluster. As shown in section 4.2 of chapter 4, the average number N_n of clusters of size n is then given by

$$\langle N_n \rangle = Z_n \exp[\beta \mu n]. \tag{5.1}$$

Here $\beta \equiv 1/k_B T$ is the reciprocal temperature, k_B is Boltzmann's constant, and Z_n is the partition function of the n-mer. It is given by

$$Z_n = \frac{V n^3}{\Lambda^{3n} n!} \int d\mathbf{r}'^{n-1} \exp[-\beta W_n(\mathbf{r}'^{n-1}; \mu)]. \tag{5.2}$$

Here $\Lambda \equiv h/\sqrt{2\pi m k_B T}$ is the thermal De Broglie wavelength, $\mathbf{r}'^{n-1}$ denotes the coordinates with the prime indicating that the coordinates are taken with respect to the center-of-mass of the cluster, and W is the potential of mean force. The potential of mean force is obtained by carrying out the integration over the coordinates of the vapor particles. That is, all possible configurations of the vapor particles will contribute to W; it is the average potential the particles in the liquid clusters feel, due to all interactions with the "solvent" particles. As shown in section 4.2, our cluster criterion is absorbed into the definition of the potential of mean force. All configurations of the particles in the cluster that do not satisfy the cluster criterion will not contribute to the partition function. To illustrate this, let us consider a cluster of non-interacting particles. The partition function of such an n-mer is

$$Z_n = \frac{V n^3}{\Lambda^{3n} n!} \int d\mathbf{r}'^{n-1} w(\mathbf{r}'^{n-1}), \tag{5.3}$$

where the function $w(\mathbf{r}^{n-1})$ is defined to be one, if its arguments satisfy the cluster criterion, and zero otherwise. Note that the volume of this "ideal-gas cluster" is well-defined and that the cluster criterion provides a natural volume scale for the cluster [11].

If we define the free-energy of an n-mer as

$$F_n \equiv -k_B T \ln Z_n, \tag{5.4}$$

Eq. (5.1) can be rewritten as

$$\langle N_n \rangle = \exp[-\beta(F_n - n\mu)] = \exp[-\beta \Delta F]. \tag{5.5}$$

An expression very similar to the one above has been obtained by Reiss *et al.* [106, 111–115]. The only difference is that we make fewer assumptions: Reiss *et al.* assumed that the surrounding gas is ideal and that there is no interaction between molecules that are inside the cluster and those outside. Instead, we have carried out the integration over the coordinates of the non-cluster ("solvent") particles, and the effect of the surrounding phase is adsorbed into the effective interactions between the particles that make up the cluster. Note also that, in the present description, we need not introduce the concept of a "shell-molecule" to arrive at an unique definition of the clusters [106, 112–115] – whether or not a molecule belongs to a cluster is uniquely defined by our cluster criterion. In particular, the present approach allows for monomeric clusters. Of course, we still have to specify the cluster criterion. Our choice for this function is described in detail in section 5.5. Here it suffices to say that it enables us to identify which particles in the system have a liquidlike density; all liquidlike particles that are connected make up a cluster. An added advantage is that the present approach does not suffer from the problem of redundant counting of configuration space [11, 111, 112]. Furthermore, the present scheme can easily be used to study crystal nucleation. In crystal nucleation the density difference between the crystallite and the surrounding liquid is usually so low that the interactions between the cluster and the surrounding medium cannot be ignored.

In practice, it is useful to express the number of clusters of size n (that is extensive) in terms of a probability (that is intensive)

$$P(n) \equiv \frac{N_n}{N}, \tag{5.6}$$

where N is the total number of particles in the system. This, in turn defines an intensive Gibbs free-energy of the cluster (where the reference state is the homogeneous phase):

$$\Delta G(n) \equiv -k_B T \ln[P(n)]. \tag{5.7}$$

The average number of clusters of size n is then given by

$$\langle N_n \rangle = N \exp[-\beta \Delta G(n)]. \tag{5.8}$$

5.3 Nucleation barrier

5.3.1 The free-energy barrier as a function of droplet size

The probability distribution function $P(n)$, as defined in Eq. (5.6), is an equilibrium property and can be measured both by Monte Carlo (MC) and by Molecular Dynamics (MD). However, at experimentally accessible degrees of supersaturation, the brute force

approach, in which we would simulate the supersaturated vapor, either by MC or by MD, and simply count the liquid clusters that spontaneously appear, would never yield an accurate measure of the nucleation barrier. In experiments, the height of the nucleation barrier is typically in the order of $75k_BT$. This means that the probability to find a cluster that has the critical size is extremely small, of the order of 10^{-30}. Hence, the numerical accuracy of any direct simulation will be very poor. To obtain good statistics for all values of n, we therefore use the umbrella sampling scheme of Torrie and Valleau [26]. The basic idea of this scheme is to bias the sampling of configuration space and correct for the bias afterwards.

We can bias the sampling by adding a fictitious potential to the true potential of our original system. In our study on crystal nucleation in a Lennard-Jones system, we used a biasing potential that was a function of a global order parameter, Q_6. This order parameter measured the overall degree of crystallinity in the system and served as a reaction coordinate from the liquid to the solid. By using the biasing potential we could move the system along the reaction coordinate from the liquid to the solid, and vice versa. In the same spirit, we could now apply a biasing potential that depends on an order parameter which is sensitive to the total number of liquid particles in the supersaturated vapor. By increasing the value of this order parameter, using the biasing potential, we could then cross the nucleation barrier and force the system to condense.

However, as explained in detail in chapter 4, the use of a global order parameter has some serious drawbacks from a computational point of view. The reason is the following: if we use the total amount of the new phase as a reaction coordinate, then the value of this reaction coordinate tells us how much of the new phase (say, liquid) we have, but now how it is distributed in space. In particular, the new phase need not be concentrated in one cluster. In fact, in a sufficiently large volume it is always entropically favourable for a cluster to break up in smaller fragments. However, for the nucleation process, we are interested in the properties of the largest connected cluster.

Rather than using a global order parameter, we therefore use a local order parameter. We define the order parameter to be the size, n, of the largest liquid cluster in the system present. The advantage of this scheme is that by using a biasing potential which is a function of this order parameter, we can directly control the size of one cluster and sample all sizes of this cluster with equal accuracy. The functional form of the biasing potential W was taken to be harmonic,

$$W[n(\mathbf{r}^N)] = \frac{1}{2}k_n \left[n(\mathbf{r}^N) - n_0\right]^2 , \tag{5.9}$$

where $\mathbf{r}^N$ denotes the atomic coordinates. The result of adding this potential to the true potential of our model system is that in every run a "window" of cluster-sizes will be sampled. The width and "location" of this window depend on k_n and n_0. By increasing n_0 we can increase the size of the cluster.

5.3.2 The free-energy barrier as a function of supersaturation

In principle, one could compute the height of the free-energy barrier for every degree of supersaturation by the scheme discussed in the previous section. However, calculating the free-energy curve all the way up to the top of the barrier is rather time consuming because a lot of "windows" have to be simulated.

We therefore followed a different approach. Only for one pressure we compute the full nucleation barrier by the umbrella-sampling technique as outlined in the previous section. This free-energy barrier is then used as a reference for the calculation of the height of the free-energy barrier at other supersaturations. The main idea is that for every pressure we only have to perform two simulations: one in the metastable vapor phase and one at the top of the barrier. For both states we can determine the variation of the free energy with pressure, from which we obtain how the height of the nucleation barrier changes with pressure. By linking the variation of the barrier height with the height of the barrier at the reference pressure, we then obtain the height of the nucleation barrier as a function of total pressure.

To make this more explicit, consider the (Landau) Gibbs free energy G, which is a function of the number of particles N, the pressure P, the temperature T and the size of the cluster n. The first differential of the Gibbs free energy is

$$dG(N,P,T,n) = \mu(n)dN + V(n)dP - S(n)dT + \left.\frac{\partial G}{\partial n}\right|_{N,P,T} dn, \tag{5.10}$$

where μ is the chemical potential, V is the volume and S is the entropy of the system. At constant total number of particles and temperature, Eq. (5.10) reduces to

$$dG(N,P,T,n) = V(n)dP + \left.\frac{\partial G}{\partial n}\right|_{N,P,T} dn. \tag{5.11}$$

Using the above equation, we can now compute the change in free energy when the pressure is varied. When we alter the pressure, the position of the top of the barrier, denoted by n^*, can change. However, at the top of the barrier, the partial derivative of the free energy G with respect to size n, $\frac{\partial G}{\partial n}$, is zero, so the last term in Eq. (5.11) drops out. In the metastable vapor $n = 0$ and remains zero, so also for the vapor phase the last term is zero. So we have for the top of the barrier

$$dG(n^*) = V(n^*)dP, \tag{5.12}$$

and, similarly, for the vapor phase,

$$dG(0) = V(0)dP, \tag{5.13}$$

from which we obtain for the variation of the barrier height ΔG^* with pressure

$$d\Delta G^* = d\left[G(n^*) - G(0)\right] = \left[V(n^*) - V(0)\right] dP. \tag{5.14}$$

The height of the free-energy barrier at a pressure P can now be obtained taking the height of the barrier at the reference pressure P_{ref}, as obtained by the umbrella-sampling technique, and by integrating Eq. (5.14):

$$\Delta G^*(P) = \Delta G^*(P_{ref}) + \int_{P_{ref}}^{P} \left[V(n^*) - V(0)\right] dP'. \tag{5.15}$$

In order to obtain a good measure for the volume at the top of the barrier, we have to determine the top of the barrier with a high accuracy, as the volume of the system strongly depends on the value of the order parameter, i.e. the size of the largest cluster. We therefore performed for every pressure not one but three simulations near the top of the barrier: one at the estimated top, and one at each side. The cluster-size probability

distribution functions of these three simulations were fitted to a polynomial to get the relative free energies (via Eq. (5.7)) of the droplets in the vicinity of the top of the barrier. From this we could then deduce the position of the top of the barrier. Finally, to obtain the volume at the top of the barrier, the value of the critical droplet size was inserted into the expression for the volume as function of droplet size, which was obtained by fitting the volume histograms to a polynomial.

5.4 Tolman length and surface of tension

The surface of a droplet in the vapor is not sharp. Rather, it is a transition layer of physical inhomogeneity in which the properties of the fluid change smoothly. However, it is convenient to treat the actual droplet in the vapor as being uniform up to an imaginary surface of zero thickness, the so-called dividing surface, which separates the droplet from the (uniform) vapor.

The position of this dividing surface can be obtained via a thermodynamic route and via a mechanical route. However, both approaches are not equivalent. Below, we indicate how we have computed both the thermodynamically and mechanically defined surface tensions and surfaces of tension. In section 5.6.5 we show that the mechanical route cannot be used to compute the height of the nucleation barrier.

5.4.1 Thermodynamic description

In the thermodynamic approach, introduced by Gibbs [3], one can derive the generalized Laplace equation (see section 2.2.2), which relates the pressure difference over the drop Δp to the location, R, of the dividing surface, and to the surface tension γ:

$$\Delta p = \frac{2\gamma(R)}{R} + \frac{\partial \gamma(R)}{\partial R}. \tag{5.16}$$

Here $\Delta p = p_l - p_v$, with p_l and p_v the pressure in the liquid and vapor region, respectively. Of course, the pressure in the vapor is always well defined and is equal to the pressure of a homogeneous (bulk) vapor phase with the same density as the density in the vapor region far away from the drop. When the droplet is large enough then the pressure inside the drop is also well-defined and is equal to that of a bulk liquid phase with a density which equals that of the density in the core of the drop. However, for smaller droplets the pressure in the core may differ from the bulk liquid pressure. Yet, it is important to realize that the generalized Laplace relation is derived from the hypothetical model system, in which the actual droplet is replaced by a droplet that has bulk properties; i.e. it is uniform in density and pressure up to the dividing surface. Therefore, the pressure p_l in the drop is that of a hypothetical bulk liquid phase which has a chemical potential $\mu_l(p_l, T)$ that is equal to the chemical potential $\mu_v(p_v, T)$ of the (bulk) vapor phase at pressure p_v.

The thermodynamically defined surface of tension is the surface for which the second term on the right-hand side of Eq. (5.16) vanishes. Another natural choice for the dividing surface is the equimolar dividing surface, which is defined as the surface for which the excess number of particles at the surface is zero (see section 2.2.4). The Tolman length [42] δ_T is usually defined as the difference δ between these two dividing

surfaces in the planar limit

$$\delta_T \equiv \lim_{R_e,R_s\to\infty} \delta = \lim_{R_e,R_s\to\infty} (R_e - R_s), \tag{5.17}$$

where R_e is the radius of the equimolar dividing surface and R_s is the radius of the surface of tension.

We have shown in chapter 2 that for any choice of the dividing surface the (Gibbs) free-energy of a droplet with radius R is given by (see Eq. (2.40))

$$\Delta G^* = -\frac{4}{3}\pi R^3 \Delta p + 4\pi R^2 \gamma(R), \tag{5.18}$$

where Δp is given by the generalized Laplace equation, i.e. Eq. (5.16). If we take for the dividing surface the surface of tension, then Eq. (5.18) reduces to

$$\Delta G^* = \frac{4}{3}\pi R_s^2 \gamma_s, \tag{5.19}$$

or, equivalently,

$$\Delta G^* = \frac{2}{3}\pi \Delta p R_s^3. \tag{5.20}$$

We have used the above equation, with ΔG^* and Δp obtained from the simulations, to compute the thermodynamical surface tension and surface of tension.

5.4.2 Mechanical description

The thermodynamic description of droplets is macroscopic in nature. In order to establish a link with molecular properties, it would seem more natural to use a mechanical picture. This approach would allow one to relate the surface tension and surface of tension of a droplet to microscopic quantities, such as the pressure tensor. However, the mechanical and thermodynamic definition are not equivalent. As a result, the surface tension and dividing surface that are computed mechanically cannot be used to predict the height of the nucleation barrier. In fact, our simulations show that the mechanical route may lead to unphysical results. Below we discuss the mechanical description.

By considering the force and moment acting on a hypothetical strip cutting the surface of the drop, Buff showed that is possible to obtain a mechanical definition of the surface tension [40, 41, 116]. The position, $R_{s,m}$, of the surface of tension is given by

$$R_{s,m} = \frac{\int_0^\infty [p_{lv}(r;R_{s,m}) - p_T(r)]\, r^2 dr}{\int_0^\infty [p_{lv}(r;R_{s,m}) - p_T(r)]\, r dr}, \tag{5.21}$$

and the surface tension, $\gamma_{s,m}$, acting on the surface of tension is given by

$$\gamma_{s,m} = \frac{1}{R_{s,m}} \int_0^\infty [p_{lv}(r;R_{s,m}) - p_T(r)]\, r dr \tag{5.22}$$

and also by

$$\gamma_{s,m} = \frac{1}{R_{s,m}^2} \int_0^\infty [p_{lv}(r;R_{s,m}) - p_T(r)]\, r^2 dr. \tag{5.23}$$

In the above equations $p_T(r)$ is the tangential pressure and p_{lv} is a step function, such that $p_{lv}(r;R_{s,m}) = p_l'$ for $r < R_{s,m}$ and $p_{lv}(r;R_{s,m}) = p_v$ for $r > R_{s,m}$. The subscript m indicates that we consider the mechanical surface of tension. There are two logical

choices for p_l': the first is the one introduced below Eq. (5.16), namely the pressure of the bulk liquid at the chemical potential of the vapor. The second is the actual, local pressure in the core of the droplet. For some of the relations that we will employ, we can choose either definition. However, as we indicate below, in some equations the choice is not free - only the second definition can be used.

From the hydrostatic equilibrium condition $\nabla \cdot \mathrm{p} = 0$ we obtain [40, 41]

$$r_v^n p_N(r_v) - r_l^n p_N(r_l) = \int_{r_l}^{r_v} \left[(n-2)p_N(r) + 2p_T(r)\right] r^{n-1} dr, \tag{5.24}$$

where $p_N(r)$ is the normal component of the pressure tensor, r_v denotes a position far away from the drop in the vapor, and r_l is a position in the drop. Integrating the step-function $p_{lv}(r; R*)$ yields

$$\int_{r_l}^{r_v} p^{lv}(r; R^*) n r^{n-1} dr = r_v^n p_v - r_l^n p_l' + {R^*}^n (p_l' - p_v) \tag{5.25}$$

Far away from the drop the local pressure is equal to the vapor pressure, i.e. $p_N(r_v) = p_T(r_v) = p_v$. Furthermore, if we take r_l at the center of the drop, i.e. $r_l = 0$, then Eq. (5.24) can be subtracted from Eq. (5.25) to give

$$p_l' - p_v = \frac{1}{{R^*}^n} \int_0^{r_v} \{n[p^{lv}(r; R^*) - p_N(r)] + 2[p_N(r) - p_T(r)]\} r^{n-1} dr. \tag{5.26}$$

The actual value of $p_N(r_l)$ drops out of the above equation provided that $r_l = 0$ and $n \neq 0$. Under those conditions we are free to choose our definition of p_l'. However, for $n = 0$ the choice of p_l' is no longer free. In that case, we must take p_l' equal to the normal component of the local pressure in the center of the droplet, i.e. $p_l' = p_N(0)$. Note that with this choice for p_l' we need not choose $r_l = 0$ to arrive at Eq. (5.26). In what follows we therefore take p_l' to be the local pressure in the center of the droplet. We stress that, except for very large droplets, this definition differs from the thermodynamic one.

For $n = 2$ Eq. (5.26) reduces to

$$p_l' - p_v = \frac{2}{{R^*}^2} \int_0^{\infty} [p_{lv}(r; R^*) - p_T(r)] r dr. \tag{5.27}$$

This relation is valid for any position of the dividing surface. If we position the dividing surface at the *thermodynamic* surface of tension with radius R_s we obtain

$$p_l' - p_v = \frac{2}{R_s^2} \int_0^{\infty} [p_{lv}(r; R_s) - p_T(r)] r dr. \tag{5.28}$$

If the core of the droplet behaves as a bulk liquid, that is, if the actual pressure p_l' in the droplet is equal to the pressure p_l of a bulk liquid with a chemical potential that is equal to that of the vapor phase, then we can combine the above equation with the Laplace equation, Eq. (5.16), to arrive at

$$\gamma_s = \frac{1}{R_s} \int_0^{\infty} \left[p_{lv}(r; R_s) - p_T(r)\right] r dr. \tag{5.29}$$

This equation has the same structure as Eq. (5.22). However, this does not imply that the thermodynamic and mechanical surface tensions and surfaces of tensions are equal. In fact, Blokhuis *et al.* [45] have shown that the positions of the surfaces can differ significantly and our simulations show that in fact they do.

It is possible to relate $R_{s,m}$ and $\gamma_{s,m}$ to $p_l' - p_v$ in an expression, which, to increase the confusion, looks like the Laplace relation. We take $R^* = R_{s,m}$ in Eq. (5.27) and combine the resulting expression with Eq. (5.22), to arrive at

$$p_l' - p_v = \frac{2\gamma_{s,m}}{R_{s,m}}. \tag{5.30}$$

So also for the mechanically defined surface tension and surface of tension, a Laplace-type relation is fulfilled. We can now exploit this relation to express $R_{s,m}$ and $\gamma_{s,m}$ in terms of $p_N(r) - p_v$, from which we can compute the mechanically defined surface tension and surface of tension. We start by combining the above equation and Eq. (5.26) with $n = 3$ and with $R^* = R_{s,m}$, and subtract the resulting expression from Eq. (5.23), to obtain

$$\int_0^{r_v} [p^{lv}(r; R_{s,m}) - p_N(r)] r^2 dr = 0. \tag{5.31}$$

This equation can be combined with Eq. (5.23) to yield

$$\gamma_{s,m} = \frac{1}{R_{s,m}^2} \int_0^{\infty} [p_N(r) - p_T(r)] r^2 dr. \tag{5.32}$$

In Refs. [40, 41] it is suggested that a similar expression can be derived for the thermodynamically defined surface tension by combining the expression following from Eq. (5.26), with $n = 3$ and $R = R_s$, and the generalized Laplace equation (Eq. (5.16)) with Eq. (5.23). However, in order to arrive at this result one has to make the assumption that the mechanical and thermodynamic description are equivalent.

We do not make the identification between the thermodynamic and mechanical description. Instead, we make use of the fact that also for the mechanically defined surface of tension a Laplace-type relation holds and use the relations that follow from the hydrostatic equilibrium condition for this dividing surface. For instance, it is possible to obtain another expression for the mechanically defined surface tension by combining Eq. (5.30) with Eq. (5.26) for $n = 0$ and $R^* = R_{s,m}$

$$\gamma_{s,m} = R_{s,m} \int_0^{\infty} [p_N(r) - p_T(r)] r^{-1} dr. \tag{5.33}$$

We can obtain the position of the mechanical surface of tension by combining the above equation with Eq. (5.32)

$$R_{s,m}^3 = \frac{\int_0^{\infty} [p_N(r) - p_T(r)]\, r^2 dr}{\int_0^{\infty} [p_N(r) - p_T(r)]\, r^{-1} dr}. \tag{5.34}$$

The three above equations can be rewritten using

$$p_T(r) = p_N(r) + \frac{r}{2} \frac{dp_N(r)}{dr}, \tag{5.35}$$

which follows from the condition of hydrodynamic equilibrium, $\nabla \cdot \mathrm{p} = 0$. We then obtain

$$R_{s,m}^3 = \frac{3}{\Delta p} \int_0^{\infty} [p_N(r) - p_v] r^2 dr, \tag{5.36}$$

$$\gamma^3_{s,m} = \frac{3}{8}\Delta p^2 \int_0^\infty [p_N(r) - p_v] r^2 dr. \tag{5.37}$$

where $\Delta p = p'_l - p_v$. We have used these equations to compute the mechanically defined surface tensions and surfaces of tension.

In the *thermodynamic* model the height of the barrier is given by Eq. (5.20). It is clear that if the mechanical and thermodynamic description would be equivalent, combining Eq. (5.20) with Eq. (5.36) would yield a *microscopic* expression for the height of the barrier (Eq. (5.38), see Refs. [12] and [117]). However, as the mechanical and thermodynamic pictures cannot be mixed, the height of the barrier cannot be expressed in terms of an integral of the pressure profile,

$$\Delta G^* \neq 2\pi \int_0^\infty [p_N(r) - p_v] r^2 dr, \tag{5.38}$$

Figure 5.5 illustrates the kind of errors that may result if the mechanical and thermodynamic pictures are confused.

We stress that the distinction between mechanical and thermodynamic expression for the surface tension should not be confused with the ambiguity in the definition of the microscopic stress tensor. Schofield and Henderson [118] have proposed a general expression for the stress tensor. This expression reflects the freedom that we have in defining the momentum flux density in a fluid. The commonly used Irving-Kirkwood pressure tensor [119], and the Harasima pressure tensor [104, 118, 120, 121], are special cases of the Schofield-Henderson expression. Both from simulations [121] and from theory [118] these expressions are known to give the same surface tension for a planar interface, as the surface tension is related to the zeroth moment of $p_N(r) - p_T(r)$. However, the position of the mechanical surface of tension, which is related to the first moment, is not insensitive to the choice of the pressure tensor. The Irving-Kirkwood expression appears to be the most natural choice as the contour joining two interacting particles, which determines where the force is acting, corresponds to a straight line. Furthermore, Blokhuis *et al.* [45] showed that the Irving-Kirkwood pressure tensor, in contrast to the Harasima pressure tensor, leads to expressions for the pressure difference, the surface tension and the Tolman length, that agree with expressions found using microscopic sum rules. We have therefore used the Irving-Kirkwood expression for the pressure tensor to compute the pressure profiles.

5.5 Computational details

We have studied homogeneous gas-liquid nucleation in a Lennard-Jones system in which the interaction potential was truncated and shifted at a cutoff radius $r_c = 2.5\sigma$, where σ is the particle diameter. We made no long-range corrections and applied cubic periodic boundary conditions. In what follows, we use reduced units, such that the Lennard-Jones well depth ϵ is the unit of energy, while the Lennard-Jones diameter σ is the unit of length.

In most experimental studies of homogeneous nucleation, the volume is fixed and nucleation of liquid droplets from the vapor phase leads to a decrease of the vapor pressure. However, as the concentration of nuclei is very small, the drop in vapor pressure is negligible and the pressure and chemical potential effectively remain constant during

the nucleation process. In principle, we could simulate the experimental situation by performing a NVT simulation. A large excess number of vapor particles would then be needed in order to keep the vapor pressure constant, which can be achieved by simulating a very large system. However, this would make the simulations unnecessarily expensive. It is much more natural to work in the NPT or in the μVT [122] ensemble. In the NPT ensemble, as the droplet is formed, the volume is adjusted such that the pressure (and the chemical potential) in the vapor will remain constant. In this ensemble it is therefore not necessary to simulate a large number of vapor particles. The same holds for the μVT ensemble. However, in this approach the insertions and removals of particles from the system is required, which can be inefficient or even impossible at high densities. We haven chosen to work in the NPT ensemble.

In our simulations, we need an operational definition of liquidlike clusters. We do this by making a distinction between particles that have a liquidlike and a vapor-like environment. liquidlike particles are particles that experience a local density that is significantly higher than that of the vapor. There is no unique definition of the local density surrounding a particle. In what follows, we use the number of particles within a spherical shell of radius q_c as a measure of the local density. The distribution functions of the number of neighbors per particle in the liquid and in the vapor are shown in Fig. 5.1. Note that the distribution functions hardly overlap. We have therefore adopted the criterion that all particles that have more than four neighbors are considered to be liquidlike.

After we have identified which particles in the system are liquidlike, we can determine the liquidlike clusters. We have applied the criterion that any two liquidlike particles that have a distance less than $q_c = 1.5$ (which corresponds to the first minimum in the radial distribution function of the liquid) belong to the same liquid cluster. Note that our definition of a cluster is close to the one used by Stillinger [110], but not

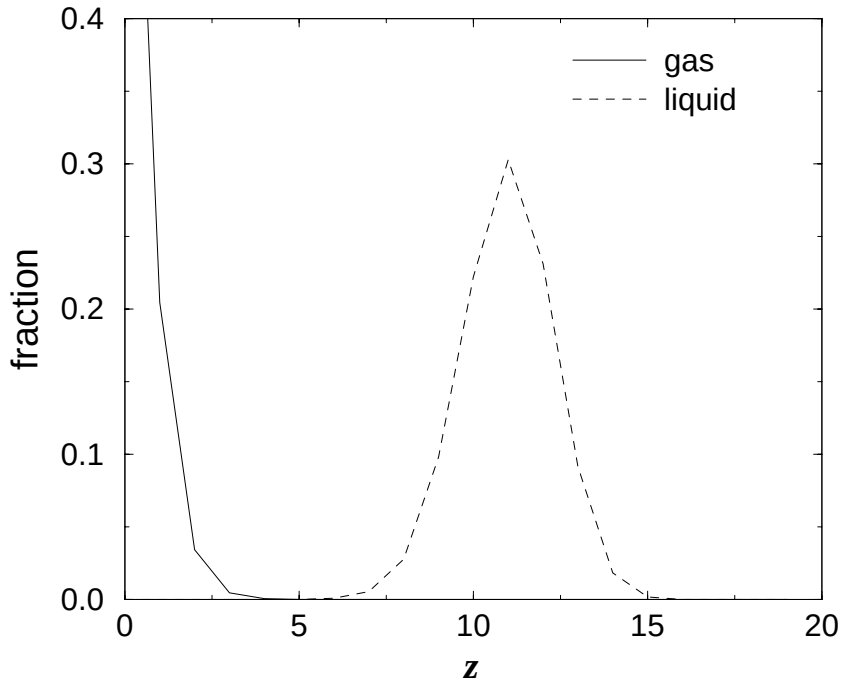

FIGURE 5.1 Distributions of the number of neighbors per particle, denoted by z, in a Lennard-Jones system for a thermally equilibrated liquid and vapor, at coexistence ($T = 0.741$, $P = 0.00783$). Two particles are considered to be neighbors if they are separated by a distance less than $q_c = 1.5$.

quite equivalent. Stillinger adopted the criterion that *any* two particles that are within a certain cutoff distance belong to the same cluster. So even particles that, in our definition, are considered to be vapor particles can be part of a liquid cluster according to Stillinger's criterion.

The nucleation barrier can be measured both by MC and MD. The advantage of MD is that it gives faster equilibration of pressure gradients through collective particle motions. However, with MD the diffusion of the system through the order-parameter window in the umbrella-sampling simulations is rather slow. The density in the vapor is very low and in MD both the liquid and vapor particles move on the same time scale. Therefore, in MD the fluctuations in the size of the largest cluster, i.e. the order parameter, are limited by the influx of particles from the vapor.

The advantage of MC is that it is particularly suited for the umbrella sampling scheme as, in contrast to MD, the forces associated with the biasing potential do not have to be calculated. Furthermore, one can perform tricks to facilitate the sampling of configuration space. In order to speed up the diffusion of particles in the vapor, the particles in the vapor phase are given a different maximum displacement from the particles in the liquid phase. Of course, this introduces a bias which needs to be corrected for in order to satisfy detailed balance. This is described in the Appendix 5.7.

We have tested both MD and MC by determining the "diffusion constant" of the order parameter at the top of the barrier. It was found that per MD-timestep or per MC cycle (in which on average every particle is given one trial displacement)

$$\sqrt{\frac{\langle \Delta n^2 \rangle_{\mathrm{MC}}}{\langle \Delta n^2 \rangle_{\mathrm{MD}}}} \approx 7 - 8. \tag{5.39}$$

However, the number of cycles performed per unit of CPU-time was three times higher for MD, so that the effective diffusion constant for MC was about two to three times that of MD. We did use MD to speed up the equilibration, but most of the actual simulations were performed using MC sampling.

In the umbrella sampling scheme, the system should sample configuration space according to the potential

$$U_i(\mathbf{r}^N) = U_o(\mathbf{r}^N) + W[n(\mathbf{r}^N)], \tag{5.40}$$

where $U_o(\mathbf{r}^N)$ is the potential of the original model system and $W[n(\mathbf{r}^N)]$ is the biasing potential as defined in Eq. (5.9). In principle, we could recompute the size of the largest cluster and the biasing potential after every MD or MC cycle, or even after every particle displacement in the MC simulations. However, this would be far too time consuming. We therefore adopted a staged scheme. In the first stage a series of MD or MC cycles is performed without the biasing potential. In the second stage, after the unbiased trajectory, the size of the cluster and the biasing potential are recalculated. To ensure that configuration space will be sampled in accordance with the potential in Eq. (5.40), the trajectory is then accepted with a probability which is determined by $\exp[-\beta \Delta W[n(\mathbf{r}^N)]]$, where $\Delta W[n(\mathbf{r}^N)]$ is the difference in biasing potential before and after the trajectory.

In the MC simulations, each trial move consisted either of an attempted particle displacement or a trial volume change. The choice between trial particle moves and trial volume moves was made at random. As we used a fixed cutoff in real coordinates for the

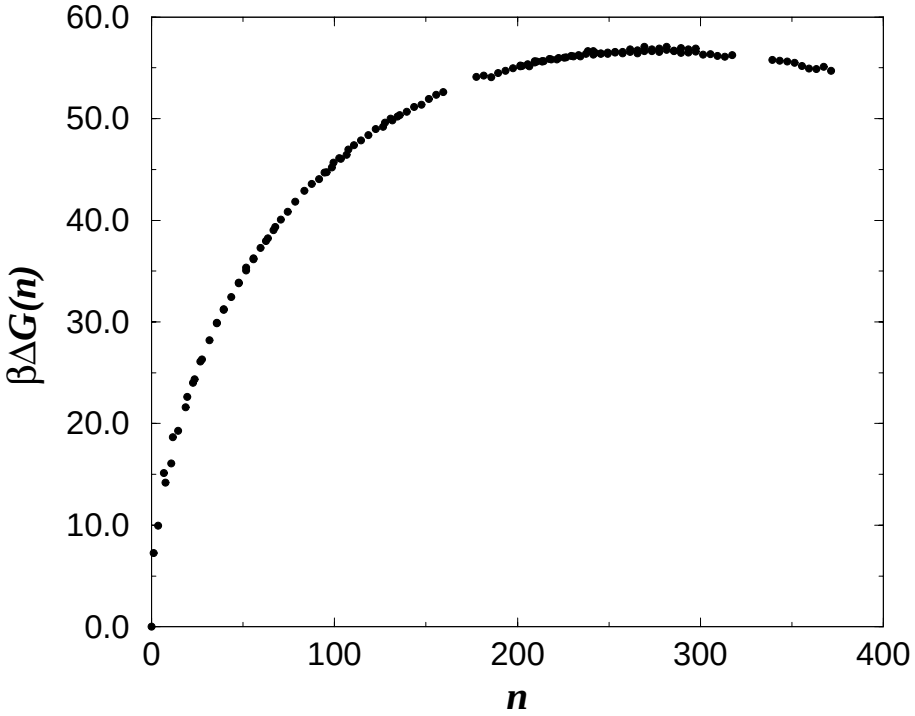

FIGURE 5.2 The Gibbs free-energy barrier as a function of the size of a cluster, denoted by n, at a supersaturation of $S = 1.53$ ($T = 0.741$, $P = 0.01202$).

intermolecular interactions, the potential energy did not scale with a volume move and we had to recalculate the total potential energy from scratch after every trial volume move. Therefore a MC cycle consisted on average of only one trial volume move and one trial displacement per particle. The acceptance ratio for both types of MC moves was kept at 50% by adjusting the maximum size of the move. The maximum displacements for the liquid and vapor particles were tuned independently.

The length of the trajectories depends on the computational cost of evaluating the order parameter and the average probability with which the trajectories are accepted. To be more precise, the efficiency ν is proportional to

$$\nu \propto \frac{P_{acc}(l)}{a + b/l}. \tag{5.41}$$

Here l is the length of the trajectories and a and b denote the computational costs of performing a MD/MC cycle and a cluster analysis, respectively. $P_{acc}(l)$ is the acceptance probability of the trajectories which depends on the trajectory length and on the force constant of the biasing potential (as well as on the steepness of the underlying free-energy barrier). Typically, for $k_n = 0.01 - 0.02$ a trajectory length of 50 MC cycles was optimal. To speed up the simulations, we used both a linked list and a neighbor list for the calculation of the energies and the identification of the clusters [68].

The number of umbrella windows for the free-energy barrier was fifteen. A typical simulation in a window consisted of an equilibration period of 100000-250000 MD steps, followed by a production run of 250000 MC cycles. The individual probability distribution functions $P(n)$ obtained in the different runs were fitted simultaneously to a polynomial. We used a polynomial fit rather than the self-consistent scheme of Ferrenberg and Swendsen [77], because not all adjacent histograms overlapped.

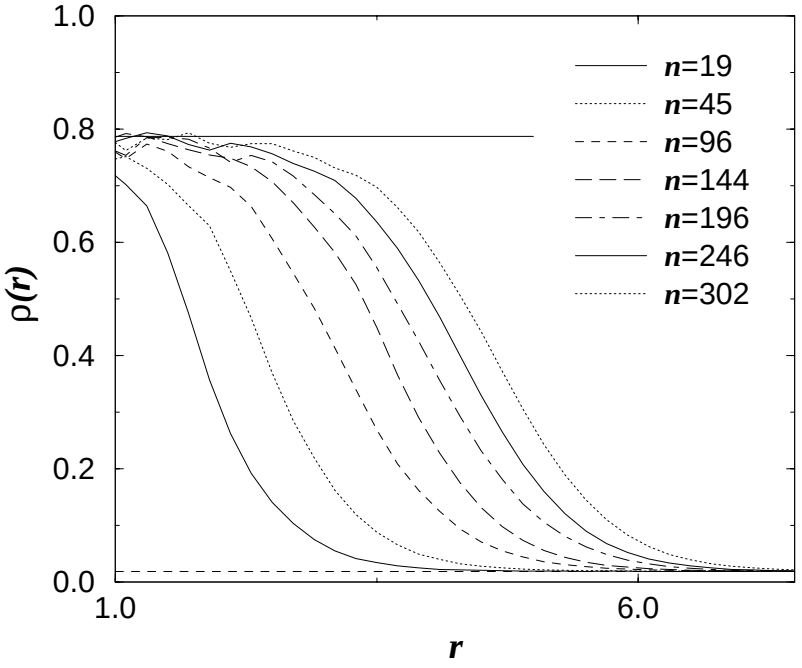

FIGURE 5.3 Density as a function of r, the distance to the center-of-mass of the clusters, for several precritical and critical nuclei at a supersaturation of $S = 1.53$ ($T = 0.741$, $P = 0.01202$). The thin horizontal dashed line denotes the density in the vapor and the thin horizontal solid line denotes the density in the bulk liquid, which has a chemical potential equal to that of the vapor phase.

5.6 Results and Discussion

We studied the nucleation of liquid droplets from the vapor as a function of supersaturation. All simulations were performed for one temperature, $T = 0.741$, which is 32% below the critical temperature ($T_c = 1.085$ [123]). At this temperature the pressure and densities of the coexisting phases are known [123]. Furthermore, in order to make a comparison with nucleation theories we have to know the surface tension. The temperature of our simulations is in the range of temperatures for which Chapela *et al.* [124] and, more recently, Holcomb *et al.* [125] computed surface tensions for planar gas-liquid interfaces.

The number of particles was $N = 864$. As the size of the largest critical nucleus obtained in the simulations, corresponding to the smallest degree of supersaturation, is around 300 particles and, more importantly, the density in the surrounding vapor is very low, with this number of particles the size of the simulation box was always large enough compared to the size of the critical droplets for system size effects not to be present.

5.6.1 The nucleation barrier

We first computed the full nucleation barrier with the umbrella-sampling technique for a reference pressure. This reference pressure was chosen to be $P = 0.01202$, which corresponds to a supersaturation $S = P/P_{coex} = 1.53$. Fig. 5.2 shows the nucleation barrier for this degree of supersaturation.

In our simulations we are not only able to study critical droplets, but also pre-and postcritical droplets. Visual inspection revealed that precritical droplets consisting of only 10-25 particles are already quite spherical. We therefore computed the density as a function of r, the distance to the center-of-mass of the cluster. Fig. 5.3 shows the radial density profiles for several precritical and critical clusters. Already for the smallest droplets the density approaches a bulk liquid density in the core. We stress

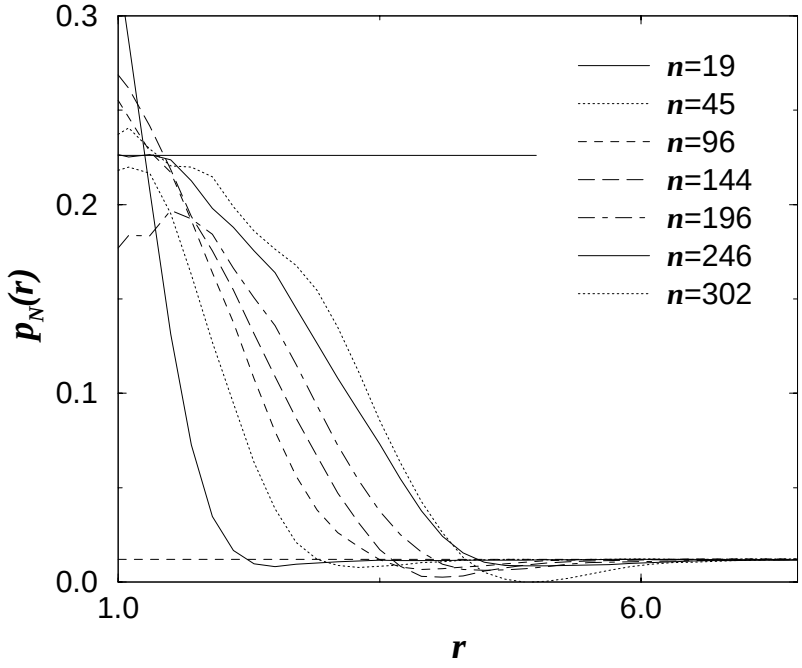

FIGURE 5.4 Radial profiles of the normal component of the pressure tensor, $p_N(r)$, for several precritical and critical nuclei at a supersaturation of $S = 1.53$ ($T = 0.741$, $P = 0.01202$). The thin horizontal dashed line denotes the pressure in the bulk vapor and the thin horizontal solid line denotes the pressure in the bulk liquid, which has a chemical potential equal to that of the vapor phase.

that this is not due to our choice of the cluster definition, which requires that a cluster particle should have at least 5 neighbors. A radial profile of the number of connections per particle shows that in the core of the liquid droplet the number of connections per particle is much larger than the threshold value of our cluster definition. In fact, it also approaches a bulk liquid value, i.e. around twelve neighbors per particle. Hence, our results are not very sensitive to the choice of the threshold value.

Fig. 5.3 also shows that the density in the core hardly increases when the clusters grows to its critical size $n^* = 280$. Furthermore, the density profiles show that the width of the interface remains essentially constant at approximately 3.5σ.

Using the Irving-Kirkwood expression for the pressure tensor [119] we also computed the pressure profiles for the precritical and critical nuclei. In Fig. 5.4 we show the radial profiles of the normal component of the pressure tensor. It is seen that all pressure profiles smoothly go to a bulk vapor value for large values of r, i.e. far away from the center of the droplet. In the center of the droplet the statistical accuracy with which the pressure can be determined is low, as the volume is small. Nevertheless, the data suggests that, except for the smallest droplets, the pressure profiles approach a plateau value in the core. In fact, the pressure in the core, as well as the density (see Fig. 5.3), approaches that of a hypothetical bulk liquid at a chemical potential that is equal to the chemical potential in the vapor phase. This indicates that the interior of the droplets shows bulk liquidlike behavior.

From the normal component of the pressure tensor we can also obtain the transverse component of the pressure tensor using Eq. (5.35). This equation shows that, when the derivative of the normal component of the pressure tensor with respect to the radius is positive, the transverse component is larger than the normal component of the pressure tensor. Under these conditions the surface would be under compression, rather than

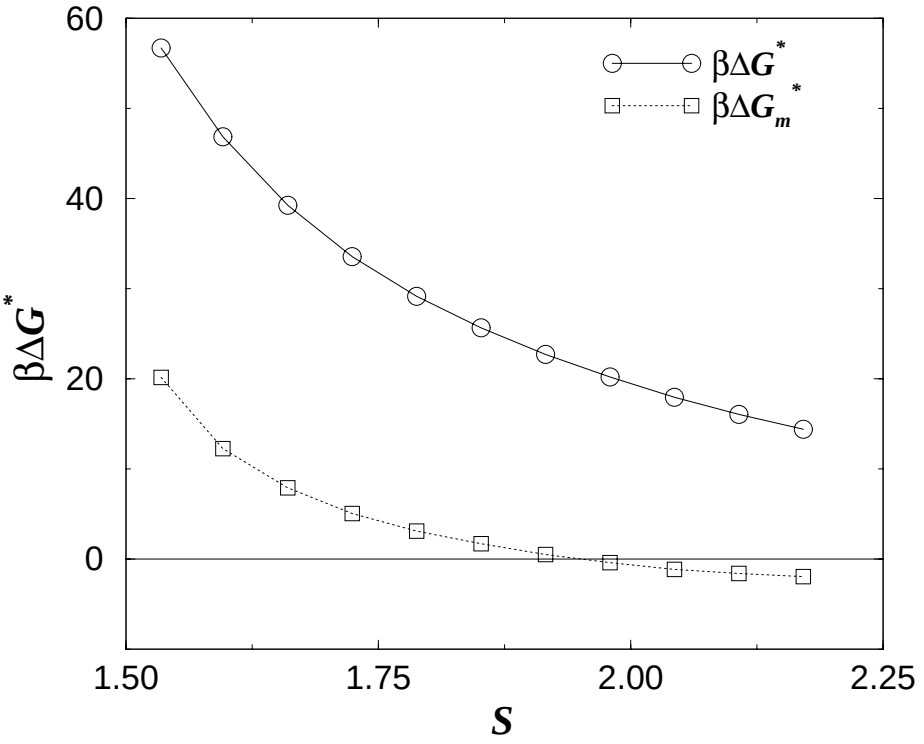

FIGURE 5.5 The height of the nucleation barrier as a function of supersaturation S for $T = 0.741$. The solid line is obtained via a thermodynamic integration technique, see Eq. (5.15). The dashed line is obtained by integrating the pressure profile, see Eq. (5.38). It is seen that the mechanical route to the nucleation barrier (dashed line) does not give the correct height of the free-energy barrier.

under tension. When the normal component is larger than the transverse component, the surface is under tension.

Fig. 5.4 shows that most of the surface of the droplets is under tension. However, at the vapor side of the interface the normal pressure becomes smaller than the vapor pressure. As the profile subsequently approaches the bulk vapor value, it is clear that there is a small region in which the derivative of the normal-pressure profile is positive. In this region the interface is under compression, rather than under tension. This behavior is also found in theoretical calculations, for different potentials [126–128], as well as in a computer-simulation study of liquid droplets by Thompson *et al.* [104], and in the computer simulations of a flat interface by Walton et al. [121].

5.6.2 Dependence on supersaturation

Using the method described in section 5.3.2, we computed the height of the nucleation barrier as a function of supersaturation. Fig. 5.5 shows the free-energy barrier as a function of supersaturation. We could not continue our simulations beyond $S = 2.2$, because at this point the height of the barrier is so low, that spontaneous nucleation of additional droplets occurs in the vapor. But before we discuss the height of the

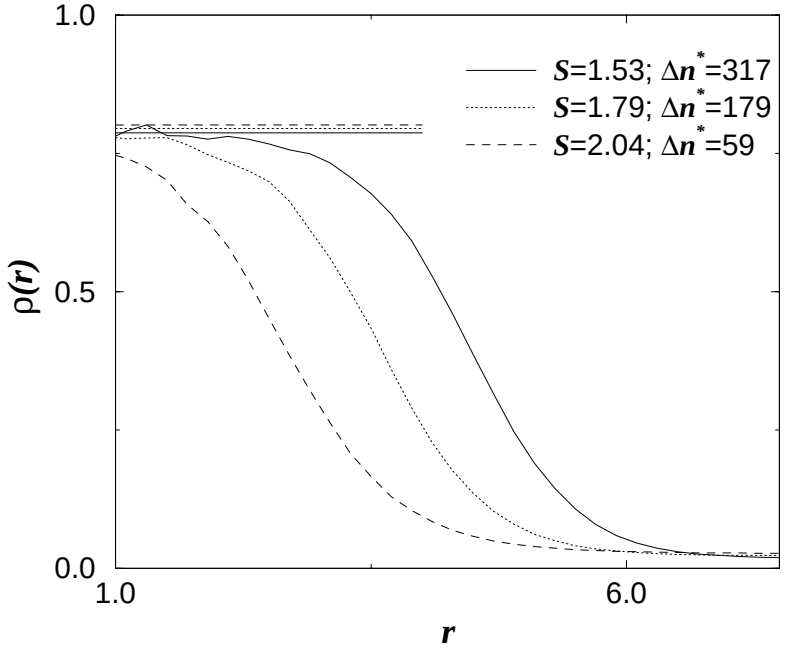

FIGURE 5.6 Radial density profiles for different critical nuclei, at different supersaturations S ($T = 0.741$). In the legends also the excess number of particles, Δn^*, is indicated. The thin horizontal lines indicate for the different supersaturations the density in the bulk liquid that has the same chemical potential as the vapor phase.

nucleation barrier as a function of supersaturation in more detail, let us first describe qualitatively how the critical nucleus changes as the supersaturation is increased.

In Figs. 5.6 and 5.7 we show, respectively, the density and pressure profiles for three critical nucleus sizes. In the legends we have also indicated the excess number of particles defined as

$$\Delta n = 4\pi \int_0^\infty [\rho(r) - \rho_v]\, r^2 dr, \tag{5.42}$$

where ρ_v is the density in the vapor (far away from the droplet). Because of the diffuse nature of the interface, the size of the critical nucleus is ambiguous and depends on the position of the dividing surface. However, the excess number of particles is independent of the position of the dividing surface and is therefore a more meaningful quantity.

Fig. 5.6 and Fig. 5.7 show that as the supersaturation is increased, the density and pressure in the core slowly decrease. This indicates that the droplet already starts to loose bulk behavior in the core. If the core of the droplet would show bulk liquid behavior, then, in order for the chemical potential in the bulk liquid core to be equal to the chemical potential in the vapor, the density and pressure in the core of the droplet have to increase when the pressure in the vapor is increased. Indeed, this behavior has been observed by Thompson *et al.* [104] and Nijmeijer *et al.* [46] in their simulations of liquid droplets. However, the droplets for which this behavior was seen, were much larger (larger than 2000 particles), than the droplets studied here. In fact, in the simulations of Thompson *et al* [104] a clear cross-over in behavior was seen for smaller droplets. In line with the present results, they found that, once the droplets are smaller than a certain size, the density and pressure in the core of the droplets decrease with increasing vapor pressure. This loss of bulk behavior is also found in several molecular theories [14, 126–128].

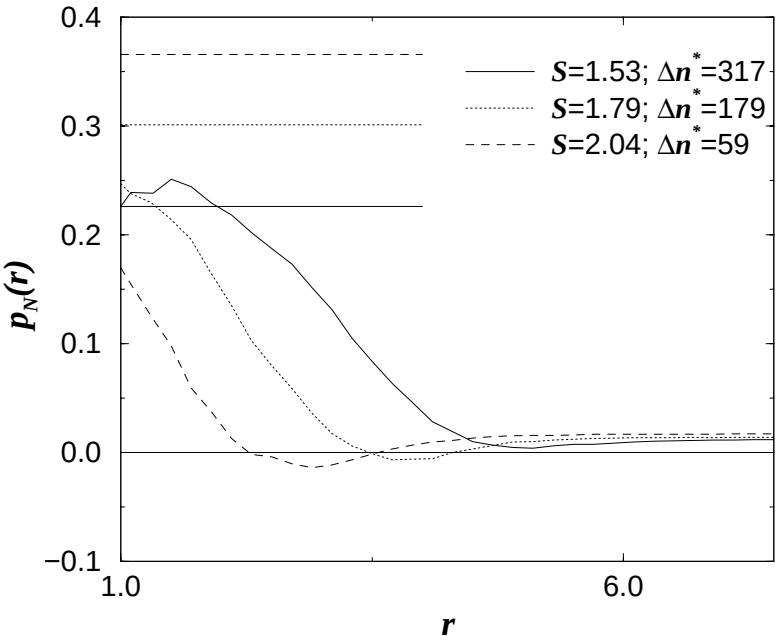

FIGURE 5.7 Radial profiles of the normal component of the pressure tensor for critical nuclei, at different supersaturations S ($T = 0.741$). The excess number of particles Δn^* is also given. The thin horizontal lines indicate for the different supersaturations the pressure in the bulk liquid that has the same chemical potential as the vapor phase.

Fig. 5.6 and Fig. 5.7 suggests that the width of the interface remains constant over the range of droplet sizes studied. Note that when the droplets become smaller, the region for which the normal pressure is smaller than the vapor pressure, increases. Moreover, the region for which $p_T > p_N$ increases as well, that is, the interface is progressively more under compression. In fact, for the smallest droplets studied, most of the interface is under compression rather than tension. This trend has also been observed by Falls *et al* [126].

5.6.3 The nucleation theorem

The nucleation theorem is a powerful tool to analyse experimental data on homogeneous nucleation [15, 50, 94, 95].The nucleation theorem states that the excess number of molecules of a given component in the critical nucleus can be obtained from the variation of the height of the barrier with the chemical potential, $\mu_{v,i}$, of that component in the vapor phase:

$$\frac{\partial \Delta G^*}{\partial \mu_{v,i}} = -\Delta n_i^*, \tag{5.43}$$

where Δn_i^* is defined as in Eq. (5.42) above.

As nucleation is a rare event, it is impossible to measure the size and composition of critical nuclei directly in an experiment. However, if one assumes that the prefactor in the expression for the nucleation rate depends only weakly on supersaturation, the nucleation theorem makes it possible to determine the size and composition of the critical nuclei as a function of the activities of the components in the vapor phase.

Several derivations of the nucleation theorem have been presented in the literature. The original derivation by Kashchiev [55] and a later one by Viisanen *et al.* [95] were based on a thermodynamic model in which the reversible work of formation of a cluster is written as the sum of a bulk term and an excess free energy term, which includes

contributions from the surface free energy. The nucleation theorem was obtained by assuming that the variation of the excess free energy of the cluster depends only weakly on the chemical potential. However, in the approach of Refs. [55] and [95] the variation of the barrier height with the gas phase activities yields the total number of particles in the cluster and not the excess number of particles in the cluster. Also an analysis based on classical nucleation theory by Strey *et al.* [94] suggests that, from the variation of the height of the barrier with the chemical potential in the vapor phase, the total number of particles rather than the excess number of particles is obtained. However, Oxtoby and Kashchiev [56], who also used a thermodynamic approach, showed that the variation of the surface free energy with the chemical potential in the vapor phase is related to the surface density of the molecules and that the nucleation theorem gives the excess number of particles and not the total number of particles in the critical cluster. All these derivations are based on thermodynamic models. It is conceivable that such an approach fails for very small droplets. However, Ford [57] gave a derivation using small system thermodynamics, which confirmed that the excess number of particles in the cluster is obtained from the variation of the height of the barrier with the gas phase activities. Moreover, the same result was obtained from a statistical mechanical analysis by Viisanen, Strey and Reiss [15]. In chapter 2 we have given a compact derivation which is also based on statistical mechanics. Furthermore, this derivation also shows that the variation of the height of the Gibbs free-energy barrier with the pressure is related to the excess volume of the system at the top of the barrier, and that the variation of the barrier height (both in the grand-canonical and in the isothermal-isobaric ensemble) with T and β gives the excess entropy and excess internal energy, respectively.

In our simulations, we compute the barrier height as a function of pressure. However, in order to compare with the nucleation theorem, we need to know the variation of the barrier height with the chemical potential of the vapor phase. The variation of the chemical potential with pressure is given by the Gibbs-Duhem relation: $\frac{d\mu}{dP}\big|_T =$

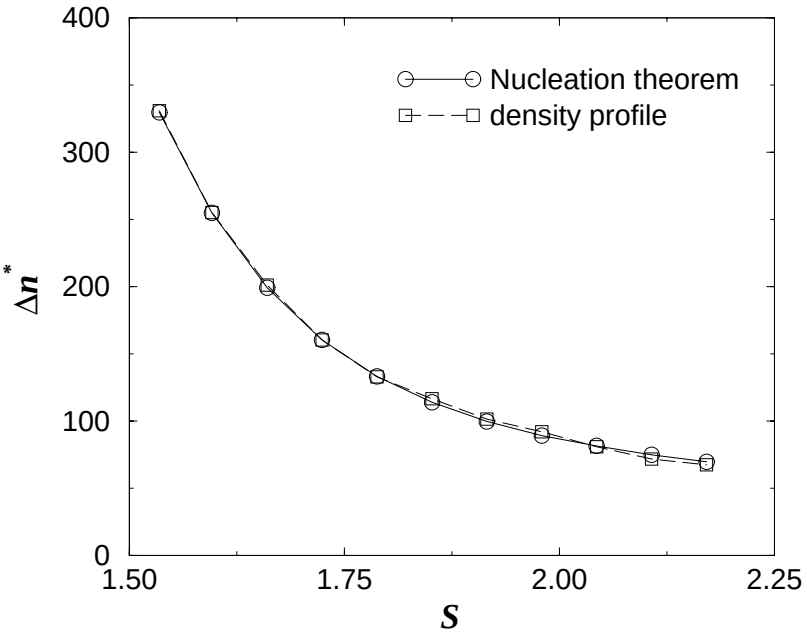

FIGURE 5.8 The excess number of particles Δn^* in the critical nuclei as a function of the supersaturation S ($T = 0.741$), as obtained from the variation of the height of the barrier with the chemical potential in the vapor phase, and as obtained by integrating the density profiles. According to the nucleation theorem they should give the same results.

$1/\rho_v$, where ρ_v is the density in the vapor. In Fig. 5.8 we show the excess number of particles in the cluster obtained via the nucleation theorem and by directly integrating the density profiles. It is seen that for all droplets sizes studied the agreement is excellent. This indicates that the method to measure the height of the barrier as a function of supersaturation described in section 5.3.2 is not only efficient, but also very accurate.

5.6.4 Deviations from Classical Nucleation Theory

Recent experiments on gas-liquid nucleation indicate that the sizes of the critical nuclei are accurately predicted by classical nucleation theory [15, 50, 51]. However, the rate of nucleation was found to be consistently higher than predicted by classical nucleation theory. In fact, it was observed that the ratio of the experimentally determined nucleation rate and the nucleation rate as predicted by CNT, although depending on temperature, was nearly independent of the supersaturation [51]. In two recent papers, McGraw and Laaksonen derived relations for the height of the barrier and the size of the critical nucleus that could provide an explanation for these observations [12, 13]. In their first paper [12] they gave a derivation which was based on the nucleation theorem. In the second paper they gave a derivation which was based on the nonuniform spherical droplet model [13]. They showed that if the nucleus has an incompressible core with a density equal to that of the bulk phase and if the number of particles within the equimolar dividing surface is correctly predicted by CNT, then the difference between the actual barrier height and the height of the barrier as predicted by CNT, is independent of the supersaturation and depends only on temperature. Using the techniques discussed in section 5.3.2 we are able to test these predictions directly.

In classical nucleation theory the size of the critical droplet is given by

$$n^* = \frac{32\pi\gamma_\infty^3}{3\rho_l^2\Delta\mu^3}, \tag{5.44}$$

where γ_∞ is the surface free energy of the planar interface and ρ_l is the density of the bulk liquid at coexistence. $\Delta\mu$ is the difference between the chemical potential μ_v in the vapor phase and the chemical potential μ_l in the bulk liquid phase, both at the pressure P in the vapor phase, i.e.

$$\Delta\mu(P) = \mu_v(P) - \mu_l(P). \tag{5.45}$$

In classical nucleation theory the height of the nucleation barrier is given by

$$\Delta G^* = \frac{16\pi\gamma_\infty^3}{3\rho_l^2\Delta\mu^2}. \tag{5.46}$$

As the cube of the surface free-energy enters the expressions for the height of the barrier and for the critical nucleus size, we need an accurate estimate for the surface free energy. Chapela *et al.* [124] and Holcomb *et al.* [125] have calculated surface free energies for a Lennard-Jones system with the same potential cutoff as used in our simulations and for a range of temperatures that encompasses our temperature. In order to obtain the surface free energy at our temperature we made a polynomial fit to their data and found $\gamma_\infty = 0.494$.

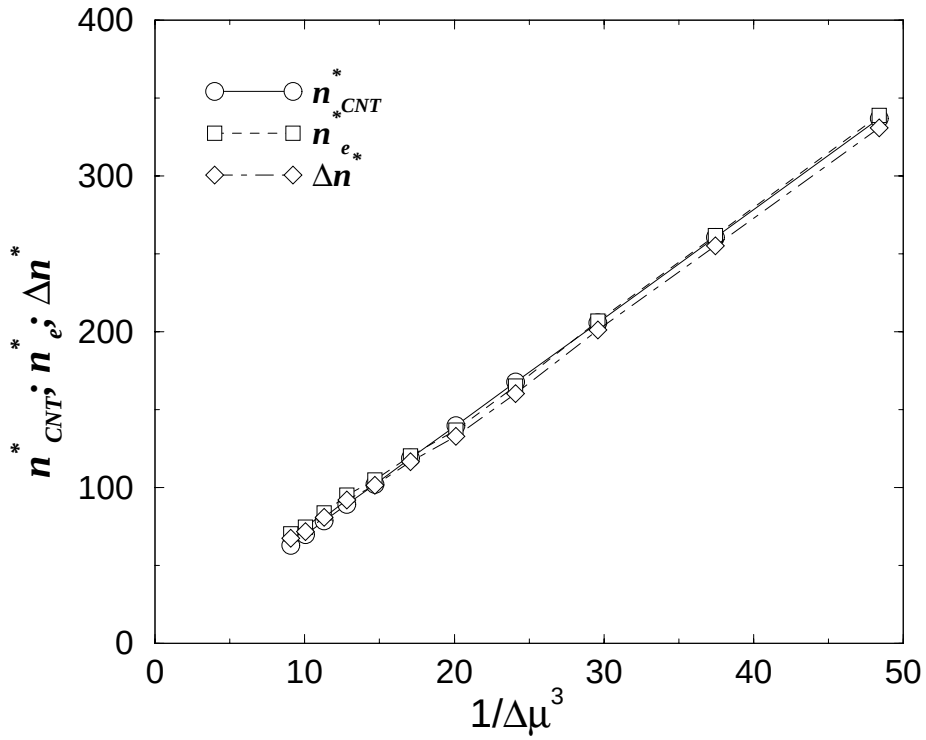

FIGURE 5.9 The number of particles in the critical nuclei as a function of $1/\Delta\mu^3$, as predicted by classical nucleation theory and as obtained from the simulations. The number of particles predicted by classical nucleation theory is indicated by n^*_{CNT} and the number of particles within the equimolar dividing surface, as obtained from the simulations, is indicated by n^*_e. For comparison we have also shown the excess number of particles, denoted by Δn^*, as obtained from the simulations. According to the relations proposed by McGraw and Laaksonen [12, 13] n^*_e is given by classical nucleation theory (n^*_{CNT}).

The chemical-potential difference $\Delta\mu(P)$ was computed by integrating the difference in inverse density between the liquid and vapor phase from the coexistence pressure:

$$\Delta\mu(P) = \int_{P_{coex}}^{P} \left[\frac{1}{\rho_v(P')} - \frac{1}{\rho_l(P')}\right] dP'. \tag{5.47}$$

Here P_{coex} is the coexisting pressure and ρ_v and ρ_l are the densities of the bulk vapor and bulk liquid phase, respectively. As the chemical potential of the vapor phase depends very strongly on pressure, the difference in chemical potential is very sensitive to the exact location of the coexistence point. We found that the data of Smit [123] was not accurate enough for our purpose and we therefore performed a more extensive Gibbs ensemble simulation [129] to calculate the coexistence point. We found that the coexistence pressure $P_{coex} = 0.00783$ and that the density of the liquid at coexistence $\rho_l = 0.766$.

Fig. 5.9 shows the number of particles in the critical nucleus, as a function of $1/\Delta\mu^2$. In the figure, we compare the predictions of CNT and the numerical results for n^*_e, the

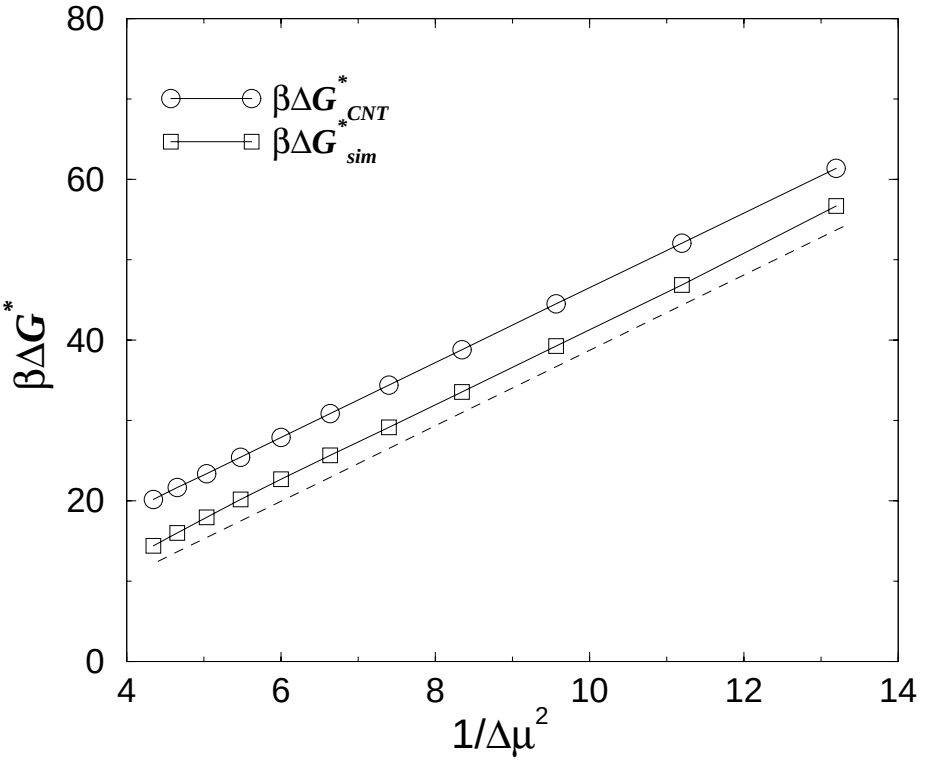

FIGURE 5.10 The height of the barrier as predicted by classical nucleation theory and as obtained from the simulations, as a function of $1/\Delta\mu^2$. The relations proposed by McGraw and Laaksonen [12, 13] predict a constant offset between the actual barrier height and the height of the barrier as predicted by classical nucleation theory. The dashed curve is a guide to the eye; it has the same slope as the curve of the classical nucleation theory prediction.

number of particles within the equimolar dividing surface:

$$n_e^* = \frac{4\pi\rho(0)}{\rho(0)-\rho_v}\int_0^\infty [\rho(r)-\rho_v]\, r^2 dr. \tag{5.48}$$

Here ρ_v is the density in the vapor, and $\rho(0)$ is the density in the core of the droplet. The statistical error in $\rho(0)$, the density in the core, is relatively large. However, as $\rho_v \ll \rho(0)$, this inaccuracy has little effect on the value of n_e^*. For the same reason, n_e^* is nearly equal to the better defined quantity Δn^*, which is shown in Fig. 5.9. But more importantly, it is seen that for all droplet sizes studied, CNT gives a good estimate for the number of particles in the critical cluster. Surprisingly, the predictions of CNT are excellent down to the smallest droplets, which consists almost exclusively of interface.

In Fig. 5.10 we show that the simulation results support the McGraw-Laaksonen predictions for the height of the barrier: the barrier height found in the simulations differs by a constant offset from the value predicted by CNT. This results appears to hold even for critical nuclei consisting of only 50-100 particles. Again, this finding is surprising because, as discussed in section 5.6.2, the cores of these nuclei do not show

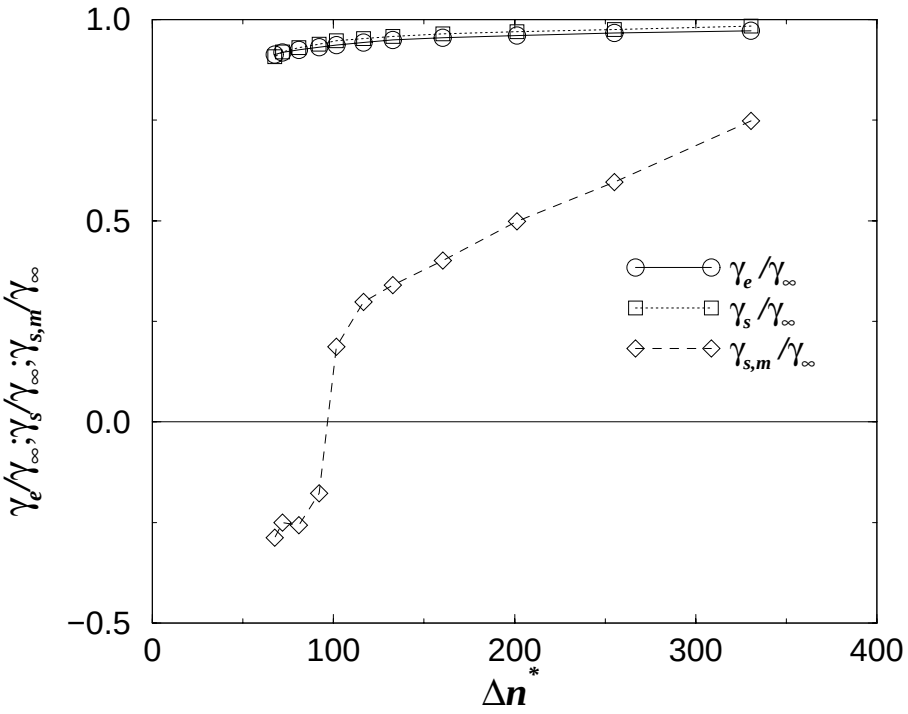

FIGURE 5.11 The thermodynamically defined surface tension γ_s and the mechanically defined surface tension $\gamma_{s,m}$ (acting at the respective surface of tensions), as well as the surface tension at the equimolar dividing surface, denoted by γ_e, as a function of the excess number of particles in the critical nuclei.

bulk behavior. In fact, McGraw and Laaksonen gave two derivations of their expressions for the height of the nucleation barrier and for the critical nucleus size: one made use of the assumption that the nucleus had an incompressible core [13], the other did not [12]. Our simulations suggest that the relations proposed in Ref. [12, 13] are quite robust. If we have the right theoretical tools to predict the offset, a better agreement between experiment and (extended) CNT can be obtained [130].

McGraw and Laaksonen [13] showed that, within their non-uniform droplet model, the offset $D(T)$ is related to the rigidity coefficient k_s:

$$\Delta G^*_{CNT} - \Delta G^* = D(T) = -4\pi k_s \ , \tag{5.49}$$

where k_s/R^2 is the elastic curvature free-energy per unit area) From our simulations we estimate $k_s = -0.31\epsilon = -0.42 k_B T$. This is smaller than the value that McGraw and Laaksonen obtained in their density functional calculations [13]. However, the discrepancy could well be due to the fact that we used a truncated Lennard-Jones potential, whereas in the density functional calculations the full Lennard-Jones potential was used.

5.6.5 Tolman Length

We computed the thermodynamically defined surface tension and surface of tension using Eqs. (5.19) and (5.20). As explained in section 5.4.1, Δp is the difference between

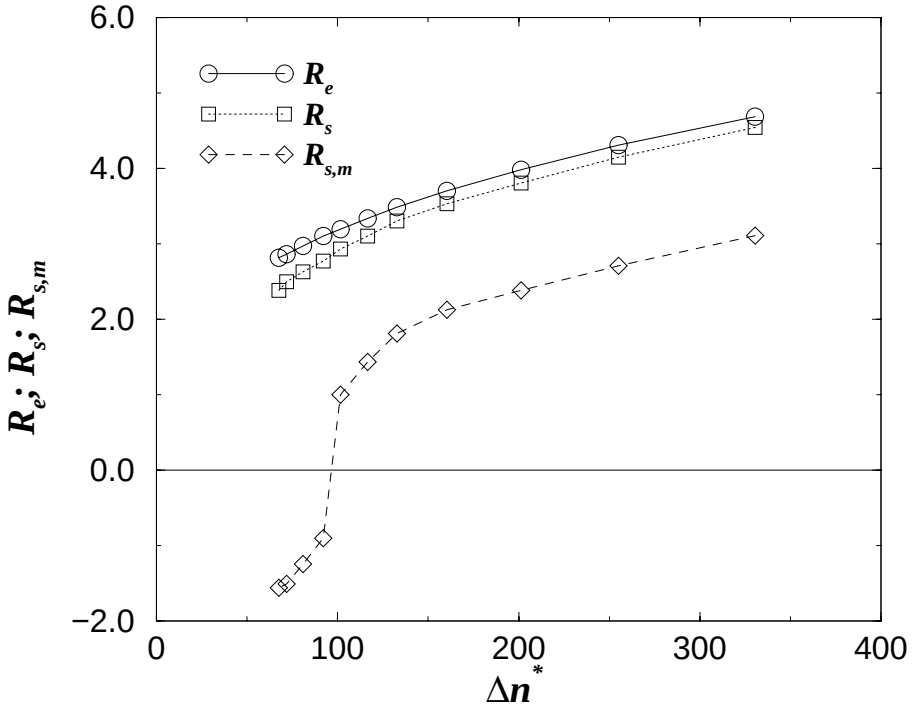

FIGURE 5.12 The radii of the equimolar dividing surface, R_e, of the thermodynamically defined surface of tension, R_s and of the mechanically defined surface of tension, $R_{s,m}$, as a function of the excess number of particles in the critical nuclei.

the pressure in the vapor and the pressure in a hypothetical bulk liquid with a chemical potential equal to that of the vapor phase. We therefore performed a series of simulations of the bulk liquid to obtain the chemical potential of the liquid as a function of P. In Fig. 5.11 and 5.12 we show the thermodynamic surface tension and the location of the surface of tension, respectively. For small droplets, the surface tension increases rapidly with droplet size, and then smoothly approaches its planar limit. Such behavior has also been found in theoretical studies [109, 126, 127].

For the sake of comparison, we have also calculated the mechanical surface tension and surface of tension using Eqs. (5.36) and (5.37). The results are shown in Fig. 5.11 and Fig. 5.12, respectively. The figures show that both the surface tension and the surface of tension become negative for clusters smaller than 100 particles. The reason for this can be understood from Fig. 5.7. As can be seen from this figure, small droplets have a progressively larger region where the pressure is lower than the vapor pressure. As discussed in section 5.6.2, this implies that the surface of small droplets is increasingly under compression. For clusters smaller than 100 particles, compression dominates and the integral in Eq. (5.36) and (5.37) becomes negative. For a cluster size of about 100 the integral in Eqs. (5.36) and (5.37) vanishes, and both $R_{s,m}$ and $\gamma_{s,m}$ cross zero.

Fig 5.12 also shows that the mechanically defined surface of tension and thermodynamically defined surface of tension are shifted with respect to one another. If we ignore the smallest droplets for which the radius of the mechanical surface tension becomes

negative, the displacement is found to be constant over the range of droplet sizes studied, and equals approximately one σ. It is thus clear that the two surfaces cannot be identified with each other. This was first pointed out by Blokhuis and Bedeaux [45] and later also found by Haye and Bruin [47] in their computer simulation study of a planar interface. Haye and Bruin [47] observed the displacement to be strongly depending on temperature, but for $T = 0.75$, which is quite close to the temperature of the present simulations, they also found a displacement close to one σ, i.e. 0.92σ.

Fig. 5.11 shows that not only the position of the surface of tension is different for the two definitions, but also the magnitude of the surface tension. In the planar limit the surface tensions should become equal [40, 41], but for smaller droplets the difference becomes quite significant. In Fig. 5.11 we also show the surface tension at the equimolar dividing surface. McGraw and Laaksonen [13] showed that within their non-uniform droplet model the surface tension at the equimolar dividing surface can be obtained from the offset between the actual barrier height and the height of the barrier as predicted by CNT:

$$\Delta G^*_{CNT} - \Delta G = 4\pi R_e^2(\gamma_\infty - \gamma_e). \tag{5.50}$$

Here γ_e is the surface tension at the equimolar dividing surface and R_e is the radius of the equimolar dividing surface, which is given by

$$R_e^3 = \frac{3}{\rho(0) - \rho_v} \int \left[\rho(r) - \rho_v\right] r^2 dr. \tag{5.51}$$

The thermodynamically defined surface of tension is the surface for which the surface tension is at its minimum [40, 41], hence γ_s should be smaller than γ_e. For the larger droplet sizes, the (Tolman) length $\delta \equiv R_e - R_s$ becomes small compared to radius of the droplet. In that limit, we should expect the surface tensions to approach each other, as the surface tension varies quadratically with $R - R_s$ (see section 2.2.3, Eq. (2.17)). We find that γ_e and γ_s are equal to within the accuracy of our simulations.

In Fig. 5.13 we have plotted δ as a function of the size of the droplets. It is seen that δ is a strong function of the size of the droplet. In fact, our results are in fair agreement with the density functional calculations of Talanquer and Oxtoby [109]. We can obtain the Tolman length by fitting δ to a polynomial and extrapolating the result to the planar limit. We find that δ_T is zero to within the accuracy of our simulations ($-0.2 < \delta_T < 0.8$). Haye and Bruin [47] have computed the Tolman length for a range of temperatures by molecular dynamics simulations. Within the error bars the Tolman length was found to be independent of temperature and equal to $\delta_T = 0.16 \pm 0.04$, which is compatible with the earlier numerical calculations by Nijmeijer *et al.* [46], who found that $|\delta_T| < 0.7$ for $T = 0.9$. Recently, Kalikmanov formulated a semiphenomenological cluster theory of the Tolman length based on the Fisher cluster model of condensation [97] combined with a Tolman-like ansatz for the microscopic surface tension of a cluster [131]. Kalikmanov performed calculations for a variety of nonpolar substances [131], which show that not too close to the critical temperature ($|(T - T_c)/T_c| > 0.1$) the Tolman length is positive and about 0.2σ. Considering the small droplet sizes that we have studied, our results are in fair agreement with the previous results.

The Tolman length describes the lowest order correction to the surface tension [42]. In chapter 2 we have shown that from the Helfrich expansion of the surface tension

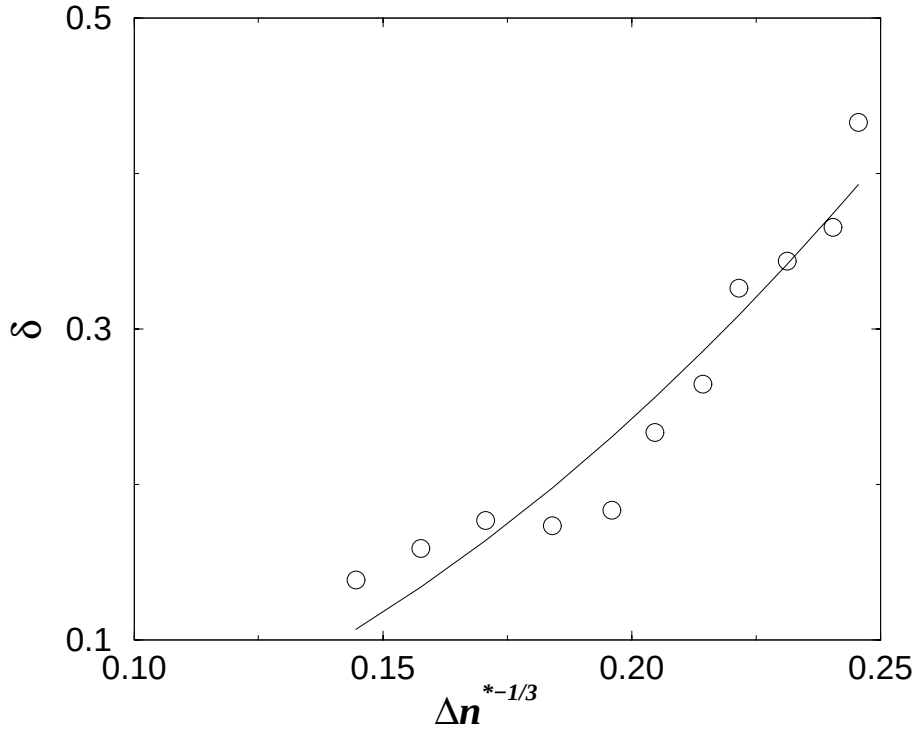

FIGURE 5.13 The difference $\delta = R_e - R_s$ between the equimolar dividing surface and the surface of tension as function of the excess number of particles, $\Delta n^{*-1/3}$, in the critical nuclei. The solid curve is a fit of the data to a function of the form $f(\Delta n^{*-1/3}) = c_1 \Delta n^{*-1/3} + c_2 \Delta n^{*-2/3}$. This corresponds to a Tolman length $\delta_T = \lim_{\Delta n^{*-1/3} \to 0} \delta = 0.0$, as (implicitly) assumed in the non-uniform droplet model of McGraw and Laaksonen [13]. Clearly, our simulations do not rule out this possibility.

around the planar interface [45] it can be derived that

$$\delta_T = -\frac{kC_o}{\gamma_\infty}, \tag{5.52}$$

where C_o is the the spontaneous curvature. In chapter 2 we have shown that k_s can be related to $k_s = 2k + \overline{k}$. Hence, provided that we would know $\overline{k}$, it would seem that we can obtain the spontaneous curvature C_o from the bending rigidity k_s (via Eq. (5.49)), and from the Tolman length and the surface tension of the planar interface γ_∞. However, we have obtained k_s using a relation derived in the model of McGraw and Laaksonen [13]. As shown in chapter 2, the expression for the curvature dependence of the surface tension in this model is only compatible with the Helfrich expansion of the surface tension if the Tolman length is zero. Therefore, computing the spontaneous curvature from Eq. (5.52) and the measured k_s is internally inconsistent. In the non-uniform droplet model of McGraw and Laaksonen it is already implicitly assumed that the Tolman-length is zero. Our simulations suggest that, for the Lennard-Jones system, this is a reasonable assumption.

Here we also would like to point out that k_s can be negative. The condition that must be fulfilled is that $\gamma(R)$ (see Eq. (2.31)) is positive. If γ would not be positive, it would be energetically favorable for a cluster to break up into smaller clusters. For vesicles, γ_∞ is close to zero, which implies $-2k < \overline{k} < 0$. For the liquid Lennard-Jones droplets, however, γ_∞ is positive, and k_s can be negative. We note here that the Helfrich expansion to second order, and the relation of McGraw and Laaksonen for the surface free energy (see Eq. (2.70)), breaks down if $\gamma(R)$ becomes negative. Then higer order terms in the expansion of the surface free energy in the inverse radii have to be taken into account. However, in the present case, this only occurs for droplets containing fewer than five to ten particles.

5.7 Conclusions

In our simulations, we have studied the structure and thermodynamics of the (pre) critical nuclei that play a role in the homogeneous nucleation of the liquid phase from the vapor. We found that the dependence of the size of the critical nucleus on the degree of supersaturation is in excellent agreement with the nucleation theorem. Furthermore, our simulations show that liquidlike clusters larger than 200 particles show bulk behavior in the core. That is, the pressure and the density in the core of the droplets are those of a bulk fluid with a chemical potential equal to that of the vapor phase. However, smaller droplets start to loose this bulk behavior. Nevertheless, the critical-nucleus sizes are still correctly predicted by classical nucleation theory. The simulation results for the height of the nucleation barrier differ by a constant amount from the prediction of classical nucleation theory, not only for large droplets, but even for quite small droplets. This constant offset can be accounted for by assuming that the surface tension depends quadratically on $1/R$ [12, 13].

For the range of droplet sizes studied here, we find a significant discrepancy between the thermodynamic and mechanical description of the surface tension. Of course, one could argue that the thermodynamic description should fail for very small droplets. But even for larger droplets, which do show bulk liquid behavior in the core, we find that the respective surfaces of tension cannot be identified with each other and that the surface tensions that follow from the different definitions are different. This implies that the height of the nucleation barrier cannot be obtained from Eq. (5.38). The failure of this equation is clearly illustrated by Fig. 5.5. The discrepancy between the free-energy barriers obtained by the thermodynamic and mechanical approaches is quite large, around $10 - 40 k_B T$. In fact, as this figure shows, the mechanical route leads to an estimate for the height of the barrier that even becomes negative–this is due to the fact that the integral of the pressure profile in Eq. (5.38) becomes negative. Hence, at present, there seems to be no "cheap" numerical alternative to the direct (umbrella-sampling) approach to compute nucleation barriers.

Appendix Detailed balance

The detailed balance condition for the transition between state i and j is

$$\rho_i P^{gen}_{i\to j} P^{acc}_{i\to j} = \rho_j P^{gen}_{j\to i} P^{acc}_{j\to i}. \tag{5.53}$$

Here, ρ_i is the Boltzmann weight of configuration i, $P^{gen}_{i\to j}$ denotes the transition matrix which determines the probability to perform a trial move from state i to state j and $P^{acc}_{i\to j}$ is the probability with which this trial move is accepted.

In the standard Metropolis scheme, the transition matrix is symmetric and the acceptance criterion only depends on the Boltzmann factors of state i and j. However, in the present scheme, liquid particles and vapor particles have different maximum displacements, which affects the transition matrix for the trial moves and needs to be taken into account in the acceptance criterion.

We rewrite Eq. (5.53) as

$$\frac{P^{acc}_{i\to j}}{P^{acc}_{j\to i}} = \frac{\rho_j}{\rho_i} \frac{P^{gen}_{j\to i}}{P^{gen}_{i\to j}}. \tag{5.54}$$

The probability to generate a move from i to j is proportional to the inverse cube of the maximum displacement, denoted by drmax, and depends on the state of the particle, s. The acceptance criterion now becomes

$$\frac{P^{acc}_{i\to j}}{P^{acc}_{j\to i}} = \frac{\rho_j}{\rho_i} \left(\frac{\mathrm{drmax}_i(s)}{\mathrm{drmax}_j(s)} \right)^3. \tag{5.55}$$

There are many possible choices for $P^{acc}_{i\to j}$ that satisfy this condition (and the obvious condition that the probability cannot exceed one). We have adopted the Metropolis rule

$$P^{acc}_{i\to j} = \mathrm{Min} \left[\frac{\rho_j}{\rho_i} \left(\frac{\mathrm{drmax}_i(s)}{\mathrm{drmax}_j(s)} \right)^3, 1 \right]. \tag{5.56}$$

However, there is one other condition that we have not mentioned yet. If a particle makes a transition from the vapor to the liquid and its displacement is larger than the maximum displacement in the liquid, then the move should be rejected. The reason is that when this move would have been accepted (and the particle would become a liquid particle), the reverse move could never be made (because the maximum displacement for liquid particles is smaller than the maximum displacement for vapor particles).

6 Rate of homogeneous gas-liquid nucleation in a Lennard-Jones system

We report a computer-simulation study of the absolute rate of homogeneous gas-liquid nucleation in a Lennard-Jones system. The height of the barrier has been computed using umbrella sampling, whereas the kinetic prefactor is calculated using molecular dynamics simulations. The simulations show that the nucleation process is highly diffusive. We find that the kinetic prefactor is a factor 10 *larger than predicted by classical nucleation theory. The height of the nucleation barrier is around* 10% *lower than predicted by classical nucleation theory.*

6.1 Introduction

The formation of liquid droplets from a supersaturated vapor is an activated process. When a vapor is supersaturated, the liquid phase is more stable than the vapor. However, due to the free-energy barrier separating the two phases, the vapor will not condense immediately. First nuclei of the new phase have to form. Two competing contributions determine the excess free energy of such nuclei. The difference in chemical potential between vapor and liquid drives the nucleation process, whereas the surface free energy frustrates the formation of nuclei. Initially, the surface free energy dominates, and hence the excess free energy of a droplet increases with size. However, beyond a certain "critical" nucleus size, the volume term takes over, and the excess free energy decreases. It is only from here on that a nucleus grows spontaneously into a bulk liquid.

The classical nucleation theory of homogeneous gas-liquid nucleation was formulated over half a century ago [4, 5]. This theory is partly phenomenological in nature. Subsequently, various modifications and extensions have been proposed [54, 96–99, 132, 133], and much progress has been made in the development of statistical-mechanical theories of nucleation [11, 14, 115]. In parallel, nucleation rate measurements have become increasingly precise. This makes it possible to test the theoretical predictions for the nucleation rate [15, 16, 33, 34, 50, 94, 95, 134–137]. However, in the experiments only the nucleation rate can be probed. It is virtually impossible to study the critical nuclei themselves. The reason is precisely that nucleation is an activated process. The rate k of such a process can be written as:

$$k = Ce^{-\beta \Delta G^*} = CP_o. \tag{6.1}$$

Here, C is a prefactor, $\beta \equiv 1/k_B T$ is the reciprocal temperature, with k_B Boltzmann's constant and T the absolute temperature, and ΔG^* is the nucleation barrier which is given by the excess free energy of the critical nucleus. The nucleation rate is the product

of two factors: (1) the probability P_o to find the system at the top of the barrier and (2) the rate C at which this barrier is crossed. In experiments the height of the barrier is typically in the order of $50 - 100 k_B T$. This implies that the probability to find a nucleus of critical size is extremely small, on the order of 10^{-12} per cm^3. Moreover, the kinetic prefactor is in the order of Gigahertz to Terahertz. This means that when a nucleus reaches its critical size, it spends only little time at the top of the barrier. Hence, nucleation is both infrequent and fast and it is very difficult to study the structure and dynamics of the critical nuclei. Experiments only measure the overall nucleation rate. It is not possible to measure the factors that determine the nucleation rate independently. It is for these reasons that computer simulation is a natural complementary tool to study the nucleation process. By employing umbrella sampling [26] we can stabilize the critical nuclei, which allows us to study the structure of a nucleus and to compute its free energy as a function of its size. Moreover, using the Bennett-Chandler scheme [28–30] we can also compute the kinetic prefactor.

Gas-liquid nucleation proceeds via the addition of single particles from the vapor. This is a sequence of uncorrelated events. As a consequence, the nucleation process is diffusive, rather than a ballistic. Recently, we have shown how the Bennett-Chandler scheme can be modified to study diffusive barrier crossings [69]. Here we apply this extended scheme to study gas-liquid nucleation in a Lennard-Jones system. The choice of the Lennard-Jones system as a model for a simple fluid is motivated by several factors: First of all, the phase behavior and surface tension of this system are known. This makes it possible to compare the simulation results with classical nucleation theory [5]. Secondly, in a chapter 5, we have computed the nucleation barrier for the Lennard-Jones system.

The rest of the chapter is organized as follows: In the next section we briefly discuss the Bennett-Chandler scheme and the modifications described in Ref. [69]. We then describe some technical aspects of the simulations. We end with a discussion of the results.

6.2 Crossing Rate

Nucleation is an activated process and the rate limiting step in the condensation of the vapor. This implies that in order to compute the rate of nucleation, we can calculate the rate at which the vapor transforms into the liquid and vice versa. We apply the Bennett-Chandler scheme [28–30] to compute rate constants for a transition between two states, A (vapor) and B (liquid), that are separated by a free-energy barrier. In the Bennett-Chandler scheme it is assumed that the reaction can be described by a first-order phenomenological rate law:

$$\Delta P_A(t) = \Delta P_A(0) e^{-t/\tau}. \tag{6.2}$$

Here P_A is the probability that the system is in state A (vapor). According to the Onsager-regression hypothesis the relaxation of the macroscopic variable P_A is given by the regression of spontaneous fluctuations of a microscopic variable, n_A, in an equilibrium system [67]:

$$\Delta P_A(t)/\Delta P_A(0) \propto \langle \Delta n_A(t) \Delta n_A(0) \rangle_{eq}. \tag{6.3}$$

Here $\Delta P_A(t)$ and $\Delta n_A(t)$ are the deviations of P_A and n_A from their equilibrium value at time t, respectively, and τ is the relaxation time.

We now have to determine the characteristic, microscopic functions, n_A and n_B, the value of which specifies whether the system is in state A (vapor) or state B (liquid). To this end, we first have to define a reaction coordinate that connects the vapor with the liquid phase. For now, let us assume that we have such a coordinate, that we denote by q_1. The transition state separating the liquid from the vapor is denoted by q_1^*. The conventional definition for the characteristic functions is

$$\begin{aligned} n_A &= \theta(q_1^* - q_1), \\ n_B &= \theta(q_1 - q_1^*), \end{aligned} \tag{6.4}$$

where θ is the Heaviside function.

We then arrive at the following microscopic expression for the rate constant k_{AB} [67]:

$$k_{AB} = \frac{\langle \dot{q}_1 \delta(q_1 - q_1^*) \theta(q_1(t) - q_1^*) \rangle_{eq}}{\langle \theta(q_1^* - q_1) \rangle_{eq}} = M(t). \tag{6.5}$$

The time correlation function $M(t)$ explicitly depends on time, whereas k_{AB} does not. Hence, the above equation is only valid if and when $M(t)$ reaches a plateau value, after an initial transitory period.

In transition state theory it is assumed that all trajectories that have crossed the top of the free-energy barrier, proceed to the final state and do not recross the barrier to the initial state. This implies that all trajectories that initially head from the top of the barrier to a given state, will end up in that state. The crossing rate that corresponds to this situation can be obtained by taking the limit $t \to 0^+$ in the expression for the transition rate in Eq. (6.5):

$$k_{TST} = \lim_{t \to 0^+} M(t) = \frac{\langle |\dot{q}_1^*| \rangle_{eq}}{2} \frac{\langle \delta(q_1 - q_1^*) \rangle_{eq}}{\langle n_A \rangle_{eq}} = \frac{\langle |\dot{q}_1^*| \rangle_{eq}}{2} P_o(q_1^*). \tag{6.6}$$

It is seen that k_{TST} is the product of two contributions. The first contribution is the average flux of trajectories over the top of the barrier, and the second contribution is the relative probability for the system to be at the top of the barrier. The probability density for the system to be at the top of the barrier, divided by the probability that it is in the vapor state is given by

$$P_o(q_1^*) = \frac{e^{-\beta F(q_1^*)}}{\int_0^{q_1^*} dq_1' e^{-\beta F(q_1')}}. \tag{6.7}$$

Only the trajectories that are in the initial state at time $-t$ and in the final state at time t, contribute to the transition rate. Those trajectories that recross the barrier do not contribute. It is conventional to express the reduction of k_{AB} due to recrossing in terms of the transmission coefficient κ, defined as

$$\kappa = \frac{k_{AB}}{k_{TST}}. \tag{6.8}$$

Ruiz-Montero *et al.* derived a general expression for the rate constant by studying the response of the system to an initial perturbation [69]. They found:

$$\begin{aligned} M(t) &\equiv \frac{\langle n_B \rangle_{eq}}{\langle \Delta n_A \Delta \chi \rangle_{eq}} \langle \dot{q}_1 \chi'(q_1) n_A(t) \rangle_{eq} \\ &= k_{AB}. \end{aligned} \tag{6.9}$$

Here n_A and n_B are again the characteristic functions and χ is the perturbation function that specifies the initial perturbation. The Bennett-Chandler expression (Eq. (6.5)) is recovered by taking for both the perturbation function and the characteristic functions a step-function. However, we have considerable freedom in our choice for both functions. This is important, because Eq. (6.5) is less useful for diffusive barrier crossings [69].

One of the main problems is that a θ-function perturbation does not prepare the system in the steady-state initially. When the initial perturbation is a step-function, we increase the probability of state A and decrease the probability of state B by the same amount. The steady-state, however, corresponds to a much smoother probability distribution. Hence, the system first has to relax to the steady-state, a process which in the case of diffusive barrier crossings can be slow. We can eliminate this problem by initially preparing the system such that it is already close to the steady state. This can be accomplished by taking the following form for the initial perturbation function [69]

$$\chi(q_1) = 1 + \epsilon(q_{1A}) \left[1 - \frac{\int_{q_{1A}}^{q_1} dq_1' e^{\beta F(q_1')}}{\int_{q_{1A}}^{q_{1B}} dq_1' e^{\beta F(q_1')}} \right]. \tag{6.10}$$

Still, we can do better. We are also free to choose other characteristic functions for n_A and n_B, as long as they only differ in the regions of configuration space that contribute negligibly to the equilibrium averages. This means that we can choose other functional forms for n_A and n_B near the top of the barrier, but not in state A or state B. We will therefore use functions that behaves like the Heaviside functions in state A and B, but vary more smoothly near the top of the barrier. The advantage is that a continuous function that varies smoothly can be expected to yield much better statistics than a step-function [69]. The characteristic functions are given by

$$n_A(q_1) = 1 - \frac{\int_{q_{1A}}^{q_1} dq_1' e^{\beta F(q_1')}}{\int_{q_{1A}}^{q_{1B}} dq_1' e^{\beta F(q_1')}} \tag{6.11}$$

and $n_B(q_1) = 1 - n_A(q_1)$.

We have computed the transmission coefficient κ in four different ways, that differ from each other in the choice for the perturbation function and the form of the characteristic function. In Fig. 6.1 we show the different functions. In the Appendix we give a derivation of the expressions for the transmission coefficients that we used in the simulations. Below we list the results:

1. The conventional way of computing the transmission coefficient. Both the initial perturbation and the characteristic function are a Heaviside function:

$$\chi(q_1) = \theta(q_1^* - q_1)/\langle \theta(q_1^* - q_1) \rangle_{eq}, \tag{6.12}$$

$$n_A(q_1) = \theta(q_1^* - q_1). \tag{6.13}$$

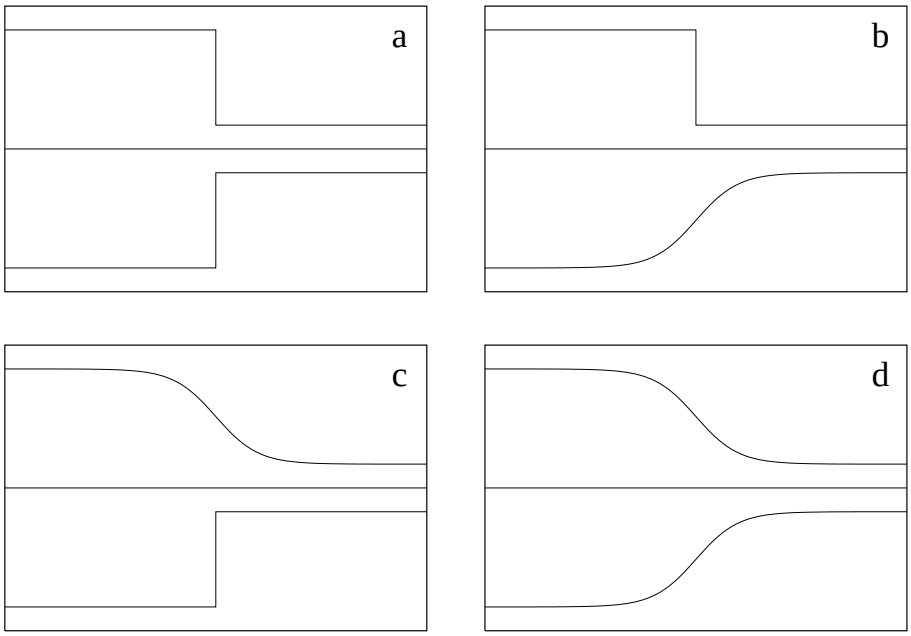

FIGURE 6.1 Sketch of the the perturbation functions and the characteristic functions. The subfigures (a) to (d) correspond to the transmission coefficients κ_1 to κ_4, defined in Eqs. (6.14)–(6.23), respectively. In the subfigures, the top panel shows the perturbation function $\chi(q_1)$ and the bottom panel shows the characteristic function $n_B(q_1) = 1 - n_A(q_1)$.

Combining Eq. (6.5) with Eq. (6.8) and using the fact that $\langle A(q_1)\delta(q_1 - q_1^*)\rangle_{eq} = \langle A\rangle_c\langle\delta(q_1 - q_1^*)\rangle_{eq}$, where the subscript c indicates that the average is over states constrained at the top of the barrier, we obtain the following expression for κ:

$$\kappa_1(t) = \langle\dot{q}_1\theta(q_1(t) - q_1^*)\rangle_c \frac{2}{\langle|\dot{q}_1^*|\rangle_{eq}}. \tag{6.14}$$

2. The initial perturbation is still a Heaviside function, but the characteristic function is now a function that behaves like the Heaviside function in state A and state B, but behaves more smoothly near the top of the barrier:

$$\chi(q_1) = \theta(q_1^* - q_1)/\langle\theta(q_1^* - q_1)\rangle_{eq}, \tag{6.15}$$

$$n_A(q_1) = 1 - \frac{\int_{q_{1A}}^{q_1} dq_1' e^{\beta F(q_1')}}{\int_{q_{1A}}^{q_{1B}} dq_1' e^{\beta F(q_1')}}. \tag{6.16}$$

This yields for the transmission coefficient

$$\kappa_2(t) = \frac{\int_0^t dt'\langle\dot{q}_1(0)\dot{q}_1(t')e^{\beta F(q_1(t'))}\rangle_c}{\int_{q_{1A}}^{q_{1B}} dq_1' e^{\beta F(q_1')}} \frac{2}{\langle|\dot{q}_1^*|\rangle_{eq}}. \tag{6.17}$$

3. The initial perturbation is the smooth function, but the characteristic function is still the Heaviside function:

$$\chi(q_1) = 1 + \epsilon(q_{1A}) \left[1 - \frac{\int_{q_{1A}}^{q_1} dq_1' e^{\beta F(q_1')}}{\int_{q_{1A}}^{q_{1B}} dq_1' e^{\beta F(q_1')}} \right], \tag{6.18}$$

$$n_A(q_1) = \theta(q_1^* - q_1). \tag{6.19}$$

The starting points for the simulations to compute the transition rate are not states at the top of the barrier, but near the top of the barrier, obtained from a biased ensemble with weighting function w. The expression for the transmission coefficients is obtained by combining Eq. (6.57) of the appendix with Eq. (6.8):

$$\kappa_3(t) = \frac{\langle \dot{q}_1(0) e^{\beta F(q_1(0))} n_B(t) w^{-1}(q_1) \rangle_w}{\int_{q_{1A}}^{q_{1B}} dq_1' e^{\beta F(q_1')}} \frac{\langle w \rangle_{eq}}{\langle \delta(q_1 - q_1^*) \rangle_{eq}} \frac{2}{\langle |\dot{q}_1^*| \rangle_{eq}}. \tag{6.20}$$

4. Both the initial perturbation and the characteristic function are smooth near the top of the barrier:

$$\chi(q_1) = 1 + \epsilon(q_{1A}) \left[1 - \frac{\int_{q_{1A}}^{q_1} dq_1' e^{\beta F(q_1')}}{\int_{q_{1A}}^{q_{1B}} dq_1' e^{\beta F(q_1')}} \right], \tag{6.21}$$

$$n_A(q_1) = 1 - \frac{\int_{q_{1A}}^{q_1} dq_1' e^{\beta F(q_1')}}{\int_{q_{1A}}^{q_{1B}} dq_1' e^{\beta F(q_1')}}. \tag{6.22}$$

Again the starting points for the computation of the flux are taken from a weighted ensemble. The expression for the transmission coefficient is found from Eq. (6.62) of the appendix and Eq. (6.8):

$$\kappa_4(t) = \frac{\int_0^t dt' \langle \dot{q}_1(0) e^{\beta F(q_1(0))} \dot{q}_1(t') e^{\beta F(q_1(t'))} w^{-1}(q_1) \rangle_w}{\left[\int_{q_{1A}}^{q_{1B}} dq_1' e^{\beta F(q_1')} \right]^2} \frac{\langle w \rangle_{eq}}{\langle \delta(q_1 - q_1^*) \rangle_{eq}} \frac{2}{\langle |\dot{q}_1^*| \rangle_{eq}}. \tag{6.23}$$

The nucleation rate is given by $k_{AB} = \kappa k_{TST}$. In order to compute k_{TST} we have to know the (relative) probability $P_o(q_1^*)$ of finding the system at the top of the barrier. In chapter 5 we have used umbrella sampling [26] to calculate the free-energy barrier and hence, $P_o(q_1^*)$ (see Eq. (6.7)). In the present chapter we simply use the result of chapter 5 for the barrier height and use this as a starting point for the computation of the transmission coefficient. We have performed molecular dynamics (MD) simulations to calculate the transmission coefficient in the four different ways described above. The starting configurations for these calculations were obtained from an umbrella-sampling simulation near the top of the barrier. Configurations exactly at the top of the barrier, needed to compute κ_1 and κ_2, were also obtained from these simulations. We stress that our computational scheme obviates the need to perform constrained MD-simulations at the top of barrier [30].

6.3 Details of the simulations

In order to calculate the nucleation rate we have to define a reaction coordinate that monitors the progress of the transition. We have considerable freedom in our choice for

the reaction coordinate. Although both the relative probability for the system to be at the top of the barrier, and the flux over the top of the barrier do depend on the choice for the reaction coordinate, the rate, which is the product of the two, does not [69]. Nevertheless, in practice it is convenient to use a local order parameter, rather than a global order parameter, such as the density of the system. The reason is that, under certain conditions, it can be entropically favorable to distribute a given amount of the new phase over many small nuclei instead of over a single large cluster (see chapter 4). In the nucleation process we are only interested in the largest liquid cluster. We therefore define the number of particles in this cluster as our reaction coordinate. To identify the particles that constitute the largest cluster, we used a geometric cluster criterion, that is derived from the one proposed by Stillinger [110]. Particles that have a significantly higher local density than the particles in the remainder of the system are identified as "liquidlike" particles. All liquidlike particles that are less than $q_c = 1.5\sigma$ apart, are considered to be connected and, therefore, belong to the same cluster. For more details, see chapter 5.

All MD-simulations were performed in the isobaric-isothermal (NPT) ensemble. To control the pressure and temperature we employed the extended system method proposed by Andersen [138] and Nosé [139]. The algorithm to integrate the equations-of-motion was derived by a Trotter factorization of the Liouville operator [140]. The reversible integrator is similar to the algorithm recently developed by Martyna *et al.* [141]. We used a time-step of 0.01τ, where $\tau = \sigma\sqrt{\epsilon/m\sigma^2}t$ is the unit of time, with m the mass, σ the Lennard-Jones diameter and ϵ the Lennard-Jones well depth. In what follows, we use reduced units, such that the Lennard-Jones well depth ϵ is the unit of energy and the Lennard-Jones diameter σ is the unit of length.

In order to calculate the transition rate, we performed umbrella simulations near the top of the barrier to generate a sequence of uncorrelated configurations. These configurations were used as initial states for the computation of the transmission coefficients in Eqs. (6.14)-(6.23). For every calculation we used 300 independent configurations. At the beginning of the unconstrained runs, all particles were given a velocity drawn from a Maxwell-Boltzmann distribution. Furthermore, we made use of the time-reversal property $\kappa(\tau) = -\kappa(-\tau)$. This means that every initial configuration was not only propagated forwards in time, but also backwards. Hence, the results that we present here were averaged over 600 trajectories.

We computed the rate of nucleation of the Lennard-Jones system under the conditions studied in chapter 5. The interaction potential was truncated and shifted at a cutoff radius $r_c = 2.5\sigma$, where σ is the Lennard-Jones particle diameter. We made no long-range correction and applied cubic periodic boundary conditions. The number of particles was $N = 864$.

6.4 Results

We have calculated the transition rate for homogeneous gas-liquid nucleation in a Lennard-Jones system at $T = 0.741$ and $P = 0.012$, corresponding to a supersaturation $S = P/P_{coex} = 1.53$. Under these conditions, the barrier height is $\beta\Delta G^* = 59.4 \pm 0.6$. We computed the transmission coefficient in four different ways, according to Eqs. (6.14)–(6.23). Figs. 6.2–6.5 show the results. First, we discuss the different ways of computing

the transmission coefficients. Next, we make a comparison with classical nucleation theory.

6.4.1 Transmission coefficient
Comparison of characteristic functions and perturbation functions

Fig. 6.2 shows the transmission coefficient, as defined in Eq. (6.14). Here we have computed the transmission coefficient in the conventional way: both the initial perturbation and the characteristic function are Heaviside functions. As explained, we expect that this perturbation gives rise to a transitory regime, in which the system relaxes to the steady-state. Indeed, as can be seen from Fig. 6.2, the transmission coefficient initially drops from the value $\kappa = 1$ at $t = 0$. This is due to recrossings. Only after a fairly long transitory period, the transmission coefficient reaches a plateau value. It also seen that the initial decay is very rapid and that the plateau value is very small. This indicates that the nucleation process is highly diffusive. A direct analysis of the trajectories support this view: the system stays close to the top of the barrier and does not end up in either minimum (gas or liquid one) during the run.

It is also clear from Fig. 6.2 that the statistical noise is large, even though averages were taken over 600 trajectories. A smoother characteristic function should increase the statistical accuracy. This is illustrated in Fig. 6.3. In this case the characteristic function is not the Heaviside-function, but the function in Eq. (6.16). This function behaves like the Heaviside function in the vapor and liquid state, but changes more smoothly near the top of the barrier. We found that this choice of the characteristic function decreases the error bar by a factor seven.

However, the drawback is that we have not prepared the system close to the steady state situation. For diffusive barrier crossings, the approach to the stationary state can be slow. Moreover, it is conceivable that the transmission coefficient *appears* to have reached a plateau value, but that in fact, it has not, due to the slow dynamics at the top

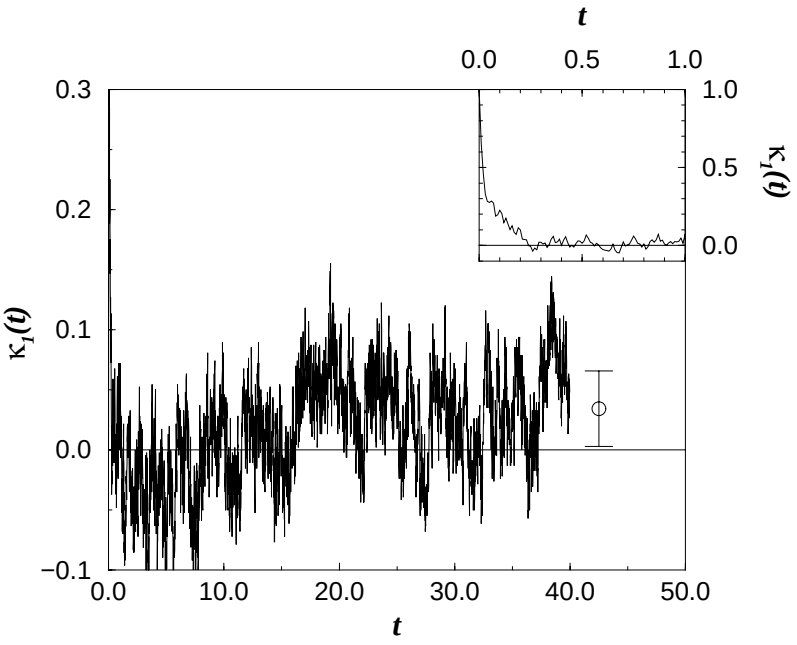

FIGURE 6.2 Transmission coefficient as a function of time for homogeneous gas-liquid nucleation in a Lennard-Jones system at a supersaturation $S = 1.53$ ($T = 0.741$, $P = 0.012$). The transmission coefficient is computed via Eq. (6.14). The plateau value is $\kappa = 0.03 \pm 0.03$. Here, and in subsequent figures, the reported estimate is based on the plateau value of κ at $20 < t < 40$.

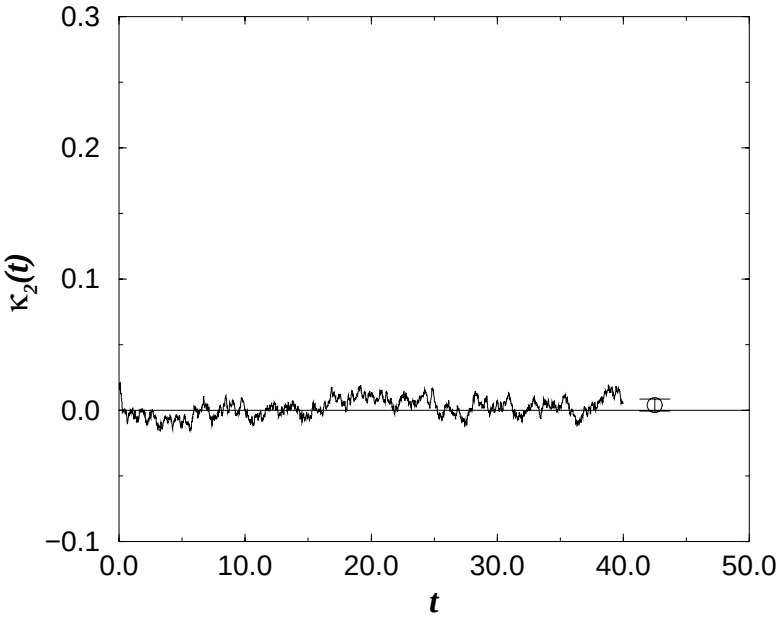

FIGURE 6.3 Transmission coefficient as a function of time for homogeneous gas-liquid nucleation in a Lennard-Jones system at a supersaturation $S = 1.53$ ($T = 0.741$, $P = 0.012$). The transmission coefficient is computed via Eq. (6.17) and is found to be $\kappa = 0.004 \pm 0.004$.

of the barrier. It is therefore advisable to prepare the system close to the steady state. To this end, we choose as the initial perturbation not a step-function, but the function given in Eq. (6.18). The result is shown in Fig. 6.4. We see that the transient regime is suppressed and that the transmission coefficient reaches its plateau value immediately. This shows that indeed the system is already close to the steady-state situation initially.

In Fig. 6.5 we show the transmission coefficient computed via Eq. (6.23). Now both the initial perturbation and the characteristic function are Heaviside-like functions that, however, vary continuously near the top of the barrier. We see that in comparison with Fig. 6.4 the error bar is slightly reduced and we use the value for κ_4 to estimate the

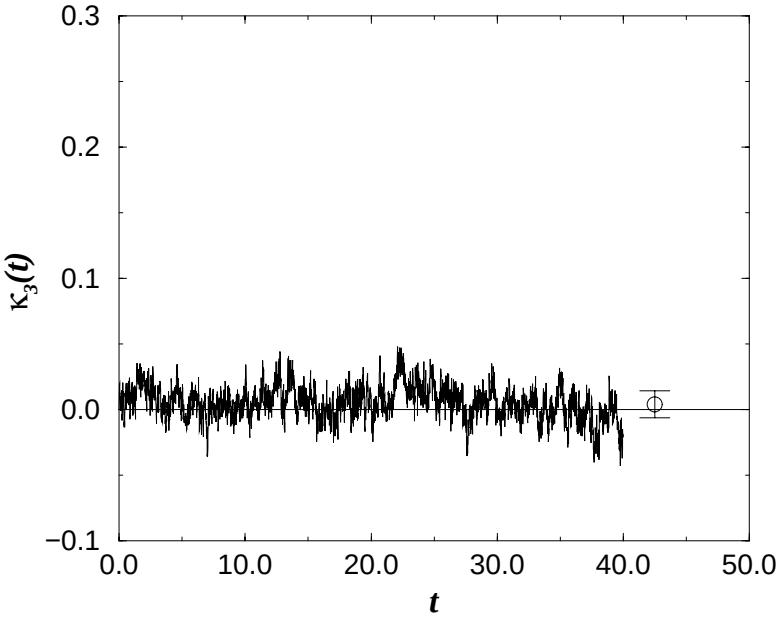

FIGURE 6.4 Transmission coefficient as a function of time for homogeneous gas-liquid nucleation in a Lennard-Jones system at a supersaturation $S = 1.53$ ($T = 0.741$, $P = 0.012$). The transmission coefficient is computed via Eq. (6.20). We find $\kappa = 0.004 \pm 0.01$.

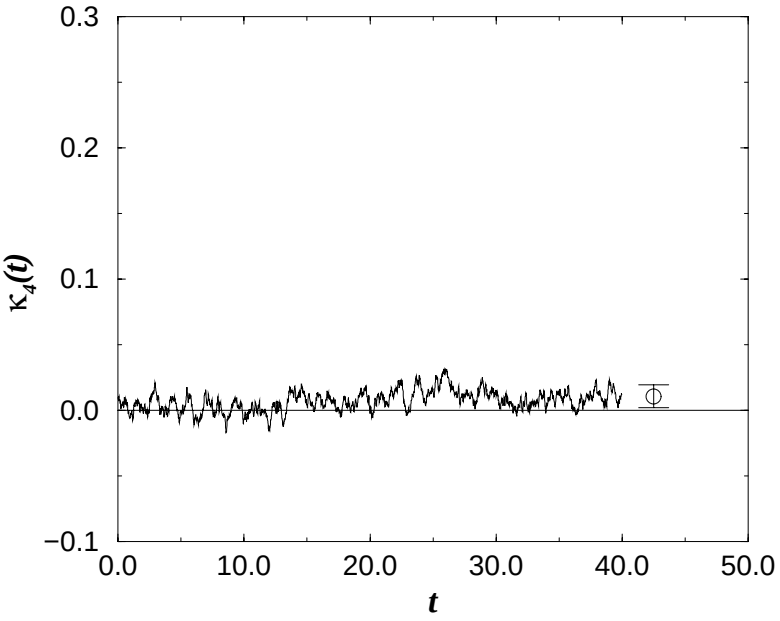

FIGURE 6.5 Transmission coefficient as a function of time for homogeneous gas-liquid nucleation in a Lennard-Jones system at a supersaturation $S = 1.53$ ($T = 0.741$, $P = 0.012$). The transmission coefficient is computed via Eq. (6.23) and is found to be $\kappa = 0.011 \pm 0.009$.

nucleation rate. We find $\kappa_4 = 0.011\tau^{-1} \pm 0.009\tau^{-1}$. This estimate is based on the plateau value of κ_4 at $20 < t < 40$. However, κ_4 appears to approach a constant value much sooner. This allows us to discard the long-time data that contribute little to the signal, but much to the noise. If we compute the plateau value of κ_4 for $2.5 < t < 10$, we find $\kappa_4 = 0.002 \pm 0.004$. At first sight this is a disappointing result: the error in the transmission coefficient is nearly 100%. However, we know that κ must be positive. Moreover, we stress that an error of one k_BT in the calculation of the barrier height leads to a larger error in the estimate of the nucleation rate. Still, in order to obtain a better estimate for the transmission coefficient, we performed additional simulations to determine κ_4. To this end we extracted 200 extra configurations from the umbrella-sampling simulation near the top of the barrier. Furthermore, we used every starting configuration not once (or actually twice as every configuration is propagated backwards and forwards in time), but ten times (or twenty times), by assigning different initial velocities to the same configuration. We thus averaged over 10000 trajectories. The result is $\kappa_4 = 0.003 \pm 0.002$, which is close to the previous result. Although the error in the transmission coefficient is still nearly 100%, it is much smaller than can be obtained with any other technique and, to our knowledge, much smaller than the error in any other computed transmission coefficient reported in the literature. Another test to verify if the result that we obtain is of the same order of magnitude, is to fit the short-time behavior of the correlation function in Eq. (6.23) to an exponential. Although the fit to an exponential is less than perfect (the actual correlation function decays faster), its integral is again of the same order of magnitude ($\kappa_4 = 0.013 \pm 0.002$).

To obtain the full nucleation rate, we can combine the value of the transmission coefficient with the prediction of transition-state theory (TST) for the crossing rate (see Eq. (6.8)). The TST-prediction is the product of the average probability for the system to be at top of the barrier and the rate at which this barrier is crossed. From the measured nucleation barrier (see chapter 5) we find that the relative probability for the system to be at the top of the barrier is $P_o = 1.63 \times 10^{-26}$. The average

Compound	k_{AB} ($\mathrm{cm^{-3}s^{-1}}$)	T (K)	P (kPa)
Ar	4.05e+05	88.88	503
Kr	2.68e+05	127	607
N2	3.09e+05	70.5	311
CH4	4.50e+05	110	442
CF4	8.49e+04	113	243
CCl4	3.84e+04	242	266
SF6	4.00e+04	149	199

TABLE 6.1 Nucleation rates k_{AB} for a number of apolar compounds, as deduced from the simulations. The values for ϵ and σ are taken from Ref. [142]. In order to facilitate a comparison with experiments we also give the temperatures T (in Kelvin) and pressures P (in kPa).

of the absolute value of the velocity of the order parameter at the top of the barrier is $\langle|\dot{q}_1|\rangle = 76.2\tau^{-1}$. Hence, the rate in the transition-state theory approximation is $k_{TST} = 6.22 \times 10^{-25}\tau^{-1}$. From k_{TST} and the transmission coefficient we get the full nucleation rate $k_{AB} = k_{TST}\kappa = 1.8 \times 10^{-27}\tau^{-1}$.

The rates found from our simulations are measured in number of nuclei per unit time. Experimental nucleation rates are often expressed as the number of nuclei formed per unit volume per unit time. To obtain such a quantity we note that

$$\begin{aligned} k = \kappa k_{TST} &= C_s \frac{\langle\delta(q - q_1^*)\rangle_{eq}}{\langle n_A\rangle_{eq}}, \\ &= C_s \frac{N(n^*)}{\sum_{n=0}^{n=n^*} N(n)}, \\ &= C_s \frac{e^{-\beta\Delta G(n^*)}}{\sum_{n=0}^{n=n^*} e^{-\beta\Delta G(n)}}. \end{aligned} \tag{6.24}$$

Here N is the total number of particles, $N(n)$ is the number of nuclei of size n and we have used that $\beta\Delta G(n) \equiv -\ln[N(n)/N]$. Note that the kinetic prefactor is given by $C_s = \kappa\langle|\dot{q}_1|\rangle_{eq}/2$. If we now multiply the above expression with $\rho_v \sum_{n=0}^{n=n^*} e^{-\beta\Delta G(n)}$, where ρ_v is the density in the vapor, we find

$$k = C_s \rho_v e^{-\beta\Delta G(n^*)}. \tag{6.25}$$

This expression for the nucleation rate yields the number of liquid particles produced per unit volume per unit time. It can be interpreted as the number density of nuclei at the top of the barrier, multiplied with the net rate C_s at which these nuclei gain particles. We find from the simulations that $C_s = 0.11 \pm 0.08$, $\rho_v = 0.0188 \pm 0.0005$ and $\beta\Delta G(n^*) = 59.4 \pm 0.6$. Hence, we finally obtain for the rate of nucleation $k = 3.5 \times 10^{-29}\sigma^{-3}\tau^{-1}$.

To our knowledge, there is a scarcity of quantitative data on nucleation in spherical, non-polar fluids, such as argon. However, in order to facilitate a future comparison of our data with experimental data, we have converted the rate constant to experimental units, i.e. units of number of nuclei formed per $\mathrm{cm^3}$ per s. We have done this for a variety of compounds that obey the principle of corresponding states. Table 6.1 shows the results. It is interesting to note that in recent experiments by Strey *et al.* on a variety of compounds [15]-[136], the measured nucleation rates were of the same order of magnitude. This illustrates that it is indeed possible to use simulation to predict nucleation rates under conditions that are typical of real experiments.

6.4.2 Comparison with classical nucleation theory

In classical nucleation theory (CNT), the rate of nucleation is given by [7]

$$k_{CNT} = Z f_e(n^*)\rho(1)e^{-\beta\Delta G(n^*)}. \tag{6.26}$$

It is seen that the rate is the product of three factors:

1. $\rho(1)e^{-\beta\Delta G(n^*)}$, where $\rho(1)$ is the number density of monomers in the supersaturated vapor and $\Delta G(n^*)$ is the height of the nucleation barrier. $\rho(1)e^{-\beta\Delta G(n^*)}$ is the concentration of nuclei that have reached the critical size. In classical nucleation theory the height of the nucleation barrier is given by

   $$\Delta G^* = \frac{16\pi\gamma^3}{3\rho_l^2\Delta\mu^2}, \tag{6.27}$$

   where γ is the surface tension of a planar interface, ρ_l is the density of a bulk liquid (which is assumed to be incompressible) and $\Delta\mu$ is the difference in chemical potential between the bulk vapor and the bulk liquid, both at the supersaturation pressure P in the vapor phase

   $$\Delta\mu = \mu_v(P) - \mu_l(P). \tag{6.28}$$

   The CNT prediction for the size of the critical nucleus is

   $$n^* = \frac{32\pi\gamma^3}{3\rho_l^2\Delta\mu^3}. \tag{6.29}$$

   In chapter 5 we compared the measured barrier height and critical nucleus size with the corresponding predictions of classical nucleation theory for various values of the supersaturation. We found that the classical nucleation theory predicts the size of the critical nuclei surprisingly well ($n^*_{CNT} = 338$ compared to $n^*_{sim} = 336$), and that the difference between the actual barrier height and the CNT prediction is independent of supersaturation. For $T = 0.741$ the barrier height found in the simulations differs by a constant offset of $5k_BT$ from the value predicted by CNT.
2. $f_e(n^*)$. $f_e(n)$ is, at coexistence, the forward rate at which a cluster of size n grows by one monomer; $f_e(n^*)$ is the rate at which critical nuclei cross the barrier. The rate at which particles impinge on the surface of a nucleus of size n is given by

   $$f_e(n) = A(n)qn_{1,e}\langle|v|\rangle/4 \tag{6.30}$$

   Here $A(n)$ is the surface area of the nucleus, q is the condensation coefficient, which is the fraction of monomers hitting the surface that actually stick, $n_{1,e}$ is the monomer density at coexistence and $\langle|v|\rangle$ is the mean molecular speed. If we assume that the gas is ideal, then the monomer concentration at the saturation (coexistence) pressure P_e is reduced from its value $\rho(1)$ at the supersaturation pressure P by a factor $S = P/P_e$, i.e. $n_{1,e} = \rho(1)/S$. For an ideal gas, the mean velocity is

   $$\langle|v|\rangle = \sqrt{\frac{8k_BT}{\pi m_1}}, \tag{6.31}$$

where m_1 is the mass of monomers. Furthermore, in classical nucleation theory it is assumed that the nuclei are spherical, yielding for the surface area:

$$A(n) = \left(\frac{36\pi}{\rho_l^2}\right)^{1/3} n^{2/3}. \tag{6.32}$$

Combining the above equations yields for the forward rate $f_e(n^*)$

$$f_e(n^*) = A(n^*)q(\rho(1)/S)\sqrt{k_B T/2\pi m_1}. \tag{6.33}$$

3. Z, the Zeldovich factor, which relates the number of critical nuclei in the equilibrium distribution to the number of critical nuclei in the steady-state distribution. It is given by

$$Z = \sqrt{Q/2\pi k_B T}, \tag{6.34}$$

where

$$Q \equiv -\left[\frac{\partial^2 \Delta G}{\partial n^2}\right]_{n^*} \tag{6.35}$$

is the second derivative of the free-energy with respect to cluster size n at the top of the barrier. Using the expression of classical nucleation theory for ΔG we get

$$Z = \sqrt{\frac{\Delta\mu}{6\pi k_B T n^*}} \tag{6.36}$$

The Zeldovich factor takes into account that not all nuclei that have reached the top actually cross it and end up in the liquid state. We find that $Z = 0.0066$. The low value of the Zeldovich factor reflects the fact that the barrier crossing is a diffusive rather than a ballistic process. It is this diffusive behavior which leads to recrossing and to a reduction of the transmission coefficient $\kappa(t)$.

Using the above expressions for f_e and Z we obtain for k_{CNT}

$$k_{CNT} = \sqrt{\frac{2\gamma}{\pi m_1}}\frac{q\rho(1)}{S\rho_l}\rho(1)e^{-\beta\Delta G(n^*)} \equiv C_{CNT}\rho(1)e^{-\beta\Delta G(n^*)}, \tag{6.37}$$

where C_{CNT} is the kinetic prefactor. The number density of monomers can be well approximated by the total number density ρ_v. Hence, in order to compare the kinetic prefactor of classical nucleation theory with the kinetic prefactor as obtained from the simulations, we should compare C_{CNT} and C_s, as defined in Eq. (6.24). The surface tension for the planar interface is $\gamma = 0.494$ and the density of the bulk liquid is $\rho_l = 0.766$. The density in the vapor is $\rho_v = 0.0188$ and the supersaturation $S = 1.53$. Furthermore, we assume that the sticking coefficient is one. Hence, the prediction of CNT for the kinetic prefactor is $C_{CNT} = 0.009$. The simulations yielded $C_{sim} = 0.11 \pm 0.08$. Considering the magnitude of the error in the simulation result, we can only make an order of magnitude comparison with the prediction of CNT. We find that the measured kinetic prefactor is about a factor 10 larger than predicted by CNT. An explanation could be that the actual area of the droplet is larger than the area of a sphere with the same number of particles as in the droplet. CNT also assumes that the critical nucleus grows by uncorrelated collisions of "freely" moving gas particles with the cluster. It is likely that the overall impingement rate of gas monomers is larger because of the attraction of the vapor particles by the cluster.

Appendix Transmission rates for diffusive barrier crossings

To compute the transition rate, we study the response of the system to an, as yet unspecified, perturbation. We first define the response function $\phi(t)$:

$$\phi(t) \equiv \frac{\Delta P_A(t)}{\Delta P_A(0)}, \tag{6.38}$$

where $\Delta P_A(t)$ is the deviation of $P_A(t) = \langle n_A(t) \rangle$, which is the probability of finding the system in state A at time t, from its equilibrium value,

$$\Delta P_A(t) = P_A(t) - P_{A,eq} = \langle \Delta n_A(t) \rangle, \tag{6.39}$$

with

$$\Delta n_A = n_A - \langle n_A \rangle_{eq}. \tag{6.40}$$

We now impose a perturbation, denoted by the perturbation function $\chi(q_1)$, such that the initial distribution function $\rho(\mathbf{q}(0); \mathbf{p}(0))$ (with $\mathbf{q}(0)$ and $\mathbf{p}(0)$ the phase space coordinates at $t = 0$) is of the form

$$\rho(q(0), p(0)) = \rho_{eq} \chi(q_1). \tag{6.41}$$

The response of the system is then given by [69]

$$\phi(t) = \frac{\langle \Delta n_A(0) \Delta \chi(t) \rangle_{eq}}{\langle \Delta n_A \Delta \chi \rangle_{eq}}. \tag{6.42}$$

Its time-derivative is

$$\frac{d\phi}{dt} = -\frac{\langle \dot{q}_1 \chi'(q_1) n_A(t) \rangle_{eq}}{\langle \Delta n_A \Delta \chi \rangle_{eq}}. \tag{6.43}$$

If we assume that the relaxation is exponential, i.e.,

$$\phi(t) = e^{-t/\tau}, \tag{6.44}$$

we find

$$\frac{1}{\tau} e^{-t/\tau} = \frac{\langle \dot{q}_1 \chi'(q_1) n_A(t) \rangle_{eq}}{\langle \Delta n_A \Delta \chi \rangle_{eq}}. \tag{6.45}$$

If we are in a time-regime $t << \tau$, we have

$$\tau^{-1} = \frac{\langle \dot{q}_1 \chi'(q_1) n_A(t) \rangle_{eq}}{\langle \Delta n_A \Delta \chi \rangle_{eq}} = \frac{k_{AB}}{\langle n_B \rangle_{eq}}, \tag{6.46}$$

where k_{AB} is the rate constant. This leads to the following microscopic expression for k_{AB}:

$$\begin{aligned} M(t) &\equiv \frac{\langle n_B \rangle_{eq}}{\langle \Delta n_A \Delta \chi \rangle_{eq}} \langle \dot{q}_1 \chi'(q_1) n_A(t) \rangle_{eq} \\ &= k_{AB}. \end{aligned} \tag{6.47}$$

The time correlation function $M(t)$ explicitly depends on time, whereas k_{AB} does not. Hence, the above equation is only valid if and when $M(t)$ reaches a plateau value, after an initial transitory period.

We can now make several choices for both the initial perturbation and the characteristic function. First, we take for the characteristic function $n_A(q_1) = \theta(q_1^* - q_1)$ and for the perturbation $\chi(q_1)$

$$\chi(q_1) = \alpha n_A(q_1), \tag{6.48}$$

where $\alpha = 1/\langle n_A \rangle_{eq}$, which follows from the normalization condition. From this we obtain

$$k_{AB} = \frac{\langle \dot{q}_1 n_B' n_B(t) \rangle}{\langle n_A \rangle_{eq}} \equiv M(t). \tag{6.49}$$

As the characteristic function is a Heaviside function, we arrive at the following expression for the rate:

$$k_{AB} = \frac{\langle \dot{q}_1 \delta(q_1 - q_1^*) \theta(q_1(t) - q_1^*) \rangle_{eq}}{\langle n_A \rangle_{eq}} \equiv M(t). \tag{6.50}$$

We will now impose a different initial perturbation. Following Ref. [69], we write the initial perturbation as

$$\rho(q_1) = \rho_{eq}[1 + \epsilon(q_1)], \tag{6.51}$$

which means that $\chi = 1 + \epsilon(q_1)$. When the system is in the steady state, $\epsilon(q_1)$ is given by [69]

$$\epsilon(q_1) = \epsilon(q_{1A}) \left[1 - \frac{\int_{q_{1A}}^{q_1} dq_1' e^{\beta F(q_1')}}{\int_{q_{1A}}^{q_{1B}} dq_1' e^{\beta F(q_1')}} \right]. \tag{6.52}$$

Here q_{1A} and q_{1B} are the values of the reaction coordinate in the states A and B, respectively. If we impose this perturbation, we will increase the rate at which the system reaches the steady-state.

From Eq. (6.47) it follows that the rate is given by

$$k_{AB} = \frac{1}{\epsilon(q_{1A}) \langle n_A \rangle_{eq}} \langle \dot{q}_1(0) \epsilon'(q_1(0)) n_A(t) \rangle_{eq}, \tag{6.53}$$

where we have used that $n_A(q_1) \approx \epsilon(q_1)/\epsilon(q_{1A})$, and $\langle \Delta n_A \Delta n_A \rangle_{eq} = \langle n_A \rangle_{eq} \langle n_B \rangle_{eq}$. We can obtain the derivative of $\epsilon(q_1)$ from Eq. (6.52). Furthermore, noticing that $n_B(t) = 1 - n_A(t)$ and that $\langle \dot{q}_1(0) \epsilon'(q_1(0)) \rangle = 0$, we find for the rate:

$$k_{AB} = \frac{\langle \dot{q}_1(0) e^{\beta F(q_1(0))} n_B(t) \rangle_{eq}}{\int_{q_{1A}}^{q_{1B}} dq_1' e^{\beta F(q_1')} \langle n_A \rangle_{eq}}. \tag{6.54}$$

As pointed out in Ref. [69], this average can be understood as a biased average, in which the constraining term is not a delta-function, but a function that has the width of the barrier. If we take the starting points from the ensemble with a biasing function $e^{\beta F(q_1)}$, then all points will be distributed almost uniformly over the entire range of q_1, as the biasing function will exactly compensate the effect of the free-energy barrier. We do not always know the precise shape of the barrier. However, this is not really important, because the main contribution to the average comes from simulations starting in the barrier region. We therefore impose a biasing potential that ensures that the initial points are near the top of the barrier. In Ref. [69] the optimal choice for the biasing

potential is discussed in some detail. We have taken our biasing potential to be a harmonic function

$$W(q_1) = \frac{1}{2}k(q_1 - q_1^*)^2. \tag{6.55}$$

We now have to correct for the biasing. We note that, in general, the average of a quantity A in the original, equilibrium ensemble, is related to the average $\langle A\rangle_w$ in the weighted ensemble, via

$$\langle A\rangle_{eq} = \frac{\langle Aw^{-1}\rangle_w}{\langle w^{-1}\rangle_w} = \langle Aw^{-1}\rangle_w \langle w\rangle_{eq}, \tag{6.56}$$

where w is the weighting function, which, in this case is $w(q_1) = e^{-\beta W(q_1)}$. Hence, the average in Eq. (6.54), becomes

$$k_{AB} = \frac{\langle \dot{q}_1(0) e^{\beta F(q_1(0))} n_B(t) w^{-1}(q_1)\rangle_w}{\int_{q_{1A}}^{q_{1B}} dq_1' e^{\beta F(q_1')} \langle n_A\rangle_{eq}} \langle w\rangle_{eq}. \tag{6.57}$$

We note that, when we know the shape of the barrier, the average of w in the equilibrium ensemble can easily be obtained via

$$\langle w\rangle_{eq} = \frac{\int_{q_{1A}}^{q_{1B}} dq_1' w(q_1) e^{-\beta F(q_1')}}{\int_{q_{1A}}^{q_{1B}} dq_1' e^{-\beta F(q_1')}}. \tag{6.58}$$

The advantage of the above biasing potential is that we shorten the transitory period. However, we can also improve the statistics in the steady-state regime. This can be accomplished by using a different form for the characteristic functions n_A and n_B. Instead of using Heaviside-functions, we take

$$n_A(q_1) = \frac{\epsilon(q_1)}{\epsilon(q_{1A})}. \tag{6.59}$$

Again, $n_B(q_1) = 1 - n_A(q_1)$, which gives

$$n_B(q_1) = \frac{\int_{dq_{1A}}^{dq_1} dq_1' e^{\beta F(q_1)}}{\int_{q_{1A}}^{q_{1B}} dq_1' e^{\beta F(q_1)}}. \tag{6.60}$$

As discussed in Ref. [69], n_A and n_B behave in much the same way as before, except for the barrier region, where it varies rapidly. That is, in region A $n_A \approx 1$, whereas in region B $n_A \approx 0$. However, we now measure a continuous function that varies smoothly, instead of counting "ones and zeros". This yields better statistics.

We can substitute the expression for n_B in Eq. (6.60) into Eq. (6.57). However, as the average of $\langle \dot{q}_1(0) e^{\beta F(q_1(0))} n_B(0) w^{-1}(q_1)\rangle_w$ vanishes, we only have to consider the change in n_B during time t:

$$n_B(t) - n_B(0) = \int_0^t dt' \dot{q}_1(t') \frac{\partial n_B(q_1(t'))}{\partial q_1} = \frac{\int_0^t dt' \dot{q}_1(t') e^{\beta F(q_1(t'))}}{\int_{q_{1A}}^{q_{1B}} dq_1' e^{\beta F(q_1)}}. \tag{6.61}$$

We then finally arrive at the following expression for the rate

$$k_{AB} = \frac{\int_0^t dt' \langle \dot{q}_1(0) e^{\beta F(q_1(0))} \dot{q}_1(t') e^{\beta F(q_1(t'))} w^{-1}(q_1)\rangle_w}{\left[\int_{q_{1A}}^{q_{1B}} dq_1' e^{\beta F(q_1')}\right]^2 \langle n_A\rangle_{eq}} \langle w\rangle_{eq}. \tag{6.62}$$

7 Gas-Liquid nucleation in partially miscible binary mixtures

We report a numerical study of homogeneous gas-liquid nucleation in a binary mixture. We study the size and the composition of the critical nucleus as a function of the composition and supersaturation of the vapor. As we make the (Lennard-Jones) mixture increasingly non-ideal, we find that there is a regime where the critical nucleus is still miscible in all proportions, even though the bulk liquid phase is not. When these critical nuclei grow, their composition "bifurcates" to approach the value of one of the two bulk phases. For more strongly non-ideal mixtures, the two species in the critical nucleus are no longer completely miscible: we observe droplets that are either rich in one species, or in the other. However, we do not find evidence for phase separation inside the critical nucleus - a scenario suggested by Talanquer and Oxtoby (J. Chem. Phys. **104***, 1993 (1996)). In fact, our simulations show that such demixed clusters have a higher free energy than critical nuclei that have an asymmetric composition.*

7.1 Introduction

Measurements of the rate of homogeneous gas-liquid nucleation provide increasingly precise and detailed information about the microscopic aspects of the nucleation process [15, 16, 50, 51, 94, 95, 136, 137]. From the measured nucleation rates, one can deduce the size and composition of the critical nuclei[56]. Such information makes it possible to test nucleation theories in much more detail than was hitherto possible. The experiments indicate that classical nucleation theory (CNT) works fairly well for one component systems of simple, non-polar molecules [50, 51]. In particular, CNT predicts the size of critical nuclei surprisingly well. However, for binary systems the agreement between the experimental observations and the predictions of CNT is worse [94, 95]. For non-ideal mixtures, CNT can even produce thermodynamic inconsistencies. Under certain conditions, CNT predicts that, at constant height of the nucleation barrier, the gas-phase activity of one component as a function of the activity of the other can have a positive slope. From the nucleation theorem [56] it would then follow that one of the two components has a negative concentration in the critical nucleus. Laaksonen and Oxtoby, who used density-functional theory to study nucleation in a mixture [143, 144], argue that the failure of CNT can be traced back to the fact that this theory does not predict the composition of the critical nucleus correctly.

Talanquer and Oxtoby [39] reported a more extensive study of the effect of composition and relative strength of the interactions on the nucleation behavior of a mixture. They studied gas-liquid nucleation in a binary mixture of Lennard-Jones particles and

found that, as expected, nearly ideal mixtures with positive (negative) deviations from ideal behavior require higher (lower) gas-phase activities for nucleation. However, for less ideal mixtures, they observed unexpected behavior. They found that in some cases, more than one type of critical nucleus could occur. In particular, they observed that nucleation of a mixture rich in the less volatile component can proceed via a nucleus that is poor in this component. More surprisingly, their theoretical analysis indicated that, under certain conditions, phase separation can take place inside the critical nucleus.

In this chapter we report a computer-simulation study of the same model system that was studied by Talanquer and Oxtoby [39]. We have developed a computational method, that allows us to efficiently compare critical clusters that correspond to the same height of the nucleation barrier. As the rate of nucleation is dominated by the height of this free-energy barrier, simulations at constant barrier height are comparable to experiments, in which the size and composition of critical nuclei are often studied at a fixed nucleation rate.

7.2 Contour of constant barrier height

At a given pressure, temperature and composition of the vapor, the excess free energy of a nucleus depends both on its size and on its composition. In the previous chapters, we have seen how, using the umbrella-sampling technique, we can stabilize not only critical, but also precritical (and postcritical) nuclei. In this way we can obtain information about the structure and free energy of these nuclei. In the present study we focus our attention mainly on the critical clusters, i.e. nuclei at the top of the free-energy barrier. At constant temperature, the height of the free-energy barrier depends both on the composition and the pressure of the vapor phase. However, as the nucleation rate is a very steep function of the barrier height, most experimental studies focus effectively on a narrow "window" of barrier heights. For this reason, we also look in our numerical simulation at the composition dependence of critical nuclei at constant barrier height. To achieve this, we adjust the pressure for every composition such that the barrier height is kept fixed at a given reference value. In principle, we could compute the full free-energy barrier to nucleation by the umbrella sampling technique, for a series of pressures in order to find the desired pressure for a given composition. However, even for only one composition and one pressure, computing the full free-energy curve is already quite time consuming. We therefore follow a different approach, which is close in spirit to the Gibbs-Duhem integration method to trace phase-coexistence curves [145].

We first compute the nucleation barrier for one pure component at a given pressure, using umbrella sampling. We then increase the activity fraction of the other component. In order to keep the height of the nucleation barrier constant, we have to adjust the pressure. Information about the required change in pressure can be obtained by simulating the system not only at the top of the barrier, but also in the metastable vapor phase. For both states we can determine how the free energy varies with the activity fraction and pressure. By setting the variation in free energy for both states equal, thus keeping the height of the barrier constant, we get a Clapeyron type of equation which yields a relation between the change in pressure with the change in activity fraction.

Let us make this approach more explicit. It will be convenient to work in the (isobaric) semi-grand ensemble. The Landau isobaric semi-grand free energy Y is the Legendre transform of the Landau Gibbs free energy G, which, for a binary system, is a function of the total number of particles N, the number of particles of species 2, N_2, the pressure P, the temperature T, and the order parameter n. The first differential of the Gibbs free energy is

$$\begin{aligned} dG(N, N_2, P, T, n) =& \mu_1(n)dN + (\mu_2(n) - \mu_1(n))dN_2 + V(n)dP + \\ & - S(n)dT + \left.\frac{\partial G}{\partial n}\right|_{N,N_2,P,T} dn, \end{aligned} \tag{7.1}$$

where μ_i is the chemical potential of species i, V is the volume and S is the entropy of the system. Now the semi-grand ensemble is obtained by a Legendre transformation between the variables N_2 and $(\mu_2 - \mu_1)$:

$$Y(N, \mu_2 - \mu_1, P, T, n) = G(N, N_2, P, T, n) - N_2(n)(\mu_2 - \mu_1), \tag{7.2}$$

or, in differential form

$$\begin{aligned} dY(N, \mu_2 - \mu_1, P, T, n) =& \mu_1(n)dN - N_2(n)d(\mu_2 - \mu_1) + \\ & V(n)dP - S(n)dT + \left(\frac{\partial Y}{\partial n}\right)_{N,P,T,\mu_2-\mu_1} dn. \end{aligned} \tag{7.3}$$

At constant temperature and number of particles Eq. (7.3) reduces to

$$dY(N, P, T, \mu_2 - \mu_1, n) = V(n)dP - N_2(n)d\Delta\mu + \left(\frac{\partial Y}{\partial n}\right)_{N,P,T,\Delta\mu} dn, \tag{7.4}$$

where $\Delta\mu = \mu_2 - \mu_1$. In order to keep the height of the barrier constant, the variation in the free energy at the top of the barrier, whose position is denoted by n^*, should be equal to the variation in the free energy in the metastable vapor phase, with $n = 0$. In general, when the activity fraction and the pressure are changed, the top of the barrier can change. However, at the top of the barrier the partial derivative of the free energy with respect to cluster size, $\frac{\partial Y(n)}{\partial n}$, is zero, so that the last term in Eq. (7.3) and Eq. (7.4) drops out. In the metastable vapor n is zero and remains zero. Hence, the last term is zero, also for the vapor phase. Eq. (7.4) then reduces to

$$\begin{aligned} dY(n^*) &= dY(0); \\ V(n^*)dP - N_2(n^*)d\Delta\mu &= V(0)dP - N_2(0)d\Delta\mu, \end{aligned} \tag{7.5}$$

from which we obtain

$$\left(\frac{dP}{d\Delta\mu}\right)^* = \frac{N_2(n^*) - N_2(0)}{V(n^*) - V(0)}, \tag{7.6}$$

where the asterisk denotes differentiation at constant barrier height. The chemical potential difference $\Delta\mu$ can be written in terms of the activities of species 1 and 2,

$$\Delta\mu = k_B T \log\left(\frac{a_2}{a_1}\right), \tag{7.7}$$

where $a_i = \exp[\beta\mu_i]$ denotes the activity of species i. We can rewrite the above expression as

$$\Delta\mu = k_B T \log\left(\frac{x_{a_2}}{1 - x_{a_2}}\right), \tag{7.8}$$

where x_{a_2} is the activity fraction of species 2, defined as

$$x_{a_2} \equiv \frac{a_2}{a_1 + a_2}. \tag{7.9}$$

We thus obtain the following expression for the variation of the pressure with activity fraction

$$\left(\frac{dP}{dx_{a_2}}\right)^* = \frac{k_B T}{x_{a_2}(1 - x_{a_2})} \frac{N_2(n^*) - N_2(0)}{V(n^*) - V(0)}. \tag{7.10}$$

To compute a contour of constant barrier height on the free-energy barrier surface, we have to integrate the above expression in the P, x_{a_2} plane by computing N_2 and V, both at the top of the barrier and in the metastable vapor. We have integrated Eq. (7.10) by a fourth-order predictor-corrector scheme. We start with $x_{a_2} = 0$, which corresponds to the limit that only one species is present. At $x_{a_2} = 0$ the value of (dP/dx_{a_2}) is undefined (see Eq. (7.10)) because both the numerator $(N_2(n^*) - N_2(0))$ and the denominator $(x_{a_2}(1 - x_{a_2}))$ vanish for $x_{a_2} = 0$. However, (dP/dx_{a_2}) itself is finite. To bootstrap the integration procedure we have adopted the scheme of Bolhuis and Frenkel [146]. Instead of calculating successive points step by step, we "guess" the first points on the P, x_{a_2} contour. For every point we perform a simulation (or actually two, one in the vapor and one at the top of the barrier) to compute the derivative of P with respect to x_{a_2} according to Eq. (7.10). Subsequently we fit the derivatives to a polynomial in x_{a_2}. The polynomial is integrated to give new pressures which are then used in the next iteration. We repeat this procedure until convergence of the pressure is reached. After we have generated the first few points on the contour in this way, we use these points to start the fourth-order predictor-corrector scheme to obtain the rest of the contour.

To compute the derivative in Eq. (7.10) we need to know the position of the top of the barrier with a high accuracy, as $N_2(n)$ and $V(n)$ strongly depend on n. For every pressure and activity we therefore perform not one, but three simulations near the top of the barrier: one at the estimated top, and one on either side. The histogram of cluster sizes near the top of the barrier is fitted to a polynomial to obtain the variation of the free energy with cluster size (via Eq. (5.7)). This allows us to locate the position of the top of the barrier. Next, to get the volume, $V(n^*)$, and the number of particles of species 2, $N_2(n^*)$, at the top of the barrier, we fit the histograms of $V(n)$ and $N_2(n)$ to polynomials and insert the value of the critical droplet size into these polynomial expressions.

7.3 The system

We studied a simple model for a binary mixture, namely one in which the particles interact via the Lennard-Jones pair potential

$$v_{ij}(r) = 4\epsilon_{ij}\left[\left(\frac{\sigma_{ij}}{r}\right)^{12} - \left(\frac{\sigma_{ij}}{r}\right)^{6}\right], \tag{7.11}$$

where r is the interparticle distance, ϵ_{ij} is the Lennard-Jones well depth corresponding to the interaction between species i and j and σ_{ij} is the corresponding Lennard-Jones diameter. Following Talanquer and Oxtoby [39] we take $\sigma_{11} = \sigma_{22} = \sigma_{12} = \sigma$.

The structure and composition of our nuclei is then determined by the values of the "volatility parameter"

$$\epsilon_{22}^* = \frac{\epsilon_{22}}{\epsilon_{11}} \tag{7.12}$$

and the "mixing parameter"

$$\Lambda^* = \frac{\Lambda}{\epsilon_{11}} = \frac{\epsilon_{11} + \epsilon_{22} - 2\epsilon_{12}}{\epsilon_{11}}. \tag{7.13}$$

The volatility parameter ϵ_{22}^* measures the relative volatility of the two components, and the mixing parameter Λ^* determines the energy of mixing particles of different species. Note that Λ^* does not measure the deviation from the Lorentz-Berthelot mixing rule ($\epsilon_{12} = \sqrt{\epsilon_{11}\epsilon_{22}}$). In fact, when $\epsilon_{12} = \sqrt{\epsilon_{11}\epsilon_{22}}$, $\Lambda^* > 0$, unless $\epsilon_{11} = \epsilon_{22}$.

In most nucleation experiments [50, 95, 136] the volume is fixed. This means that the nucleation of a liquid droplet leads to a decrease in vapor pressure, and in general, also to a change in the composition of the vapor phase. However, as already indicated, the concentration of critical nuclei is usually so small, that the change in pressure and composition is negligible. That is, when a critical nucleus is formed, the activities of the species in the vapor phase are unaltered. In principle, we could simulate the experimental situation by performing a NVT -simulation. However, a large excess number of particles would then be required in order to keep the vapor phase activities constant. It is therefore much more natural to work in the isobaric-semi-grand ($NPT\Delta\mu$)-ensemble or in the grand-canonical (μVT)-ensemble. In both ensembles a liquid droplet can be formed at constant chemical potentials of the vapor species without actually having to simulate an excessive number of vapor particles. In the grand-canonical ensemble this is accomplished by the insertion and removal of particles. However, at high densities the insertion probability can be too low to obtain reasonable statistics. It is then more convenient to work in the isobaric-semi-grand ensemble. In this ensemble, the volume of the system is adjusted such that the pressure in the vapor surrounding the liquid drop is maintained at a constant value, irrespective of the size of the liquid cluster (see chapter 5). In addition, in a semi-grand Monte Carlo simulation, the composition in the vapor is kept constant, by allowing for Monte Carlo moves that swap the identity of particles (see e.g. Ref. [147]). Hence, this approach effectively mimics the experimental situation in which the gas phase activities are constant, but it avoids the insertion and removal of particles, that is required in the grand-canonical ensemble. More details about the Monte Carlo scheme that is used to study (pre) critical nuclei, can be found in chapter 5.

The number of particles in all simulations was $N = 864$. As the size of the largest critical cluster in our simulations was less than 600 particles and the density of the surrounding vapor is very low, the system size was always sufficiently large that system-size artifacts can be excluded. We have truncated the potential at $r_c = 2.5\sigma$ and shifted the potential such that it is zero at the cutoff. No long-range corrections were made. We applied cubic periodic boundary conditions. In what follows, we use reduced units, such that ϵ_{11} is the unit of energy and σ is the unit of length.

7.4 Results and discussion

In order to facilitate comparison of our findings with recent experiments [50, 94, 95, 136] and theories[39] on nucleation in binary systems, we will use, as much as possible, the same notation as employed in these publications. In these studies the "onset activities" $a_{i0} = \exp[\beta\mu_{i0}]$ are defined as those activities for which the nucleation rate (in experiments) or the height of the barrier (in theory) is kept at a fixed reference value. As we do not determine the nucleation rate itself, but the height of the nucleation barrier, we follow Talanquer and Oxtoby [39] and define the onset activities as those activities for which the height of the barrier is constant. This seems reasonable, as the rate of nucleation depends strongly on the barrier height, and only weakly on the kinetic prefactor. We can therefore expect that the onset activities follow the same behavior as the experimentally determined onset activities, that correspond to a fixed nucleation rate.

The composition of the clusters is usually expressed in terms of the normalized activity fraction of one of the components. The normalized activity fraction of component 2 is defined as

$$x_{a_{2n}} \equiv \frac{a_{2n}}{a_{1n} + a_{2n}}, \tag{7.14}$$

where the normalized onset vapor activities a_{1n} are given by

$$a_{in} \equiv a_{i0}/a_{i0}^0 \tag{7.15}$$

and a_{i0}^0 represents the onset activity for the *pure* vapor of component i.

We performed two sets of simulations. The first set corresponds to asymmetric mixtures, for which $\epsilon_{22}^* = 1.1$. The second corresponds to symmetric mixtures with $\epsilon_{22}^* = 1.0$. The starting point for all simulations was the one-component system with $x_{a_2} = 0.0$, *i.e.* a system consisting of pure species 1. In chapter 5 we computed the height of the nucleation barrier in this system for $T = 0.741$ (which is 32% below the critical temperature $T_c = 1.085$ [123]) and $P = 0.01202$, which corresponds to a supersaturation $S = 1.53$. At this degree of undercooling, the height of the nucleation barrier is $56.7k_BT$. In the present simulations, we keep the temperature constant, but vary the activity fraction and pressure according to Eq. (7.10). In this way, we ensure that the height of the barrier remains constant. Hence, all results that we present below refer to a reference barrier height $\Delta Y_0^* = 56.7k_BT$.

7.4.1 Asymmetric mixtures

We first discuss the behavior of the asymmetric mixtures, as they provide a good test for the integration scheme discussed in section 7.2. The volatility parameter is $\epsilon_{22}^* = 1.1$. The fact that $\epsilon_{22}^* > 1$ means that component 1 is the more volatile component. We studied asymmetric mixtures with this value of the volatility parameter for three different values of the mixing parameter Λ^*: $\Lambda^* = 0.1$, 0.3 and 0.5. As the volatility parameter is held constant, the two one-component limits, with $x_{a_{2n}} = 0.0$ and $x_{a_{2n}} = 1.0$, are the same for all three values of Λ^*. This can be used as a test for the accuracy of the integration scheme discussed in section 7.2: although we do not know beforehand what value of the pressure is required to get the reference barrier height $Y_0 = 56.7k_BT$ in the limit $x_{a_{2n}} = 1.0$, we do know that this pressure cannot depend on Λ^*. Fig. 7.1 shows the pressure as a function of the activity fraction for the three different mixtures. It is

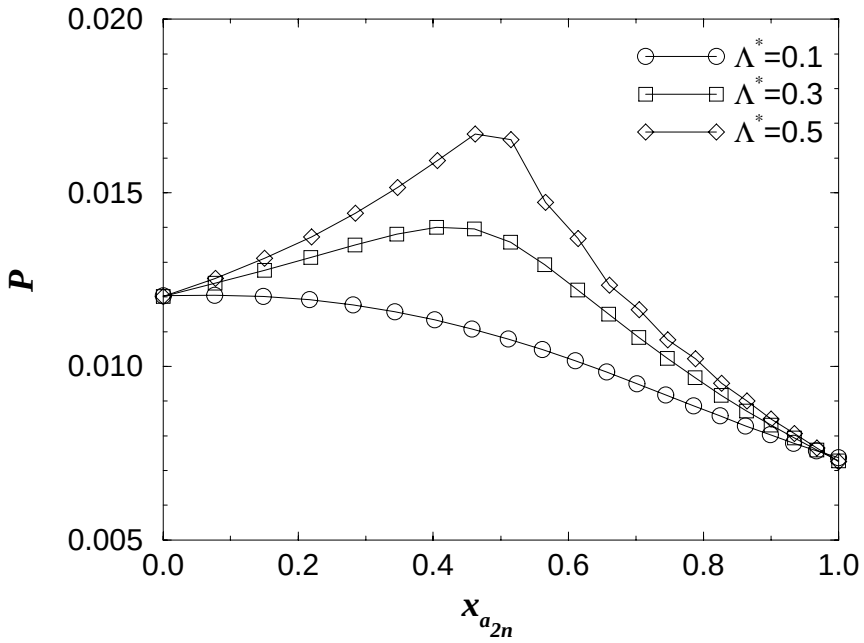

FIGURE 7.1 The reduced pressure P as a function of the normalized activity fraction $x_{a_{2n}}$ for an asymmetric mixture with $\epsilon^*_{22} = 1.1$ for three different values of the mixing parameter Λ^*. All curves correspond to a reference work of formation of $\Delta Y^*_0 = 56.7 k_B T$. In this figure and all subsequent figures, we use $\sigma_{11} = \sigma_{22} = \sigma_{12}$ as our unit of length and ϵ_{11} as our unit of energy. In all cases, $k_B T/\epsilon_{11} = 0.741$.

seen that at intermediate values of the activity fraction, the pressures are different for the different types of mixtures. However, in the one-component limits the pressures are the same ($P(x_{a_{2n}} = 1.0) = 0.00730 \pm 0.00007$). This means that the integration scheme is not only an efficient, but also an accurate method to compute contours of constant free energy on the free-energy barrier surface.

Fig. 7.1 shows that, as the activity fraction is increased from zero, the pressure initially increases. In other words, mixing inhibits the nucleation process and the higher the value of the mixing parameter, the larger the increase in pressure. At some point however, the pressures goes down again as the nuclei become enriched in the less volatile component. This is illustrated in Fig. 7.2, where we show the excess number of particles of species 1 and 2 as a function of the activity fraction for $\Lambda^* = 0.3$. The excess number of particles of species i is defined as

$$\Delta n_i = 4\pi \int_0^\infty (\rho_i(r) - \rho_{v,i}) r^2 dr, \tag{7.16}$$

where $\rho(r)_i$ is the density of species i in a spherical shell of radius r around the center-of-mass of the cluster and $\rho_{v,i}$ is the density of species i in the vapor. The excess number of particles in a critical nucleus is a quantity that can be deduced from experiments using the nucleation theorem [56].

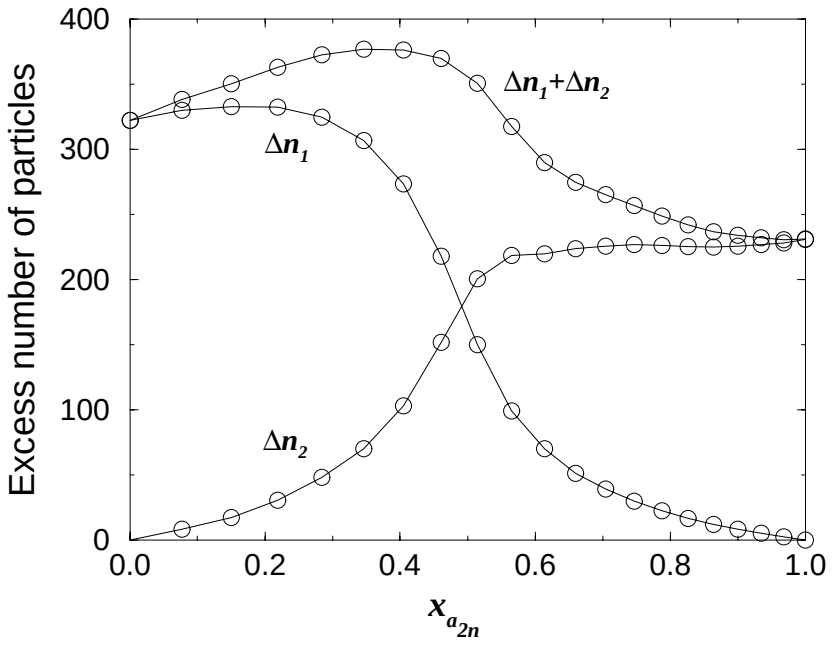

FIGURE 7.2 Size and composition of the critical nuclei as a function of the normalized activity fraction $x_{a_{2n}}$ in a binary system with $\epsilon^* = 1.1$ and $\Lambda^* = 0.3$, corresponding to a nucleation barrier of height $\Delta Y_0^* = 56.7 k_B T$. Δn_1 and Δn_2 are the excess numbers of particles of species one and two, respectively.

In the limit $x_{a_{2n}} = 0.0$, the critical nucleus contains some 325 particles. When the activity fraction is increased, the concentration of species 2 increases. But as mixing of the two species is unfavorable, the relative concentration of species 2 in the cluster is initially less than in the vapor phase. Moreover, the total number of particles in the critical nucleus increases with $x_{a_{2n}}$. However, at an activity fraction of $x_{a_{2n}} = 0.4$, component 2 begins to dominate the nucleation process and the fraction of this species in the critical nucleus rapidly increases. At the same time, the total number of particles in the cluster starts to decrease. At $x_{a_{2n}} = 1.0$ (pure species 2) the critical cluster size is 235 particles. Note that this cluster size is smaller than the critical nucleus size at $x_{a_{2n}} = 0.0$. This is due to the fact that species 2 is less volatile than species 1.

Let us next examine the structure of the critical nuclei. Clarke *et al.* [148] reported a computer-simulation study of binary liquid Lennard-Jones clusters *in vacuo*. The simulations of Ref. [148] were performed at a reduced temperature $T = 0.31$, which is less that half the temperature that we imposed during our simulations. Clarke *et al.* found that for $\epsilon_{22}^* \neq 1.0$ and $\Lambda^* > 0.0$, spherical clusters can occur that consist of a core rich in the less volatile component, coated by a shell rich in the more volatile component. Such behavior is to be expected on the basis of macroscopic (wetting) arguments. However, under the conditions studied in our simulations, we find little evidence for the existence of such compositional inhomogeneities. In almost all clusters that we studied, the two species appeared well mixed. Only for the critical nuclei at $\Lambda^* = 0.5$ and $x_{a_{2n}} = 0.52$ do

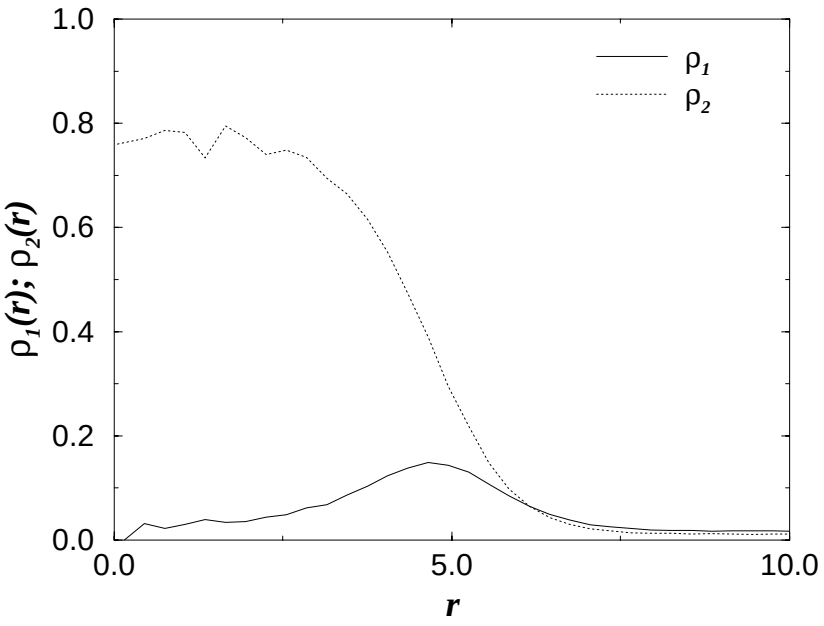

FIGURE 7.3 Radial density profile of species one and two for a critical nucleus in a system with $\epsilon^*_{22} = 1.1$ and $\Lambda^* = 0.5$. The normalized activity fraction is $x_{a_{2n}} = 0.52$ and the height of the nucleation barrier is $\Delta Y^*_0 = 56.7 k_B T$. Units as in Fig.1.

we find that the concentration of species 1 (the more volatile component) is significantly higher in the surface than in the core of the droplet (see Fig. 7.3).

7.4.2 Symmetric mixtures

We studied symmetric mixtures, for which $\epsilon^*_{22} = 1.0$, for the following values of the mixing parameter Λ^*: $\Lambda^* = -0.1, 0.1, 0.3, 0.5$ and 0.7. The symmetric mixture with $\Lambda^* = 0.0$ corresponds to an ideal-mixture, that is, $\epsilon_{11} = \epsilon_{22} = \epsilon_{12}$. We will use this "mixture" as a reference. The mixtures for $\Lambda^* \leqslant 0.3$ are weakly non-ideal and the species are fully miscible in the bulk liquid. However, for $\Lambda^* > 0.3$, the species demix in the bulk. Below, we first discuss the weakly non-ideal mixtures and subsequently the mixtures that show a macroscopic miscibility gap.

7.4.2.1 *Weakly non-ideal liquid mixtures* The weakly non-ideal liquid mixtures do not show bulk liquid-liquid phase separation and, not surprisingly, the two species are also fully mixed in the critical nuclei. However, depending on the sign of Λ^*, nucleation is either enhanced or hindered by mixing. Fig. 7.4 shows the pressure as a function of the activity fraction. Note that as species 1and 2 have identical properties, the figure is symmetric around $x_{a_{2n}} = 0.5$. For comparison, we also show the contour (a straight line) for the ideal mixture. For negative values of Λ^*, mixing of the two species in the critical cluster lowers the pressure that is needed to maintain a constant barrier height. In other words, mixing enhances the nucleation process. For positive values of Λ^* the vapor pressure has to be increased in order to keep the height of the barrier constant.

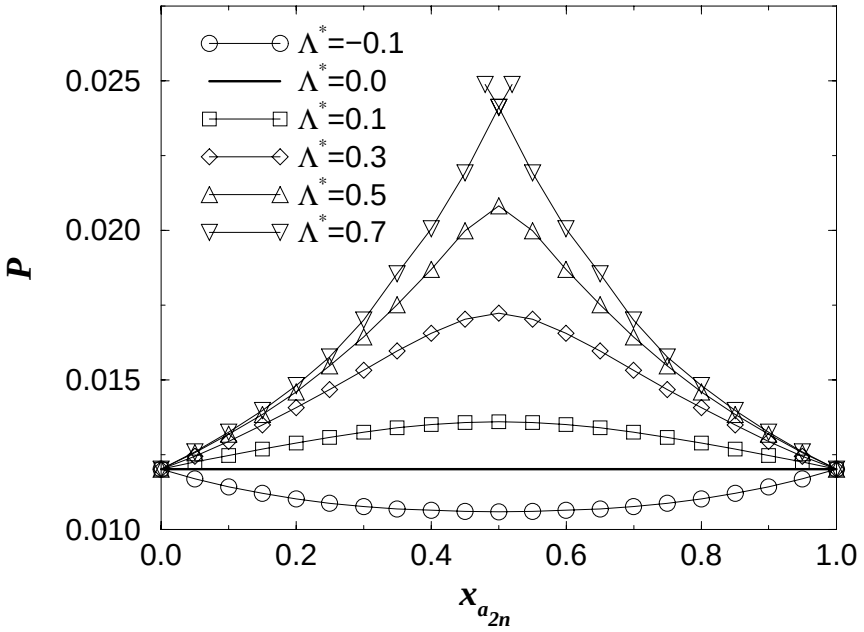

FIGURE 7.4 The reduced pressure P as a function of the normalized activity fraction $x_{a_{2n}}$ for symmetric mixtures ($\epsilon^*_{22} = 1.0$) with different values of the mixing parameter Λ^* ($\Delta Y^*_0 = 56.7 k_B T$). The curve for the ideal mixture with $\epsilon^*_{22} = 1.0$ and $\Lambda^* = 0.0$ is indicated by the straight solid line. Units as in Fig.1.

This behavior can be understood by examining the compositions of the critical nuclei. Fig. 7.5 shows the excess number of particles of species 1 and 2 as a function of the activity fraction for $\Lambda^* = -0.1$ and $\Lambda^* = 0.1$. Again, we also show the (trivial) result for the ideal mixture. For such a mixture, both the composition of the critical nucleus and that of the vapor phase are equal to the activity fraction. Moreover, for an ideal mixture the size of the critical nucleus does not depend on composition.

For negative values of Λ^* the critical-nucleus size shrinks when the species are mixed. Moreover, critical nuclei are enriched in the minority component when compared to the ideal mixture. For positive values of Λ^*, the opposite behavior is found. This can be seen more clearly in Fig. 7.6, which shows the molar fraction x_2 of species 2 in the critical nucleus as a function of the activity fraction $x_{a_{2n}}$ (i.e. the composition in the dilute vapor).

7.4.2.2 *Demixing transition* Let us now consider the more strongly non-ideal mixtures that have a tendency to demix in the bulk, i.e. mixtures with large positive values of Λ^*.

When Λ^* is increased, the critical clusters become increasingly enriched in the majority component as compared to the ideal mixture. Fig. 7.7 shows the composition of the critical cluster as a function of the activity fraction for $\Lambda^* = 0.5$. It is seen that up to an activity fraction of $x_{a_{2n}} = 0.5$, the cluster almost exclusively consists of species 1, whereas for an activity fraction $x_{a_{2n}} > 0.5$ it consists almost only of species 2. Still,

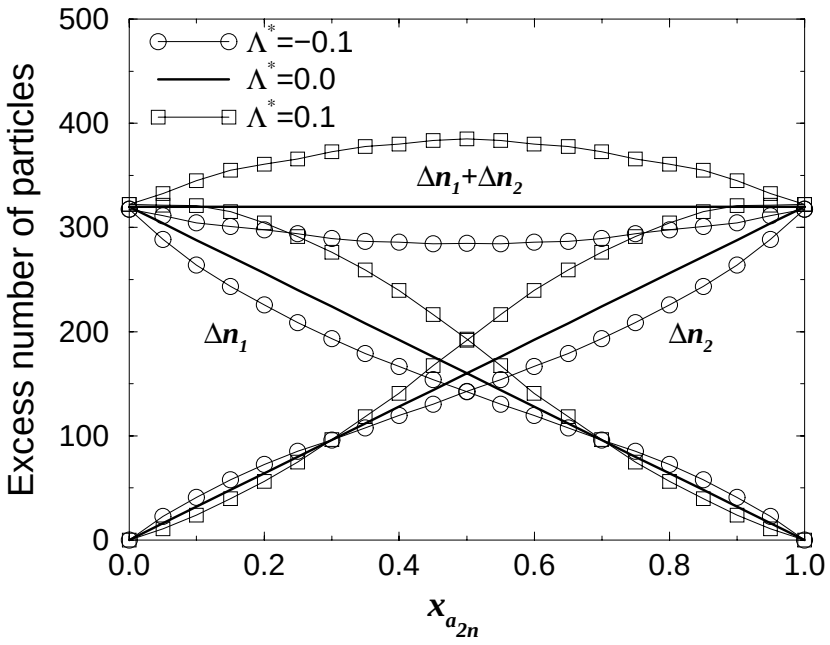

FIGURE 7.5 The excess number of particles of species 1 and 2 (as well as their sum) in critical nuclei as a function of the normalized activity fraction $x_{a_{2n}}$ for three symmetric mixtures that differ in the value of Λ^*. The ideal mixture with $\epsilon^*_{22} = 1.0$ and $\Lambda^* = 0.0$ is indicated by the straight solid lines and the onset work of formation is $\Delta Y^*_0 = 56.7 k_B T$.

for $x_{a_{2n}} = 0.5$, $x_2 = 0.5$. That is, at $x_{a_{2n}} = 0.5$, both species are present in equal amounts in the critical cluster. Yet, at $\Lambda^* = 0.5$, the bulk liquid already exhibits phase separation. We thus have a situation in which the species are mixed in the cluster, but phase separated in the bulk liquid. A natural question to ask is therefore the following: how do these critical nuclei develop into a bulk liquid?

To answer this question, we have computed the free energy as a function of the composition for clusters of different size, at $\Lambda^* = 0.5$ and $x_{a_{2n}} = 0.5$. We have studied a pre-critical cluster of 255 particles, a pre-critical cluster of 368 particles, a cluster near the top of the barrier of 472 particles, and a postcritical cluster of 571 particles. Fig. 7.8 shows the free energy as a function of composition x_2 for these clusters. It is seen that the free-energy curve of the cluster of 255 particles only shows one broad minimum at $x_2 = 0.5$. However, for a cluster size of around 368 particles, the free-energy curve starts to develop two minima, centered at $x_2 = 0.3$ and $x_2 = 0.7$, separated by a small free-energy barrier at $x_2 = 0.5$. For larger cluster sizes, the minima shift to the one-component limits and the free-energy barrier separating the two minima increases. As the mixture is symmetric, the free-energy curves are symmetric around $x_2 = 0.5$.

The important point to note, is that the saddle-point that separates the stable liquid from the metastable vapor, does not correspond to a critical cluster in which both species are mixed and equally present. Rather, there are two saddle points of equal free energy. Both saddle-points correspond to a critical cluster of around 440 particles, but at one the

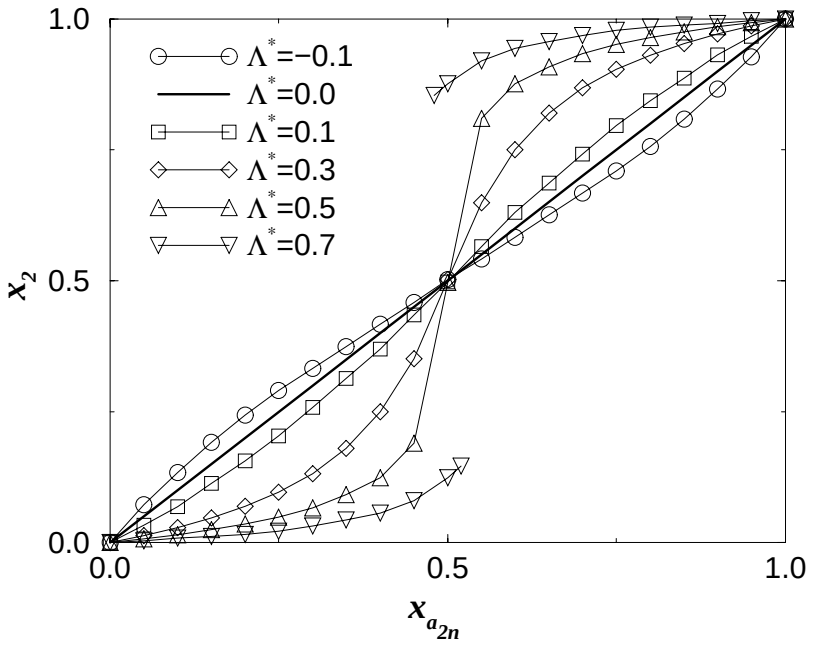

FIGURE 7.6 Cluster composition x_2 as a function of the normalized activity fraction $x_{a_{2n}}$ for (symmetric) mixtures with $\epsilon_{22}^* = 1.0$ and an onset work of formation $\Delta Y_0^* = 56.7 k_B T$. The ideal mixture with $\epsilon_{22}^* = 1.0$ and $\Lambda^* = 0.0$ is indicated by the thick solid line.

cluster is of composition $x_2 = 0.3$, whereas the composition in the cluster at the other saddle-point is $x_2 = 0.7$. However, the free-energy barrier separating the two saddle-points is still so low that the critical cluster can easily jump back and forth between them.

As the critical nucleus evolves into a postcritical nucleus, there comes a point where the free-energy barrier that separates the two minima becomes too large for the cluster to cross. Two "channels" in the free-energy landscape have developed, one leading to a bulk liquid rich in species one, the other to a bulk liquid rich in species two. Although both pathways for the formation of the bulk liquid are equally probable and both bulk liquid phases are equally likely to occur, once the system has chosen either path, it has to follow that path–it cannot make the transition to the other channel anymore.

Yet, because rapid interconversion between the two critical nuclei is possible, the nucleation theorem would indicate a 50-50 composition of the critical nucleus. Clearly, this refers to the average composition of the critical nucleus. In particular, a macroscopic droplet of phase 1 may well have evolved from a critical nucleus that was rich in species 2. Hence, this implies that experiments on nucleation in moderate non-ideal mixtures, the nucleation theorem will not reveal the true saddle-point in the nucleation pathway. Recent experiments by Viisanen *et al.* on nucleation in binary mixtures of nonane with short-chain alcohols, may well belong to this category [136]. In fact, it would be interesting if the nucleation rates of the two phases of the bulk liquid could be measured independently: if the "bifurcation" in the free-energy landscape occurs after the critical

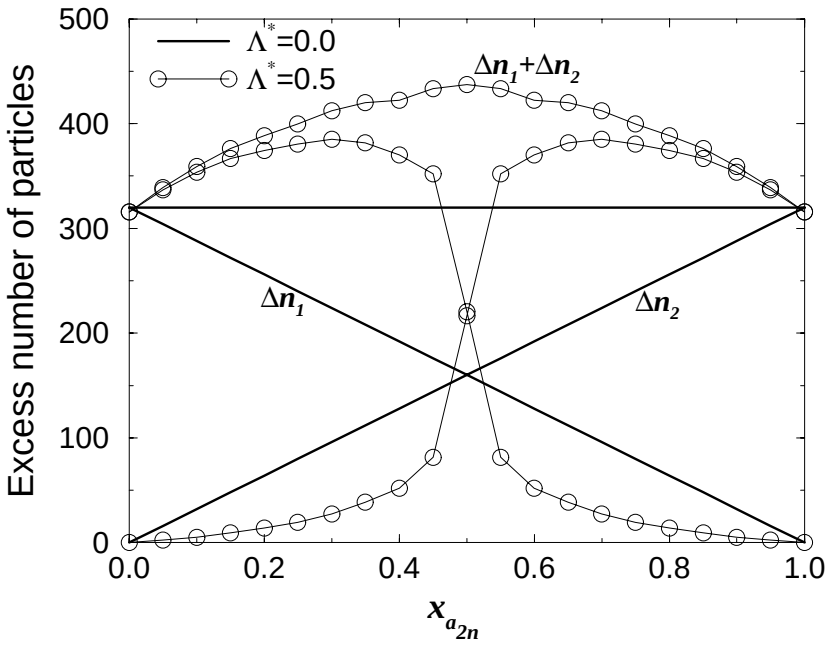

FIGURE 7.7 Size and composition of the critical nuclei as a function of the normalized activity fraction $x_{a_{2n}}$ for a symmetric mixture ($\epsilon^*_{22} = 1.0$) with $\Lambda^* = 0.5$ ($\Delta Y^*_0 = 56.7 k_B T$). For comparison we also inidicate the composition of the ideal mixture with $\epsilon^*_{22} = 1.0$ and $\Lambda^* = 0.0$.

nucleus is formed, then the nucleation theorem will reveal the same critical nucleus for both liquids. However, if there is a high free energy barrier between the critical nuclei that evolve into the two bulk phases, then the two nucleation rates will reveal the existence of two distinct critical nuclei. In our model system, this would be the case for $\Lambda^* = 0.7$.

For $\Lambda^* = 0.7$ and $x_{a_{2n}} = 0.5$ the path for the formation of the bulk liquid bifurcates for clusters that are appreciably smaller than the critical-nucleus. We now have two different types of critical nuclei, one rich in component 1 and the other rich in component 2. At $x_{a_{2n}} = 0.5$ the two types of critical nuclei are of equal free energy and are formed with equal probability. However, once the critical nucleus of either type is formed, it cannot transform into the other type, due to the large free-energy barrier separating the two saddle-points. Furthermore, the dependence of both the pressure and the cluster composition x_2 on the activity fraction $x_{a_{2n}}$ for $\Lambda^* = 0.7$, exhibits hysteresis at $x_{a_{2n}} = 0.5$, as can be seen in Figs. 7.4 and 7.6, respectively. This is due to the free-energy barrier separating the two types of nuclei. Only at $x_{a_{2n}} = 0.52$ (or $x_{a_{2n}} = 0.48$) the height of the barrier is sufficiently reduced that the transition from one type of cluster to the other can take place on the time-scale of a simulation.

The possibility of the simultaneous occurrence of two types of critical clusters was predicted by Talanquer and Oxtoby [39], using density functional theory, and by Ray *et al.* [149] using classical nucleation theory. The present simulations confirm this prediction. Of course, as the simulations illustrate, only at $x_{a_{2n}} = 0.5$ do both types correspond

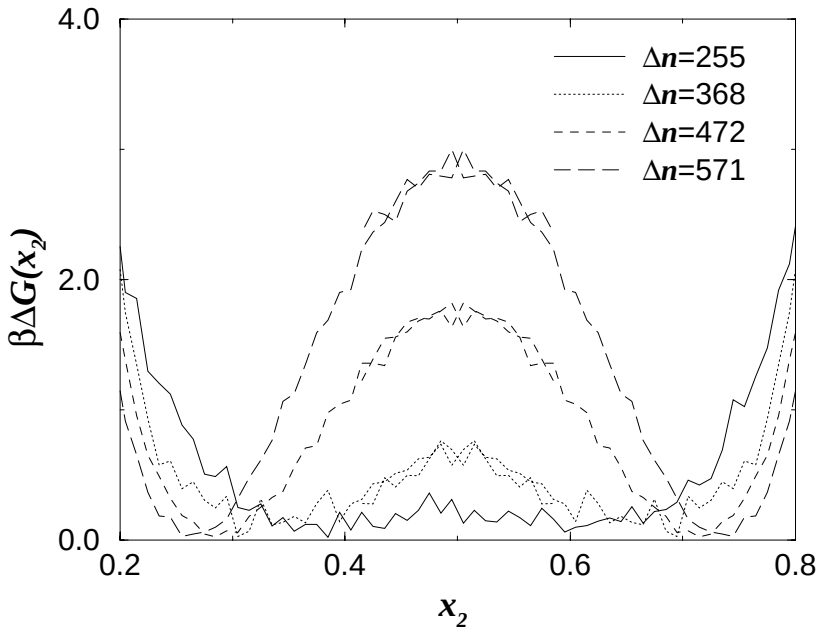

FIGURE 7.8 Excess free energy as a function of the composition x_2 for nuclei of different size in a system with $\epsilon^*_{22} = 1.0$ and $\Lambda^* = 0.5$. The activity fraction is $x_{a_{2n}} = 0.5$ and the imposed pressure $P = 0.021$, corresponding to a barrier height of $\Delta Y_0^* = 56.7 k_B T$. The size of the critical cluster, i.e. the cluster at the top of the free-energy barrier, is around 440 particles. In order to facilitate the comparison of the free-energy curves we have set the free energy of the minima to zero.

to the same free energy. For $0.48 < x_{a_{2n}} < 0.5$ the clusters rich in component 1 have the lowest free energy, and for $0.5 < x_{a_{2n}} < 0.52$, those that are rich in component 2.

An interesting prediction that was made on basis of density-functional theory by Talanquer *et al.* [39] is that, when the mixtures exhibit a large miscibility gap in the bulk, cylindrical critical nuclei can appear. The remarkable feature of these nuclei is that the species have (micro) phase-separated inside the nucleus. In fact, this type of nucleus has been observed by Clarke *et al.*[148] in a computer-simulation study of binary liquid Lennard-Jones clusters *in vacuo*. In our simulations, we explored in some detail the possibility of micro-phase separation in critical clusters. Talanquer and Oxtoby [39] predict that such cluster should appear for $\Lambda^* \geq 0.6$ and $x_{a_{2n}} = 0.5$. As discussed above, we find that for $x_{a_{2n}} = 0.5$ and $\Lambda^* \geq 0.5$, the saddle points that separate the bulk liquid from the metastable vapor correspond to nuclei that are enriched in one of the species. We never found evidence for free-energy saddle points that correspond to cylindrical nuclei. This is not in contradiction to the findings of Clarke et al.[148]: our simulations do not rule out the possibility that phase-separated clusters form at the top of the barrier separating the two saddle points. However, such clusters then correspond to local free-energy maxima and should play no role in the nucleation process. We have examined the structure of nuclei at the top of the barrier and in the vicinity of

$x_2 = 0.5$. For $\Lambda^* = 0.5$ we found that, at the top of the (shallow) ridge separating the two critical nuclei, the species were mixed, rather than phase separated. Even when we "prefabricated" a cylindrical cluster and constrained the cluster at a molar fraction of around 0.5, we found that after typically 5000 MC-cycles the species mixed again, and that the, initially cylindrical droplets transform into a spherical shape. For $\Lambda^* = 0.7$, the situation is slightly more complex. The "unprepared" clusters at the top of the ridge were not cylindrical, although a visual inspection of the snapshots indicated that the species have a strong tendency to phase separate. Nuclei that were prepared in a phase-separated, cylindrical configuration, remained there for the length of the simulation, provided that the composition of the cluster was kept fixed at $x_2 = 0.5$. However, as soon as the composition of the cluster was allowed to adjust, all phase-separated clusters transformed back into a spherical clusters that were enriched in one of the two species. This illustrates that the cylindrical nuclei correspond to local free energy *maxima* and therefore cannot play a significant role in the nucleation process.

7.5 Conclusions

We have developed a new scheme to study critical nuclei involved in gas-liquid nucleation of binary mixtures. Our numerical scheme allows us to compare clusters that have the same barrier height, but different compositions. The numerical scheme was found to be both efficient and accurate. Using it, we performed a detailed study of the composition of critical nuclei in binary systems. The results of our simulations support the density functional predictions of Talanquer and Oxtoby [39] on the nucleation of weakly non-ideal mixtures. These mixtures condense via a single type of critical nucleus, in which the components of the mixture can be mixed in all proportions. Depending on the value of the mixing parameter, mixing either enhances or inhibits nucleation.

For the nucleation of mixtures that show a macroscopic miscibility gap, the pictures that emerges is more complex. We find that nucleation in these systems can still be initiated by clusters in which both species are mixed. However, when the cluster size increases, the path bifurcates and two channels develop, corresponding to nuclei enriched in one of the two components. In all cases, the critical nuclei are found to have a spherical shape. The cylindrical, micro-phase separated nuclei predicted by Talanquer and Oxtoby [39], only appear at the top of the free-energy ridge separating the two types of critical nuclei. The cylindrical clusters do not correspond to saddle-points and they probably play no role in the nucleation of immiscible mixtures.

The cluster size at which the bifurcation of the path occurs depends on the value of the mixing parameter. Hence, whether or not one or two types of critical nuclei can be formed depends on the supersaturation and the value of the mixing parameter. For larger values of Λ^*, larger supersaturations, corresponding to smaller critical-nucleus sizes, are required in order to find mixed critical nuclei. Correspondingly, when the nucleation process is dominated by one type of critical cluster at a given supersaturation, it can proceed via two types of nuclei at smaller supersaturation. This also implies that, in experiments on the nucleation behavior of partially miscible or immiscible mixtures, care should be taken when deriving the composition of the critical nuclei from the variation of the nucleation rate with supersaturation [136]. Our simulations suggest that the measured average composition of the nucleus need not be the most likely one.

8 Coil-Globule Transition in Gas-Liquid Nucleation of Polar Fluids

We report a computer-simulation study of homogeneous gas-liquid nucleation in a model for strongly polar fluids. We find that the nucleation process is initiated by chain-like clusters. As the cluster size is increased, the chains become longer. However, beyond a certain size, the nuclei collapse to form compact, spherical clusters. Nevertheless, in the interface of the collapsed nuclei a high degree of chain formation is preserved. We compare the interface of the collapsed nuclei with the planar interface and find that the interface of the globule-like nuclei differs markedly from the flat interface. Classical nucleation theory underestimates both the size of the critical nucleus and the height of the nucleation barrier.

8.1 Introduction

The formation of a water droplet from the vapor is probably one of the best known examples of homogeneous nucleation of a polar fluid. However, the best known is not the same as best understood. In fact, recent experiments indicate that classical nucleation theory seriously overestimates the rate of nucleation for strongly polar substances, such as acetonitrile, nitrobenzene and benzonitrile [33, 34].

As the variation in the nucleation rate is dominated by the variation in the free-energy barrier, the evaluation of the nucleation barrier is of primary importance. In order to calculate the free-energy barrier that separates the liquid from the metastable vapor phase, in classical nucleation theory it is assumed that the nuclei at the top of the nucleation barrier, the so-called critical nuclei, are compact, spherical objects, that behave like small droplets of bulk fluid. In chapter 5 we have shown that, for a typical non-polar fluid, the well-known Lennard-Jones system, the critical nuclei are indeed compact, more or less spherical clusters. This is not surprising as the interaction potential is isotropic. However, the interaction potential of a polar fluid is anisotropic. It has therefore been suggested that in the critical nuclei the dipoles are arranged in an anti-parallel head-to-tail configuration [33, 34], giving the clusters a non-spherical, prolate shape, which changes the volume to surface ratio. In the oriented dipole model introduced by Abraham [150], it is assumed that the dipoles are perpendicular to the interface, yielding a size dependent surface tension due to the effect of curvature of the surface on the dipole-dipole interaction. However, in a density-functional study of a weakly polar Stockmayer fluid, it was found that on the liquid (core) side of the interface of critical nuclei, the dipoles are not oriented perpendicular to the surface, but parallel [151].

In the present study, we report on a computer simulation study of the structure and free energy of critical nuclei, as well as pre-and postcritical nuclei, of a highly polar Stockmayer fluid. In the Stockmayer system, the particles interact via a Lennard-Jones pair potential plus a dipole-dipole interaction potential

$$v(\mathbf{r}_{ij}, \boldsymbol{\mu}_i, \boldsymbol{\mu}_j) = 4\epsilon \left[\left(\frac{\sigma}{r_{ij}} \right)^{12} - \left(\frac{\sigma}{r_{ij}} \right)^{6} \right] - 3(\boldsymbol{\mu}_i \cdot \mathbf{r}_{ij})(\boldsymbol{\mu}_j \cdot \mathbf{r}_{ij})/r_{ij}^5 + \boldsymbol{\mu}_i \cdot \boldsymbol{\mu}_j / r_{ij}^3. \tag{8.1}$$

Here ϵ is the Lennard-Jones well depth, σ is the Lennard-Jones diameter, $\boldsymbol{\mu}_i$ denotes the dipole moment of particle i and $\mathbf{r}_{ij}$ is the vector joining particle i and j.

The phase behavior of this system has been studied in detail by computer simulation [152, 153] and by density-functional theory [154], as well as by more phenomenological theories [155]. The simulations suggest that a minimum amount of dispersive attraction is required to observe gas-liquid phase coexistence [152]. If the attractive forces are too small in comparison to the strength of the dipolar interactions, as for soft sphere [35] and hard sphere [36, 156] dipolar fluids, the system appears unable to condense to form a liquid, but generates a "gel" of chains of dipoles that align head-to-tail.

In the present study we are interested in the nucleation behavior of strongly polar fluids; the reduced dipole moment $\mu^* = \mu/\sqrt{\epsilon\sigma^3} = 4$. This dipole moment is still well below the threshold value of $\mu^* = 5$ [153] beyond which the Stockmayer system does not show gas-liquid phase coexistence anymore. In fact, it is comparable to that of water, although the nucleation behavior of water is probably more dominated by hydrogen-bonding.

The rest of the chapter is organized as follows. We first present a new approach to determine the size distribution of liquid clusters in a vapor. In section 8.3 we give the computational details of the simulations and we end with a discussion of the results.

8.2 Determination of cluster-size distribution

In homogeneous gas-liquid nucleation the density is usually so low that without association the gas would be ideal. However, the temperature is low enough for particles to associate into dimers, trimers, etc.. Still, the concentration of n-mers is so low that we can safely ignore their mutual interactions. We thus have an ideal "solution" of n-mers in the vapor phase.

The identification of a cluster is not unambiguous and can only be performed explicitly after choosing a criterion that must be fulfilled by the particles that constitute an n-mer. For now, let us assume that we have such a criterion. We can then define the partition function Z_n of an n-mer (see chapter 4) as

$$Z_n = \frac{V n^3}{\nu^n n!} \int d\mathbf{r}'^{n-1} w_n(\mathbf{r}'^{n-1}) \exp[-\beta U_n(\mathbf{r}'^{n-1})], \tag{8.2}$$

where $\beta \equiv 1/k_B T$ is the reciprocal temperature, with k_B Boltzmann's constant and T the absolute temperature, V is the total volume of the system, $\mathbf{r}'^{n-1}$ denotes the coordinates with the prime indicating that the coordinates are taken with respect to the center-of-mass of the cluster, $U_n(\mathbf{r}'^{n-1})$ is the interaction energy, $w_n(\mathbf{r}'^{n-1})$ is the cluster

criterion and ν is the thermal volume

$$\nu = \Lambda^3 \times \frac{h^3}{\sqrt{(2\pi k_B T)^3 I_1 I_2 I_3}}, \tag{8.3}$$

where Λ is the thermal De Broglie wavelength and I_1, I_2, I_3 are the principle moments of inertia.

We have adopted a geometric cluster criterion. All particles that are within a cutoff-distance $q_c = 1.5$ from each other are considered to be "connected", and, therefore, belong to the same cluster. Thus the cluster criterion $w_n(\mathbf{r}'^{n-1})$ is given by

$$\begin{aligned} w_n(\mathbf{r}'^{n-1}) &= 1, \text{if all } n \text{ particles are mutually connected;} \\ &= 0, \text{otherwise.} \end{aligned} \tag{8.4}$$

As the interactions between the clusters is neglected, the number of clusters N_n is given by (see chapter 4)

$$N_n = Z_n \exp[\beta \mu n], \tag{8.5}$$

where μ is the imposed chemical potential. The number of clusters of size N_n is an extensive quantity that depends on the size of the system. We therefore define an intensive probability $P(n)$,

$$P(n) \equiv N_n / N, \tag{8.6}$$

that relates the average number N_n of clusters of size n to the total number of particles N in the system. The free-energy Ω of a cluster is defined as

$$\beta \Delta\Omega(n, \mu, V, T) \equiv -\ln[P(n)]. \tag{8.7}$$

The cluster-size probability distribution function $P(n)$ is an equilibrium quantity and can be measured both by Monte Carlo and Molecular Dynamics. In principle, one could measure $P(n)$ simply by simulating a metastable vapor and counting the number of clusters. However, at moderate supersaturations, only small n-mers will be formed that have a free energy Ω in the order of a couple of $k_B T$. But, critical nuclei, that is nuclei at the top of the free-energy barrier separating the stable liquid from the metastable vapor, have a free energy in the order of $50 - 75 k_B T$. Hence, the probability that such critical nuclei will be formed spontaneously is extremely small. To obtain good statistics for all cluster sizes, we have therefore used the umbrella sampling technique [26]. The main idea is to bias the sampling of configuration space and correct for the bias afterwards. We can bias the sampling of configuration of space by adding a fictitious potential that is a function of an order parameter to the true potential of our model system. As explained in detail in chapter 4 the use of a global order parameter, such as the density of the system or the total number of liquid particles, has some serious drawbacks from a computational point of view. If the volume is large, it will be always be entropically favorable to distribute a given amount of the new phase over many but small clusters, rather than over one relatively large liquid cluster. In fact, if the volume is sufficiently large, the change in free energy associated with a small homogeneous density fluctuation will be smaller than the change in free energy due to the formation of a liquidlike droplet. However, for the nucleation process, we are interested in the largest liquid cluster that grows to its critical size. We therefore exploit the fact that the clusters

can be decoupled from the surrounding vapor and simulate only one cluster in the grand canonical ensemble. The order parameter is taken to be the size of this cluster.

Kusaka et al. [122] showed how the size distribution of a cluster can be obtained in the grand canonical ensemble. In their scheme, all particles in the system are considered to be part of the same cluster. Consequently, all density fluctuations in the system participate in the nucleation event. However, this requires that the volume of the system is chosen carefully. On the one hand, the volume should be larger than the spatial extent of the physical cluster in it. On the other hand, as discussed above, the volume should also not be too large. If the volume is too large, the cluster will break up into many small clusters (see chapter 4).

The use of a geometric cluster criterion does not only provide a unique definition of the cluster, but also circumvents this problem. For large system sizes, it ensures that the particles that make up the cluster are always connected. But more importantly, it is not even required that the volume into (from) which the particles are inserted (removed) is larger than the size of the cluster. This is particularly important when the cluster is not compact but ramified. In the scheme by Kusaka [122] and in the approach of Lee, Barker and Abraham [100] it is conceivable that the constraining sphere biases the shape of the nucleus. In contrast, our scheme does not impose a certain cluster shape.

In order to see this, consider the combined system shown in Fig. 8.1. In our grand-canonical MC scheme, we only consider particle additions to and removals from a spherical volume V_s around the center-of-mass of the cluster. The center-of-mass is computed for the cluster excluding the particle to be added or removed. The acceptance probability for the insertion (removal) of particles into (from) a sphere of volume V_s placed in a system of volume V is given by [157]

$$\begin{aligned}\alpha(n \to n+1) &= \frac{V_s w(\mathbf{r}^{n+1})}{(M+1)w(\mathbf{r}^n)} \exp\left[\beta\mu\right] \exp\left[-\beta\left[U(\mathbf{r}^{n+1}) - U(\mathbf{r}^n)\right]\right] \\ \alpha(n+1 \to n) &= \frac{(M+1)w(\mathbf{r}^n)}{V_s w(\mathbf{r}^{n+1})} \exp\left[-\beta\mu\right] \exp\left[-\beta\left[U(\mathbf{r}^n) - U(\mathbf{r}^{n+1})\right]\right].\end{aligned} \tag{8.8}$$

Note that in the above expressions the number of particles M in the sphere is appearing, but not the total number of particles n in the cluster. Still, the potential energy U contains not only contributions from the interactions between particles inside the sphere, but also from interactions between particles in- and outside the sphere. Note also that only the volume of the sphere enters the expression and not the total volume of the system. The cluster criterion is included in the acceptance criterion to ensure that the cluster remains connected.

8.3 Computational details

8.3.1 Nucleation barrier

We have computed the cluster-size distribution via the grand canonical scheme discussed in section 8.2. However, rather than checking for the connectivity of the particles in the cluster at every trial move, we adopted a staged scheme in which we only checked for the connectivity of the cluster at fixed intervals.

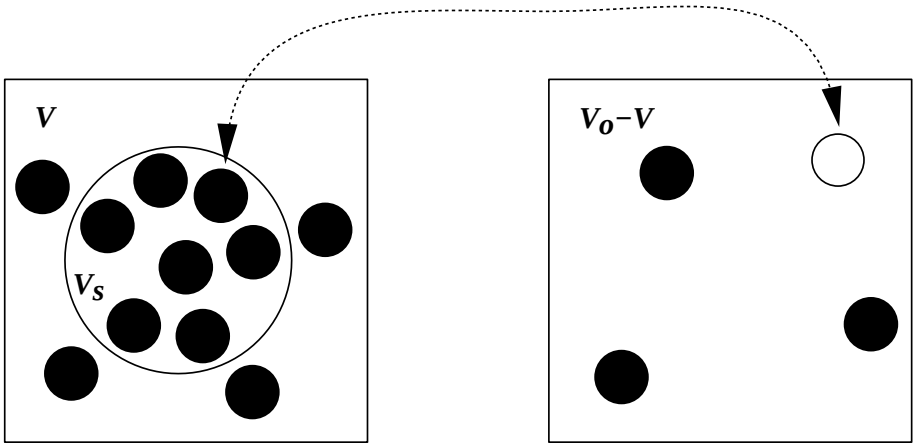

FIGURE 8.1 Ideal gas ($N_o - N$ particles, volume $V_o - V$) can exchange particles with an N-particle system of volume V. The particles are only removed/inserted from/into a sphere of volume V_s, containing M of the N-interacting particles.

In the first stage a series of Monte Carlo cycles is performed. In each MC cycle, we try to both displace particles and insert or remove particles. In one cycle, on average every particle is given one trial displacement and the choice between the trial insertion/removal moves and the trial displacement moves is made at random, with 60% probability for the latter. The trial displacements are accepted with the usual Metropolis acceptance criterion. That is, we do not check whether the connectivity of the cluster is broken. Only in the second stage, after this sequence of typically 5-10 MC-cycles, we will check whether all particles are still connected to one another. If not all particles are mutually connected with each other, we reject the entire sequence.

When a particle is to be inserted, we first determine the center-of-mass of the cluster. The particle is then inserted at a random position inside a sphere centered at the center-of-mass of the cluster. The addition of a particle is accepted with a probability

$$\begin{aligned} &\mathrm{acc}(n \to n+1) = \\ &\min\left[1, \frac{V_s}{M+1} \exp\left[\beta\mu\right] \exp\left[-\beta\left[U(\mathbf{s}^{n+1}) + W(n+1) - U(\mathbf{s}^n) - W(n)\right]\right]\right], \end{aligned} \tag{8.9}$$

where $W(n)$ is the biasing potential. The biasing potential was taken to be a harmonic function of the cluster size n

$$W(n) = \frac{1}{2} k_n (n - n_0)^2. \tag{8.10}$$

When a particle has to be removed, we first randomly select the particle to be removed. In order to preserve the symmetry of the underlying Markov chain, we then determine the center-of-mass of all particles except the particle to be removed and check whether the selected particle is inside the sphere centered at the center-of-mass. If the particle is outside the sphere, we repeat this procedure, until we have found a particle

which is inside the sphere. The removal of the particle is then accepted with a probability

$$\begin{aligned}&\mathrm{acc}(n \to n-1) = \\ &\min\left[1, \frac{M}{V_s}\exp\left[-\beta\mu\right]\exp\left[-\beta\left[U(\mathbf{s}^{n-1}) + W(n-1) - U(\mathbf{s}^n) - W(n)\right]\right]\right].\end{aligned} \tag{8.11}$$

The height of the barrier should not depend on the size of the sphere. In particular, the sphere need not contain the entire cluster. We have verified that the results are indeed insensitive to the size of the sphere. However, the size of the sphere does affect the efficiency of the simulation. If the sphere is large, the insertion and removal probability, given by Eq. (8.9) and Eq. (8.11), are relatively large. However, the probability that the connectivity of the cluster is broken after the Monte Carlo sequence, will also be increased, and thus the probability that the trajectory has to be rejected. For smaller spheres the balance is reversed. In addition, if the sphere is very small, it can happen that the sphere does not contain any particle to be removed. We found that, depending on the shape and size of the clusters, a sphere of radius $5 - 10\sigma$ is optimal.

The number of umbrella windows for the free-energy barrier was 25. Most simulations in a window consisted of an equilibration period of 5×10^5 cycles, followed by a production run of $5 \times 10^5 - 2 \times 10^6$ cycles. Especially for the smaller clusters very long production runs were required, as they exhibit strong shape fluctuations. The results that we report here are free of hysteresis.

8.3.2 Coexistence point

The coexistence point was determined by calculating the chemical potential as a function of pressure for both the vapor and liquid phase. The chemical potential and pressure at coexistence was then found from the intersection.

In order to obtain for the vapor phase the chemical potential as a function of pressure, we first determined for a vapor at low pressure P_o (so low that association of monomers does not occur), the chemical potential by the Widom insertion technique [158]. The chemical potential μ as a function of pressure was then obtained by integrating the inverse density ρ as a function of pressure P

$$\mu(P) = \mu(P_o) + \int_{P_o}^{P} \frac{1}{\rho(P')} dP'. \tag{8.12}$$

For the liquid phase we have to follow a different procedure, as the strong first-order phase transition separating the liquid from the vapor phase rules out the integration along the isotherm from a low-density vapor. We therefore exploited the fact that the liquid-vapor critical point of the Lennard-Jones system ($T_c = 1.316$ [123]) is much lower than that of the Stockmayer system ($T_c = 5.07$ [153]). We first computed the chemical potential for a Lennard-Jones system at a reference density $\rho_o = 0.8$ by Widom insertion at low density and integration along the equation-of-state (see Eq. (8.12)). After we have obtained the chemical potential for the Lennard-Jones system at ρ_o, we can determine the chemical potential for the Stockmayer system at this density by computing the reversible work to switch on the dipolar interactions.

In order to find a reversible path from the Lennard-Jones system to the Stockmayer system, we have used the following interaction potential

$$v(\lambda) = v_{LJ} + \lambda v_{dip}. \tag{8.13}$$

For $\lambda = 1$ the above interaction potential is given by Eq. (8.1), whereas for $\lambda = 0$ the interaction potential reduces to the Lennard-Jones potential. The chemical potential $\mu(\lambda = 1, \rho_o)$ of the Stockmayer system is now related to the chemical potential $\mu(\lambda = 0, \rho_o)$ of the Lennard-Jones system via

$$\mu(\lambda = 1, \rho_o) = \mu(\lambda = 0, \rho_o) + \int_0^1 \langle v_{dip} \rangle_\lambda d\lambda + \frac{1}{\rho_o} \left[P(\lambda = 1) - P(\lambda = 0) \right]. \tag{8.14}$$

Once we know the chemical potential of the Stockmayer system at a given density ρ_o (and pressure P_o), we can obtain the chemical potential as a function of pressure by integrating along the equation of state (see Eq. (8.12)).

All simulations of the bulk phases were performed using a system size of 256 particles. The simulations to compute equation-of-states were performed in the isothermal-isobaric (NPT) ensemble, whereas the simulations to calculate the free-energy difference between the Stockmayer system and the Lennard-Jones system were done in the canonical (NVT) ensemble. In the simulations, the Lennard-Jones potential was truncated at half the box size and the standard long-range corrections were added [147]. The long-range dipolar interactions were handled with the Ewald summation technique using "conducting" boundary conditions [159]. Cubic periodic boundary conditions were applied.

8.3.3 Surface tension

The surface tension was computed from a direct MC simulation of the two coexisting phases, using the Ewald-summation technique to handle the long-range dipolar interactions. A liquid slab was brought in contact with a vapor, from which the surface tension γ was obtained by measuring

$$\gamma = \frac{1}{2} L_z (P_{zz} - \frac{1}{2}(P_{xx} + P_{yy})). \tag{8.15}$$

Here $P_{\alpha\alpha}$ is the $\alpha\alpha$ element of the pressure tensor and L_z is the length of the system in the direction perpendicular to the interface. The factor of $1/2$ outside the bracket arises from the fact that we have two liquid-vapor interfaces in the system. In the appendix we describe how we have computed the pressure tensor.

In order for the density and pressure to approach bulk liquid values in the middle of the slab, the slab should not be too thin. We therefore used a rectangular simulation box, which allows for a relatively thick slab in comparison to the total number of particles in the system. The sides were of length $L_x = L_y = 1/4 L_z$, for the x-, y- and z-direction, respectively, and periodic boundary conditions were applied in all three coordinate directions. The maximum number of reciprocal lattice vectors parallel to the interface was $|k_x^{max}| = |k_y^{max}| = 7$, whereas the number of wave vectors perpendicular to the interface was $|k_z^{max}| = 28$. The larger number of reciprocal vectors in the z-direction makes the simulations significantly longer, but this is unavoidable in order to achieve the same convergence of the Ewald-sum in all principal directions.

The Lennard-Jones interaction potential was truncated at $r_c = 0.5L_x$ and the tail correction to the surface tension was evaluated from [160]

$$\gamma_{tail} = 12\pi\epsilon \int_{\infty}^{\infty} \int_{-1}^{1} \rho(z_1)\rho(z_2)(1-3s^2)r^{-4} dr ds dz_1, \tag{8.16}$$

where $s = (z_1 - z_2)/r$ and z_1 and z_2 are the position of particles 1 and 2, respectively. The density profile was fitted to a hyperbolic tangent function of the form

$$\rho(z) = \frac{1}{2}(\rho_l + \rho_v) - \frac{1}{2}(\rho_l - \rho_v)\tanh[(z - z_o)/d], \tag{8.17}$$

where ρ_l and ρ_v are the densities of the liquid and vapor respectively, and z_o and d are parameters for the location of the dividing surface and the thickness of the surface. With the above fit for the density profile, the tail correction becomes [160]

$$\gamma_{tail} = 12\pi\epsilon(\rho_l - \rho_v)^2 \int_0^1 ds \int_{r_c}^{\infty} dr \coth(rs/d)(3s^3 - s)r^{-3}. \tag{8.18}$$

In order to establish that our system is in equilibrium we also studied the real-space contribution to the normal and tangential components of the pressure tensor as a function of z. When the system is in equilibrium, the normal component should be equal to the transverse component away from the interfaces.

For an inhomogeneous fluid there is no unambiguous way to calculate the components of the pressure tensor. We have used the Irving-Kirkwood convention [119]. The system is divided into N_s slabs parallel to the interface. The local normal ($p_N(s)$) and tangential $p_T(s)$ components of the pressure tensor are given by

$$p_N(s) = k_B T\langle\rho(s)\rangle + \frac{1}{V_s}\left\langle \sum_{i,j}{}^{s} \frac{z_{ij}^2}{r_{ij}} f(\mathbf{r}_{ij}, \boldsymbol{\mu}_i, \boldsymbol{\mu}_j) \right\rangle, \tag{8.19}$$

and

$$p_T(s) = k_B T\langle\rho(s)\rangle + \frac{1}{2V_s}\left\langle \sum_{i,j}{}^{s} \frac{x_{ij}^2 + y_{ij}^2}{r_{ij}} f(\mathbf{r}_{ij}, \boldsymbol{\mu}_i, \boldsymbol{\mu}_j) \right\rangle, \tag{8.20}$$

where $\rho(s)$ is the average density in slab s, $V_s = L_x L_y L_z/N_s$ is the volume of the slab and $f(\mathbf{r}_{ij}, \boldsymbol{\mu}_i, \boldsymbol{\mu}_j) = -\frac{\partial v(\mathbf{r}_{ij}, \boldsymbol{\mu}_i, \boldsymbol{\mu}_j)}{\partial r_{ij}}$ is the force acting between particle i and j. $\sum_{i,j}^{s}$ denotes a summation that runs over all pairs of particles i and j for which the slab s (partially) contains the line that connects them. The contribution to the virial of a slab from a given pair is determined by the ratio to which the slab contains the line.

We performed a simulation with 512 particles and one with 2000 particles, to check for finite-size effects. The number of equilibration cycles was 100000 and the number of production cycles was 200000.

8.4 Results and discussion

All simulations were performed at $T^* = k_B T/\epsilon = 3.5$ (with k_B Boltzmann's constant), which is approximately 30% below the critical temperature of $T_c^* = 5.07$ [153]. We first study the formation of a critical nucleus at an imposed chemical potential $\mu = -26.0\epsilon$. This corresponds to a supersaturation $S = (P/P_{coex} \approx \exp[\beta\Delta\mu]) = 1.26$, where $\Delta\mu =$

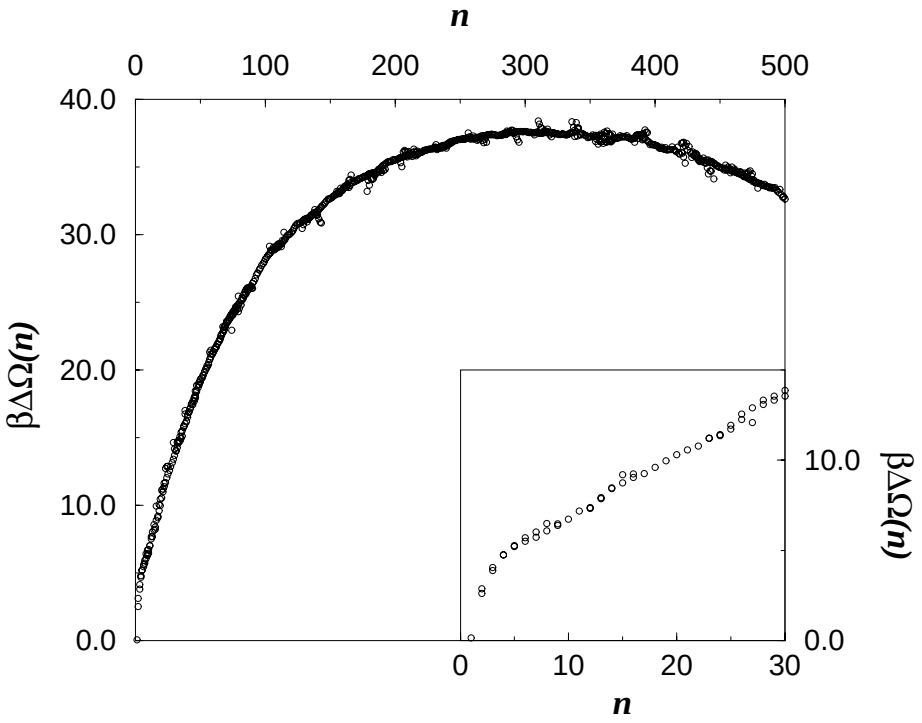

FIGURE 8.2 The excess free energy $\beta\Delta\Omega$ of a cluster as a function of its size n, for a Stockmayer system at $S = 1.26$ and $T^* = 3.5$. The reduced dipole moment $\mu^* = \mu/\sqrt{\epsilon\sigma^3} = 4$.

$\mu - \mu_{coex}$, with μ (P) the imposed chemical potential (pressure), and μ_{coex} (P_{coex}) the chemical potential (pressure) at coexistence. Fig. 8.2 shows the excess free energy of a cluster as a function of its size at this degree of supersaturation.

From the free-energy barrier measured at this degree of supersaturation, we can directly obtain the nucleation barrier at *any* degree of supersaturation, as long as the interactions between the clusters can be neglected. In that case the partition function Z_n of an n-mer is independent of fugacity. That is, the configuration integral of Z_n in Eq. (8.2) does not depend on the imposed chemical potential. We can then combine Eq. (8.2) and Eq. (8.5) with Eq. (8.7) to arrive at

$$\begin{aligned}\beta\Delta\Omega(n,\mu',V,T) = \beta\Delta\Omega(n,\mu,V,T) - \beta(\mu'-\mu)n \\ + \ln\left[\rho(\mu')/\rho(\mu)\right],\end{aligned} \tag{8.21}$$

where $\rho = N/V$ is the total number density in the system. We have verified that our simulations indeed satisfy this equation by computing the free-energy barriers for two different chemical potentials. Furthermore, we have compared the structure of the nuclei at one chemical potential with that at the other chemical potential. The analysis of the structural order parameters, which will be discussed below, indicate that the nucleus structure is independent of the imposed fugacity. This provides further evidence that the sampling of configuration space and hence the evaluation of the configuration integral in Eq. (8.2) does not depend on the chemical potential. We have therefore determined

the free-energy barrier as a function of supersaturation from the computed free-energy barrier at $S = 1.26$, using Eq. (8.21).

As the structure of the clusters does not depend on the imposed fugacity, we only discuss the structure analysis performed at $S = 1.26$. After the structure analysis we will consider how the nucleus structure determines the free-energy barrier. We compare the free-energy barrier, as well as the critical nucleus size, with the corresponding predictions of classical nucleation theory. However, in order to compare the structure of the nuclei with that of the bulk liquid, we first investigate the structural order in the liquid.

8.4.1 Equilibrium phase behavior

Stevens and Grest found evidence for the existence of dipolar order in the fluid phase, albeit for different conditions (i.e. higher temperature and pressure) [153]. We therefore checked whether the bulk liquid also exhibits ferro-electric ordering at the temperature and range of pressures at which we study the nucleation process.

Ferro-electric ordering can be characterized by the order parameter P_1, which is defined as

$$P_1 = \frac{1}{N}\sum_{i=1}^{N} |\hat{\boldsymbol{\mu}}_i \cdot \hat{\mathbf{d}}| = \frac{1}{\mu N}|\mathbf{M} \cdot \hat{\mathbf{d}}|, \tag{8.22}$$

where $\hat{\boldsymbol{\mu}}_i$ is a unit vector specifying the orientation of the dipole of particle i, $\mathbf{M}$ is the total dipole moment of the system and $\hat{\mathbf{d}}$ is the director, which is the eigenvector corresponding to the largest eigenvalue of the $\mathbf{Q}$-tensor

$$\mathbf{Q} = \frac{1}{N}\sum_{i=1}^{N}\left(\frac{3}{2}\hat{\boldsymbol{\mu}}_i\hat{\boldsymbol{\mu}}_i - \frac{\mathbf{I}}{2}\right). \tag{8.23}$$

For a fully ordered system $P_1 = 1$. We found that P_1 did not differ significantly from zero for the bulk liquid at the temperature and supersaturations considered in the simulations. Hence, the system does not show significant ferro-electric ordering.

Yet, it is conceivable that in the bulk liquid a high degree of chain formation is present. We therefore examined the chain-size distribution. We have adopted the following chain-criterion: particles i and j are part of the same chain if for both particles the dot-product $\hat{\boldsymbol{\mu}}_{i/j} \cdot \hat{\mathbf{r}}_{ij}$ exceeds a certain threshold. Fig. 8.3 shows the chain size distribution for different threshold values. As expected, the size distribution is slightly sensitive to the value of the threshold. Still, it is clear that most chains consist of only one to four particles and that chain formation is not very pronounced. We therefore conclude that the bulk liquid at the temperature and range of pressures considered in the simulations is isotropic.

8.4.2 Coil-Globule transition

In classical nucleation theory it is assumed that even the smallest droplets are spherical. In fact, this is a reasonable approximation for a typical model system for non-polar fluids, the Lennard-Jones system. In chapter 5 we showed that precritical nuclei as small as 10 particles are already quite compact, spherical objects. However, the interaction potential of the Lennard-Jones system is isotropic, whereas the dipolar interaction potential is anisotropic. It is possible that this affects the shape of the small clusters. Indeed, for

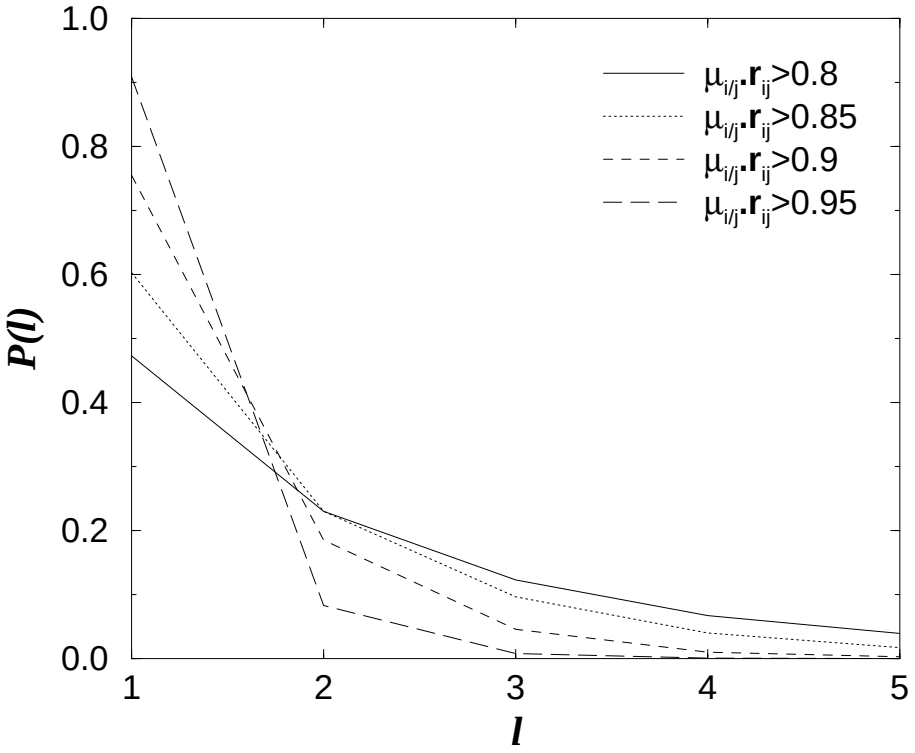

FIGURE 8.3 Probability distribution functions of the chain-length l in a a thermally equilibrated bulk liquid at a supersaturation of $S = 1.76$ ($T^* = 3.5$ and $P^* = 0.005$). The different curves correspond to different threshold values of the chain-criterion (see text).

bulk hard-sphere and soft-sphere dipolar fluids at low temperature, it has been observed that particles associate into chains [35, 36]. On the other hand, as discussed in the previous section, the bulk liquid is isotropic.

We find that clusters containing up to thirty particles form chains in which the particles align head-to-tail. In fact, we find a whole variety of differently shaped clusters in dynamical equilibrium with each other: linear chains, branched-chains, and ring-"polymers". As the cluster size is increased, the "polymers" become longer. But, beyond a certain size, the clusters collapse to form a compact globule. In order to quantify this, we determined the size dependence of the radius of gyration, as well as the three eigenvalues of the moment-of-inertia tensor $\mathbf{I}$

$$\mathbf{I} = \frac{1}{n}\sum_{i=1}^{n} \mathbf{r}_i \mathbf{r}_i, \tag{8.24}$$

where $\mathbf{r}_i$ is the vector joining particle i and the center-of-mass of the cluster. In Fig. 8.4 we show the square of the radius of gyration, divided by $n^{2/3}$. For a compact, spherical object R_g^2 scales with $n^{2/3}$, whereas for chains R_g^2 scales with n^{α}, where $1.2 < \alpha < 2$, depending on the stiffness of the chain. Hence, for chain-like clusters $R_g^2/n^{2/3}$ should increase with n, whereas for a globule it should approach a constant value.

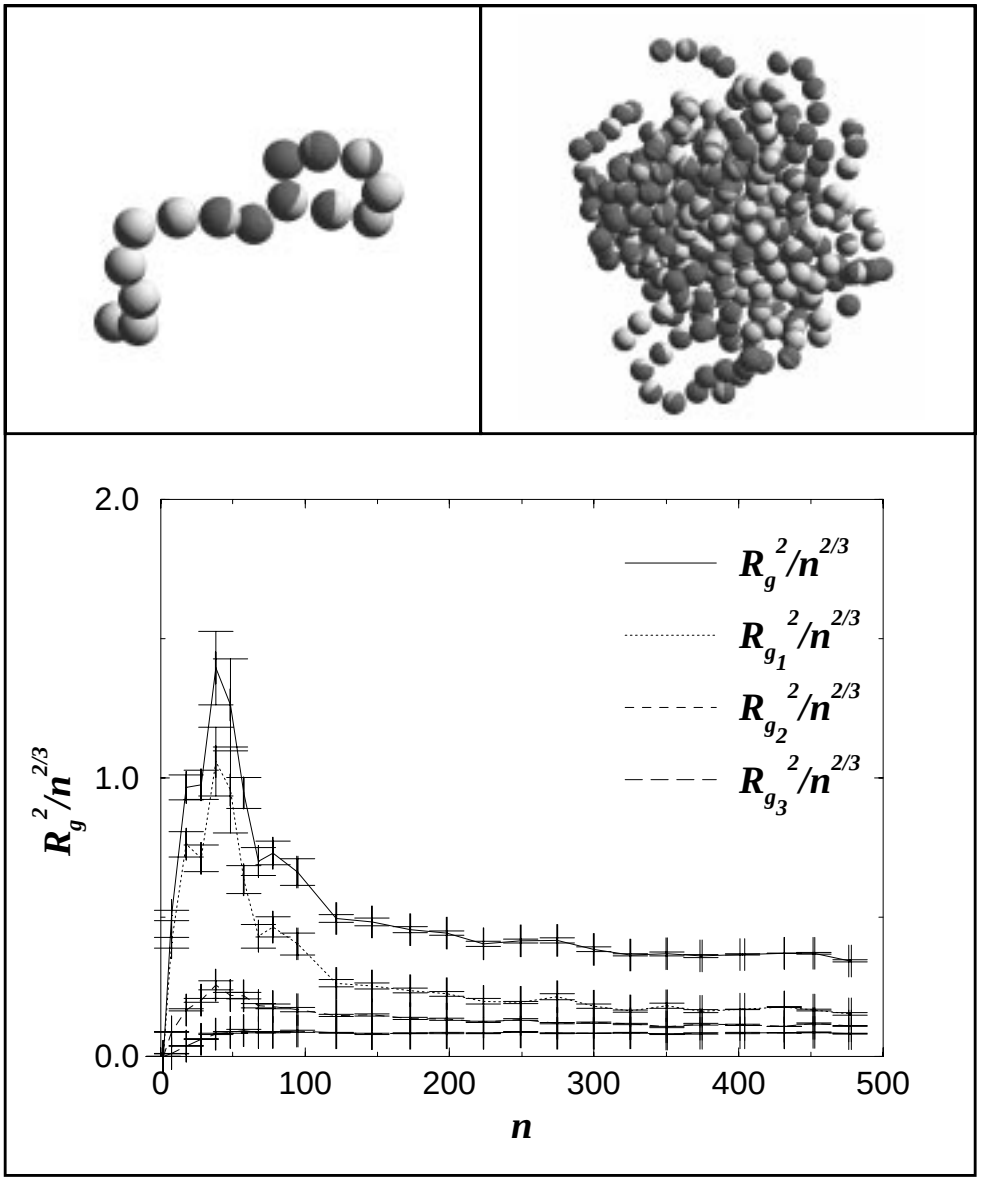

FIGURE 8.4 Radius of gyration R_g, and the three eigenvalues of the moment-of-inertia tensor, as a function of cluster size n, at $S = 1.26$ and $T^* = 3.5$. Initially, the clusters are chain-like (snapshot top left), but at a cluster size of $n \approx 30$ they collapse to compact, spherical nuclei (snapshot top right).

Fig. 8.4 shows that initially $R_g^2/n^{2/3}$ increases with the size of the cluster. Moreover, one eigenvalue of the moment of the inertia matrix is much larger than the other two, which indicates the strong tendency of clusters to form chains. However, at a cluster size of about 30 particles $R_g^2/n^{2/3}$ starts to decrease and approaches a constant value at a cluster size of around 200 particles. Furthermore, at that point the three eigenvalues of the moment-of-inertia tensor have also approached each other: the cluster has collapsed to a compact spherical object.

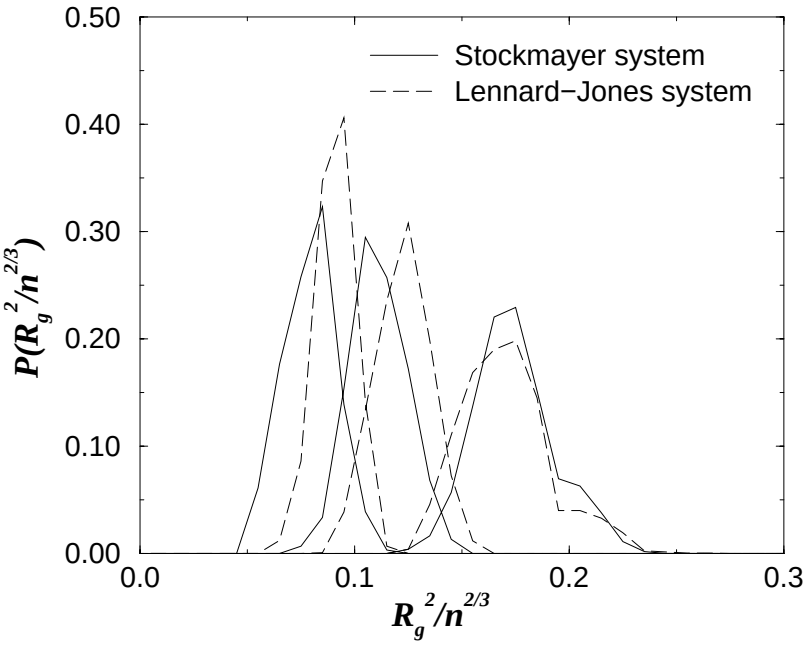

FIGURE 8.5 The distribution functions of the three eigenvalues of the moment-of-inertia tensor for a cluster of around 300 particles in a Stockmayer system at $T^* = 3.5$ ($= 0.7T_c$) and $S = 1.26$. For comparison we also show the distribution functions for a Lennard-Jones cluster of comparable size ($n \approx 300$) and at the same temperature with respect to the critical temperature ($T = 0.7T_c$). In this and subsequent figures σ is the unit of length.

8.4.3 Structure of collapsed nuclei

8.4.3.1 *No global order* An examination of the snapshots of the larger, globule-like nuclei confirm that they are compact, more or less spherical objects. To study this in more detail, we have measured the probability distribution functions of the three eigenvalues of the moment-of-inertia tensor. Fig. 8.5 shows the result. For comparison we also indicate the distribution functions for a Lennard-Jones cluster of comparable size (and at the same temperature with respect to the critical temperature). Note that compared to the Stockmayer cluster the distribution functions of the Lennard-Jones cluster are displaced to somewhat higher values. This is due to the slightly lower density in the Lennard-Jones cluster. Yet, for both the Lennard-Jones system and the Stockmayer system the distribution functions of the three eigenvalues overlap. Hence, the clusters are quite spherical, although the larger spread of the distribution functions of the polar cluster indicates that this cluster exhibits more pronounced fluctuations around the spherical shape. We do not find evidence for a prolate shaped cluster, in which the molecules are aligned in an anti-parallel head-to-tail arrangement, as suggested by Wright and El-Shall [33, 34]. A prolate structure would have two small eigenvalues and one significantly larger eigenvalue of the moment-of-inertia tensor. As can be seen from Fig. 8.5, this is not the case. Furthermore, both the nematic order parameter P_2, which is the largest eigenvalue of the $\mathbf{Q}$ tensor defined in Eq. (8.23), and the ferro-electric order parameter P_1 (see Eq. (8.22)) are zero, indicating that there is no net parallel or anti-parallel alignment of the dipoles in the cluster.

We also investigated the degree of circulating orientational order. To this end, we computed the order parameter

$$\mu_{11} = |\boldsymbol{\mu}_{11}| = \left(\sum_{\alpha=x,y,z} \mu_{11\alpha}^2 \right)^{1/2}, \tag{8.25}$$

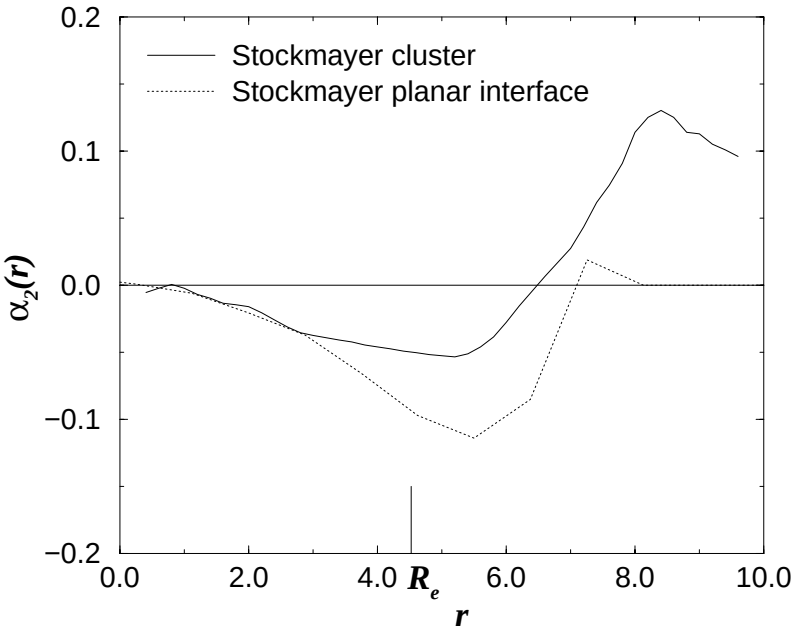

FIGURE 8.6 The profile of the orientational order parameter a_2, as defined in Eq. (8.27), for a planar interface at coexistence and for a cluster of approximately 300 particles at a supersaturation $S = 1.26$. The profile of the planar interface is shifted such that its equimolar dividing surface coincides with that of the cluster, as indicated by the vertical line at R_e.

with

$$\mu_{11\alpha} = \frac{1}{n}\sum_{i=1}^{n}(\hat{\mathbf{e}}_\alpha \times \hat{\mathbf{r}}_i)\cdot\hat{\boldsymbol{\mu}}_i, \tag{8.26}$$

where $\hat{\mathbf{e}}_\alpha$ is a unit-vector in the α-direction, $\hat{\boldsymbol{\mu}}_i$ denotes the orientation of the dipole of particle i, and $\hat{\mathbf{r}}_i$ is the unit vector from the center-of-mass of the cluster to particle i. This order parameter was introduced by Singer et al. [161] and measures the degree to which the cluster contains dipoles circulating about a particular axis. Singer et al. [162] have studied Stockmayer clusters consisting of 50 particles with a reduced dipole moment of $\mu^* = \sqrt{3}$, and found that the (liquid) clusters had an oblate shape with a large degree of circulating orientational order up to $T^* = 0.8$, which is 60% below T_c^*. However, this temperature is much lower than in the present simulations ($T^* = 0.7T_c^*$) and indeed we do not find evidence for an oblate shape (one eigenvalue of the moment-of-inertia tensor would then be significantly smaller than the other two), nor do we find any significant circulating orientational order ($\mu_{11} < 0.14$). Hence, the global order parameters indicate that the large, collapsed clusters are spherical with no net global orientational order.

8.4.3.2 *Interfacial structure* In the previous section, we found that the larger, collapsed nuclei are spherical, with no net global orientational order. Let us next examine the *local* order. Given the spherical shape of the clusters it is meaningful to analyze the local order as a function of the distance r to the center-of-mass of the cluster. Fig. 8.6 shows the radial profile of α_2, which is defined as

$$\alpha_2 = \sqrt{5/4\pi}\langle P_2(\cos\theta)\rangle, \tag{8.27}$$

where θ is the angle between the director of the dipole and the normal to the surface. It measures the degree to which the dipoles are oriented perpendicular to the surface. It is seen that α_2 approaches zero in the center of the droplet. This indicates that the orientation of the dipoles in the core of the droplets is isotropic and suggests that the core of the droplet shows bulk liquid behavior. To verify this we have measured the

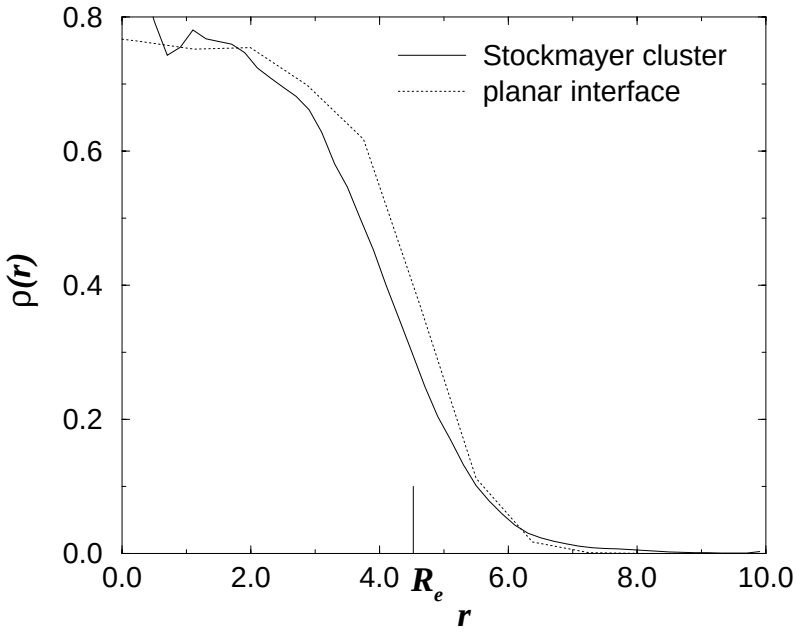

FIGURE 8.7 Density profile for a planar vapor-liquid interface at coexistence and for a cluster of around 300 particles at a supersaturation $S = 1.26$ ($T^* = 3.5$). The density profile of the planar interface is shifted such that the equimolar dividing surface of the planar interface coincides with the equimolar dividing surface of the cluster. The equimolar dividing surface is indicated by the vertical line at R_e.

density profile, which is shown in Fig. 8.7. It is seen that also the density approaches a bulk liquid value in the core of the droplets. It thus seems that the core of the larger, collapsed nuclei are characterized by bulk liquid properties.

However, in the interface the nuclei start to loose their bulk liquid character. Fig. 8.6 shows that near the interface the orientation of the dipoles is not isotropic. In agreement with previous simulation results [162, 163] and theoretical studies [151] we find that at the liquid (core) side of the interface the dipoles tend to orient parallel to the interface, whereas at the vapor side they prefer a perpendicular orientation. Hence, the assumption that the dipoles are oriented perpendicular to the surface at the *liquid* side of the interface [150], is not justified for this polar fluid.

In most nucleation theories it is assumed that the surface tension of a cluster is that of a planar interface at coexistence. It is therefore natural to compare the structure of the interface of the nuclei with that of the flat interface. Fig. 8.6 shows the comparison for the α_2-profile. It is seen that also for the planar interface the dipoles tend to align parallel to the interface at the liquid side, but perpendicular to the interface at the vapor side. However, the ordering is much more pronounced for the planar interface at the liquid side. In contrast, at the vapor side the ordering is stronger for the cluster interface.

Still, both for the planar interface and the interface of the nuclei, α_2 changes sign after the equimolar dividing surface. In this respect, our findings are in agreement with those of Singer et al. [162]. However, the simulation results are in contradiction with the results of a density functional study of homogeneous nucleation in a (weakly) polar fluid, in which it was found that both for the planar interface and for the cluster interface, α_2 changes sign *before* the equimolar dividing surface [151].

In our study of crystal nucleation in a Lennard-Jones system we found that the structure of the small clusters, that initiate the nucleation process, still persists in the interface of the larger clusters. To be more precise, we observed that the structure in the

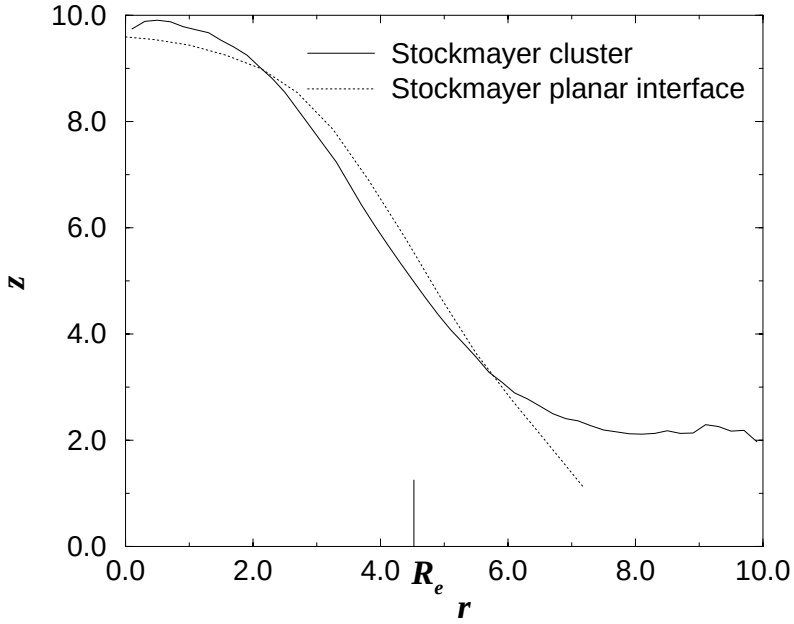

FIGURE 8.8 Radial profile of the coordination number for a Stockmayer cluster at $S = 1.26$ and $T^* = 3.5$ (solid line). The coordination number z is defined as the number of particles within a cutoff-distance $q_c = 1.5\sigma$. For comparison we also give the coordination number profile for a planar interface (dotted curve), which is shifted in such a way that its equimolar dividing surface coincides with that of the cluster, which is indicated by the vertical line at R_e.

core is that of the thermodynamically most stable phase, but that the core is "wetted" by a shell with a structure characteristic for the smaller clusters. We have therefore examined whether in the present case we also find traces of the tendency to form chains at the surface of the larger, collapsed, clusters.

A visual inspection (see Fig. 8.4) of these clusters suggests that loops of dipolar chains stick out of the surface (leading to a positive value of α_2, see Fig. 8.6). In order to quantify this behavior, we have computed the radial profile of the coordination number for a cluster of around 300 particles. This is shown in Fig. 8.8. It is seen that the coordination number smoothly approaches a value of two at the vapor side of the interface. Such behavior is expected if the particles on the vapor side of the interface belong to chains. For comparison, we have also shown in Fig. 8.8 the coordination number profile for the planar interface. As the number density in the vapor is extremely low, smaller than $1 \times 10^{-3}\sigma^{-3}$, it was not possible to get accurate statistics beyond $r = 6.75\sigma$. However, it is clearly seen that at the vapor side of the planar interface the coordination number drops below two. Hence, the planar interface is smoother than the interface of the clusters. Also an inspection of the density profiles (see Fig. 8.7) shows that the planar interface is sharper than the interface of a collapsed cluster of around 300 particles–the width of the interface of the cluster is some 25% larger. Most likely, the planar interface is sharper because the stronger dispersion interactions with the bulk causes the dipole chains to adsorb.

8.4.4 Comparison with classical nucleation theory

In classical nucleation theory (CNT) the excess free of a cluster as a function of its size is given by

$$\beta\Delta\Omega(n) = \beta\left[\left(\frac{36\pi}{\rho_l^2}\right)^{1/3}\gamma n^{2/3} - \Delta\mu n\right]. \tag{8.28}$$

where ρ_l is the density of the bulk liquid (which is assumed to be incompressible), γ is the surface tension of a planar vapor-liquid interface at coexistence, and $\Delta\mu = \mu_v(P_v) - \mu_l(P_v)$ is the difference in chemical potential between a bulk liquid and a bulk vapor, both at the imposed pressure P_v.

The prediction of classical nucleation theory for the height of the nucleation barrier and the size of the critical nucleus can be obtained by taking the derivative of Eq. (8.28) with respect to the cluster size n. We then find for the height of the barrier

$$\beta\Delta\Omega^* = \beta\frac{16\pi\gamma^3}{3\rho_l^2\Delta\mu^2}, \tag{8.29}$$

and for the size of the critical nucleus

$$n^* = \frac{32\pi\gamma^3}{3\rho_l^2\Delta\mu^3}. \tag{8.30}$$

In order to compare our simulation results with classical nucleation theory we computed γ by the procedure outlined in section 8.3.3. We found $\gamma = 1.34 \pm 0.07\epsilon/\sigma^2$. As the density in the vapor is much lower than the density in the liquid, the $\mu(P)$ curve of the vapor phase is much steeper than that of the liquid. We therefore made the common assumption that the difference in chemical potential can be approximated by $\Delta\mu = \mu_v(P_v) - \mu_l(P_v) \simeq \mu_v(P_v) - \mu_{coex}$. The chemical potential at coexistence was determined using the method discussed in section 8.3.2 and was found to be $\mu_{coex} = -26.82 \pm 0.02\epsilon$. The density of the liquid at this chemical potential is $\rho_l = 0.78 \pm 0.01\sigma^{-3}$.

Let us now discuss in more detail the basic assumptions of classical nucleation theory that lead to Eqs. (8.28)–(8.30). First of all, it is assumed that the nuclei behave like small droplets of bulk liquid that are spherical. As discussed previously, the larger nuclei, comprising more than approximately 200 particles, are quite spherical. However, the smaller clusters, that initiate the nucleation process in this system, are not compact, spherical objects, but chain-like aggregates. As a consequence, the variation in free energy with cluster size is not as predicted by classical nucleation theory. We note that if the clusters were perfectly rigid chains, the variation in free energy with cluster size would be linear. Indeed, as can be seen from Fig. 8.2, we find that after $n \approx 5$ the increase in cluster free energy is very linear with its size. The barrier shape predicted by classical nucleation theory (see Eq. (8.28)) is only recovered after the clusters have collapsed.

The linear regime in the size dependence of the cluster free energy has a remarkable consequence for the dependence of the critical nucleus size on supersaturation (see Fig. 8.9b). When the supersaturation is increased, the height of the nucleation barrier and the critical nucleus size decrease. However, at a supersaturation of $S = 1.8$ ($1/(\beta\Delta\mu)^3 = 5.25$), the critical clusters have reached a size at which the variation in free energy with cluster size is linear. At this point, the top of the barrier is flat, and

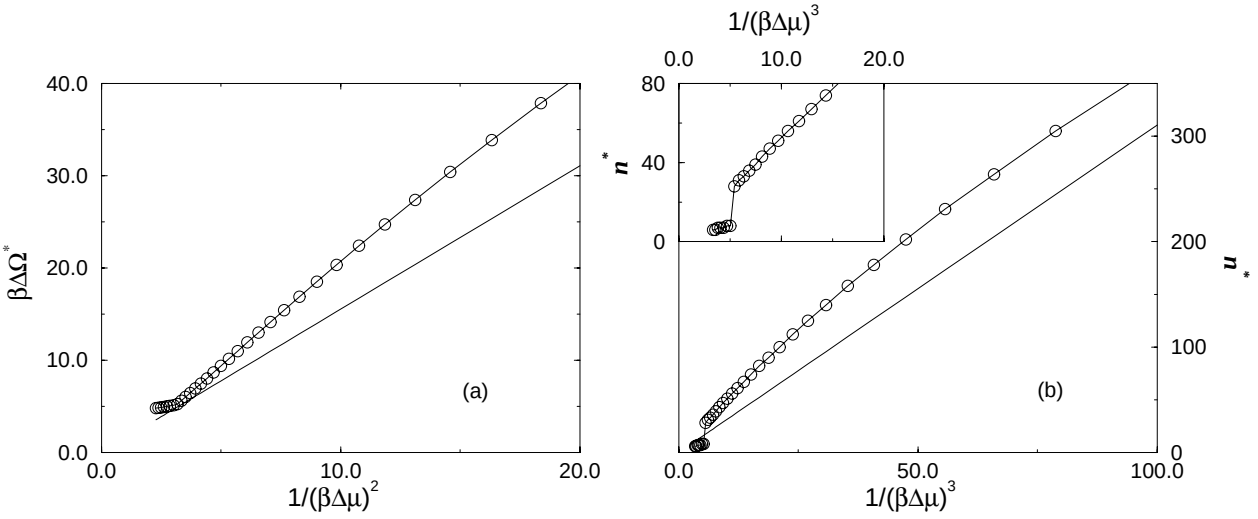

FIGURE 8.9 Comparison of the simulation results (open circles) with classical nucleation theory (straight solid line) for a Stockmayer system at $S = 1.26$ and $T^* = 3.5$: (a) nucleation barrier; (b) size of the critical cluster.

a small increase in the supersaturation leads to a jump in the critical cluster size (see inset of Fig. 8.9b).

It is thus clear that at large supersaturation, where the critical nuclei are relatively small, the polymer-like character of the clusters leads to strongly non-classical nucleation behavior. However, even for the collapsed globule-like nuclei, the simulation results show large deviations from classical nucleation theory. This can be seen from Fig. 8.9. This figure shows the comparison between the simulation results and the predictions of classical nucleation theory for the height of the barrier and the critical nucleus size. Clearly, the theory underestimates both the size of the critical nucleus and the height of the nucleation barrier. As the variation in the nucleation rate is dominated by the variation in the barrier height, our results are in qualitative agreement with the experiments on strongly polar fluids [33, 34], in which it was found that classical nucleation theory seriously overestimates the nucleation rate.

We would like to understand the origin of this discrepancy between classical nucleation theory and the simulations. As mentioned, the larger, collapsed nuclei are spherical. Also the assumption of classical nucleation theory that the cores of these nuclei show bulk liquid behavior seems to be justified, as the density and the orientational order parameter α_2 approach bulk liquid values in the center of the droplets.

However, CNT neglects the variation of surface tension with droplet size. In fact, McGraw and Laaksonen [13] showed that the interfacial curvature free energy can cause a significant correction to the barrier height as predicted by classical nucleation theory. They derived relations [12, 13] for the barrier height and the critical nucleus size, that could provide an explanation for the discrepancy between experiment and classical nucleation theory for a variety of nonpolar and weakly polar fluids [130]. In particular, McGraw and Laaksonen [13] showed that if CNT correctly predicts the size of the critical nucleus, then the curvature correction yields a constant offset between the actual barrier height and the height of the barrier as predicted by classical nucleation theory.

It is interesting to note that this behavior has been observed in both a density functional study [13, 12] and in our computer simulation study of gas-liquid nucleation in the Lennard-Jones system (see chapter 5). It was found that for a wide range of cluster sizes CNT gives a correct prediction of the critical nucleus size and that the deviation from the predicted barrier height is constant, i.e. independent of cluster size.

However, for this polar system, the displacement between the measured barrier height and the predicted height of the barrier is not constant, as can be seen from Fig. 8.9. More clearly, the critical nucleus size is not correctly predicted by CNT. Hence, in contrast to the (non-polar) Lennard-Jones fluid, the scaling relations are not obeyed for this highly polar fluid. A possible explanation could be that, whereas the interface of a Lennard-Jones critical nucleus is nearly indistinguishable from the planar interface, for this system the structure of the interface of the critical clusters is still markedly different from the planar interface.

Finally, it is interesting to consider the implications of our findings for the nucleation behavior of polar fluids without attractive dispersion forces. For these fluids, the tendency to form chains will be even more pronounced and the point at which the clusters collapse will shift to larger cluster sizes. This means that condensation will be preceded (and possibly preempted) by the growth of very large, polymer-like clusters. It is conceivable that the "gel"-like phase observed in the simulations of Refs. [36, 152] is, in fact, an interpenetrating network of uncollapsed dipolar chain clusters.

Appendix Pressure tensor

For pair-wise additive potentials, such as the Lennard-Jones potential, the $\alpha\beta$ element of the pressure tensor can be evaluated from the virial equation for the pressure

$$P_{\alpha\beta} = \rho k_B T + \frac{1}{V}\sum_{i<j}^{N} r_{ij\alpha} f_{ij\beta}, \tag{8.31}$$

where $\mathbf{r}_{ij}$ is the vector between i and j and $f_{ij\beta}(\mathbf{r}_{ij}, \boldsymbol{\mu}_i, \boldsymbol{\mu}_j) = -\frac{\partial v(\mathbf{r}_{ij}, \boldsymbol{\mu}_i, \boldsymbol{\mu}_j)}{\partial r_{ij\beta}}$ is the intermolecular force. However, in the Ewald sum, that contains a real space contribution and a reciprocal space contribution, the pressure tensor cannot be written as in Eq. 8.31.

The electrostatic energy U_{dip} of the dipolar interactions in the Stockmayer system, embedded in a material with infinite dielectric constant, is [159]

$$\begin{aligned} U_{dip} =& \frac{1}{2}\sum_{i\neq j}^{N}(\boldsymbol{\mu}_i \cdot \boldsymbol{\mu}_j)B(r_{ij}) - (\boldsymbol{\mu}_i \cdot \mathbf{r}_{ij})(\boldsymbol{\mu}_j \cdot \mathbf{r}_{ij})C(r_{ij}) - \frac{2\alpha^3}{3\sqrt{\pi}}\sum_{i=1}^{N}\mu_i^2 + \\ & \frac{2\pi}{V}\sum_{\mathbf{k}\neq 0} Q(k)M(\mathbf{k})M(-\mathbf{k}), \end{aligned} \tag{8.32}$$

where α is the convergence parameter,

$$B(r) \equiv \left[\frac{2\alpha r}{\sqrt{\pi}}\exp(-\alpha^2 r^2) + \mathrm{erfc}(\alpha r)\right] \Big/ r^3, \tag{8.33}$$

$$C(r) \equiv \left[\frac{2\alpha r}{\sqrt{\pi}}(3 + 2\alpha^2 r^2)\exp(-\alpha^2 r^2) + 3\mathrm{erfc}(\alpha r)\right] \Big/ r^5, \tag{8.34}$$

with erfc the complementary error function, and

$$Q(k) \equiv \frac{\exp(-k^2/4\alpha^2)}{k^2}, \tag{8.35}$$

and

$$M(\mathbf{k}) \equiv \sum_{i=1}^{N} i(\boldsymbol{\mu}_i \cdot \mathbf{k}) \exp(i\mathbf{k} \cdot \mathbf{r}_i). \tag{8.36}$$

Here $\mathbf{k}$ are the reciprocal lattice vectors, which are defined as

$$\mathbf{k} \equiv (2\pi l/L_x, 2\pi m/L_y, 2\pi n/L_z), \tag{8.37}$$

where l, m and n are integers.

The first two terms in Eq. (8.32) are the real-space contributions, the third term is the so-called self term expressing the self-energy of the dipoles, and the last term in Eq. (8.32) is the reciprocal space contribution. The real-space contribution to the pressure tensor is obtained by evaluating the second term on the right hand side of Eq. (8.31)

$$\begin{aligned} P_{\alpha\beta} =& \frac{1}{2V} \sum_{i \neq j}^{N} r_{ij\alpha} \{ C(r_{ij}) [r_{ij\beta} (\boldsymbol{\mu}_i \cdot \boldsymbol{\mu}_j) + \mu_{i\beta} (\boldsymbol{\mu}_j \cdot \mathbf{r}_{ij}) + \mu_{j\beta} (\boldsymbol{\mu}_i \cdot \mathbf{r}_{ij})] + \\ & \frac{C'(r_{ij})}{r_{ij}} r_{ij\beta} (\boldsymbol{\mu}_i \cdot \mathbf{r}_{ij}) (\boldsymbol{\mu}_j \cdot \mathbf{r}_{ij}) \}, \end{aligned} \tag{8.38}$$

where

$$C'(r) \equiv \frac{\partial C}{\partial r} = - \left[15 \mathrm{erfc}(\alpha r) + \frac{2\alpha r}{\sqrt{\pi}} (15 + 10\alpha^2 r^2 + 4\alpha^4 r^4) \exp(-\alpha^2 r^2) \right] \Big/ r^6. \tag{8.39}$$

In order to calculate the reciprocal space contribution to the pressure tensor we have followed the procedure of Nosé and Klein [164]. In this procedure the pressure tensor is obtained from the variation in potential energy with a deformation of the system. The reciprocal space contribution to the pressure tensor is

$$\begin{aligned} P_{\alpha\beta} =& \frac{2\pi}{V^2} \sum_{\mathbf{k} \neq 0} Q(k) \{ M(\mathbf{k}) M(-\mathbf{k}) \left(\delta_{\alpha\beta} - \frac{2k_\alpha k_\beta}{k^2} - \frac{k_\alpha k_\beta}{2\alpha^2} \right) + \\ & M(\mathbf{k}) V_{\alpha\beta}(-\mathbf{k}) + M(-\mathbf{k}) V_{\alpha\beta}(\mathbf{k}) \}, \end{aligned} \tag{8.40}$$

where $V_{\alpha\beta}(\mathbf{k})$ is given by

$$V_{\alpha\beta}(\mathbf{k}) = \sum_{i=1}^{N} i\mu_{i\alpha} k_\beta \exp(i\mathbf{k} \cdot \mathbf{r}_i). \tag{8.41}$$

A similar expression has been independently derived by Heyes [165], although in Ref. [165] a minus sign in the second exponential on the right hand side of Eq. (34) is missing.

We found that the above expressions for the pressure tensor could be used as a convergence test for the Ewald-summation. From the definition of the dipolar interaction potential (see Eq. (8.1)) and from the definition of the virial equation for the pressure

(see Eq. (8.31)) it can be verified that for dipolar interactions the interaction energy is equal to the virial, i.e.

$$\sum_{i<j}^{N} v(\mathbf{r}_{ij}, \boldsymbol{\mu}_i, \boldsymbol{\mu}_j) = \frac{1}{3} \sum_{i<j}^{N} \mathbf{r}_{ij} \cdot \mathbf{f}(\mathbf{r}_{ij}, \boldsymbol{\mu}_i, \boldsymbol{\mu}_j). \tag{8.42}$$

Hence, the virial and thus the pressure can be directly obtained from the potential energy. On the other hand, the virial should also given by the trace of the stress tensor, i.e. by the sum of the traces of the stress tensors in Eqs. (8.38) and (8.40). In Fig. 8.10 we compare the two ways of obtaining the pressure. It is seen that the pressures obtained via the two routes nicely converge to the same value after $|k_x^{max}| = |k_y^{max}| = 1/4|k_z^{max}| = 7$.

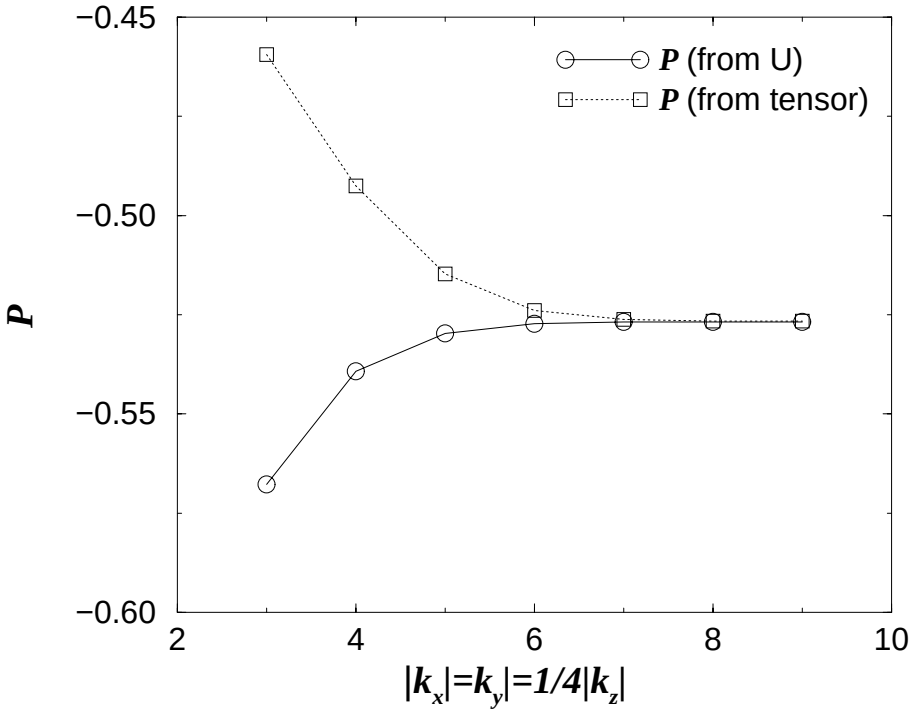

FIGURE 8.10 Convergence test for the Ewald summation. Indicated are two ways of obtaining the pressure, as a function of the number of reciprocal lattice vectors. The line with the open circles gives the pressure obtained from the potential energy. The dotted curve with the square symbol gives the pressure obtained via the trace of the pressure tensor, i.e. via Eq. (8.38) and Eq. (8.40). It is seen that both routes give the same pressure after $|k_x^{max}| = |k_y^{max}| = 1/4|k_z^{max}| = 7$.

9 Enhancement of Protein Crystal Nucleation by Critical Density Fluctuations

Numerical simulations of homogeneous crystal nucleation using a model for globular proteins with short range attractive interactions show that the presence of a metastable fluid-fluid critical point drastically changes the pathway for the formation of a crystal nucleus. Close to this critical point, the free-energy barrier for crystal nucleation is strongly reduced and hence the crystal nucleation rate increases by many orders of magnitude. As the location of the metastable critical point can be controlled by changing the composition of the solvent, the present work suggests a systematic approach to promote protein crystallization.

9.1 Introduction

Due to rapid developments in biotechnology, we are witnessing an explosive growth in the number of proteins that can be isolated. However, the determination of the three-dimensional structures of proteins by X-ray crystallography, remains a time-consuming process. One bottleneck is the difficulty of growing good protein crystals. In his book on this subject, McPherson [166] wrote *"The problem of crystallization is less approachable from a classical analytical standpoint, contains a substantial component of trial and error, and draws more from the collective experience of the past century. [$\cdots$] It is much like prospecting for gold"*. The experiments clearly indicate that the success of protein crystallization depends sensitively on the physical conditions of the initial solution [166–168]. It is therefore crucial to understand the physical factors that determine whether a given solution is likely to produce good crystals.

Recent studies have shown that not just the strength, but also the range of the interactions between protein molecules is of crucial importance for crystal nucleation. In 1994, George and Wilson [169] demonstrated that the success of protein crystallization appears to correlate with the value of B_2, the second osmotic virial coefficient of the protein solution.

The second virial coefficient describes the lowest order correction to the van 't Hoff law for the osmotic pressure Π:

$$\frac{\Pi}{\rho k_B T} = 1 + B_2\rho + (\text{terms of order } \rho^2) \tag{9.1}$$

where ρ is the number density of the dissolved molecules, k_B is Boltzmann's constant, and T is the absolute temperature. For macromolecules, B_2 can be determined from static light scattering experiments [170]. Its value depends on the effective interaction

between a pair of macromolecules in solution [171]:

$$B_2 = 2\pi \int r^2 dr[1 - \exp[-\beta v(r)]] \tag{9.2}$$

where $\beta \equiv 1/k_B T$ and $v(r)$ is the interaction energy of a pair of molecules at distance r.

George and Wilson measured B_2 for a number of proteins in various solvents. They found that for those solvent conditions that are known to promote crystallization, B_2 was restricted to a narrow range of small negative values. For large positive values of B_2 crystallization did not occur at all, whereas for large negative values of B_2 protein aggregation, rather than crystallization, took place. This correlation has been extended to over 20 distinct proteins with a wide variety of crystal structures and interaction potentials [37].

Recently, Rosenbaum, Zamora and Zukoski [37, 38] established a link between the work of George and Wilson and a computer-simulation study by Hagen and Frenkel [172], who studied the effect of the range of intermolecular attractions on the phase diagram of spherical colloids in colloid-polymer mixtures. In colloid-polymer mixtures, the range of interaction between the colloids can be controlled by tuning the radius-of-gyration of the polymer. Since the theoretical work of Gast, Hall and Russel [173, 174], it is known that the range of attraction between spherical colloids has a drastic effect on the overall appearance of the phase diagram. If the range of attraction is long in comparison to the diameter of the colloids, the phase diagram of the colloidal suspension resembles that of an atomic substance, such as argon: depending on the temperature and density, the colloids can occur in three phases (Fig.1A) – a dilute colloidal fluid (analogous to the vapor phase), a dense colloidal fluid (analogous to the liquid phase), and a colloidal crystal phase. However, when the range of the attraction is reduced, the fluid-fluid critical point moves towards the triple point, where the solid coexists with the dilute and dense fluid phases. At some point, the critical point and the triple point will coalesce. If the range of attraction is made even shorter (less than some 25% of the colloid diameter), only two stable phases remain: one fluid and one solid (Fig.1B). However, the fluid-fluid coexistence curve survives in the metastable regime below the fluid-solid coexistence curve (Fig.1B). This is indeed found in experiments [175–178] and simulations [172].

Why is this relevant for protein crystallization? First of all, globular proteins in solution often have short-ranged attractive interactions. In fact, a series of studies [179–182] show that the phase diagram of a wide variety of proteins is of the kind shown in Fig.1B. Moreover, the range of the effective interactions between proteins can be changed by the addition of non-adsorbing polymer (such as poly-ethylene glycol) [176, 183] or by changing the pH or salt concentration of the solvent [166, 167].

The interesting observation presented by Rosenbaum, Zamora and Zukoski [37, 38] is that the conditions under which a large number of globular proteins can be made to crystallize, map onto a narrow temperature range, or, more precisely, a narrow range in the value of the osmotic second virial coefficient, of the computed fluid-solid coexistence curve of colloids with short-ranged attraction [172]. If the temperature is too high, crystallization is hardly observed at all, whereas if the temperature is too low, amorphous precipitation rather than crystallization occurs. Only in a narrow window

around the metastable critical point, high-quality crystals can be formed. Several authors had already noted that a similar crystallization window exists for colloidal suspensions [184, 185]. The aim of the present study is to use simulation to gain insight into the physical mechanism responsible for the enhanced crystal nucleation. We show that the presence of a metastable fluid-fluid critical point is essential.

The rate-limiting step in crystal nucleation is the crossing of the free-energy barrier. We have computed the free-energy barrier for homogeneous crystal nucleation for a model "globular" protein. We show that in the "window" where successful protein crystallization is observed, the free-energy barrier for homogeneous crystal nucleation is anomalously low. Moreover, our simulations shed light on the mechanism responsible for the easier crystal nucleation in this window–the formation of a critical nucleus is assisted by the presence of strong density fluctuations in the vicinity of the metastable fluid-fluid critical point.

The rest of the chapter is organized is as follows. In the next section we first briefly describe the model and its phase-diagram. We then present the simulation techniques to compute the free-energy barriers in section 9.3 and we end with a discussion of the results.

9.2 Model

Rosenbaum, Zamora, and Zukoski [37, 38] argued that for proteins the range of the interaction potential is short compared to their size. Hence, proteins and other globular macromolecules should fall into a class of materials where only fluid and crystal equilibrium will be observed. To test this conjecture, Rosenbaum *et al.* [37, 38] examined the solubility behavior for a number of globular proteins in terms of two experimentally accessible parameters, the density ρ and the sticky sphere parameter τ. The sticky sphere parameter τ is related to the second virial coefficient of the osmotic pressure, B_2, and is defined as

$$\tau = \frac{1}{4(1 - 3B_2/2\pi\sigma^3)} = \frac{1}{4(1 - B_2/B_{2,HS})}, \tag{9.3}$$

where $B_{2,HS}$ is the second virial coefficient for hard-spheres of diameter σ. As mentioned, B_2 can be measured by static light scattering.

Rosenbaum, Zamora, and Zukoski [37, 38] found that a variety of globular proteins display a common solubility curve when compared on equal footing (i.e. on the basis of ρ and τ). This indicates that the solubility boundary is only weakly dependent on particle type and suggests that the phase-boundaries are insensitive to the details of the interaction potential. Moreover, they showed that the crystal-fluid phase boundaries of the proteins in solution can be mapped onto the fluid-solid sublimation curve of the hard-core Yukawa potential [172], provided that σ/κ, the particle diameter scaled by the Yukawa screening length, is larger than seven. For these values of σ/κ, the range of the attractive part of the Yukawa potential is less than one-sixth of the hard-core diameter and the liquid-vapor critical point has become metastable. This clearly shows that the phase-behavior of globular macromolecules such as proteins can indeed be explained as arising from attractive interactions which have a range that is small compared to the particle diameter.

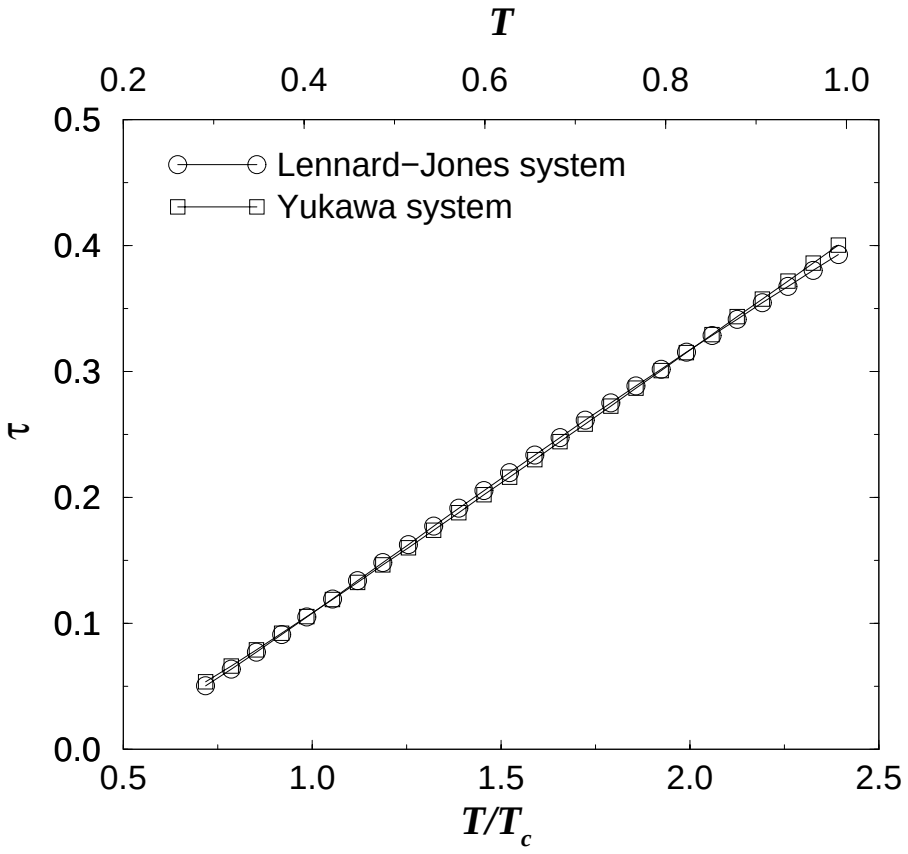

FIGURE 9.1 The sticky-sphere parameter τ, defined in Eq. (9.3) for the modified Lennard-Jones potential with $\alpha = 50$ (see Eq. (9.4)) and the hard-core Yukawa potential with $\sigma/\kappa = 7$, as a function of the temperature T. T_c is the temperature of the metastable liquid-vapor critical point in the modified Lennard-Jones system.

As the details of the interaction potential are of minor importance, we have some freedom in choosing an interaction potential for our model. A natural choice would be the hard-core Yukawa potential. However, this interaction potential shows a discontinuity in the derivative at $r = \sigma$, which makes it not very convenient for Molecular Dynamics (MD). For the interaction between particles we therefore chose a suitable generalization of the Lennard-Jones potential:

$$v(r) = \begin{cases} \infty & (r < \sigma) \\ \frac{4\epsilon}{\alpha^2}\left(\frac{1}{[(r/\sigma)^2-1]^6} - \alpha\frac{1}{[(r/\sigma)^2-1]^3}\right) & (r \geq \sigma) \end{cases} \tag{9.4}$$

where σ denotes the hard-core diameter of the particles and ϵ the well depth. The width of the attractive well can be adjusted by varying the parameter α. The value of α was tuned in such a way that the parameter τ equals that of the hard-core Yukawa potential for $\sigma/\kappa = 7$ at the (metastable) liquid-vapor critical point. The value of B_2 is given by

Eq. (9.2) and $B_{2,HS}$ for the modified Lennard-Jones potential in Eq. (9.4) is given by

$$B_{2,HS} = \frac{2}{3}\pi\sigma^3 + 2\pi \int_{\sigma}^{r_{min}} r^2 dr[1 - \exp[-\beta v_{12}(r)]], \tag{9.5}$$

where r_{min} is the minimum of the potential in Eq. (9.4) and $v_{12}(r)$ is the repulsive part of the modified Lennard-Jones potential:

$$v_{12}(r) = \frac{4\epsilon}{\alpha^2} \frac{1}{[(r/\sigma)^2 - 1]^6}. \tag{9.6}$$

We found that for $\alpha = 50$ the τ-parameter of the modified Lennard-Jones potential was equal to that of the hard-core Yukawa potential with $\sigma/\kappa = 7$ at the metastable liquid-vapor critical point. But we would like to mention that not only at the critical point of the Yukawa model the sticky-sphere parameters are equal, but over a wide ranges of temperatures, which is shown in Fig. 9.1.

In order to map out the phase-diagram for our model protein we have performed Gibbs-ensemble Monte Carlo simulations to determine the liquid-vapor coexistence curve [129]. The solid-fluid coexistence line was computed using the procedure developed by Meijer and El Azhar [186], which combines elements of the Clausius-Clapeyron integration technique with free-energy difference calculations. In all simulations, the interaction potential was truncated and shifted at $r_c = 2.0\sigma$. In what follows, we use reduced units, such that ϵ is the unit of energy and σ is the unit of length.

The Gibbs-ensemble simulations were performed for a system size of $N = 216$ and $N = 512$ particles. As the temperature is relatively low, the particles are rather "sticky" giving rise to high-frequency, low-amplitude oscillations superimposed on low-frequency, high-amplitude fluctuations of the densities in both boxes. We therefore had to perform extensive simulations, in order to obtain accurate statistics. The number of equilibration cycles was at least 1×10^5, and the number of production cycles was more than 1×10^6. One Gibbs-ensemble cycle consisted, on average, of one trial displacement of every particle, one attempt per particle to exchange it between the two simulation boxes, and

TABLE 9.1 Coexistence data for the (metastable) vapor-liquid coexistence. T is the reduced temperature, T/T_c is the reduced temperature scaled by the critical temperature T_c, ρ is the density and u is the potential energy per particle. The number in brackets denotes the accuracy of the last digit. The "-" indicates that the boxes changed identity during the simulations.

		Vapor phase			Liquid phase		
T	T/T_c	ρ_v	P_v	u_v	ρ_l	P_l	u_l
0.357	0.854	0.023 (7)	0.007 (1)	-0.17 (5)	0.68 (1)	0.01 (1)	-3.12 (5)
0.364	0.871	0.028 (8)	0.009 (2)	-0.19 (7)	0.66 (1)	0.00 (1)	-3.04 (7)
0.370	0.885	0.04 (1)	0.010 (2)	-0.24 (8)	0.65 (1)	0.01 (1)	-2.94 (8)
0.377	0.902	0.04 (1)	0.013 (3)	-0.29 (9)	0.63 (2)	0.01 (1)	-2.81 (8)
0.385	0.921	0.06 (1)	0.016 (3)	-0.4 (1)	0.60 (2)	0.02 (1)	-2.7 (1)
0.392	0.938	0.08 (1)	0.020 (3)	-0.5 (1)	0.57 (3)	0.02 (1)	-2.5 (1)
0.400	0.957	0.11 (3)	0.03 (1)	-	0.53 (4)	0.03 (1)	-

TABLE 9.2 Coexistence data for the fluid-solid coexistence curve; T is the reduced temperature, T/T_c is the reduced temperature scaled with the critical temperature T_c, ρ is the density, u is the potential energy per particle, and P is the coexistence pressure. The number in brackets denotes the accuracy of the last digit.

		Fluid phase		Solid phase		
T	T/T_c	ρ_f	u_f	ρ_s	u_s	P
6.000	14.354	0.687 (5)	-0.80 (4)	0.764 (3)	-1.57 (4)	46.71 (3)
1.500	3.589	0.657 (6)	-2.23 (3)	0.781 (5)	-3.26 (6)	8.44 (2)
0.900	2.153	0.629 (9)	-2.29 (5)	0.824 (4)	-4.07 (7)	3.271 (3)
0.650	1.555	0.567 (7)	-2.07 (4)	0.853 (1)	-4.65 (2)	1.067 (7)
0.580	1.388	0.508 (6)	-1.84 (3)	0.861	-4.83 (1)	0.520
0.545	1.304	0.43 (1)	-1.57 (4)	0.865	-4.92 (2)	0.283
0.530	1.268	0.391 (9)	-1.43 (4)	0.867	-4.96 (1)	0.199
0.515	1.232	0.32 (2)	-1.18 (7)	0.868	-4.99 (2)	0.131
0.500	1.196	0.22 (2)	-0.87 (6)	0.870	-5.04 (1)	0.0831
0.485	1.160	0.140 (8)	-0.60 (4)	0.872	-5.07 (1)	0.0518
0.470	1.124	0.085 (4)	-0.39 (2)	0.873	-5.11 (2)	0.0329
0.455	1.089	0.052 (2)	-0.259 (8)	0.875	-5.16 (1)	0.0207
0.440	1.053	0.0322 (9)	-0.173 (7)	0.877	-5.19	0.0129
0.420	1.005	0.0169 (2)	-0.098 (2)	0.879	-5.23	0.0067
0.400	0.957	0.0086	-0.055 (1)	0.881	-5.29	0.0033
0.370	0.885	0.0028	-0.021 (1)	0.884	-5.36	0.0010
0.340	0.813	0.0008	-0.007	0.887	-5.43	0.0003
0.310	0.742	0.0002	-0.002	0.889	-5.49	0.00005

two attempts to exchange volume between the two boxes. To check that the liquid and vapor phases had reached equilibrium, we verified that both the chemical potential and the pressure in the "liquid" and "vapor" box were equal. The coexistence data is collected in Table 9.1.

The integration scheme to trace the fluid-solid coexistence curve requires that one set of points on this curve is already known. The starting point for the simulations was chosen to be the infinite temperature limit $\beta \to 0$, where the "protein" model reduces to the hard-sphere model for which the densities of the coexisting phases, as well as the coexistence pressure, are known. The size of the system was $N = 108$ particles. Table 9.2 shows the coexistence data.

From the computed densities of the coexisting liquid and vapor phases, the critical point can be estimated by using the law of rectilinear diameter [123] and assuming that the shape of the binodal is described by a power law with the 3D-Ising critical exponent $\beta = 0.32$. The critical point is $T_c = 0.42 \pm 0.01$ and the critical density is $\rho_c = 0.30 \pm 0.02$. The pressure at the critical point is estimated to be $P_c = 0.041 \pm 0.007$.

Combing the data of the Gibbs-ensemble simulations and the integration scheme for the fluid-solid coexistence curve, we obtain the phase diagram shown in Fig. 9.2. We see that our model globular protein reproduces the phase behavior of protein solutions

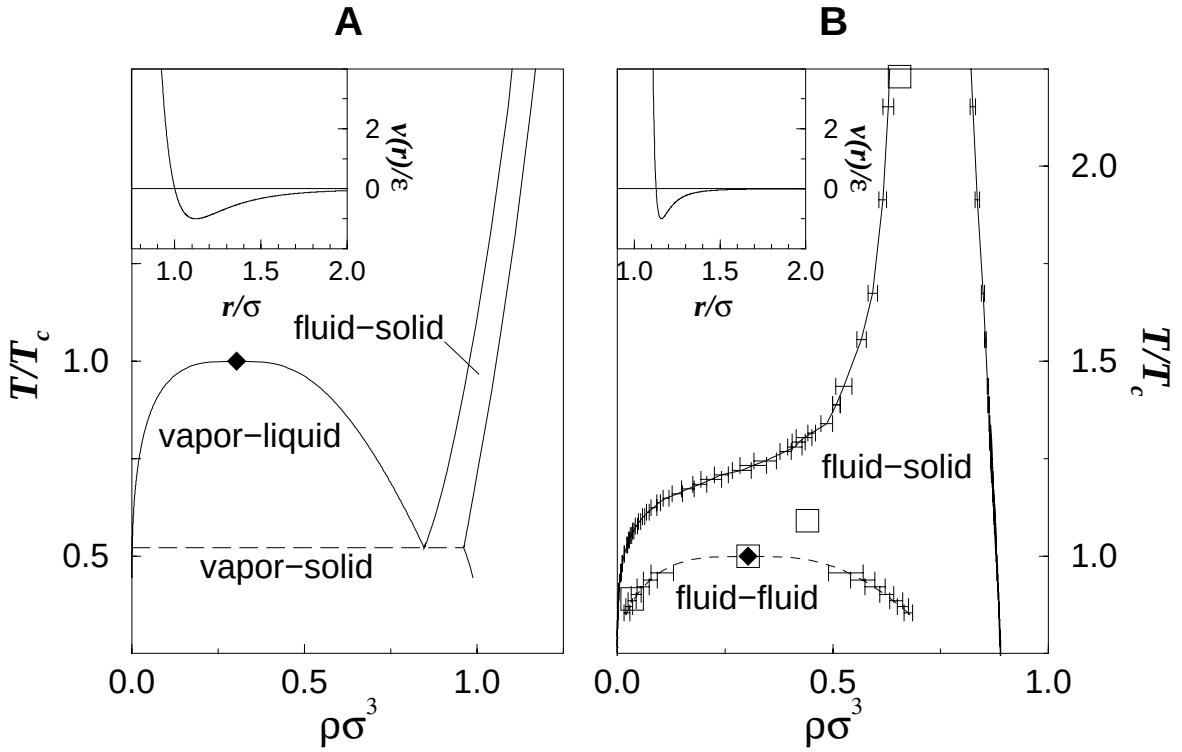

FIGURE 9.2 (A): Typical phase diagram of a molecular substance with a relatively long-ranged attractive interaction. The phase diagram shown here corresponds to the Lennard-Jones 6–12 potential ($v(r) = 4\epsilon[(\sigma/r)^{12} - (\sigma/r)^6]$ – solid curve in insert) [79]. The dashed line indicates the triple point. (B): Typical phase diagram of colloids with short-ranged attraction. The phase diagram was computed for the potential given in Eq. 9.4 (solid curve in insert), with $\alpha = 50$. In both figures, the temperature is expressed in units of the critical temperature T_c, while the number density is given in units σ^{-3}, where σ, the effective diameter of the particles is defined in the expression for $v(r)$. The diamonds indicate the fluid-fluid critical points. In both figures, the solid lines indicate the equilibrium coexistence curves. The dashed curve in B indicates the metastable fluid-fluid coexistence. Crystal-nucleation barriers were computed for the points denoted by open squares.

studied in [179–182]. The fluid-fluid coexistence curve is located in the metastable region some 20 % below the equilibrium crystallization curve.

It is clear that the potential in Eq. (9.4) provides a simplified description of the effective interaction between real proteins in solution: it accounts both for direct and for solvent-induced interactions between the globular proteins. However, we would like to stress that we can map this phase-diagram, by the procedure described above, onto the experimentally determined phase-diagrams for the proteins in solution studied by Rosenbaum *al.* [37, 38].

9.3 Free-energy landscape

Crystallization in real protein solutions may take days or weeks. In a simulation, it takes even longer, because the volume that can be studied by simulations is orders of magnitude smaller, and the probability of forming a crystal is decreased by the same amount. Hence, we cannot use conventional molecular dynamics to study protein crystal nucleation under realistic conditions.

But in chapter 4 we have seen how the umbrella sampling technique does allow for the sampling of configuration space near the top of the barrier and enables us to measure of the free-energy of a nucleus as a function of its size. If the interaction between the clusters can be neglected, the number N_n of clusters of size n is given by

$$N_n = Z_n \exp[\beta\mu n], \tag{9.7}$$

where μ is the imposed chemical potential and Z_n is the partition function of an n-mer, defined as

$$Z_n = \frac{Vn^3}{\Lambda^{3n} n!} \int d\mathbf{r}'^{n-1} \exp[-\beta W_n(\mathbf{r}'^{n-1})]. \tag{9.8}$$

Here Λ is the thermal De Broglie wavelength and W_n is the potential of mean force. We would like to mention that in order to arrive at this expression, we do not have to make the assumption that the clusters are decoupled from the surrounding medium. We have integrated out the coordinates of the solvent particles, and the effect of the surrounding medium is adsorbed into the effective interactions between the cluster particles. This is of particular importance for crystal nucleation, as the density difference between the crystal and the surrounding liquid is so low that we cannot neglect the interactions between cluster and solvent particles.

We do have to assume that we have a cluster criterion that enables us to assign particles to clusters. The question now is: which particles constitute a crystalline cluster? That is, what type of cluster criterion do we have to use?

The intuitive choice would be to use a crystallinity criterion. After all, we are interested in the formation of a crystalline critical nucleus. However, as indicated in the introduction, we expect that crystallization near the metastable critical point is strongly influenced by critical density fluctuations. We therefore used not only a crystallinity criterion, but also a density criterion. For most of the simulations, we have used the same density criterion as the one used in our study of homogeneous gas-liquid nucleation in a Lennard-Jones system, see chapter 5. It is a criterion that enables us to identify those particles that have a significantly denser local environment than particles in the remainder of the system. The local density of a particle is determined by the number of particles within a spherical shell of radius $q_c = 1.5$. If the number of neighbours exceeds a certain threshold (in this case nine), then the particle is considered to be a "high-density" particle.

For one point in the phase diagram for which we have computed the free-energy barrier, at $T = 2.23T_c$, the density difference between the undercooled fluid and the solid is so small, that the respective distribution functions of the number of neighbours overlap considerably. For this point, we followed a slightly different procedure, which consists of two steps. We first assign to every particle a label, either a one or a zero, depending on whether or not the particle satisfies the local density criterion that it has more than

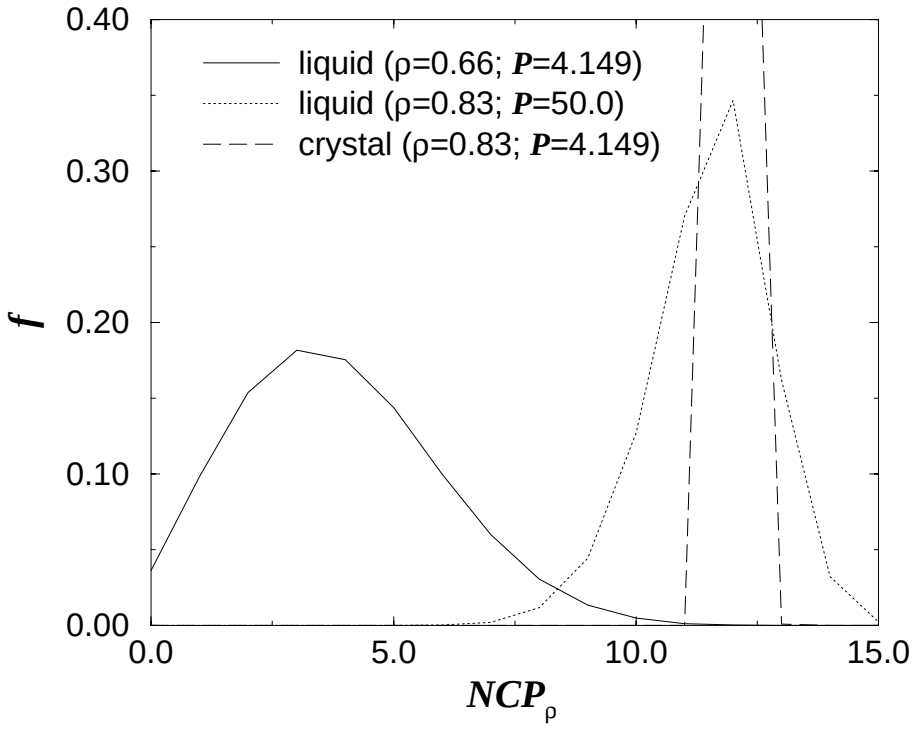

FIGURE 9.3 Distribution function f of the number of neighbors, NCP_ρ, that satisfy the density criterion (see Text) for a liquid of density $\rho = 0.66$, an (fcc) crystal at $\rho = 0.83$, and a liquid at $\rho = 0.83$ ($T = 2.23T_c$, pressures P are indicated in figure). It is seen that the distribution function for the liquid phase of $\rho = 0.62$ exhibits little overlap with the distribution functions of the other two phases. The threshold value for the density criterion was taken to be nine.

eleven neighbours. We then consider a particle as a "high-density" particle when the number of neighbours that satisfy this density criterion is larger than a threshold value of nine. We illustrate the technique in Fig. 9.3, where we show the distribution functions of the number of high-density neighbours for an undercooled liquid at a density $\rho = 0.66$, an fcc-crystal at a density $\rho = 0.83$, and a (compressed) liquid at this density. It is seen that the distribution function for the liquid of the lower density shows only small overlap with the distribution functions of the other two phases. Hence, also for this region of the phase diagram we have a well-defined criterion to identify the particles that have a significantly higher local density than the particles in the rest of the system.

After we have identified the high-density particles in the system, we can assign them to clusters. As before, we have applied the criterion that any two high-density particles that are neighbours belong to the same cluster. The number of particles in the largest cluster is denoted by N_ρ.

Now that we have determined which particles belong the largest high-density cluster (be it liquid or solidlike), we classify each particle in this cluster as either solidlike or liquidlike. To this end, we have used the same crystallinity criterion as the one used

in chapter 3 on homogeneous crystal-nucleation in a Lennard-Jones system. We denote the number of solidlike particles in the cluster of N_ρ high-density particles by N_{crys}.

In our simulations, we determine the free-energy "landscape" of this cluster as a function of the two coordinates N_ρ and N_{crys} by measuring the probability distribution function $P(N_\rho, N_{crys})$:

$$\beta\Delta G(N_\rho, N_{crys}) \equiv -\ln[P(N_\rho, N_{crys})]. \tag{9.9}$$

In order to sample all values of N_ρ and N_{crys} with equal accuracy, we have employed the umbrella sampling technique [26]. The form of the biasing potential $W(N_\rho, N_{crys})$ was taken to be

$$W(N_\rho, N_{crys}) = \frac{1}{2}k_{N_\rho}(N_\rho - N_{\rho,0})^2 + \frac{1}{2}k_{N_{crys}}(N_{crys} - N_{crys,o})^2. \tag{9.10}$$

The umbrella sampling method was embedded in a hybrid MD-MC scheme. In this scheme, molecular dynamics trajectories are used to generate collective trial Monte Carlo moves. To be more specific, each Monte Carlo move consists of three steps:

1. New particle velocities are sampled from a Maxwellian distribution;

2. An MD-trajectory is performed, starting with the current configuration and the new velocities. In principle, we could add the biasing potential to the Hamiltonian of the system, and generate the MD-trajectory according to this extended Hamiltonian. It would require that the forces associated with the biasing potential have to be computed. However, the nice feature of the hybrid MD-MC scheme is that we do not have to do so. We can simply perform a trajectory without the biasing potential and correct for it in the next step.

3. We accept or reject the new configuration with an acceptance probability

$$P_{acc} = \mathrm{Min}\left[1, \exp[-\beta(\Delta H + \Delta W(N_\rho, N_{crys}))]\right], \tag{9.11}$$

where ΔH is the change in the Hamiltonian of the system (without the biasing potential) and ΔW is the change in the biasing potential. We have included the term $\Delta W(N_\rho, N_{crys})$ to ensure that configuration space is sampled according to the extended Hamiltonian (i.e., with the biasing potential). If the trajectory is rejected, the particle coordinates are set back to their original values.

In order to generate the isothermal-isobaric (NPT) ensemble, the MD-trajectory is performed in the isoenthalpic-isobaric (NPH) ensemble. For this, we have used the equations of motion of Andersen [138]. In order for the scheme to satisfy detailed balance, the MD-algorithm should be time reversible. Moreover, it should be area preserving. In the Appendix we give our algorithm, which satisfies both conditions; it is derived by a Trotter factorization of the Liouville propagator via the procedure proposed by Tuckerman, Berne and Martyna [140].

The size of the system was determined by the requirement that the largest nucleus in the system should not "feel" its periodic neighbours. For most of the simulations a system size of $N = 500$ particles was sufficient. In these simulations, we applied cubic periodic boundary conditions. For the simulation at $T = 2.23T_c$, the density of the liquid surrounding the nucleus is so large that we had to use a much larger system, of

$N = 3000$ particles, although truncated octahedral periodic boundary conditions were applied to reduce the number of particles as much as possible. A neighbour list was used to speed up the simulations.

To map out a two-dimensional free-energy landscape is computationally expensive: the number of umbrella-windows was between 100 and 150. Typically, a simulation in a window consisted of an equilibration period of 10000-25000 collective Monte Carlo moves, followed by a production run of 25000 to 50000 MC-moves. The length of one MD-trajectory, corresponding to one collective MC-move, depended on the density of the surrounding medium: from 10 timesteps in the simulations of crystal nucleation from the high-density liquid, to 100 timesteps for crystal nucleation from the vapor. The hybrid MD-MC scheme allows for a relatively large timestep as the energy does not have to be conserved along the trajectory. On the other hand, the larger the time-step, the lower the probability with which the trajectory will be accepted. Moreover, the short range of the potential demands a relatively small timestep. We found that a time-step of 0.0025τ was optimal.

9.4 Results

We studied the free-energy barrier for four different points in the phase diagram: one well above the metastable critical point ($T = 2.23T_c$), one at T_c, and the remaining two at $0.89T_c$ and $1.09T_c$. In order to make a comparison on equal footing, we chose the degree of supercooling such that classical nucleation theory would predict the same value for the height of the nucleation barrier for our all systems. In classical nucleation theory the barrier height ΔG^* is given by

$$\frac{\Delta G^*}{k_B T} = \frac{16\pi\gamma^3}{3k_B T\rho^2\Delta\mu^2}, \tag{9.12}$$

where γ is the free-energy density per unit area of the solid-liquid interface, ρ is the number density of the solid phase, and $\Delta\mu$ is the difference in chemical potential between the fluid and the solid. It is the thermodynamic driving force for crystallization.

As the solid is nearly incompressible, we can take for the density of the "supercooled" solid phase, the density at coexistence, which we have computed by the integration scheme discussed in section 9.2. The difference in chemical potential was approximated by

$$\Delta\mu \approx \Delta h\frac{T_m - T}{T_m}, \tag{9.13}$$

where Δh is the enthalpy change per particle on freezing at coexistence and T_m is the coexistence temperature. The data for Δh could also easily be obtained from the integration scheme. To compute the surface free-energy for a solid-liquid interface is much harder and we have not tried to do so. Rather, we have used Turnbull's empirical rule which states that γ is proportional to Δh [6]. The constant of proportionality between γ and Δh varies from one substance to the next, and is not known *a priori*. Therefore, we do not know the absolute value of the prediction of classical nucleation theory for the barrier height, but we do know that it is constant for the simulation points. The parameters characterizing the points studied in the simulation have been collected in Table 9.3.

T/T_c	T_m/T_c	$(T_m - T)/T_m$	$\Delta H(T_m)/(k_B T_m)$	$\rho_{cr}(T_m)$	$\Delta G^*/k_B T$
0.89	1.04	0.136	-12.59	0.877	75
1.0	1.14	0.123	-10.35	0.872	53
1.09	1.22	0.109	-8.153	0.869	83
2.23	2.39	0.069	-2.996	0.814	128

TABLE 9.3 Parameters characterizing the simulations described in the text. Meaning of symbols – T: absolute temperature, T_c: critical temperature. T_m: melting temperature. $\Delta H(T_m)/(k_B T_m)$: ratio of solid-fluid enthalpy difference and thermal energy at coexistence. $\rho_{cr}(T_m)$: density of the crystal phase at coexistence (in units σ^{-3}). $\Delta G^*/k_B T$: nucleation barrier height divided by $k_B T$.

For all points, we studied the free-energy landscape and the lowest free-energy path for the formation of the critical nucleus. The free-energy landscape was determined as a function of N_ρ and N_{crys}. In a crystal nucleation event, we start from the homogeneous liquid ($N_\rho \approx N_{crys} \approx 0$). When a nucleus is formed, the free energy increases, until it reaches a saddle-point, corresponding to the critical nucleus. From there on, the nucleus will grown spontaneously. As explained in detail in section 9.3, the structure of the nucleus that is formed can be characterized by N_ρ and N_{crys}. If a high-density liquidlike droplet forms in the system, we expect N_ρ to become large, while N_{crys} remains essentially zero. In contrast, for a normal crystallite, we expect that N_ρ is proportional to N_{crys}.

Fig. 9.4 shows the free-energy landscape for $T = 0.89T_c$ and $T = T_c$. The free-energy landscapes for the other two points are qualitatively similar to the one for $T = 0.89T_c$ and will not be shown here. We find that away from T_c (both above and below), the path of lowest free energy is one where the increase in N_ρ is proportional to the increase in N_{crys} (Fig.2A). Such behavior is expected if the incipient nucleus is simply a small crystallite. However, around T_c, critical density fluctuations lead to a striking change in the free-energy landscape (Fig.2B). First, the route to the critical nucleus leads through a region where N_ρ increases while N_{crys} is still essentially zero. In other words: the first step towards the critical nucleus is the formation of a liquidlike droplet. Then, beyond a certain critical size, the increase in N_ρ is proportional to N_{crys}, that is, a crystalline nucleus forms inside the liquidlike droplet.

Clearly, the presence of large density fluctuations close to a fluid-fluid critical point has a pronounced effect on the route to crystal nucleation. But, more importantly, the nucleation barrier close to T_c is much lower than at either higher or lower temperatures (Fig. 9.5 and Table 9.3). The observed reduction in ΔG^* near T_c by some $30 k_B T$ corresponds to an increase in nucleation rate by a factor 10^{13}. One could interpret this observation as follows: near the fluid-fluid critical point, the wetting of the crystal nucleus by a liquidlike layer results in a value of the interfacial free-energy γ, and therefore of the barrier height ΔG^*, that is much lower than would be estimated on the basis of Turnbull's rule. In fact, in a recent paper, Haas and Drenth [187] note that the experimentally determined interfacial free energy of small protein crystals [188, 189] is much smaller than the value predicted on the basis of their version of Turnbull's rule.

Finally, let us consider the implications of this reduction of the crystal nucleation barrier near T_c. An alternative way to lower the crystal nucleation barrier would be to quench the solution deeper into the metastable region below the solid-liquid coexistence curve. However, such deep quenches often result in the formation of amorphous aggregates [37, 38, 169, 176–178, 182]. Moreover, in a deep quench, the thermodynamic

FIGURE 9.4 Contour plots of the free-energy landscape along the path from the metastable fluid to the critical crystal nucleus, for our system of spherical particles with short-ranged attraction. The curves of constant free energy are drawn as a function of N_ρ and N_{crys} (see text) and are separated by $5k_BT$. (A): The free energy landscape well below the critical temperature ($T/T_c = 0.89$). The lowest free-energy path to the critical nucleus is indicated by a dashed curve. This curve corresponds to the formation and growth of a highly crystalline cluster. (B): As (A), but for $T = T_c$. In this case, the free-energy valley (dashed curve) first runs parallel to the N_ρ axis (formation of a liquidlike droplet), and then moves towards a structure with a higher crystallinity (crystallite embedded in a liquidlike droplet). The free energy barrier for this route is much lower than the one in (A).

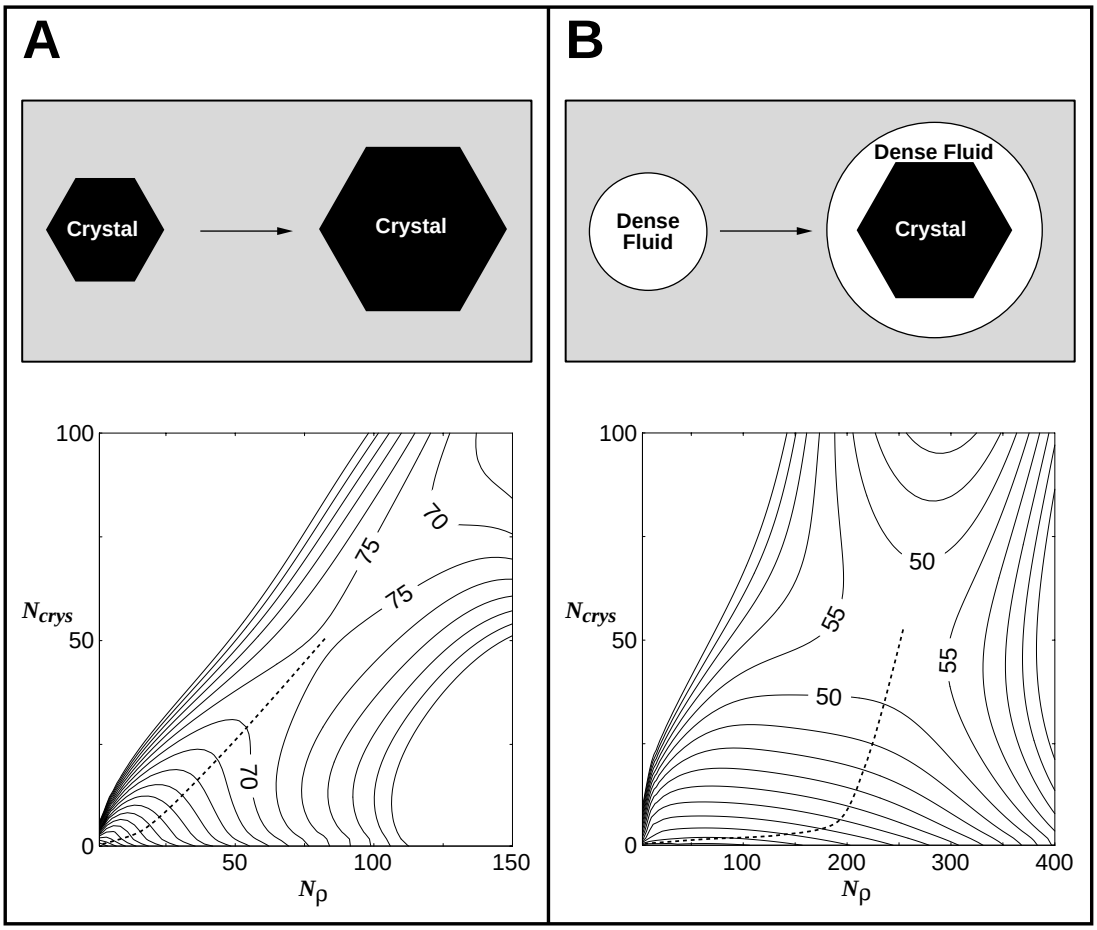

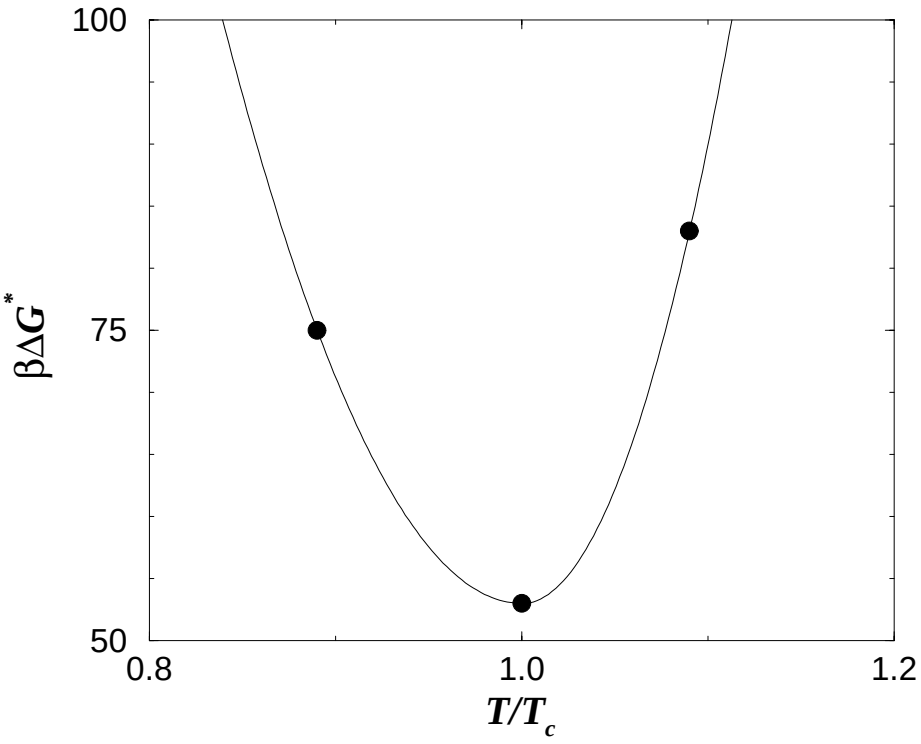

FIGURE 9.5 Variation of the free-energy barrier for homogeneous crystal nucleation, as a function of T/T_c, in the vicinity of the critical temperature. The solid curve is a guide to the eye. The nucleation barrier at $T = 2.23T_c$ is $128k_BT$ and is not shown in this figure. If Turnbull's phenomenological rule for γ would hold [6], Eq. (9.12) would predict a constant nucleation barrier. But the simulations show that the nucleation barrier goes through a minimum around the metastable critical point (see text).

driving force for crystallization ($\mu_{liq} - \mu_{cryst}$) is also enhanced. As a consequence, the crystallites that nucleate will grow rapidly and far from perfectly [167]. In contrast, by adjusting the solvent conditions (for instance by the addition of non-ionic polymer) and thereby changing the range of interaction, such that a metastable fluid-fluid critical point is located just below the sublimation curve, we can selectively speed up the rate of crystal nucleation, but not the rate of crystal growth, nor the rate at which amorphous aggregates form. We hope that the present results will stimulate experimentalists to explore this approach to protein crystallization.

Clearly, our description of the early stages of protein crystallization is highly simplified. Yet, we believe that the mechanism for enhanced crystal nucleation that we find is quite general. The phase diagram shown in Fig.1B is likely to be the rule, rather than the exception for compact macromolecules. Moreover, it occurs both in the bulk and in (quasi) two-dimensional systems (such as membranes). It is therefore tempting to speculate that Nature already makes extensive use of critical density fluctuations to facilitate the formation of ordered structures.

Appendix MD-algorithm

Following Andersen [138], the Hamiltonian for the isoenthalpic-isobaric (NPH) ensemble can be written as

$$H = \frac{1}{2mV^{3/2}} \sum_{i=1}^{3N} p_i^2 + \sum_{i<j} U(V^{1/3} x_{ij}) + \frac{p_V^2}{2W} + P_{ext} V. \tag{9.14}$$

Here x_i are the coordinates r_i scaled with the length of the box $L = V^{1/3}$, where V is the volume of the system, $p_i = mV^{2/3}\dot{x}_i$ denote the momenta conjugate to x_i, U is the potential energy, $p_V = W\dot{V}$ is the momentum conjugate to the volume V and W is the mass of the piston. From this Hamiltonian the following equations of motion are derived:

$$\begin{aligned}
\dot{x}_i &= \frac{\partial H}{\partial p_i} = \frac{p_i}{mV^{2/3}}, \\
\dot{p}_i &= -\frac{\partial H}{\partial x_i} = V^{1/3} F_i(\mathbf{x}, V), \\
\dot{V} &= \frac{\partial H}{\partial p_V} = \frac{p_V}{W}, \\
\dot{p}_V &= -\frac{\partial H}{\partial V} = P_{int}(\mathbf{p}, \mathbf{x}) - P_{ext},
\end{aligned} \tag{9.15}$$

where $F_i = -\frac{\partial U}{\partial r_i}$ is the force acting on particle i and $P_{int}(\mathbf{p}, \mathbf{x})$ is the internal pressure. We have decomposed the Liouville operator into four parts:

$$iL = iL_1 + iL_2 + iL_3 + iL_4, \tag{9.16}$$

where we have chosen

$$\begin{aligned}
iL_1 &= \sum_{i=1}^{3N} \frac{p_i}{mV^{2/3}} \frac{\partial}{\partial x_j}, \\
iL_2 &= \frac{p_V}{W} \frac{\partial}{\partial V}, \\
iL_3 &= \sum_{i=1}^{3N} V^{1/3} F_i(\mathbf{x}) \frac{\partial}{\partial p_i}, \\
iL_4 &= F_V(\mathbf{p}, \mathbf{x}) \frac{\partial}{\partial p_V}.
\end{aligned} \tag{9.17}$$

Here $F_V(\mathbf{p}, \mathbf{x}) = P_{int}(\mathbf{p}, \mathbf{x}) - P_{ext}$ is the "force" acting on the volume V. We have employed a Trotter factorizaton of the Liouville propagator that yields the following propagator accurate to $O(\Delta t^2)$:

$$U(\Delta t) = e^{iL_4(\Delta t/2)} e^{iL_3(\Delta t/2)} e^{iL_2(\Delta t/2)} e^{iL_1(\Delta t)} e^{iL_2(\Delta t/2)} e^{iL_3(\Delta t/2)} e^{iL_4(\Delta t/2)}. \tag{9.18}$$

From this we obtain the integrator:

$$
\begin{aligned}
p_V(\Delta t/2) &= p_V(0) + \frac{\Delta t}{2} F_V[\mathbf{p}(0), \mathbf{x}(0)], \\
p_i(\Delta t/2) &= p_i(0) + \frac{\Delta t}{2} V^{1/3} F_i[\mathbf{x}(0), V(0)], \\
V(\Delta t/2) &= V(0) + \frac{\Delta t}{2} \frac{p_V(\Delta t/2)}{W}, \\
x_i(\Delta t) &= x(0) + \Delta t \frac{p_i(\Delta t/2)}{m V^{2/3}}, \\
V(\Delta t) &= V(\Delta t/2) + \frac{\Delta t}{2} \frac{p_V(\Delta t/2)}{W}, \\
p_i(\Delta t) &= p_i(\Delta t/2) + \frac{\Delta t}{2} V^{1/3} F_i[\mathbf{x}(\Delta t), V(\Delta t)], \\
p_V(\Delta t) &= p_V(\Delta t/2) + \frac{\Delta t}{2} F_V[\mathbf{p}(\Delta t), \mathbf{x}(\Delta t)].
\end{aligned}
\tag{9.19}
$$

Because of the symmetric factorization of the Liouville propagator, the propagator in Eq. (9.18) is a unitary operator, and the integrator is time-reversible. The algorithm is area-preserving because we used scaled coordinates. Note also that we have sandwiched the propagation of V between the propagation of x_i and p_i. This ensures that we have to compute the force only once per time-step.

Bibliography

[1] D. B. Fahrenheit, Phil. Trans. Roy. Soc. **39**, 78 (1724).
[2] W. Ostwald, Z. Phys. Chem. **22**, 289 (1897).
[3] J. W. Gibbs, *The Scientific Papers of J. Willard Gibbs*, Dover, New York (1961).
[4] M. Volmer and A. Weber, Z. Phys. Chem. **119**, 227 (1926).
[5] R. Becker and W. Döring, Ann. Phys. **24**, 719 (1935).
[6] K. F. Kelton, in *Crystal Nucleation in Liquids and Glasses*, edited by H. Ehrenreich and D. Turnbull, Academic Press, Boston (1991) Vol. 45.
[7] D. W. Oxtoby, J. Phys. Condens. Matter. **4**, 7627 (1992).
[8] W. J. Boettinger and J. H. Perepezko, in *Rapidly Solidified Crystalline Alloys*, edited by S. K. Das, B. H. Kear and C. M. Adam, The Metallurgical Society of AIME, New York (1985).
[9] L. Bosio, A. Defrain, and I. Epenboin, J. de Phys. **27**, 61 (1966).
[10] J. H. Perepezko and I. E. Anderson, in *Synthesis and Properties of Metastable Phases*, edited by E. S. Machlin and T. J. Rowland, PA:TMS-AIME, Warrendale (1980).
[11] H. Reiss, W. K. Kegel, and J. L. Katz, Phys. Rev. Lett. **78**, 4506 (1997).
[12] R. McGraw and A. Laaksonen, Phys. Rev. Lett. **76**, 2754 (1996).
[13] R. McGraw and A. Laaksonen, J. Chem. Phys. **106**, 5284 (1997).
[14] D. W. Oxtoby and R. Evans, J. Chem. Phys. **89**, 7521 (1988).
[15] Y. Viisanen, R. Strey, and H. Reiss, J. Chem. Phys. **99**, 4680 (1993).
[16] K. N. H. Looijmans, C. C. M. Luijten, and M. E. H. van Dongen, J. Chem. Phys. **103**, 1714 (1995).
[17] M. J. Mandell, J. P. McTague and A. Rahman, J. Chem. Phys. **66**, 3070 (1977).
[18] M. Tanemura, Y. Hiwatari, H. Matsuda, T. Ogawa, N. Ogita, and A. Ueda, Prog. Theor. Phys. **58**, 1079 (1977).
[19] J. N. Cape, J. L. Finney, and L. V. Woodcock, J. Chem. Phys. **75**, 2366 (1981).
[20] M. J. Mandell, J. P. McTague, and A. Rahman, J. Chem. Phys. **64**, 3699 (1976).
[21] C. S. Hsu and A. Rahman, J. Chem. Phys. **71**, 4974 (1979).
[22] R. D. Mountain and A. C. Brown, J. Chem. Phys. **80**, 2730 (1984).
[23] S. Nosé and F. Yonezawa, J. Chem. Phys. **84**, 1803 (1986).
[24] J. Yang, H. Gould, and W. Klein, Phys. Rev. Lett. **60**, 2665 (1988).
[25] W. C. Swope and H. C. Andersen, Phys. Rev. B **41**, 7042 (1990).
[26] G. M. Torrie and J. P. Valleau, Chem. Phys. Lett. **28**, 578 (1974).
[27] J. S. van Duijneveld and D. Frenkel, J. Chem. Phys. **96**, 4655 (1992).
[28] C. H. Bennett, in *Algorithms for Chemical Computations*, edited by R. E. Christofferson, Am. Chem. Soc., Washinton, D.C. (1977).
[29] D. Chandler, J. Chem. Phys. **68**, 2959 (1978).
[30] E. A. Carter, G. Ciccotti, J. T. Hynes, and R. Kapral, Chem. Phys. Lett. **156**, 472 (1989).
[31] G. Ciccotti, in *Computer Simulations in Materials Science*, edited by M. Meyer and V. Pontikis, Kluwer, Dordrecht (1991).
[32] S. Alexander and J. P. McTague, Phys. Rev. Lett. **41**, 702 (1978).
[33] D. Wright, R. Caldwell, C. Moxeley, and M. S. El-Shall, J. Chem. Phys. **98**, 3356 (1993).
[34] D. Wright and M. S. El-Shall, J. Chem. Phys. **98**, 3369 (1993).
[35] M. J. Stevens and G. S. Grest, Phys. Rev. Lett. **72**, 3686 (1994).
[36] J. J. Weis and D. Levesque, Phys. Rev. Lett. **71**, 2729 (1993).
[37] D. Rosenbaum, P. C. Zamora, and C. F. Zukoski, Phys. Rev. Lett. **76**, 150 (1996).
[38] D. Rosenbaum and C. F. Zukoski, J. Crystal Growth **169**, 752 (1996).
[39] V. Talanquer and D. W. Oxtoby, J. Chem. Phys. **104**, 1993 (1996).
[40] S. Ono and S. Kondo, in *Encyclopedia of Physics*, edited by S. Flugge, Springer, Berlin (1960) Vol. 10.

[41] J. S. Rowlinson and B. Widom, *Molecular Theory of Capillarity*, Clarendon, Oxford (1982).
[42] R. C. Tolman, J. Chem. Phys. **17**, 333 (1949).
[43] H. B. Callen, *Thermodynamics and an Introduction to Thermostatistics*, John Wiley & Sons, New York, 2nd edition (1985).
[44] W. Helfrich, Z. Naturforsch **28c**, 693 (1973).
[45] E. M. Blokhuis and D. Bedeaux, J. Chem. Phys. **97**, 3576 (1992).
[46] M. J. P. Nijmeijer, C. Bruin, A. B. Woerkom, A. F. Bakker, and J. M. J. van Leeuwen, J. Chem. Phys. **96**, 565 (1992).
[47] M. J. Haye and C. Bruin, J. Chem. Phys. **100**, 556 (1994).
[48] J. Zeldovich, J. Expr. Theor. Phys. (Russia) **12**, 525 (1942).
[49] J. Frenkel, *Kinetic Theory of Liquids*, Clarendon, Oxford (1946).
[50] R. Strey, Y. Viisanen, and P. E. Wagner, J. Chem. Phys. **103**, 4333 (1995).
[51] R. M. Nyquist, V. Talanquer, and D. W. Oxtoby, J. Phys. Chem. **103**, 1175 (1995).
[52] W. G. Courtney, J. Chem. Phys. **35**, 2249 (1961).
[53] C. L. Weakliem and H. Reiss, J. Phys. Chem. **98**, 6408 (1994).
[54] J. Lothe and G. M. Pound, J. Chem. Phys. **36**, 2080 (1962).
[55] D. Kashchiev, J. Chem. Phys. **76**, 5098 (1982).
[56] D. W. Oxtoby and D. Kashchiev, J. Chem. Phys. **100**, 7665 (1994).
[57] I. J. Ford, J. Chem. Phys. **105**, 8324 (1996).
[58] I. N. Stranski and D. Totomanow, Z. Physikal. Chem. **163**, 399 (1933).
[59] W. Klein and F. Leyvraz, Phys. Rev. Lett. **57**, 2845 (1986).
[60] R. E. Cech, J. Met. **8**, 585 (1956).
[61] H.-M. Lin, Y.-W. Kim, and T. F. Kelly, Acta Metall. **36**, 2537 (1988).
[62] W. Löser, T. Volkmann, and D. M. Herlach, Mat. Sci. Eng. **A178**, 163 (1994).
[63] P. Harrowell and D. W. Oxtoby, J. Chem. Phys. **80**, 1639 (1984).
[64] L. D. Landau and E. M. Lifshitz, *Statistical Physics*, Pergamon, London, 3rd edition (1980).
[65] R. M. Lynden-Bell, J. S. van Duijneveldt, and D. Frenkel, Mol. Phys. **80**, 801 (1993).
[66] S. Glasstone, K. J. Laidler and H. Eyring, *The theory of rate processes*, McGraw-Hill, New York (1941).
[67] D. Chandler, *Introduction to Modern Statistical Mechanics*, Oxford University Press, New York (1987).
[68] M. P. Allen and D. J. Tildesley, *Computer Simulation of Liquids*, Clarendon, Oxford (1987).
[69] M. J. Ruiz-Montero, D. Frenkel, and J. J. Brey, Mol. Phys. **90**, 925 (1997).
[70] P. J. Steinhardt, D. R. Nelson, and M. Ronchetti, Phys. Rev. B **28**, 784 (1983).
[71] J. D. Honeycutt and H. C. Andersen, J. Phys. Chem. **90**, 1585 (1986).
[72] A. D. J. Haymet, Chem. Phys. Lett. **107**, 77 (1984).
[73] J. Yang, H. Gould, W. Klein, and R. D. Mountain, J. Chem. Phys. **93**, 711 (1990).
[74] R. Eppenga and D. Frenkel, Mol. Phys. **52**, 1303 (1984).
[75] S. Nosé, in *Computer Simulations in Materials Science*, edited by M. Meyer and V. Pontikis, Kluwer, Dordrecht (1991).
[76] D. J. Adams, CCP5 Quarterley **10**, 30 (1983).
[77] A. M. Ferrenberg and R. H. Swendsen, Phys. Rev. Lett. **63**, 1195 (1989).
[78] C. K. Bagdassarian and D. W. Oxtoby, J. Chem. Phys. **100**, 2139 (1994).
[79] J. P. Hansen and L. Verlet, Phys. Rev. **184**, 151 (1969).
[80] B. W. van de Waal, J. Chem. Phys. **90**, 3407 (1989).
[81] J. Farges, M. F. de Feraudy, B. Raoult, and G. Torchet, J. Chem. Phys. **78**, 5067 (1983).
[82] L. L. Boyer and J. Q. Broughton, Phys. Rev. B **42**, 11461 (1990).
[83] J. D. Honeycutt and H. C. Andersen, J. Phys. Chem. **91**, 4950 (1987).
[84] L. A. Báez and P. Clancy, J. Chem. Phys. **102**, 8138 (1995).
[85] J. Q. Broughton and G. H. Gilmer, J. Chem. Phys. **84**, 5759 (1986).
[86] D. W. Oxtoby, private communication.
[87] H. A. Kramers, Physica **7**, 284 (1940).
[88] D. Turnbull and J. C. Fisher, J. Chem. Phys. **17**, 71 (1949).
[89] J. Q. Broughton, G. H. Gilmer, and K. A. Jackson, Phys. Rev. Lett. **49**, 1496 (1982).
[90] E. Burke, J. Q. Broughton, and G. H. Gilmer, J. Chem. Phys. **89**, 1030 (1989).

[91] M. J. P. Brugmans and W. L. Vos, J. Chem. Phys. **103**, 2661 (1995).
[92] Z. W. Salsburg and W. W. Wood, J. Chem. Phys. **37**, 798 (1962).
[93] R. Agrawal and D. A. Kofke, Mol. Phys. **85**, 23 (1995).
[94] R. Strey and Y. Viisanen, J. Chem. Phys. **99**, 4693 (1993).
[95] Y. Viisanen, R. Strey, A. Laaksonen, and M. Kulmala, J. Chem. Phys. **100**, 6062 (1994).
[96] H. Reiss, J. L. Katz, and E. R. Cohen, J. Stat. Phys. **2**, 83 (1968).
[97] M. E. Fisher, Physics **3**, 255 (1967).
[98] A. Dillmann and G. E. A. Meier, Chem. Phys. Lett. **89**, 71 (1989).
[99] V. I. Kalikmanov and M. E. H. van Dongen, Europhys. Lett. **21**, 7645 (1993).
[100] J. K. Lee, J. A. Barker, and F. F. Abraham, J. Chem. Phys. **58**, 3166 (1973).
[101] D. J. McGinty, J. Chem. Phys. **58**, 4733 (1973).
[102] M. Rao, B. J. Berne, and M. H. Kalos, J. Chem. Phys. **68**, 1325 (1978).
[103] N. G. Garcia and J. M. S. Torroja, Phys. Rev. Lett. **47**, 186 (1981).
[104] S. M. Thompson, K. E. Gubbins, J. P. R. B. Walton, R. A. R. Chantry, and J. S. Rowlinson, J. Chem. Phys. **81**, 530 (1984).
[105] D. J. Lee, M. M. Telo da Gama, and K. E. Gubbins, J. Chem. Phys. **85**, 490 (1986).
[106] C. L. Weakliem and H. Reiss, J. Chem. Phys. **99**, 5374 (1993).
[107] X. C. Zheng and D. W. Oxtoby, J. Chem. Phys. **94**, 4472 (1991).
[108] V. Talanquer and D. W. Oxtoby, J. Chem. Phys. **100**, 5190 (1994).
[109] V. Talanquer and D. W. Oxtoby, J. Phys. Chem. **99**, 2865 (1995).
[110] F. H. Stillinger, J. Chem. Phys. **38**, 1486 (1963).
[111] H. Reiss, A Tabazadeh, and J. Talbot, J. Chem. Phys. **92**, 1266 (1990).
[112] H. M. Ellerby, C. L. Weakliem, and H. Reiss, J. Chem. Phys. **95**, 9209 (1991).
[113] H. M. Ellerby and H. Reiss, J. Chem. Phys. **97**, 5766 (1992).
[114] C. L. Weakliem and H. Reiss, J. Chem. Phys. **101**, 2398 (1994).
[115] K. J. Oh, X.C. Zeng, and H. Reiss, J. Chem. Phys. **107**, 1242 (1997).
[116] F. P. Buff, J. Chem. Phys. **23**, 419 (1955).
[117] A. Laaksonen and R. McGraw, Europhys. Lett. **35**, 367 (1996).
[118] P. Schofield and J. R. Henderson, Proc. R. Soc. Lond. A **379**, 231 (1982).
[119] J. H. Irving and J. G. Kirkwood, J. Chem. Phys. **18**, 817 (1950).
[120] A. Harasima, Adv. Chem. Phys. **1**, 203 (1958).
[121] J. P. R. B. Walton, D. J. Tildesley, and J. S. Rowlinson, Mol. Phys. **48**, 1357 (1983).
[122] I. Kusaka, Z.-G. Wang, and J. H. Seinfeld, J. Chem. Phys. **108**, 3446 (1998).
[123] B. Smit, J. Chem. Phys. **96**, 8639 (1992).
[124] G. A. Chapela, G. Saville, S. M. Thompson, J. S. Rowlinson, J. Chem. Soc. Faraday Trans. II **8**, 1133 (1977).
[125] C. D. Holcomb, P. Clancy, and J. A. Zollweg, Mol. Phys. **78**, 437 (1993).
[126] A. H. Falls, L. E. Scriven, and H. T. Davis, J. Chem. Phys. **75**, 3986 (1981).
[127] G. H. Peters and J. Eggenbrecht, J. Phys. Chem. **95**, 909 (1991).
[128] I. Hadjiagapiou, J. Phys. Condens. Matter. **6**, 5303 (1994).
[129] A. Z. Panagiotopoulos, Mol. Phys. **61**, 813 (1987).
[130] V. Talanquer, J. Chem. Phys. **106**, 9957 (1997).
[131] V. I. Kalikmanov, Phys. Rev. E **55**, 3068 (1997).
[132] S. L. Girschick, J. Chem. Phys. **94**, 826 (1991).
[133] G. Wilemski, J. Chem. Phys. **103**, 1119 (1995).
[134] J. L. Katz, J. Chem. Phys. **52**, 4733 (1970).
[135] M. M. Rudek, J. A. Fisk, V. M. Chakarov, and J. L. Katz, J. Chem. Phys. **105**, 4707 (1996).
[136] Y. Viisanen, P. E. Wagner, and R. Strey, J. Chem. Phys. **108**, 4257 (1998).
[137] K. N. H. Looijmans, C. C. M. Luijten, and M. E. W. van Dongen, J. Chem. Phys. **103**, 1714 (1995).
[138] H. C. Andersen, J. Chem. Phys. **80**, 2384 (1980).
[139] S. Nosé, J. Chem. Phys. **81**, 511 (1984).
[140] M. Tuckerman, B. J. Berne, and G. J. Martyna, J. Chem. Phys. **97**, 1990 (1992).
[141] G. J. Martyna, M. E. Tuckermann, D. J. Tobias, and M. L. Klein, Mol. Phys. **87**, 1117 (1996).

[142] J. O. Hirschfelder, C. F. Curtiss, and R. B. Bird, *Molecular Theory of Gases and Liquids*, John Wiley & Sons, New York (1954).
[143] A. Laaksonen and D. W. Oxtoby, J. Chem. Phys. **102**, 5803 (1995).
[144] A. Laaksonen and D. W. Oxtoby, J. Chem. Phys. **106**, 7268 (1997).
[145] D. A. Kofke, J. Chem. Phys. **98**, 4149 (1993).
[146] P. Bolhuis and D. Frenkel, J. Chem. Phys. **106**, 666 (1997).
[147] D. Frenkel and B. Smit, *Understanding Molecular Simulation, From Algorithms to Applications*, Academic Press, San Diego (1996).
[148] A. S. Clarke, R. Kapral, and G. N. Patey, J. Chem. Phys. **101**, 2432 (1994).
[149] A. K. Ray, M. Chalam, and L. K. Peeters, J. Chem. Phys. **85**, 2161 (1986).
[150] F. F. Abraham, Science **168**, 833 (1970).
[151] V. Talanquer and D. W. Oxtoby, J. Chem. Phys. **99**, 4670 (1993).
[152] M. E. van Leeuwen and B. Smit, Phys. Rev. Lett. **71**, 3991 (1993).
[153] M. J. Stevens and G. S. Grest, Phys. Rev. E **51**, 5976 (1995).
[154] B. Groh and S. Dietrich, Phys. Rev. E **54**, 1687 (1996).
[155] H. Zhang and M. Widom, Phys. Rev. E **49**, **R**3591 (1994).
[156] J. M. Caillol, J. Chem. Phys. **98**, 9835 (1993).
[157] A. Papadopoulou, E. D. Becker, M. Lupkowski, and F. van Swol, J. Chem. Phys. **98**, 4897 (1993).
[158] B. Widom, J. Chem. Phys. **39**, 2808 (1963).
[159] S. W. de Leeuw, J. W. de Perram, and E. R. Smith, Ann. Rev. Phys. Chem. **37**, 245 (1986).
[160] J. Alejandre, D. J. Tildesley, and G. A. Chapela, J. Chem. Phys. **102**, 4574 (1995).
[161] H. B. Lavender, K. A. Iyer, and S. J. Singer, J. Chem. Phys. **101**, 7856 (1994).
[162] D. Lu and S. J. Singer, J. Chem. Phys. **103**, 1913 (1995).
[163] A. P. Shreve, J. P. R. B. Walton, and K. E. Gubbins, J. Chem. Phys. **85**, 2178 (1986).
[164] S. Nosé and M. L. Klein, Mol. Phys. **50**, 1055 (1983).
[165] D. M. Heyes, Phys. Rev. B **49**, 755 (1994).
[166] A. McPherson, *Preparation and analysis of protein crystals*, Krieger Publishing, Malabar (1982).
[167] S. D. Durbin and G. Feher, Ann. Rev. Phys. Chem. **47**, 171 (1996).
[168] F. Rosenberger, J. Crystal Growth **166**, 40 (1996).
[169] A. George and W. W. Wilson, Acta Crytallogr. D **50**, 361 (1994).
[170] E. G. Richards, *An Introduction to physical properties of large molecules in solution*, Cambridge University Press, Cambridge (1980).
[171] T. L. Hill, *An Introduction to Statistical Thermodynamics*, Dover, New York (1986).
[172] M. H. J. Hagen and D. Frenkel, J. Chem. Phys. **101**, 4093 (1994).
[173] A. P. Gast, W. B. Russell, and C. K. Hall, J. Colloid Interface Sci. **96**, 251 (1983).
[174] A. P. Gast, W. B. Russell, and C. K. Hall, J. Colloid Interface Sci. **109**, 161 (1986).
[175] H. N. W. Lekkerkerker, W. C. K. Poon, P. N. Pusey, A. Stroobants, and P.B. Warren, Europhys. Lett. **20**, 559 (1992).
[176] S. M. Ilett, A. Orrock, W. C. K. Poon, and P. N. Pusey, Phys. Rev. E **51**, 1344 (1995).
[177] W. C. K. Poon, A. D. Pirie, and P. N. Pusey, Faraday Discuss. **101**, 65 (1995).
[178] W. C. K. Poon, Phys. Rev. E **55**, 3762 (1997).
[179] C. R. Berland, G. M. Thurston, M. Kondo, M. L. Broide, J. Pande, O. O. Ogun, and G. B. Benedek, Proc. Natl. Acad. Sci. USA **89**, 1214 (1992).
[180] N. Asherie, A. Lomakin, and G. B. Benedek, Phys. Rev. Lett. **77**, 4832 (1996).
[181] M. L. Broide, T. M. Tominc, and M. D. Saxowsky, Phys. Rev. E **53**, 6325 (1996).
[182] M. Muschol and F. Rosenberger, J. Chem. Phys. **107**, 1953 (1997).
[183] A. McPherson, J. Biol. Chem. **251**, 6300 (1976).
[184] A. Kose and S. Hachisu, J. Colloid Interface Sci. **55**, 487 (1976).
[185] C. Smits, J. S. van Duijneveldt, J. K. G. Dhont, H. N. W. Lekkerkerker, and W. J. Briels, Phase Transitions **21**, 157 (1990).
[186] E. J. Meijer and F. El Azhar, J. Chem. Phys. **106**, 4678 (1997).
[187] C. Haas and J. Drenth, J. Crystal Growth **154**, 126 (1995).
[188] A. J Malkin and A. McPherson, J. Crystal Growth **128**, 1232 (1992).
[189] A. J Malkin and A. McPherson, J. Crystal Growth **133**, 29 (1993).

Summary

In this thesis we present a numerical study of pathways for homogeneous nucleation.

In chapter 2 we review the thermodynamics of small droplets. In addition, we discuss the theory that is most widely used to describe the nucleation process, classical nucleation theory. We consider the discrepancy between classical nucleation theory and experiments, and discuss the extensions of classical nucleation theory proposed by McGraw and Laaksonen (J. Chem. Phys. **106**, 5284 (1997)) to resolve the discrepancy. We also present a derivation of the nucleation theorem, which plays an important role in analyzing experimental data as it allows for the determination of the size and composition of the critical nucleus from the measured nucleation rates.

In chapter 3 we study the rate of homogeneous crystal nucleation and the structure of crystal nuclei in a Lennard-Jones system. The height of the nucleation barrier is computed using umbrella sampling, whereas the kinetic prefactor is calculated using molecular dynamics simulation. The simulations show that the barrier crossing is a diffusive process. Nevertheless, the kinetic prefactor is some two orders of magnitude larger than predicted by classical nucleation theory. The height of the nucleation barrier is in fair agreement with classical nucleation theory. Although the Lennard-Jones system is known to have a stable face-centered cubic (fcc) structure below the melting line, the precritical nuclei are found to be body-centered cubic (bcc) ordered. But as they grow, they become more fcc ordered in the core. Yet, in the interface a high degree of bcc ordering is retained. Furthermore, it is found that the density falls of faster than the structural order parameter, which is in agreement with the predictions of density functional calculations (P. Harrowell and D. W. Oxtoby, J. Chem. Phys. **80**, 1639 (1984)) .

In the next chapter, we discuss the choice of the reaction coordinate. Using a global order parameter, precritical nuclei may break up for entropic reasons. At some point, however, the nuclei combine to form a relatively large cluster. We present a method that allows us to avoid the entropic nuclei break up.

In chapter 5 we report on a computer-simulation study of homogeneous gas-liquid nucleation in a Lennard-Jones system. Using umbrella sampling we compute the free energy of a cluster as a function of its size. A thermodynamic integration scheme is employed to determine the height of the nucleation barrier as a function of supersaturation. In agreement with the relations derived by McGraw and Laaksonen (J. Chem. Phys. **106**, 5284 (1997)), we find that the offset between the barrier height as predicted by classical nucleation theory and the height of the nucleation barrier as obtained from the simulations, is constant, and independent of supersaturation. The critical-nucleus size is correctly predicted by classical nucleation theory. Furthermore, our simulations illustrate that the mechanical and the thermodynamical surfaces of tension and surface tensions differ significantly. In particular, we show that the mechanical definition of the surface tension cannot be used to compute the barrier height.

In chapter 6 we compute the rate of homogeneous gas-liquid nucleation in a Lennard-Jones system. We focus on the calculation of the transmission coefficient. The simulations show that the nucleation process is highly diffusive. As a result, the transmission coefficient κ is very low, $\kappa = 0.003 \pm 0.002$. Nevertheless, the kinetic prefactor is about one order of magnitude larger than predicted by classical nucleation theory.

In the next chapter, we report on a study of homogeneous gas-liquid nucleation in a binary Lennard-Jones mixture. We investigate the size and composition of the critical nucleus as a function of the composition and supersaturation of the vapor. As we make the mixture increasingly non-ideal, we find that there is a regime, where the species in the critical nucleus are still miscible, even though in the bulk liquid phase they are not. When these critical nuclei grow, their composition "bifurcates" to approach the value of one of the two bulk phases. For more strongly non-ideal mixtures, the two species in the critical nucleus are no longer miscible: the droplets are rich in one of the two types of species. We do not find evidence for cylindrical, micro-phase separated nuclei, as suggested by Talanquer and Oxtoby (J. Chem. Phys. **104**, 1993 (1996)). Our simulations show that such demixed clusters have a higher free energy than critical nuclei that have an asymmetric composition and therefore probably play no important role in the nucleation process.

In chapter 8 we study homogeneous gas-liquid nucleation in a model for strongly polar fluids. While the measured nucleation rates of non-polar substances are in fair agreement with the predictions of classical nucleation theory, the nucleation rates of strongly polar substances are seriously overestimated by the theory. Several nucleation scenarios have been proposed, in which the anisotropic nature of the interaction potential is taken into account. However, the picture that emerges from the simulations is different from the theoretical predictions. The simulations show that the nucleation process is initiated by chain-like clusters. As the cluster size is increased, the chains become longer. However, beyond a certain size, the chains collapse to form compact, spherical clusters. Nevertheless, in the interface a high degree of chain formation is preserved. As a consequence, the interface of the collapsed nuclei differs markedly from the planar interface. This could explain why classical nucleation theory underestimates both the size of the critical nucleus and the height of the nucleation barrier.

Finally, in chapter 9, we report on a numerical study of homogeneous crystal nucleation in a model system for globular proteins. Proteins are notoriously difficult to crystallize. The experiments indicate that the success of protein crystallization depends very sensitively on the physical conditions of the initial solution. In particular, it has been found that the proteins only crystallize in a rather narrow region in the phase-diagram. However, the origin of this crystallization "window" remained unclear. Our simulations show that the presence of a metastable critical point drastically changes the pathway for the formation of a critical nucleus. Near the critical point, the nucleus that is formed initially is not simply a small crystallite, but rather a high-density liquidlike droplet. Only when this liquidlike droplet has reached a certain size, does it start to crystallize inside the core. More importantly, the alternative pathway that is followed near the critical point, strongly reduces the height of the nucleation barrier and hence increases the nucleation rate by many orders of magnitude. As the location of the metastable critical point can be controlled by changing the solvent conditions, the simulations suggest a more systematic approach to promote protein crystallization.

Samenvatting

Iedereen weet dat water bevriest bij nul graden Celcius, en kookt bij honderd graden Celcius. Water kan dus verschillede vormen of fasen aannemen. Elke fase heeft zijn eigen karakteristieke eigenschappen. Toch zijn de bouwstenen van water in zijn verschillende verschijningsvormen steeds dezelfde.

De verschillen in eigenschappen worden bepaald door de manier waarop de bouwstenen in de fasen zijn gerangschikt. Stel dat we met een enorm sterke microscoop, die zo'n miljard keer vergroot, naar een glas water zouden kijken. Een momentopname van wat we dan zien is hieronder, in het midden, schematisch weergegeven. We zien geen

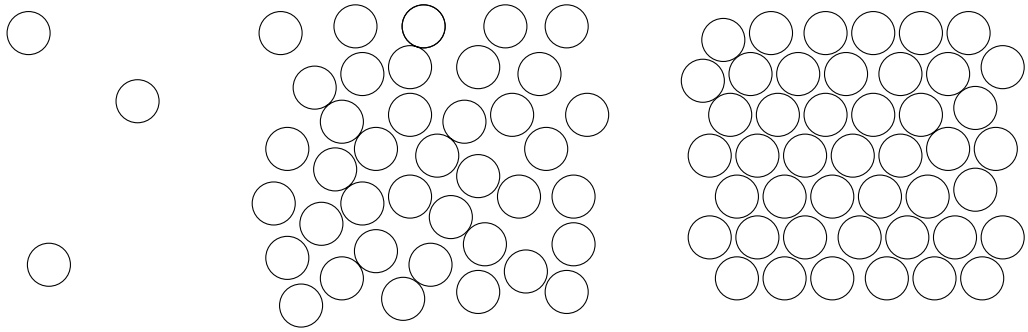

gladde, continue vloeistof meer, maar deeltjes, met gaten daartussen. Deze deeltjes zijn de watermoleculen en vormen de bouwstenen van het water. Ze bewegen kriskras door elkaar, botsen tegen de wand van het glas, en botsen tegen elkaar. Toch blijven ze bij elkaar in de buurt - het water verdwijnt niet uit het glas. De reden is dat de moleculen elkaar op afstand aantrekken. Maar op korte afstand stoten de moleculen elkaar weer af; ze kunnen dan ook niet in elkaar door dringen.

Als we het water verwarmen, zien we dat de moleculen steeds sneller gaan bewegen. Eerst blijft de onderlinge afstand tussen de moleculen klein. Maar op een gegeven moment zullen de deeltjes zo snel bewegen, dat de attractieve krachten tussen de moleculen niet meer sterk genoeg zijn om ze bijeen te houden: de moleculen stuiven uiteen. Het water raakt aan de kook en maakt dan een *fasenovergang* van de vloeibare fase naar de dampfase. Hierbij verandert de dichtheid, het aantal moleculen per liter, van het water sterk; de dichtheid van stoom is (meestal) vele malen lager dan die van vloeibaar water.

Wat gebeurt er nu als water bevriest? Wanneer de temperatuur van het water verlaagd wordt, zullen de deeltjes steeds langzamer gaan bewegen. Daardoor komen de moleculen dichter bij elkaar te zitten; de dichtheid neemt toe. Net zoals bij het koken, zal op het moment dat het water bevriest, er een plotselinge verandering in de dichtheid optreden. In tegenstelling tot de meeste stoffen, echter, neemt bij water de dichtheid iets af wanneer het bevriest. Dit is ook de reden dat we 's winters kunnen schaatsen. Maar het karakteristieke kenmerk van deze fasenovergang is dat de moleculen zich gaan

ordenen. In ijs bewegen de deeltjes niet meer kriskras door elkaar heen, maar nemen ze een min of meer vaste positie op een rooster in. Dergelijke stoffen, waarin de moleculen gerangschikt zijn volgens een regelmatig patroon, heten kristallijn. Omdat de deeltjes in een kristal nauwelijks meer ten opzichte van elkaar kunnen bewegen, is een kristal vast en hard. Niet alle vaste stoffen zijn overigens kristallijn: zoals in een kristal nemen de deeltjes in sommige stoffen wel vrijwel gefixeerde posities in, maar zijn ze niet 'netjes' geordend. Deze stoffen heten amorf of worden ook wel een glas genoemd.

De fase waarin een stof zich manifesteert hangt niet alleen af van de temperatuur, maar ook van de druk. Terwijl het kookpunt van water op zeeniveau bij 100°C ligt, is het gedaald tot 93°C op 2000 meter hoogte, waar de druk lager is. Op de drukafhankelijkheid van het kookpunt is ook de werking van de snelkookpan gebaseerd. In een snelkookpan wordt water onder hogere druk (dan atmosferische druk) aan de kook gebracht. Door de hogere druk zal het water bij een hogere temperatuur gaan koken, waardoor het eten sneller gaar wordt. In de industrie laat men vaak vloeistoffen kristalliseren door niet zozeer de temperatuur te verlagen, als wel door de druk sterk op te voeren.

Tot nu toe zijn we er steeds vanuit gegaan dat water, bij atmosferische druk, bij nul graden bevriest en bij honderd graden Celcius kookt. Toch is dit niet vanzelfsprekend. Al aan het begin van de achttiende eeuw ontdekte Fahrenheit dat schoon water *onderkoeld* kan worden tot min negen graden Celcius zonder te bevriezen. Pas wanneer hij kleine ijskristallen toevoegde, bevroor het water, en steeg de temperatuur van het ijs-water 'mengsel' naar nul graden, het *coëxistentiepunt*.

De reden dat zuiver water pas na toevoeging van ijskristallietjes bevriest, is dat deze fungeren als kiemen voor het kristallisatieproces. In 'normaal' water, initiëren stofdeeltjes vaak het bevriezen van water. Dit wordt heterogene nucleatie genoemd. Bij afwezigheid van zulke kiemen moet het water als het ware van binnenuit bevriezen. Dit proces, homogene nucleatie genaamd, is veel 'moeilijker', omdat de eerste kiemen, kleine ijskristallietjes, spontaan gevormd moeten worden. In het water bewegen de

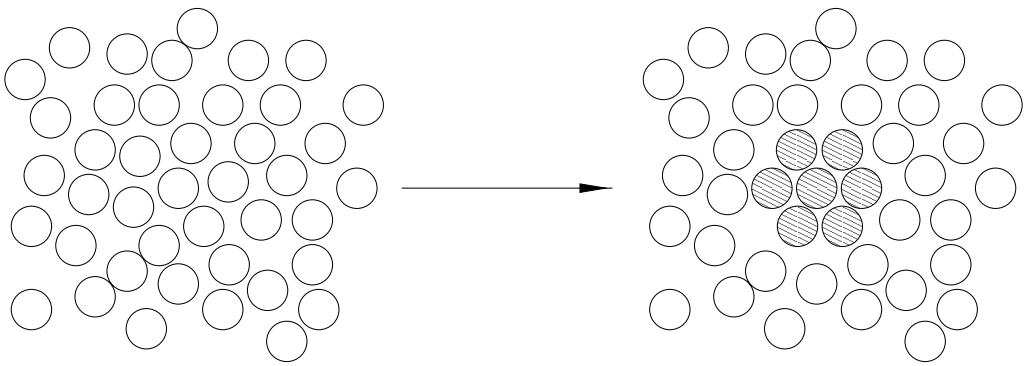

moleculen kriskras door elkaar heen. Om eem kiem te vormen, moet een aantal deeltjes toevallig in een kristallijne configuratie samenkomen. De kans dat door een dergelijke spontane fluctuatie een kristallietje van zo'n zeven deeltjes gevormd wordt, is echter klein, minder dan een honderste per kubieke centimeter. Bovendien zullen de meeste van deze kristallietjes weer oplossen in het water. De kiemen moeten namelijk een bepaalde energiebarrière, de zogeheten nucleatiebarrière, overwinnen om uit te kunnen groeien tot een groot kristal.

Zoals een bal altijd naar het laagste punt rolt omdat het daarmee zijn potentiële energie kan minimaliseren, zo zal een kiem altijd zijn *vrije energie* willen minimaliseren. De energie van een kiem hangt af van zijn grootte, zoals hieronder schematisch is weergegeven[1]. Kiemen op de top van de barrière worden kritieke kiemen genoemd.

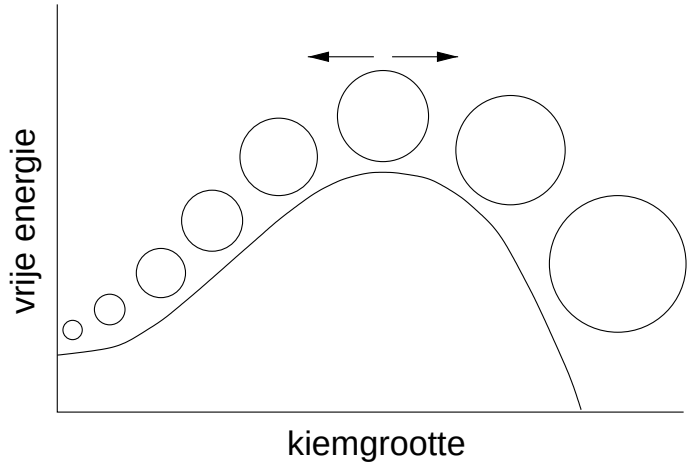

Kiemen die kleiner zijn dan de kritieke kiemgrootte, de zogeheten prekritieke kiemen, kunnen hun energie verlagen door te 'krimpen'; deze kiemen hebben de neiging weer op te lossen in de vloeistof. Kiemen die daarentegen groter zijn dan de kritieke kiemgrootte, de zogenaamde postkritieke kiemen, kunnen hun energie minimaliseren door juist te groeien. Kiemen moeten dus een bepaalde kritieke grootte bereiken om door te kunnen groeien tot een groot ijskristal.

De barrièrehoogte wordt bepaald door de temperatuur en de druk. Bij nul graden Celcius en atmosferische druk, het coëxistentiepunt voor water, is de hoogte van de nucleatiebarrière voor het bevriezen van zuiver water oneindig. Om deze reden zal water, als we het langzaam afkoelen, helemaal niet bevriezen bij nul graden. We moeten de temperatuur eerst verder verlagen om de hoogte van de barrière te reduceren. Pas wanneer het water zo ver is onderkoeld dat de kiemen de barrière kunnen overwinnen, zal het water bevriezen.

De structuur van de kiemen op de top van de barrière bepaalt de hoogte van de nucleatiebarrière en daarmee de snelheid van de fasenovergang. Om deze reden richten alle theorieën zich op het beschrijven van deze kritieke kiemen.

In de meest populaire nucleatietheorie, de zogenaamde klassieke nucleatieheorie, wordt aangenomen dat de kiemen bolvormig zijn. Bovendien wordt verondersteld dat de structuur van de kiemen gelijk is aan de structuur van de fase die uiteindelijk gevormd wordt. Dus, om weer het voorbeeld van water te nemen, er wordt aangenomen dat de moleculen in een klein ijskristallietje (de kiem) opdezelfde manier gerangschikt zijn als in 'bulk' ijs.

Maar welke vaste fase van ijs wordt eigenlijk gevormd? Over het algemeen kunnen stoffen namelijk niet in één vaste toestand voorkomen, maar in verscheidene. Zo is onlangs een negende vaste fase van ijs ontdekt. Bij een gegeven druk en temperatuur is één fase altijd het meest stabiel. Deze fase heeft de laagste vrije energie. Als een

[1] In de genoemde analogie correspondeert de *grootte* van de kiem met de *positie* van de bal.

vloeistof in een andere, minder stabiele vaste toestand is gekristalliseerd, kan de stof in principe zijn vrije energie nog verder minimaliseren, door te transformeren naar de meest stabiele vaste fase. Vaak is dit evenwel niet mogelijk. Dergelijke fasen, die niet meer over kunnen gaan in een stabielere fase, worden *metastabiel* genoemd.

Het lijkt voor de hand te liggen dat als een vloeistof wordt onderkoeld, de meest stabiele vaste fase gevormd zal worden. Dit is immers de meest gunstige eindtoestand voor het systeem. Toch is het voorstelbaar dat het *pad* naar een metastabiele fase 'makkelijker' is, en dat, als gevolg daarvan, een metastabiele structuur gevormd zal worden. Aan het eind van de vorige eeuw formuleerde Ostwald reeds zijn stappenregel, die zegt dat in eerste instantie niet de meest stabiele fase gevormd wordt, maar een fase die meer op de vloeistof 'lijkt'. Ook meer recentelijk zijn er theorieëen ontwikkeld die voorspellen dat niet de meest stabiele structuur wordt gevormd, maar een metastabiele structuur.

Hoewel verscheidene theorieën zijn opgesteld, is ons inzicht op moleculair niveau nog steeds beperkt. Een van de belangrijkste oorzaken is dat de theoretische voorspellingen moeilijk te toetsen zijn in een experiment. Kritieke kiemen worden weinig gevormd. De kans dat een kleine kiem de top van de barrière haalt is minder dan een miljardste. Bovendien, als kiemen de top van de barrière al halen, verblijven ze er maar heel kort, minder dan een duizendste van een milliseconde. Het is dus bijna onmogelijk om de kritieke kiemen in een experiment te kunnen 'zien'. Toch is het precies de structuur en de dynamica van deze kiemen die bepalen welke fase gevormd wordt en hoe snel.

Een 'computerexperiment' kan hier uitkomst bieden. In computersimulaties bootsen we het gedrag van moleculen na. We weten tijdens een simulatie op elk moment waar de moleculen zich bevinden. Dit stelt ons in staat de kiemen op de top van de nucleatiebarrière nauwkeurig te onderzoeken. Bovendien kunnen we een goed inzicht krijgen in hoe deze kiemen gevormd worden. Computersimulaties is dus een zeer geschikt instrument om de *paden waarlangs homogene nucleatie verloopt*, te bestuderen.

In dit proefschrift bestuderen we condensatie en kristallisatie in verscheidene modelsystemen, wat ons in staat stelt een aantal theoretische voorspellingen te verifiëren. In hoofdstuk 2 bieden we achtergrond informatie over de thermodynamica van het nucleatieproces. We leiden in dit hoofdstuk een aantal (standaard) relaties af, die we in de latere hoofdstukken zullen gebruiken.

In hoofdstuk 3 bestuderen we kristalnucleatie in een veelgebruikt model systeem, het zogenaamde Lennard-Jones systeem. De meest stabiele vaste fase beneden het vriespunt is de vlakgecentreerde kubische (fcc) fase. Maar, zoals reeds aangegeven, kristallisatie is in essentie een dynamisch proces, en we mogen niet *a priori* verwachten dat de meest stabiele fase ook daadwerkelijk gevormd zal worden. Meer in het bijzonder, een aantal theorieën voorspelt dat de vloeistof niet in de fcc fase, maar in een metastabiele, lichaamsgecentreerde kubische (bcc) fase zal kristalliseren. Om deze theorieën te toetsen zijn sinds de jaren zeventig jaren verscheidene simulatiestudies uitgevoerd. De resultaten waren echter niet eenduidig: alhoewel in sommige studies aanwijzingen voor de vorming van een bcc fase gevonden werden, vond men in de meeste studies kristallisatie van de fcc fase. Daarnaast moest in al deze studies de vloeistof sterk worden onderkoeld om een nucleatie-event te kunnen waarnemen. Wij hebben een techniek toegepast die het mogelijk maakt om nucleatie bij matige, meer realistische, onderkoeling te onderzoeken.

En, het blijkt dat onze simulaties uitsluitsel kunnen geven over de vraag welke rol de bcc-structuur speelt in het nucleatieproces. Zoals hieronder schematisch is weergegeven, nemen de kiemen die het nucleatieproces initiëren, een bcc structuur aan. Als de kiemen

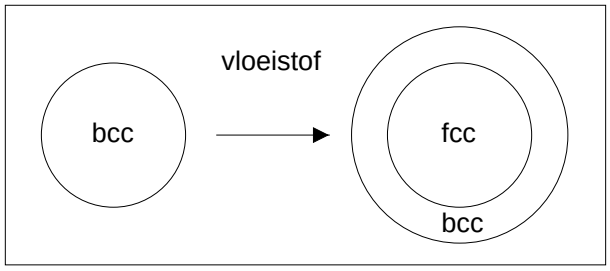

echter groter worden, transformeert hun kern naar de stabiele fcc structuur. Niettemin blijft aan de buitenkant van de kiemen, op het grensvlak met de vloeistof, een sterke mate van bcc-ordening bestaan.

In het volgende hoofdstuk verfijnen we de simulatietechniek, waardoor we beter in staat zijn de prekritieke kiemen te bestuderen. In hoofdstuk 5 passen we de nieuwe techniek toe in een studie naar de nucleatie van een vloeistof druppel vanuit de dampfase. Het modelsysteem is weer het Lennard-Jones systeem. Het blijkt dat de structuur van de vloeistof druppels goed voorspeld wordt door de theorieën. Bovendien stemt de hoogte van de nucleatiebarrière redelijk overeen met de theoretische voorspellingen. Verder gaan we in dit hoofdstuk in op het grensvlak tussen een druppel en de damp. Op moleculair niveau is de grens tussen een druppel en de damp niet scherp - de dichtheid van de moleculen neemt, vanuit het midden van de druppel, *geleidelijk* af. De grens is dus tot op zekere hoogte arbitrair. Het is dan ook mogelijk om verschillende definities van het grensvlak te geven. Tot nu toe werd verondersteld dat de verschillende definities dezelfde locatie van het grensvlak geven. Als gevolg hiervan zou de hoogte van de nucleatiebarrière op een relatief simpele manier uitgerekend kunnen worden. Onze simulaties tonen aan dat de verschillende definities niet equivalent zijn, en dat de eenvoudige manier om de barrièrehoogte uit te rekenen 'fout' is.

De hoogte van de nucleatiebarrière bepaalt het aantal kritieke kiemen. In het volgende hoofdstuk rekenen we de snelheid uit van de kiemen op de top van de barrière. Bovendien bepalen we de *transmissiecoëfficiënt*. De transmissiecoëfficient geeft de fractie kritieke kiemen aan dat daadwerkelijk uitgroeit tot een macroscropische druppel. Als de transmissiecoëfficiënt coëfficient één is, groeien alle kiemen op de top van de barrière uit tot een grote vloeistof druppel. Het nucleatieproces heet dan ballistisch. Over het algemeen zullen echter niet alle druppeltjes doorgroeien. Sommige kiemen zullen toch weer verdampen. Deze kiemen dragen dan niet bij aan de nucleatiesnelheid. De nucleatiesnelheid wordt dus gegeven door het produkt van het aantal kiemen op de top van de barrière, de snelheid van de kiemen op de top van de barrière, en de transmissiecoëfficiënt.

Uit de simulaties volgt dat voor gas-vloeistof nucleatie de transmissiecoëfficiënt erg laag is, veel lager dan het geval is voor kristalnucleatie. Dit komt doordat de top van de nucleatiebarrière op microscopische schaal vlak is, waardoor de kiemen, als ze de top van de barrière hebben bereikt, niet onmiddelijk zullen 'doorrollen' naar de eindtoestand aan de andere kant van de barrière, maar als het ware de tijd hebben om af te remmen, en weer te verdampen.

Tot nu toe zijn we er steeds vanuit gegaan dat alle moleculen in het systeem identiek zijn. In het volgende hoofdstuk bestuderen we de nucleatie van *mengsels* van vloeistoffen vanuit de dampfase. Een belangrijke vraag die met betrekking tot mengsels gesteld kan worden, is of de moleculen mengbaar zijn of niet. Zo mengen bijvoorbeeld water en alcohol heel goed, maar olie en water niet; in het geval van olie en water treedt fasenscheiding op. In hoofdstuk 7 richten we ons voornamelijk op dergelijke mengsels. Wij vonden in de simulaties namelijk dat moleculen zoals olie en water, waarvan je dus zou verwachten dat ze niet goed mengbaar zijn, in kleine druppels wel degelijk goed mengen. De vraag die rijst is: hoe groeien deze kleine druppels, waarin de moleculen gemengd voorkomen, uit tot een vloeistof, waarin de moleculen zijn fasengescheiden?

De simulaties laten zien dat eigenlijk alleen in de allerkleinste druppels de moleculen echt goed mengen. Wanneer de druppels groter worden, verrijken ze zich in één van beide componenten. Toch kan een kleine druppel bestaande uit hoofdzakelijk de ene component, door uitwisseling met moleculen in het gas, nog overgaan in een druppel die rijk is in de andere component, omdat voor kleine druppels de vrije energiebarrière tussen beide soorten druppels laag is. Naarmate de kiemen groter worden, neemt de hoogte van deze barrière toe. Op een bepaald moment zal de barrière zo hoog worden, dat de overgang van het ene type cluster naar het andere niet meer gemaakt kan worden: een druppel is rijk in één van beide componenten, en blijft rijk in diezelfde component.

In hoofdstuk 8 onderzoeken we condensatie in een model voor polaire vloeistoffen. De condensatie van een druppel water, een polaire vloeistof, is waarschijnlijk het bekendste voorbeeld van homogene nucleatie. Het bekendst betekent echter nog niet het best begrepen. Integendeel, terwijl klassieke nucleatietheorie de nucleatiesnelheid van apolaire moleculen redelijk voorspelt, overschat de theorie de nucleatiesnelheid van polaire moleculen aanzienlijk.

Polaire moleculen hebben een positieve 'kop' en een negatieve 'staart'. De interactie tussen twee moleculen is het gunstigst wanneer ze kop-aan-staart liggen. Om de discrepantie tussen theorie en experiment te verklaren heeft men dan ook verschillende nucleatiescenario's opgesteld waarin deze anisotrope wisselwerking tussen de moleculen een belangrijke rol speelt. Zo is bijvoorbeeld voorgesteld dat de druppels niet een bolvorm aannemen, zoals bij apolaire moleculen, maar de vorm van een rugbybal.

De simulaties tonen een geheel ander beeld. De kiemen die het nucleatieproces initiëren zijn geen compacte druppels, maar ketens, waarin de moleculen kop-aan-staart liggen. In eerste instantie, als het aantal moleculen in de ketens toeneemt, worden de ketens langer. Bij een bepaalde grootte, echter, 'klonteren' de ketens plotseling samen en vormen de moleculen alsnog een compacte druppel. Aan de buitenkant van de druppels blijven niettemin de ketens bestaan, zoals hieronder in 'snapshots' van de simulaties is te zien.

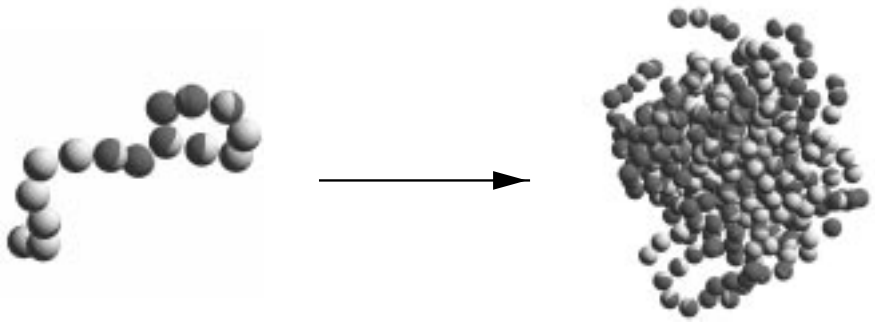

Hoofdstuk 9, tenslotte, gaat over eiwitkristallisatie. Ten gevolge van de snelle ontwikkelingen in de biotechnologie worden steeds meer eiwitten geïsoleerd. Het bepalen van de drie-dimensionale structuur van de eiwitten met behulp van röntgendiffractie, is echter nog steeds een tijdrovend proces. Eén van de redenen is dat eiwitten moeilijk te kristalliseren zijn. De experimenten laten zien dat eiwitten alleen onder hele specifieke condities kristalliseren. Bovendien zijn deze condities vaak niet op voorhand te bepalen. Met als gevolg dat eiwit kristallisatie voornamelijk een kwestie van trial and error is.

De computersimulaties die we hebben uitgevoerd aan een model voor bolvormige eiwitten, hebben onthuld waarom deze eiwitten alleen onder bepaalde condities makkelijk kristalliseren. Onder deze condities treden sterke dichtheidsfluctuaties in het systeem op. Deze dichtheidsfluctuaties veranderen het pad voor de vorming van kritieke kiemen drastisch. In afwezigheid van de sterke dichtheidsfluctuaties wordt het reguliere scenario gevolgd, waarbij kristallijne kiemen het kristallisatieproces initiëren.

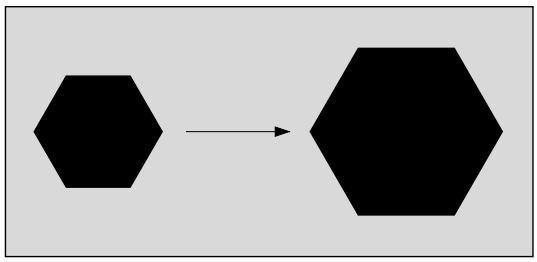

In aanwezigheid van de sterke dichtheidsfluctuaties kristalliseert het eiwit volgens de Ostwald stappenregel. In eerste instantie worden helemaal geen kristallijne kiemen gevormd. Door de sterke dichtheidsfluctuaties is het mogelijk om eerst druppels te vormen, waarin de eiwitten dichter bij elkaar zitten dan in de omringende vloeistof. Pas in de tweede stap treedt kristallisatie op: als de vloeistof druppels groot genoeg zijn, kristalliseren ze van binnenuit tot kristallijne kritieke kiemen; de kristallijne kritieke kiemen groeien vervolgens uit tot een groot kristal.

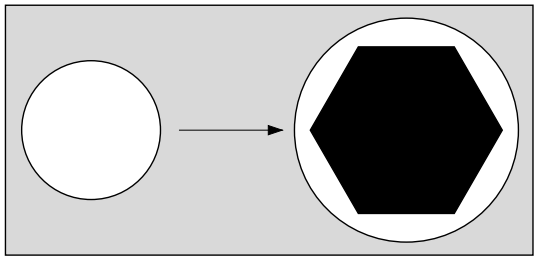

Het is dus duidelijk dat de sterke dichtheidsfluctuaties het pad waarlangs homogene nucleatie verloopt, beïnvloeden. Maar waarom vergemakkelijkt dit ook het kristallisatieproces? Het antwoord is dat het alternatieve pad, dat door deze dichtheidsfluctuaties gevolgd kan worden, de nucleatiebarrière sterk verlaagt, met zo'n 30%. Dit klinkt misschien niet zo veel. Maar omdat de nucleatiesnelheid sterk af hangt van de hoogte van de nucleatiebarrière, betekent deze reductie in de barrièrehoogte dat de nucleatie in aanwezigheid van deze dichtheidsfluctuaties meer dan een biljoen keer sneller verloopt.

Dankzij de simulaties begrijpen we nu waarom eiwitten onder bepaalde condities sneller kristalliseren. Wellicht dat de resultaten van de simulaties leiden tot een meer gerichte aanpak van eiwitkristallisatie.

Dankwoord

Vanaf deze plaats wil ik een aantal mensen bedanken die hebben bijgedragen aan de totstandkoming van dit proefschrift. Allereerst wil ik mijn promotor, Daan Frenkel, bedanken. Zijn enthousiaste reacties op nieuwe resultaten hebben mij altijd zeer gestimuleerd. Bovendien heb ik genoten van de discussies die wij hebben gevoerd. Dat ik Daan in de discussies niet alijd kon bijbenen, heeft voor mij het plezier nooit kunnen drukken. Integendeel, zijn originele ideeën, en zijn gave om elegante verklaringen en oplossingen voor problemen te vinden, hebben veel indruk op mij gemaakt.

I would like to thank David Oxtoby for the nice time I had in Chicago. The work I performed at the James-Franck institute was the starting point for the study on gas-liquid nucleation of polar fluids discussed in chapter 8. The James-Franck institute is a good place to work, not only because of the enthusiastic people, but also because of the basketball games on every Monday and Thursday. And Chicago is definitely one of the most impressive cities I have seen in my life so far.

It is a pleasure to thank Maria-José Ruiz-Montero. I enjoyed our collaboration, that resulted in chapter 3 and chapter 6.

Ook wil ik alle collega's van het Amolf bedanken. Het plezier in het werk wordt niet in de laatste plaats door de sfeer op de werkvloer bepaald. In dit verband wil ik met name Maarten Hagen noemen. Zijn immer positieve instelling heeft er toe geleid dat het met mijn werk wel goed moest gaan. Ronald Blaak wil ik graag bedanken voor de hulp die hij geboden heeft bij het maken van de 'snapshots'. En Evert Jan Meijer bedank ik voor het uitrekenen van een gedeelte van het fasendiagram in hoofdstuk 9. Ook Bela Mulder wil ik graag met naam noemen. De genoeglijke stemming tijdens de gesprekken over de boeken van Voskuil en andere onderwerpen zullen mij lang bijblijven. Paul Schuddeboom bedank ik voor de vele briefwisselingen die we per email hebben gevoerd - alhoewel ik nog steeds geloof dat beter pianospelen een kwestie is van harder studeren.

Als computersimulator heb je misschien niet zo veel technische ondersteuning nodig. Toch wil ik graag Jan van Elst, Ben Ockhuysen en de mensen van het rekencentrum SARA bedanken voor de snelle assistentie die ze altijd hebben verleend bij computerstoringen, problemen met de printer, of als ik weer nieuwe schijfruimte nodig had.

Furthermore, I would like to thank my sparring partner in the discussions about the thermodynamics of nucleation, Ignacio Pagonabarraga. Without the stimulating discussions I would still be struggling with the Tolman-length, the mechanical and thermodynamic definitions of surface tensions, and many other aspects of this tricky subject. The difficulty with the thermodynamics of small droplets is not so much in deriving relationships between thermodynamic quantities. Rather, the problem is judging whether the obtained expressions are useful, because they can easily be identities or even incorrect. In this respect I would like to thank Edgar Blokhuis, who was often consulted as referee when Ignacio and I had opposite opinions.

Mijn ouders bedank ik voor de vele kritische vragen die ze altijd hebben gesteld. Door de moeilijke 'lekenvragen' werd ik gedwongen goed na te denken over het onderzoek. Maar als laatste wil ik graag Heleen bedanken, vanwege alle steun die ze mij al die jaren heeft gegeven.